ADVANCED SIMULATION OF DEBRIS FLOWS BASED ON A MULTI-PHASE SMOOTHED PARTICLE HYDRODYNAMICS

馬, 楊帆

https://hdl.handle.net/2324/7329487

出版情報：Kyushu University, 2024, 博士（工学）, 課程博士
バージョン：
権利関係：

ADVANCED SIMULATION OF DEBRIS FLOWS BASED ON A MULTI-PHASE SMOOTHED PARTICLE HYDRODYNAMICS

Yangfan Ma

ADVANCED SIMULATION OF DEBRIS FLOWS BASED ON A MULTI-PHASE SMOOTHED PARTICLE HYDRODYNAMICS

A Thesis Submitted
In Partial Fulfillment of the Requirements
For the Degree of
Doctor of Engineering

By
Yangfan Ma

九州大学

to the
DEPARTMENT OF CIVIL AND STRUCTURAL ENGINEERING
GRADUATE SCHOOL OF ENGINEERING
KYUSHU UNIVERSITY
Fukuoka, Japan

July, 2024

DEPARTMENT OF CIVIL AND STRUCTURAL ENGINEERING
GRADUATE SCHOOL OF ENGINEERING
KYUSHU UNIVERSITY
Fukuoka, Japan

CERTIFICATE

The undersigned hereby certify that they have read and recommended to the Graduate School of Engineering for the acceptance of this thesis entitled, "***Advanced Simulation of Debris Flows based a Multi-Phase Smoothed Particle Hydrodynamics***" by **Yangfan Ma** in partial fulfillment of the requirements for the degree of **Doctor of Engineering**.

Dated: July, 2024

Thesis Supervisor:

____

Prof. Mitsuteru ASAI, Dr. Eng.

Examining Committee:

____

Prof. Kasama Kiyonobu

____

Prof. Gonghui Wang

ABSTRACT

Catastrophic debris flow, characterized as rapid, gravity-driven heterogeneous mixtures of viscous fluid and solids, are complex in terms of material composition and exhibit unpredictable spatiotemporal evolution. These phenomena pose one of the greatest threats to human society due to their high flow velocity, extreme impact force, and extensive run-out distances. Due to their complex physical nature, the prediction, modelling, and theoretical description of debris-flow physical processes remain acknowledged as open and multidisciplinary challenges in earth science. This thesis addresses the major unresolved issues in the numerical analysis of debris flows by developing and applying advanced numerical simulation methods.

Smoothed particle hydrodynamics (SPH) is widely used in hydrodynamic problems and geotechnical engineering due to its superior ability to handle large deformations, free surface flows, and post-failure scenarios. The discrete element method (DEM), on the other hand, offers unparalleled insight into the discontinuous and heterogeneous nature of granular materials. These particle type simulation models have great potential to solve several open questions in numerical soil flow analysis. The first major issue is the modeling of erosion, entrainment, and deposition, which are the primary processes in debris flows. These processes exhibit morphological changes, and phase changes from solid to fluid, and vice versa. Erodible beds can then increase the total mass and momentum of debris. This phenomenon is referred to as positive feedback of debris flow and can be negative in the case of dry sediments. Positive and negative feedbacks of debris flow are secondary major issues. By addressing the open questions in modeling debris flows, this paper proposes a two-layer multiphase smoothed particle hydrodynamics (TLMP-SPH) model for simulating viscous debris flows. In addition, a coupled SPH-DCDEM scheme is also developed by combining the DEM for boulder-rich debris flows. Finally, the application of these advanced simulation models to field-scale disaster prediction is discussed.

In this thesis, these issues are discussed in detail and appropriately addressed.

The contents of this study are organized as follows:

Chapter 1 presents the background, scope, and objectives of the study, along with an outline of the thesis organization. It details the classification and triggers of debris flows and emphasizes the threats posed by debris flows and the associated disaster chains. Additionally, it briefly discusses the methodologies available for analyzing these disasters.

Chapter 2 offers a detailed review of debris-flow prediction and numerical simulation methods. It then concentrates on the research frontiers, engineering application, and existing issues of SPH and DEM. Furthermore, it introduces the fundamental theories of the SPH and SPH-DEM coupled methods utilized in this study.

Chapter 3 develops a Two-Layer, Multi-Phase SPH (TLMP-SPH) model to simulate the rheological characteristics and dynamic processes of viscous debris flows, including erosion, entrainment, and deposition. It begins with a comprehensive introduction to various rheological models of debris flows and their implementation in the SPH scheme. The Herschel-Bulkley-Papanastasiou (HBP) rheological model is integrated with different yield criteria to capture complex processes such as erosion and entrainment. To ensure stable phase transitions on steep terrains, a specific phase transition model is developed. Finally, several numerical tests are conducted for verification. This study offers an innovative paradigm based on multiphase flow particle modeling, potentially informing better analysis and prediction.

Chapter 4 pioneers a hydro-poro-mechanics-based pore water pressure algorithm embedded within the TLMP-SPH scheme to simulate the pore pressure response and flow momentum growth of debris flows on beds with varying wetness. To address scale effects, this method is rigorously tested and validated through a series of large-scale flume experiments conducted by the United States Geological Survey (USGS). The findings reveal that the model proficiently captures and replicates the intricate dynamics of flow momentum growth, reflected in erosion-induced variations in volume and mobility. Our methodology establishes a definitive link between volumetric water content and pore pressure response, further emphasizing its ability to characterize levee-channel and deposition morphology. This study represents the first attempt to model debris flow on beds of varying wetness from a particulate perspective.

Chapter 5 constructs a two-way resolved SPH-DCDEM coupling scheme for dynamic simulation of boulder-rich debris flows. In this approach, fine-grained materials and viscous fluid are generalized to a viscoplastic flow following the HBP non-Newtonian flow dynamics. The DCDEM represents irregular boulders with much larger particle scales, explicitly defining the interaction forces between fluid and solids, and among solid particles. Similarly, numerical tests on the collapse of multi-layered aluminum columns and debris-flow impacting on varying sloping bed are conducted. The results indicate the capability of the applied approach in both solid-solid and solid-fluid systems.

Chapter 6 extends the proposed method to field-scale hazard prediction, applying it to real-world cases, including the 2010 Yohutagawa debris-flow event in Japan and the 2010 Hongchun Gully debris-flow event in China. The first example is simulated using TLMP-SPH for the viscous-type debris flow, while the second simulation utilizes the two-way resolved SPH-DCDEM. These simulation results successfully reproduce the dynamic processes of both events, particularly depicting the deposition morphology on the alluvial fan. By adjusting the water content of the bed sediment, the entrainment volume in the Yohutagawa event is calibrated. This study demonstrates the potential of the proposed TLMP-SPH multiphase flow model for practical engineering applications.

Chapter 7 summarizes the conclusions of the study and proposes recommendations for future research.

ACKNOWLEDGMENTS

During my time pursuing a Ph.D. with the Structural Analysis Laboratory and the Geo-disaster Prevention Laboratory at Kyushu University, I experienced one of the most rewarding periods of my academic career. The freedom, rigor, and pursuit of truth that characterize the academic atmosphere here have greatly benefited me. The Department of Civil and Structural Engineering at Kyushu University provided me with a robust platform and ample support for my research. There are many people I should thank; without their invaluable assistance, this dissertation would not have been possible.

First and foremost, I would like to express my heartfelt gratitude to my supervisor, Prof. Dr. Mitsuteru Asai. Two years ago, when I faced the significant decision of changing research groups, he welcomed me without hesitation and has been a dedicated guide for my research ever since. Especially during the early stages when I encountered bottlenecks in my research, his patient instruction and understanding were invaluable. Throughout my Ph.D. studies, he provided me with the best research environment and a stimulating academic atmosphere, from which I greatly benefited. He imparted professional knowledge, scientific thinking, technical skills, and the essential abilities needed for research. Every discussion and lecture with him were immensely enlightening, and our collaboration and interactions were always enjoyable. He consistently offered insightful solutions to the challenges I faced in my research. Without his profound insights and valuable advice, completing this dissertation would have been exceedingly difficult.

I would like to express my sincere gratitude to another supervisor, Prof. Dr. Guangqi Chen, for his invaluable guidance and advice on my research. Three years ago, he accepted me as a Ph.D. student and helped me secure the Chinese Government Scholarship for overseas studies, allowing me to pursue my studies in Japan. I am truly grateful to him. His extensive knowledge and rigorous academic standards have greatly influenced me. The COVID-19 prevented me from traveling to Japan during my first year of doctoral studies, hindering my research progress.

Fortunately, Professor Chen frequently organized online group meetings, providing continuous guidance and support throughout my studies. He is a dedicated scholar who invests significant time and effort into scientific research, and his commitment has continually inspired and motivated me in my own research endeavors.

I would also like to express my sincere gratitude to my master's supervisor, Prof. Dr. Zheng Han at Central South University, China. He guided me step-by-step into the world of scientific research and provided me with the opportunity to study abroad. As a young and outstanding scholar, he is active in the fields of geological disaster prevention and numerical computation. Throughout my doctoral studies, I consistently benefited from his valuable guidance and support. Without his selfless dedication, I would not have achieved what I have today. I aspire to follow his example and continue pursuing the path of truth and exploration.

I would like to express my deepest gratitude to members of my dissertation committee, Prof. Dr. Mitsuteru Asai, Prof. Dr. Gonghui Wang, and Prof. Dr. Kiyonobu Kasama, for their valuable time and effort in reviewing my thesis.

I wish to extend my heartfelt thanks to all the friends and colleagues in Geo-disaster Prevention Laboratory and Structural Analysis Laboratory, particularly Dr. Jingyao Gao, Dr. Hongyun Fan, Dr. Rongfu Yan, Dr. Chi Lu, Dr. Yi Li, Dr. Kumpei Tsuji, Dr. Yifei Zhao, Dr. Mengxia Han, Mr. Zhiyuan Li, Mr. Chaofan Feng, Mr. Changze Li, Mr. Wenming Wang, Mr. Junyan Yu, Mr. Gaoyuan Lv, Mr Nuofeng Lin, Mr. Ziqi Gao, Mr. Zhi Li, Mr. Jiale Xu, Mr. Shota Deguchi, Mr. Shujiro Fujioka, Ms. Siyu Peng, Ms. Yifang Qin, Ms. Souphavanh SENESAVATH. I would also like to extend my sincere thanks to all my friends in China, Japan, and other countries.

I would like to acknowledge the China Scholarship Council (CSC) for providing me with the opportunity and scholarship to pursue my doctoral degree at Kyushu University.

Most importantly, I am deeply grateful to my parents, grandmother, girlfriend, and other family members for their love and encouragement. Their unwavering support and understanding throughout my research and daily life have been crucial to my pursuit of a doctoral degree.

TABLE OF CONTENTS

LIST OF FIGURES

List of Tables

GLOSSARY

Symbols

α, β, γ	Cartesian tensor coordinate directions (superscripts)
i, j	Target and neighboring particles (subscripts)
F	Function of a numerical or physical variable
Ω	Domain of interests, support domain of SPH
$\delta(x-x')$	Dirac delta function
$<\ldots>$	SPH interpolation and approximation
h	SPH smoothing length, the size of the kernel's support domain
W	Weighting or kernel function
$R=\left\|x_i-x_j\right\|/h$	Non-dimensional distance between particles
α_d	Dimensional normalizing factor for kernel function
V	Total volume
m	Mass
ρ	Density
N	Number of total particles within support domain
∇	Gradient (nabla) operator
$\mathbf{f(x)}$	SPH approximation of a vector quantity
$(\nabla\cdot\mathbf{f})$	SPH approximation of its divergence
S^i	The region of interior particles truncated by the boundary
$\tilde{W}$	Kernel correction term
$\nabla\tilde{W}$	Correction gradient operator
L_i	Correction matrix
∇^2	Laplace operator
$\mathbf{v}$, $\boldsymbol{\sigma}$, $\mathbf{g}$	Vectors of velocity, stress, and gravity
Γ	Dissipated term
P	Isotropic pressure
$\boldsymbol{\tau}$	Viscous stresses
γ	Isentropic coefficient

c_s	Numerical speed of sound
ξ	Numerical speed coefficient
μ_w	Total viscosity of water
$\dot{\boldsymbol{\varepsilon}}^{\alpha\beta}$	Deviatoric strain rate
Π_{ij}	Artificial viscosity term
$\bar{c}_{ij}$, $\bar{\rho}_{ij}$, $\bar{h}_{ij}$	Mean speed of sound, density, and smoothing length
a_{bd}	Artificial viscosity coefficient
υ_k	Kinematic viscosity
$\vec{\tau}_{ij}$	Sub-particle stress tensor
v_t	Turbulent eddy viscosity
Δl	Particle space
C_s	Smagorinsky constant
δ_d	Dimensionless coefficient in density diffusion term
ψ_{ij}^{α}	Bulk viscosity diffusion operator
ρ_{ij}^{H}	Hydrostatic pressure difference between particle pairs
Ns	Intermediate step used in Verlet scheme
Δt	Variable time-step
Co	Courant number
D'	Diffusion coefficient
C	Particle concentration
$\mathbf{Fr}$	Particle shifting magnitude
$\mathbf{n}$, $\mathbf{s}$	Normal and tangent unit vector
$\mathbf{b}$	Bi-tangent unit vector
M_I	Body mass
$\mathbf{I}_I$	Inertial tensor
$\mathbf{\Omega}_I$	Angular velocity
$\mathbf{R}_I$	Center of gravity
$\mathbf{F}_n$, $\mathbf{F}_t$	Normal and tangential components of contact force
e_n	Degree of dissipation in DEM
$k_{n,ij}$	Stiffness constant between particles
δ_{ij}	Particle overlap

$\mathbf{e}_{ij}$	Unit vector directed from one mass center to the other
$\gamma_{n,ij}$	Damping constant
$\dot{\delta}_{ij}$	Rate of normal deformation
C_n	Empirical tuning parameter
E	Young modulus
υ	Poisson ratio
μ_f	Friction coefficient
μ_{eff}	Effective viscosity term
μ	Apparent dynamic viscosity
τ_y	Yield stress
$\dot{\boldsymbol{\gamma}}$	Shear strain rate
Π_D	Second invariant of the strain rate tensor
c	Cohesion
φ	Internal friction angle
p_w	Pore water pressure
α_φ, κ_c	Yield coefficients in Drucker-Prager Criterion
J_2	Second invariant of the deviatoric shear stress tensor
n_s, n_w	Volume fractions of the solid and water phase
K_w, K_a	Bulk modulus of water and air
$\mathbf{q}_w$	Vectors of Darcy velocity
$\mathbf{F}$	Vector of external body force
k	Hydraulic conductivity
γ_w	Unit weight of water
H_e	Elevation head
$\boldsymbol{\varepsilon}_t$, $\boldsymbol{\varepsilon}_w$, $\boldsymbol{\varepsilon}_a$	volumetric strain rate of total, pore water, and air
S_r	Saturation degree
n_w	Volumetric water content

CHAPTER 1

INTRODUCTION

1.1. BACKGROUND

The term "*debris flow*" embraces a large variety of phenomena, including "*debris slides*", "*debris torrents*", "*debris floods*", "*mudflows*", "*mudslides*", "*mud spates*", "*lahar flow*", "*debris avalanche*" and "*Yama-tsunami*" (Pierson and Costa 1987; Iverson et al. 1997; Takahashi 2007; Han 2015). As rapid, gravity-driven heterogeneous mixtures of viscous fluid and solids (Iverson et al. 2010; Pudasaini and Fischer 2020), debris flows are distinct from related events such as rock avalanches, turbidity currents, and sediment-laden water floods based on two fundamental characteristics: (i) both solid and fluid forces strongly influence the motion, and the momentum transfer between each phase synergistically sustain the type of motion (Iverson et al. 1997; Takahashi 2007), and (ii) they exhibit poor sortability with a variety of material compositions. As depicted in Figure 1.1, geophysical flows are characterized by their multiscale nature (rock, debris, mud, water, snow, and ice), and multiphase composition (solid, fluid, air) (Pudasaini and Mergili 2019); however, a genuine multi-phase model capable of quantifying and modeling those hazardous phenomena is still lacking. On one hand, such unsteady and inhomogeneous flows, complex in their spatiotemporal evolution, are difficult to reproduce in the laboratory due to heterogeneity and scale effects (Iverson et al. 2010; Mangeney et al. 2010; Iverson et al. 2011; Iverson 2015; Haas and Woerkom 2016; Delannay et al. 2017). On the other hand, because the nonlinear coupling and feedback mechanisms of erosion, deposition, and phase transition remain poorly understood, the evolving volume, run-out extent, and impact force of these flows are often largely underestimated (Pudasaini and Krautblatter 2021).

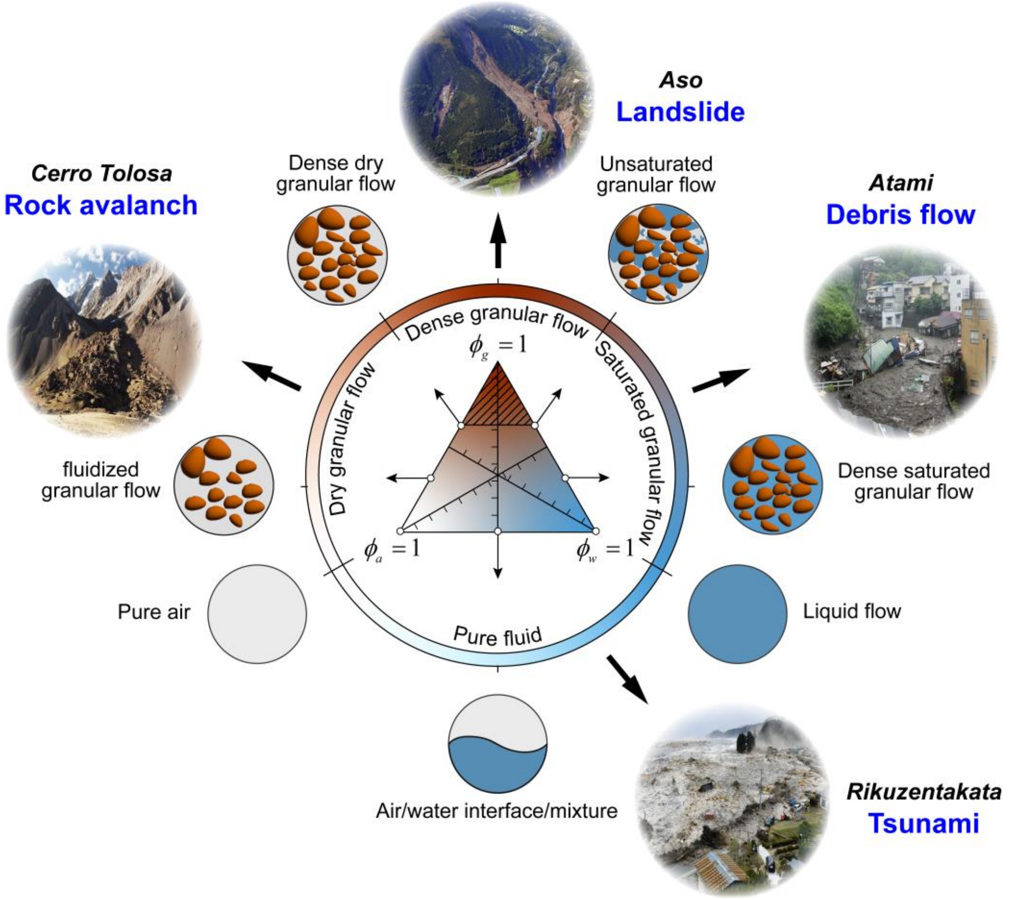

Figure 1.1 Various gravity-driven geophysical flow disasters and their material compositions.

1.1.1. Catastrophic debris flows in recent decades

Debris flows are among the most hazardous geophysical phenomena, posing substantial threat to human society due to their rapid flow velocity, extreme impact force, and extensive run-out distances (Hürlimann et al. 2019; Ma et al. 2023). Such events transpire in partial or complete liquefaction beds prone to erosion, play a significant role in the global sediment cycle (Syvitski et al. 2022) and landscape evolution (Stock and Dietrich 2003; Berger et al. 2011b; Iverson et al. 2011; Perron 2017). Given the increased landscape exploitation and climate instability, along with a recent estimate that about 8.2% of the global population live in landslide-prone regions (Jia et al. 2021), an escalation in debris-flow disasters is anticipated (Gariano and Guzzetti 2016; Mondini et al. 2023).

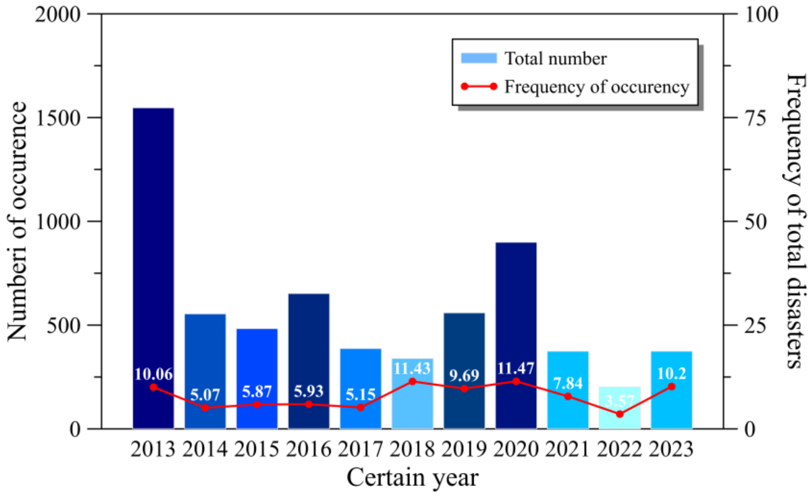

Figure 1.2 Statistics on debris flow disasters in China over the past decade (Source: Ministry of Natural Resources, PRC, www.mnr.gov.cn).

Over the last two decades, debris flow and process chains have caused more than 700 billion yen in damage and 525 fatalities in Japan (Shinohara and Kume 2022). In China, 6,370 catastrophic debris flow events were reported from 2013 to 2023, accounting for 5 to 10 percent of all geological disasters each year, as detailed in Figure 1.2. Many hazardous debris-flow events, which have resulted in catastrophic and economic losses, have been reported in recent decades. For instance, a recent study (Zhang and Zhang 2017) indicates that in the Wenchuan earthquake-affected area, the volume of active landslides has decreased by over 70% in recent years. However, debris flow frequency fluctuated with rainfall, causing several major events. Notable examples include the September 2008 event in Beichuan (Tang et al. 2009; Zhang and Zhang 2017), the August 2010 events in Yingxiu (Figure 1.3a), Dujiangyan, and Qingping (Tang et al. 2012; Xu et al. 2012; Yu et al. 2013), and the August 2019 event in Wenchuan (Chen et al. 2021; Xiong et al. 2021). These events have become a persistent threat in active fault regions after earthquakes, with debris-flow activity potentially lasting up to 30 years before returning to pre-earthquake levels (Cui et al. 2011; Yang et al. 2023). Another recent event (Figure 1.3b) occurred in Atami, Japan, causing 27 deaths and destroying 136 buildings (Zhang et al. 2022). Additionally, the 2024 Noto Peninsula earthquake induced at least 281 landslides that cut off roads and isolated villages, greatly increasing the number of casualties (Gomez 2024).

(a)

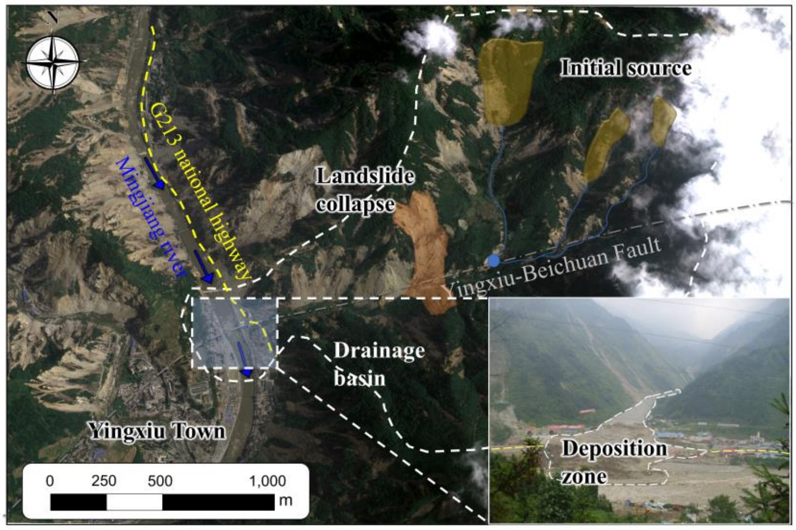

(b)

Figure 1.3 (a) Image of the 2010 Yingxiu debris-flow event in China. Modified from Ma et al. (2023). (b) Image of the 2021 Atami debris-flow event, data from www.straitstimes.com/global.

As the world population and urbanization continue to increase, the overall impacts of debris flows are expanding on a global scale. As of 2011, a total of 230 events with 77,779 fatalities have been recorded (Dowling and Santi 2014), and susceptibility to such events is still increasing (Kurilla and Fubelli 2022). To sum up, the potential threat of debris flows and their associated hazard chain processes will persist, underscoring the urgent need for more comprehensive research into their dynamic mechanisms, prevention and control measures, and predictive modeling techniques.

1.1.2. Types of debris flow and triggering factors

Debris flows typically consist of a heterogeneous mixture of fine particles (clay, silt, and sand) and coarse materials (gravel, cobbles, and boulders) with varying amounts of pore fluid (Winter et al. 2005; Pudasaini and Mergili 2019). Various classifications of debris flows have been proposed. Among these schemes, the one proposed by Takahashi (2007) is widely recognized, who developed a classification scheme and existence criteria for debris flows in a broader sense based on the concentration of coarse particles, distinguishing between: (i) the quasi-static debris flow, where Coulomb friction stress dominates, and (ii) dynamic debris flows. Further, dynamic debris flows can be sub-classified into "*stony-type*", "*turbulent-muddy-type*", and "*viscous-type*" based on the dominant stresses, as illustrated in Figure 1.4. These three flow regimes are dominated by particle collision stress, turbulent mixing stress, and viscoplastic stress, respectively. The more general case corresponds to a "*hybrid-type*" where these three stresses combine to form the total inner shearing stress. When the concentration exceeds the threshold value of 0.50, as recommended by Campbell (1990)), the quasi-static Coulomb stress becomes dominant, causing the flow to transition into quasi-static motion. Considering that both collision and turbulent stress are caused by inertial motion, Takahashi (2009) further included the stony, hybrid, and turbulent-muddy debris flows under the category of "*inertial debris flow*", where inertial stress dominates the flow dynamics and the Bagnold number (Bagnold 1954) is large. By contrast, the viscous-type contain large amounts clay or mud slurry, which occur in areas with a low Reynolds number is defined as "hyper-concentrated flow" (Pierson 1980; Major and Pierson 1992), with plastic strength resulting from interstitial viscous fluid. For each specific type of debris flow, different rheological models typically adopt one of the two aforementioned mechanisms.

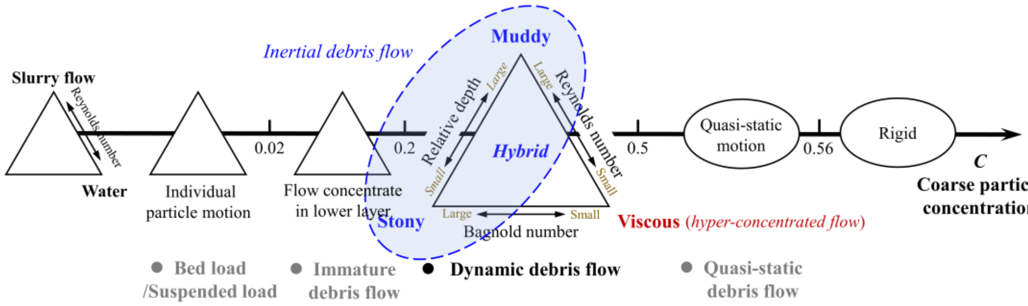

Figure 1.4 Classification of debris-flow types based on concentration of coarse particle and dominant stresses, modified from Takahashi (2007).

Based on the topographic and geological characteristics of occurrence locations, Winter et al. (2005) distinguished between two forms of debris flows: hillslope (open-slope) debris flows and channelized debris flows. The former primarily occurs on hillsides or steep slopes, forming sheet tracks or merging into existing ditches (Cruden 1996). These flows may move rapidly and are often accompanied by large amounts of soil, rock, and vegetation; however, their flow paths are usually shorter. In contrast, the flow dynamics of channelized type follow the topographic features and therefore more directly affected by the morphology of the valley or gully. These flows are characterized by higher density and erosivity, exhibiting enhanced mobility (Berger et al. 2011a).

Classifications based on triggering factors and occurrence processes offer an alternative perspective. It is widely recognized that gravitational flows are closely related to climatic, volcanic, and seismic activities, thereby serving as proxies for the temporal changes in these activities (Hibert et al. 2011; Hibert et al. 2014; Delannay et al. 2017). Consequently, these risks are particularly pronounced in scenarios involving geologically active and climate-driven activities, which include, but are not limited to, post-seismic collapses (e.g., Tang et al. 2011b; Tang et al. 2012; Kawamura et al. 2019; Gomez 2024), high-intensity rainfall (e.g., Tang et al. 2011b; Lee et al. 2021; Zhang et al. 2022), dam breaching or lake failure (e.g., Clague et al. 1985; Li et al. 2011; Chen et al. 2022), volcanic eruption (e.g., Scott et al. 1996; Cas et al. 2011; Lube et al. 2020), post-wildfire (e.g., Jakob et al. 2005a; Cannon and DeGraff 2009; Raymond et al. 2020), and accelerated snowmelt (e.g., Walter et al. 2020; Chiarle et al. 2021).

Table 1.1 Summary of the triggering factors for debris flow initiation.

Types	Preparatory factors	Direct triggering factors
Internal causes	Pore water pressure, poor drainage, weak jointed rocks, low vegetation cover, slope ripening and soil development	Groundwater washing, pore water pressure, permeability of soils, freezing and snowmelt,
External causes	Land use and construction activities, weathering (physical or chemical), surface run-off flow, steep terrain, superficial deposits, rock mass source	Earthquakes and tremors, landslides, shocks and vibrations, rainfall and storm, wildfire, dam collapse,

Fundamentally, Landslides occur when gravitational force surpasses the strength of the soil and rock that forming the slopes (Winter et al. 2005). Relatively, as landslides transition into debris flows, this change occurs gradually, with the key distinction lying in the effects of pore water, which imparts fluid-like deformation to debris flows and enables even boulder-rich debris to move through winding channels, over gentle slopes, and around obstacles (Iverson et al. 1997). Based on the duration and operation pattern (internal or external causes) of triggering factors, Winter et al. (2005) categorized the causes of debris flows into two types: (i) preparatory factors, which make the slope increasingly susceptible to failure without actually initiating it, and (ii) direct triggering factors, which initiate movement, as detailed in Table 1.1. This research focuses on the propagation phase and numerical analysis, while the study of initiation mechanisms is another crucial problem at the heart of geophysical studies that would require a paper in itself.

1.1.3. MULTI-HAZARD CHAINS INDUCED BY DEBRIS FLOWS

The typical "earthquake-landslide-debris flow disaster chain" has received widespread attention because multi-hazard chains often lead to more serious damage and losses than single events (Delmonaco et al. 2006; Tarvainen et al. 2006; Marzocchi et al. 2009; Zhu et al. 2021; Zheng et al. 2023a). As illustrated in Figure 1.5, debris flows and their subsequent hazards can occur as part of a sequence triggered by earthquakes or independently, such as from a typhoon storm. The direct risks of single events are evident, including extensive run-out extent (high mobility), erosion-induced excessive volume, and significant impact force. While previous studies have primarily focused on individual hazards, a systematic study on the chain process is still lacking. Recently, some progress has been made in understanding co-seismic landslides and their subsequent cascade effects (e.g., Ma and Xu 2019; Han et al. 2021a; Zhou et al. 2022). However, predicting and modeling multi-hazard chains induced by debris flows remains a significant challenge due to the nonlinear coupling processes among landslides, debris flows, erodible beds, dams, dammed lakes, and even dam-breach floods (Zhu et al. 2021). These secondary hazards can substantially amplify the damage, involving the interaction of multiple physical fields, such as fluid dynamics, solid mechanics, and thermodynamics.

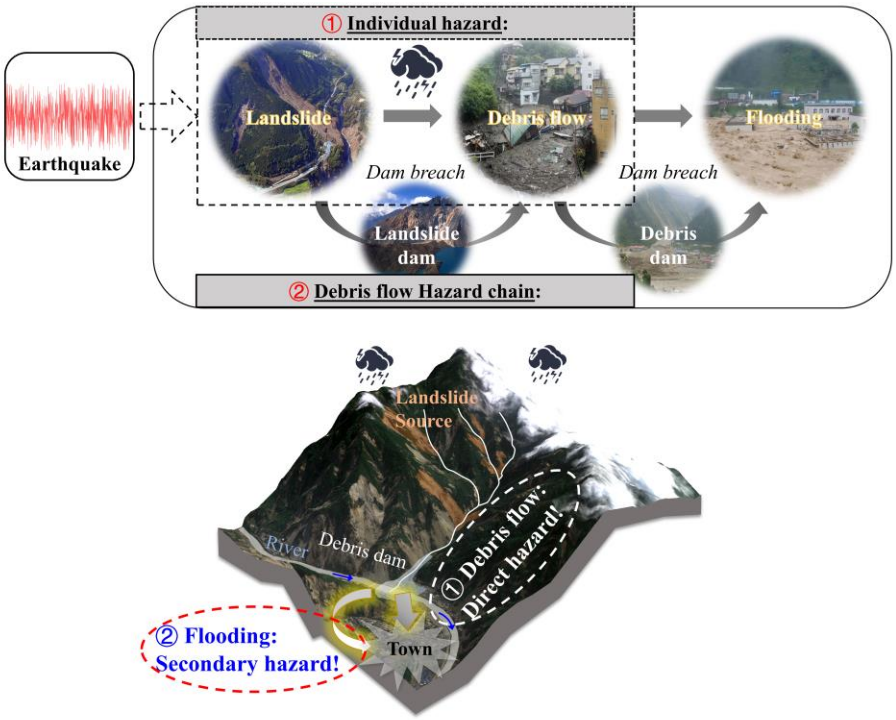

Figure 1.5 Schematic of debris-flow disaster chains in mountain regions.

In recent years, improvements in the seismic capacity of housing have made casualties due to building collapses virtually non-existent (Bilham 2009). However, post-earthquake and heavy rainfall-induced debris flows, and their secondary hazards are still catastrophic. As aforementioned, seismic events loosen the soil mass on slopes resulting in a considerable amount of unstable material on steep slopes in the catchment (Ma et al. 2023). In the five years since the Wenchuan earthquake, more than 500 debris flows have occurred (Guo et al. 2016). In these cases, landslide (or debris) dams and their associated outburst floods often form in succession. For example, in the 2010 Zhouqu incident, debris flows truncated two rivers and formed a dammed lake, ultimately causing a horrific tragedy in which 1,557 people died (Tang et al. 2011a). In summary, the analysis and modeling of debris flow disasters should not only focus on the individual event but also consider the geological conditions, topography, sedimentary beds, and other factors throughout the watershed. The numerical modeling and analysis theory presented in this paper is formally based on this foundation.

1.2. KEY ISSUES AND EXISTED PROBLEM

As previously noted, the mobility and disruptive of debris flows are associated with erosion-induced excessive volume, material properties, and topography (Pudasaini and Krautblatter 2021). They are characterized by enormous impact force, exceptional travel distance, and extensive inundation area. Accordingly, estimating key parameters of the flow dynamics, including flow volume, velocity, flow depth, travel distance, and impact area, is crucial for assessing debris-flow hazards, designing protective structures, and implementing mitigation measures (Rickenmann 1999; Dowling and Santi 2014; De Haas et al. 2020). Moreover, the material properties of debris flows, including grain sorting, density, and moisture content, significantly affect their rheological behavior and dynamic characteristics, ultimately altering their depositional patterns (Takahashi 2007; Iverson et al. 2010; Delannay et al. 2017; Pudasaini and Mergili 2019; Zheng et al. 2021). Table 1.2 summarizes these parameters and presents their influence on debris-flow magnitude, mobility, and destructive potential.

Table 1.2 Summary of the critical parameters for debris-flows prevention and mitigation, refer from Hungr et al. (1999), Han (2015), and Wong et al. (2018).

	Key parameters	Manner of influence
Flow dynamics	Volume (V)	Represent debris-flow magnitude
	Velocity (v)	Determine potential momentum
	Flow depth (h)	Influence erosivity and impact force
	Travel distance (L)	Indicate impact area
	Impact force (F)	Determine potential damage
Material properties	Grain size distribution	Influence flow dynamics
	Density (ρ)	
	Viscosity (μ)	
	Water content (n_w)	Influence sediment strength and flow mobility
	Porosity (n)	
	Shear strength	
	Cohesion (c)	
	Internal friction angle (φ)	

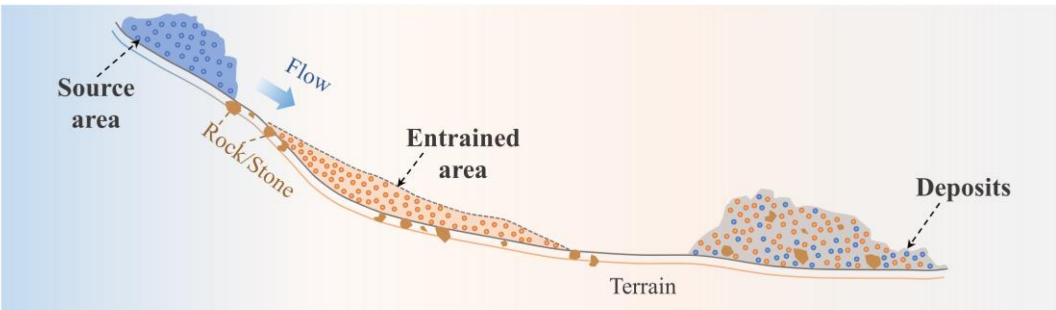

Figure 1.6 Schematic of the dynamic process and behaviors of debris flow.

To investigate the time-space variation of these key parameters during debris-flow moving, the dynamic behaviors, including initiation, erosion, entrainment, and deposition process, along with their underlying mechanisms and interrelationships, should be rigorously scrutinized (Figure 1.6). It should be noted that, although the terms "*erosion*" and "*entrainment*" are used interchangeably in much of the historical literature (e.g., Pierson 1980; Stock and Dietrich 2003; Mangeney et al.

2010; Berger et al. 2011a; Iverson et al. 2011; Haas and Woerkom 2016), recent studies distinguish between these two distinct processes based on their objects of action, sequential order, and energy balance (Pudasaini and Krautblatter 2021). Specifically, erosion is the process by which overlying flow (water and suspended particles) cuts and removes surface materials (e.g., soil, rock, and plant). Entrainment, on the other hand, refers to the incorporation of these eroded materials into the debris flow mixture. In addition, the term "*scour*" is frequently used in a similar context (e.g., Theule et al. 2015; Haas and Woerkom 2016; Zheng et al. 2023b), and is considered a specific type of erosion, though it is more commonly associated with river engineering involving pure water or minimal sediment. Based on the geotechnical framework of Schofield and Wroth (1968), McCave (2006) identified four distinct modes of erosion: entrainment, floc erosion, surface erosion, and mass erosion. This categorization was similarly used by Jacobs et al. (2011) and Winterwerp et al. (2012), differentiating erosion patterns based on the contributions of turbulent water movement and dynamic pressure to bed failure. In this sense, floc erosion occurs when flow-induced peak bed shear stresses dislodge individual flocs from the bed surface. Surface erosion corresponds to the drained bed-failure process, which occurs when the mean bed shear stress exceeds the mean erosion threshold. In contrast, mass erosion, also referred to as entrainment by Winterwerp et al. (2012), is an undrained process during which bed external stress greatly exceeds the local shear strengthen resulting from pore water pressure gradients. Both surface and mass erosion can be defined as mass failures (Takahashi 2007; McCoy et al. 2012) entrained along the bed sediment interface. On this basis, Haas and Woerkom (2016) examined the various factors influencing erosion patterns, such as channel slope, flow velocity, flow depth, discharge, material composition, and shear stress. Their experiments observed variations in spatial bed scour patterns, with bed particles being entrained both grain by grain (i.e., progressive scour, as illustrated in Figure 1.7a and en masse. In most instances, the failure of bed sediments during passage of the flow front is considered to follow a progressive slab-by-slab manner, also defined as mass movement or progressive entrainment (Iverson et al. 2011; Iverson 2012; McCoy et al. 2012; Iverson 2015;

Zheng et al. 2021), as depicted in Figure 1.7b. The erosion front progresses from the flow-bed interface downward through a series of failures, each with thicknesses of many particle sizes but with depths smaller than the total sediment thickness (McCoy et al. 2012; Haas and Woerkom 2016; Zheng et al. 2023b).

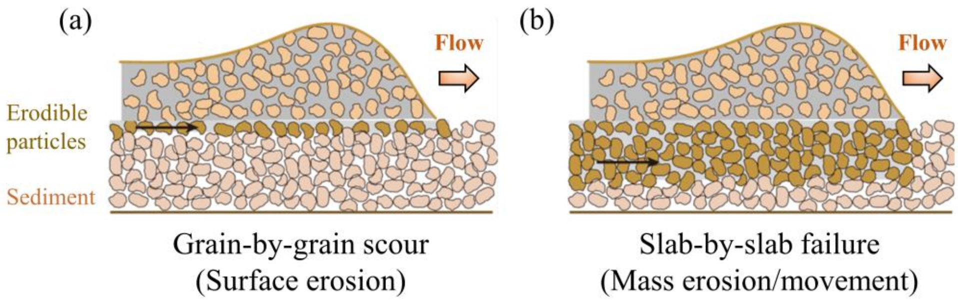

Figure 1.7 Illustration of the erosion mode in debris flow. (a) Progressive grain-by-grain scour pattern; (b) mass failure follows a slab-by-slab manner. Modified from Zheng et al. (2023b).

As described in Chapter 1.1.2, frequent interparticle contact dominates the friction behavior of debris flow in typical geographical contexts, a feature referred to as the grain-inertia regime (Bagnold 1954; Armanini et al. 2009). In this thesis, the processes of erosion and entrainment are defined and studied separately. Erosion encompasses scouring, surface erosion, and mass erosion, implying interaction between the overlying flow and the erodible bed sediment. Initiation processes, including how a landslide evolves into a debris flow, are not the focus of here. The key processes of debris-flow dynamic behaviors are listed as follows:

- **Initiation**: refers to the process in which materials such as soil, rock, and water transition from a stationary state to a flowing state under specific conditions (Iverson 1997).

- **Erosion**: refers to the process in which debris flows, through the physical action of overlying fluids and particles, cut and remove materials from the surface or bed sediment during flow (Stock and Dietrich 2003).

- **Entrainment**: refers to the process in which debris flows incorporate eroded particles into the fluid and move them along with the flow (Major and Pierson 1992).

- **Deposition**: refers to the process in which particulate matter in debris flows separates from the fluid and deposits onto the surface when the flow stops or slows down (Takahashi 1981).

Another critical problem in debris-flow dynamics is deposition. The deposition process occurs as the gravitational driving force decreases with the reduction in slope and base friction increases, leading to a gradual deceleration and cessation of the mass flow. In simpler terms, deposition arises from the external shear resistance exerted by the basal boundary (Gassen and Cruden 1989; Iverson 2012). Numerous studies have corroborated that mechanical deposition is the reverse process of erosion (McDougall and Hungr 2005; Iverson 2012; Pudasaini and Fischer 2020). However, the physical description of this inverse process has been debated due to the explosively sputtering response, also known as the rocketing effect (Pudasaini and Fischer 2020), observed in some cases (e.g., Issler 2014). A pivotal recent study (Pudasaini and Fischer 2020) showed that deposition begins not when the sliding mass starts to decelerate, but as soon as the bed's frictional resistance exceeds that of the flowing materials During erosion, the flow gains mass, whereas during deposition, the basal substrate gains mass. The deposited material becomes denser, grains interlock, and effective friction rises as the mass transitions from a dynamic to a static state (Pudasaini and Hutter 2007). Moreover, gravitational force is reduced during the transition and run-out phases. All these factors collectively contribute to the deceleration and eventual deposition of mass flows. These deposited materials also alter the terrain and ultimately become part of the substrate, participating in subsequent gravity flow activities.

Deposition typically occurs unevenly due to variations in flow properties and topographical effects, which cause some materials to halt while others continue moving (Delannay et al. 2017). Consequently, the deposition area may contain channels and levees. It is widely accepted that polydispersity-related segregation processes greatly impact the depositional morphology of geophysical flows (e.g., Félix and Thomas 2004; Johnson et al. 2012; Kokelaar et al. 2014). Typical examples include the levee-channel morphology of self-channeling flows (e.g., Mangeney et al. 2007; Iverson et al. 2010; Johnson et al. 2012) and the dewatering of alluvial fans (e.g., Pastor et al. 2023).

In general, the propagation phase, including erosion, entrainment, and deposition, is a dominant and complex mechanical processes that is still poorly understood in debris flows (Pudasaini and Fischer 2020; Pudasaini and Krautblatter 2021). This problem can be explained in part by two key issues, (i) flow-momentum growth and feedback effects of debris flows are unclear and hard to quantify when bed sediments are overridden and progressive entrained; (ii) multi-phase modelling of debris-flows dynamics, including viscous fluid and large boulders, remains absent.

1.2.1. KEY ISSUE 1: FLOW-MOMENTUM GROWTH AND FEEDBACK EFFECT OF THE UNDERLYING BED SEDIMENT ON THE EROSION PROCESS

The concept of flow-momentum growth and transmit in debris flows was first defined in Iverson (1997) and further emphasized by Iverson et al. (2011), highlighting the critical impact of volumetric water content in erodible bed. This concept encompasses the combined spatiotemporal effects of change in (i) flow mass (volume) and (ii) flow velocity resulting from the interactions between the intrusive flow and the underlying basal or bed sediment. Field and laboratory studies consistently indicate that erosion, entrainment, and deposition processes (EEDPs), associated with the flow-substrate feedback effects, greatly influence the flow depth and velocity (Zheng et al. 2021), in turn, determine the mobility of debris flows and the topography of valleys (Mangeney et al. 2010; Berger et al. 2011a; Iverson et al. 2011; Gregoretti et al. 2019; Vicari et al. 2022a). In certain cases, erosive debris flows exhibit significantly higher mobility and considerable volume amplification. Conversely, other instances show a reduction in mobility, with little to no increase in volume, or potentially even a decrease. The extent of this effect depends on whether the bed deposits facilitate or impede the overall movement of the debris flow. We refer to the former as "*positive feedback*" and the latter as "*negative feedback*". Iverson et al. (2011) first observed the feedback effects of debris flows on beds with varying configurations during typical full-scale entrainment experiments, as depicted in Figure 1.8.

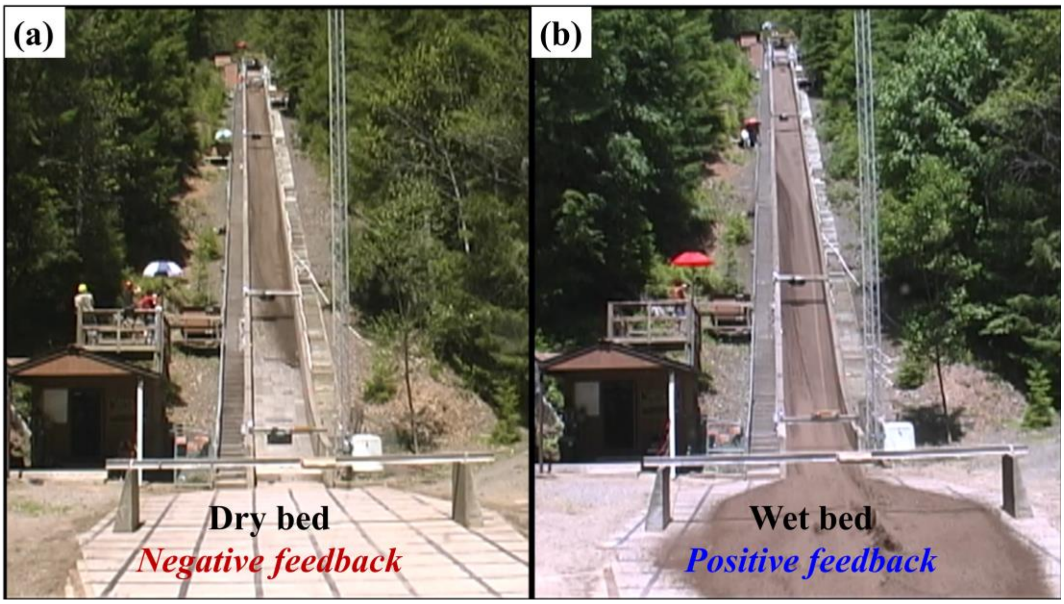

Figure 1.8 Photographs of the USGS debris-flow flume experiment. (a) Debris flow on a dry erodible bed; (b) debris flow on a wet erodible bed. Figures modified from Logan and Iverson (2007).

Despite considerable efforts (e.g., Iverson 1997; Iverson et al. 2011; Haas and Woerkom 2016; Pudasaini and Krautblatter 2021; Zheng et al. 2021) to explain the mechanisms of EEDPs in the recent decades, research on momentum growth and feedback effects of debris flow remains absent, and most previous studies have focused on a single aspect, such as erosion-induced excessive volume or mobility variation. On one hand, the magnitude and destructive potential of debris flows can increase dramatically by side collapse and entraining bed materials as they traverse steep slopes and channels (Jakob et al. 2005c; Iverson et al. 2011; Haas and Woerkom 2016; Pudasaini and Krautblatter 2021). For instance, a typical debris-flow event occurred in Hunnedalen, Norway, on June 2, 2016, following intense rainfall, which initially measured about 2,000 m³ but grew to 20,000 m³ due to entrainment, ultimately burying a regional road (Vicari et al. 2021). On the other hand, the erosion and entrainment process, in turn, impact the deposition pattern and run-out extent. As previously noted, these dynamic processes are not separate but may occur simultaneously and mutually influence each other. The quantification of these processes is based on key parameters such as flow velocity, volume, and flow depth. Changes in flow momentum and feedbacks, which integrate variations in these parameters, are defined and measured in detail in the following sections.

1.2.2. KEY ISSUE 2: MULTI-PHASED MODELLING OF DEBRIS FLOWS: VISCOUS-TYPE AND VISCOUS-STONY-TYPE

One of the significant characteristics that distinguishes debris flows from other gravity-driven mass flows is their dual nature, exhibiting attributes of both solids and fluids. Their rheological features and flow behaviors vary depending on the material composition, particularly the percentage of coarse grains (Takahashi 2007; Takahashi 2009). As shown in Figure 1.4, coarse particle content is a crucial factor in classifying debris flow types. By contrast, the interstitial fluid provides high fluidity, enabling the transport of large boulders. Such cases are extensively documented in the literatures (e.g., Larsen et al. 2006; Suwa et al. 2009; Pierson 2020; Wang et al. 2022). This thesis focuses on the two most common types of debris flow in mountainous areas: viscous-type and viscous-stony type (referred to herein as hybrid type). Turbulent-muddy-type debris flows contain a large amount of water, silt, clay, and mud, which gives them both the high viscosity of viscous debris flows and a significant turbulent characteristic due to the high-water content. Therefore, they are more similar to sediment-laden floods in river engineering and are beyond the scope of this thesis.

Viscous-type debris flows primarily consist of fine-grained materials (such as clay, silt, and fine sand) and water, with their fluid behavior and rheological characteristics mainly influenced by viscous forces (Major and Pierson 1992; Iverson 1997; Parsons et al. 2001). Due to their relatively homogeneous and uniform material composition, they are often described using continuum models, and previous studies have mostly been based on the single-phase flow paradigm. As the water content increases, these debris flows can potentially transform into flood disasters containing a large amount of sediment. The debris flows in the Jiangjia Gully, China, are renowned examples of viscous-type (Jakob et al. 2005b). Other typical examples can be found in Hübl and Steinwendtner (2001) and Wang et al. (2005). Moreover, there is another type of debris flow composed of a mixture of water and non-cohesive particles (Armanini et al. 2009). Although it contains some solid particles, these grains are generally small in size and relatively well-sorted. In this paper, they will be collectively referred to as viscous-type debris flows. Despite extensive studies in the past decades focusing on single-phase and single-layer models, there is an urgent need for a model that comprehensively considers the interactions between the overlying debris flow and the underlying sedimentary bed, as mentioned above, to more accurately understand their physical mechanisms and design prevention measures. This topic will be elaborated upon in Chapter 3 and 4.

The viscous-stony (hybrid) debris flow is a complex type that combines the characteristics of both viscous and stony flows, we can also regard this as a scenario of a viscous debris flow carrying large boulders. Its material composition includes coarse particles such as gravel, stones, and boulders, in addition to the fine materials found in viscous debris flows. These components enhance the non-Newtonian properties of the flow, affecting its overall dynamic behavior and significantly increasing its potential for destructiveness (Si et al. 2022; Wang et al. 2022; Yu et al. 2023). As such, the analysis of the physical mechanisms, numerical modeling, and disaster prediction of this type of debris flow has always been a huge challenge in the field of geophysical flows (Delannay et al. 2017). For purely stony-type, particle collision stress plays a leading role, and previous studies have mostly used discrete medium models to describe their dynamic behaviors. However, modeling and predicting the spatiotemporal evolution of hybrid type debris flows are quite difficult due to their multi-phase, multi-scale, and multi-physical nature, involving inhomogeneous and unsteady flows (Iverson 2015; Delannay et al. 2017; Pudasaini and Mergili 2019; Pudasaini and Fischer 2020). On one hand, the diversity in material composition makes it impossible to simplify the modeling to a single continuous or discrete medium model. It is necessary to consider a coupled model that includes water, clay, silt, and other continuous media, as well as irregular coarse particles. On the other hand, multi-phase flow also means that processes related to phase transition need to be rigorously validated and consistently implemented. The aforementioned factors make the modeling of strongly coupled multi-scale multi-phase flows extremely challenging. The interactions between multi-scale particles, as well as the contact and interactions between particles and boundaries, require enormous computational resources. This disadvantage is exponentially magnified in a three-dimensional computational framework. Therefore, in Chapter 5, we will attempt to develop a solution that balances efficiency and computational accuracy.

1.3. Methodologies for analyzing debris flows

The study of debris flows dates back to the early 20th century (Johnson 1984; Iverson 1997; Takahashi 2007). With the deepening research into natural disasters and geological phenomena, the methods and theories for studying debris flows have become increasingly refined. The main categories are as follows:

- **Field Observations and Surveys**: Field observations are crucial for determining initial and final conditions of geophysical flows, including the volume and nature of materials involved, type and duration of mass release, triggering processes, and deposit morphology. They also provide insights into material properties, boundary conditions such as the nature of the ambient fluid, underlying topography, and substrate type, and help elucidate the mechanisms that govern the dynamics and deposition of these flows (Delannay et al. 2017).

Field monitoring can be conducted in real-time by installing monitoring equipment (such as seismometers, rain gauges, and ground-based radar) to track the occurrence, flow, and deposition processes of debris flows. Some typical examples of field research studies can be found in Larsen et al. (2006), Suwa et al. (2009), Berger et al. (2011a), Hibert et al. (2011), Tang et al. (2011a), Tang et al. (2011b), Kawamura et al. (2019) and Walter et al. (2020). This technology is also commonly used in large-scale model experiments to obtain disaster data that closely approximates field conditions, as illustrated in Figure 1.9. Furthermore, remote sensing technologies such as satellite imagery (e.g., Tofani et al. 2013), drones (e.g., Niethammer et al. 2012), and LiDAR (Light Detection and Ranging) (e.g., Martha et al. 2010) have gradually become important supplementary techniques in recent field investigation studies for large-scale debris flow monitoring and terrain analysis. Satellite imagery provides wide-area, multispectral, long-term data, drones offer high-resolution and flexible on-site observations, and LiDAR delivers high-precision, three-dimensional terrain data. The combination of these three technologies can significantly enhance the depth and breadth of debris flow monitoring, providing scientific basis and technical support for disaster prevention and mitigation (Huang and Fan 2013).

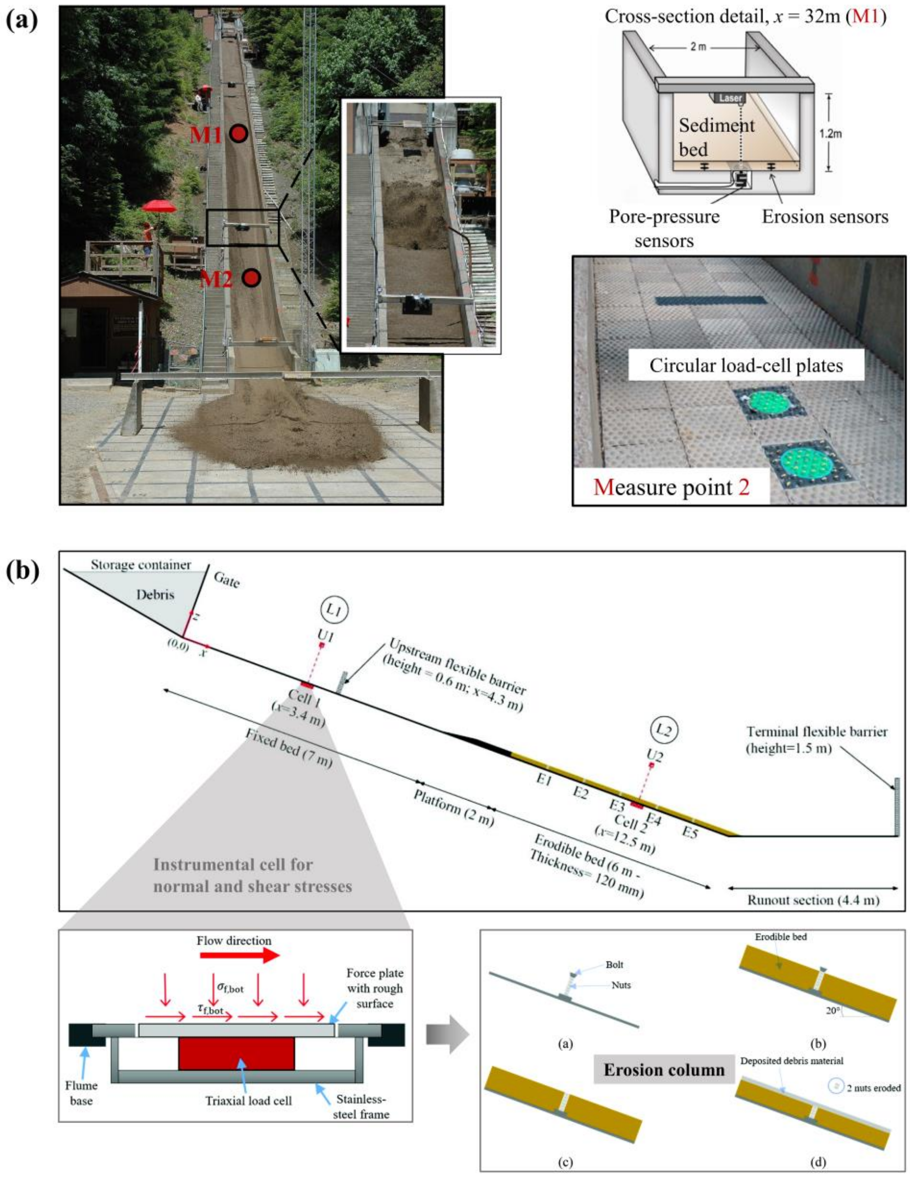

Figure 1.9 (a) Photographs of the USGS debris-flow flume experiment, modified from Iverson et al. (2010) and Iverson et al. (2011). (b) Cross section of the flume and instrumentation layout, modified from Vicari et al. (2022a).

Despite this, they still face several significant limitations. These include limited coverage, high time and labor costs, substantial safety risks, data accuracy and consistency issues due to varying methods, difficulties in real-time monitoring, environmental factors interfering with observations, equipment limitations under extreme conditions, and the complexity of data processing and analysis. In details, field measurement of the evolving basal boundaries is arduous and resource-intensive, as erosion tracks are often obscured by subsequent flows (Mangeney 2011).

- **Laboratory Experiments**: Laboratory experiments on debris flows can be categorized based on their test objectives into three types: physical model tests, material property tests, and rheological experiments (Huang and Fan 2013). These correspond to the study of debris flow dynamics, the physical and mechanical properties of materials, and rheological characteristics, respectively. While based on size, they can be further divided into small-scale and large-scale experiments. Small-scale experiments have low costs, short durations, and allow for easy control of variables and repeatability. However, they are affected by scale effects and simplified configurations (Iverson et al. 2010; Mangeney et al. 2010; Iverson et al. 2011; Iverson 2015; Haas and Woerkom 2016; Delannay et al. 2017). As a typical heterogeneous multiphase flow, field-scale test facilities are essential to address scaling issues related to pore pressure diffusion in water-laden debris flows (Vicari et al. 2022a). Large-scale flume experiments, on the other hand, can obtain higher precision and resolution data, closely resembling actual debris flow behavior with minimal scale effects. However, they often exhibit more violent behavior, are costly, and have lower repeatability (Iverson et al. 2011; Johnson et al. 2012; Iverson 2015; Vicari et al. 2022a).

- **Theoretical Analysis**: Theoretical analysis involves applying fundamental physical, mathematical, and geomechanical principles to model and analyze debris flows. This analysis can be broadly categorized into several aspects: In fluid dynamics, the Navier-Stokes (NS) equations are solved under appropriate boundary and initial conditions to simulate flow behavior. Alternatively, simplifications such as the shallow water equations (SWEs) are employed for thin, spread-out flows. In geomechanics, analysis is commonly conducted for flow dynamics by applying stress-strain relationships to model the deformation and failure of debris material (Jakob et al. 2005c). Stability is analyzed using limit equilibrium methods to predict potential failure surfaces, providing insight into the conditions leading to the initiation of debris flows. This helps in understanding material strength and failure mechanisms. Furthermore, the flow behaviors of mixture flows are studied by developing constitutive models to describe the relationship between stress and strain rate, which can capture complex flow behaviors such as shear thinning or thickening (Han et al. 2019). However, theoretical models often rely on simplifications that may not fully capture real-world complexities. Additionally, complex theoretical models can be computationally demanding.

To sum up, theoretical analysis is a powerful tool in debris flow research, offering insights into the fundamental mechanics, material properties, and dynamic behaviors of debris flows. Despite its limitations, when combined with numerical, experimental and observational data, it provides a comprehensive approach to understanding and mitigating debris flow hazards.

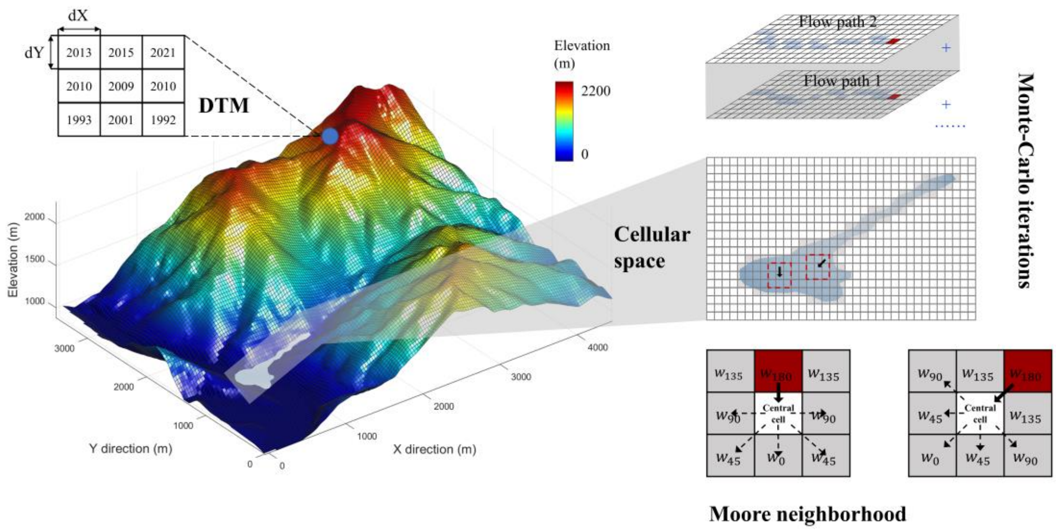

Figure 1.10 Illustration of the basic concept of the Cellular Automaton (CA) Model. Figure from Ma et al. (2023).

- **Statistical and Probabilistic Analysis**: This class of methods can be subdivided into Frequency analysis, probabilistic-based methods, and data-driven methods. Frequency analysis involves using historical data and field observations to statistically determine the occurrence frequency and distribution characteristics of debris flows. This method is typically combined with GIS (Geographic Information System) technology to analyze and predict disaster-prone areas by collecting extensive climate, geological, and hydrological data (e.g., Di et al. 2008; Chen and Yu 2011; Cavalli et al. 2017). This approach facilitates disaster mapping and forecasting.

Probabilistic-based methods use stochastic iterative models (such as Monte Carlo simulations and Bayesian networks) to assess the risk and impact range of debris flow occurrences. They are particularly effective, and therefore suitable for hazard mapping and run-out extent delineation at regional scales (Ma et al. 2023). Notable research in this field includes the D8-based single flow direction algorithms (e.g., O'Callaghan and Mark 1984; Gamma 2000) and multi-flow direction algorithms (e.g., Quinn et al. 1991; Horton et al. 2013). On this basis, the cellular automaton (CA) model, a more comprehensive flow routing algorithm, has been proposed and is widely used to understand gravitational behavior (Iovine et al. 2005; Hürlimann et al. 2008; Scheild and Rickenmann 2011; Guidolin et al. 2016; Han et al. 2017; Han et al. 2021b), as detailed in Figure 1.10. To date, many families of codes have been well-developed, remarkable studies include the SCIDDICA family models (Avolio et al. 2000; Avolio et al. 2013), which are applied to various kinds of earth flow by constantly updating transition rules and cellular patterns (e.g., square, hexagonal in D'Ambrosio et al. (2003) and Han et al. (2024)). Other notable models include the CAESAR models (Coulthard et al. 2007; Coulthard et al. 2013; Pasculli and Audisio 2015), the TopFlowDF model (Scheidl and Rickenmann 2010; Scheild and Rickenmann 2011), the Flow-R (Horton et al. 2013; Kang and Lee 2018), and the r.randomwalk (Mergili et al. 2015). Therefore, instead of solving the shallow water equations (SWEs), CA models use simple transition rules to provide a versatile method for modeling complex systems. Probabilistic-based approaches offer the benefits of straightforward data acquisition and broad applicability on a large scale. However, their limitations are evident in providing detailed descriptions of case-specific features and in conducting rheological analyses (Horton et al. 2013; Han et al. 2021b).

Recently, data-driven techniques have emerged as alternative tools in disaster vulnerability assessment (e.g., Mondini et al. 2023) and dynamic process analysis (e.g., Deguchi and Asai 2023; Li et al. 2023). These approaches significantly outperform conventional numerical models in computational efficiency. Nonetheless, their application in practical scenarios is impeded by the relative scarcity and inconsistency of historical disaster data, as well as by the high non-linearity of flow processes (Linardos et al. 2022).

- **Physics-Based Numerical Simulations**: This type of method is based on classical physical laws, such as the conservation of mass, momentum, and energy, to describe the dynamic behavior of debris flows. Mathematically, physics-based numerical methods represent physical laws and debris flow processes through partial differential equations (PDEs) or algebraic equations, and discretize continuous mathematical models into solvable numerical forms, such as the finite difference method (FDM), finite element method (FEM), or finite volume method (FVM). These methods can further be classified based on the form of discrete elements into grid-based approaches, particle-based approaches, and coupled approaches. They are solved in 1D, 2D, or 3D spaces depending on the computational requirements.

Physics-based approaches have evolved from one-dimensional, single-phase models to sophisticated three-dimensional, multiphase coupled versions, resulting in a division into Eulerian and Lagrangian schemes. In fact, most existing methods are based on Eulerian descriptions in two dimensions, wherein a set of depth-average equations are solved to quantitatively describe the spatiotemporal evolution of flow dynamics. In recent years, this method has been extensively developed and expanded into frameworks that encompass multiple mechanics and phases (e.g., Pudasaini 2012; Pudasaini and Mergili 2019; Pudasaini and Fischer 2020). Accordingly, research into full form Navier-Stokes computation methods based on the Lagrangian particle paradigm has surged recently. The shift has resulted in an exponential increase in computational demand, accompanied by the challenges in complex boundary treatments. The occasion in tackling the problem arises from recent advancements in massively parallel particle hydrodynamics technology

(Crespo et al. 2015; Bower et al. 2021; Mniszewski et al. 2021).

Overall, these physics-based numerical methods have their pros and cons. Selecting an appropriate method requires considering the specific requirements of debris flow simulation, terrain complexity, flow characteristics, and computational resources. The physical characteristics, applicable range, and research progress of various physics-based numerical methods will be discussed in detail in Chapter 2.

1.4. SCOPES AND OBJECTIVES

1.4.1. METHODOLOGY SELECTION

The overview of methodologies reveals a variety of approaches available for assessing debris-flow dynamics and behaviors. In this thesis, we choose physics-based numerical methods to study the physical mechanisms and rheological behavior of debris flows due to their low cost, relatively short duration, and ability to describe the global evolution of multiple variables. Specifically, we will develop and apply the state-of-the-art numerical simulation methods for the following two common types of debris flows in mountainous areas:

(1) **Viscous-type debris flow**: As previously mentioned, due to the relatively homogeneous material composition in viscous debris flows, various numerical models based on the discretization of continuous media are applicable. However, this does not mean that single-phase flow models sufficiently reflect their complex nonlinear rheological characteristics. At a minimum, the mass and momentum exchange between the overlying flow and the underlying sediments requires a physically unified description, and the phase change processes involved must be stably and smoothly realized. Additionally, numerous studies (Johnson et al. 2012; Han et al. 2015; Nagl et al. 2020) have shown significant nonlinear characteristics in the velocity and momentum redirection in the depth direction of debris flows. Therefore, traditional two-dimensional depth-averaged models are inadequate because these features are fundamental for comprehending the dynamics of debris flow interactions with bed sediment and structural elements (Vicari et al. 2022b). As such, a fully three-dimensional, multi-phase particle method is developed and

applied to the erosive debris flows. Previous particle-based approaches such as the smooth particle hydrodynamics (SPH) methods, the discrete element method (DEM), and the material point method (MPM), are generally limited to single-layer frameworks or small-scale applications due to the complexity in debris-flow dynamics and mechanisms, as well as the huge computational consumption. In Chapters 3 and 4, these issues are specifically discussed and addressed.

(2) **Viscous-stony-type (hybrid-type) debris flow**: Building on the viscous type, this class of debris flows further considers the impact of large boulders. Therefore, it is necessary to develop a coupled model that comprehensively considers both continuous media (water, silt, mud, etc.) and discrete media (coarse gravel), as well as the fluid-solid coupling interactions between them. The model must ensure the compatibility and consistency of modeling methods for both continuous and discrete media while balancing computational efficiency and accuracy. In Chapter 5, we will provide a detailed introduction to this coupled approach.

1.4.2. Objectives of the thesis

This study focuses on the widespread hazards of viscous and viscous-stony debris flows in mountainous areas. It aims to develop and apply advanced particle-based numerical simulation methods that address multi-scale, multi-phase, and multi-physical mechanisms to investigate their complex nonlinear rheological characteristics and dynamic behaviors. Specifically, this thesis examines the erosion, entrainment, and deposition processes (EEDPs) of debris flows, associated flow mass and momentum growth, and the feedback of eroded sediments. On this basis, the study will further develop and apply a physics-based coupled approach that also considers the impact of large boulders on flow dynamics and potential destructiveness. These issues are key research challenges and hotspots in the field of geophysical flows and numerical modeling. The main research objectives are detailed as follows:

(1) Develop a particle-based 3D multi-phase method for simulating viscous debris flows;

(2) Model and analyze the complex erosion, entrainment, and deposition processes (EEDPs) of debris flows;

(3) Model and analyze the flow mass and momentum growth, as well as the feedback effects during the EEDPs of debris flows;

(4) Develop a coupled particle-based method for debris flows with large boulders;

(5) Apply and validate the proposed methods to the field-scale case studies.

1.5. FRAMEWORK OF THE THESIS

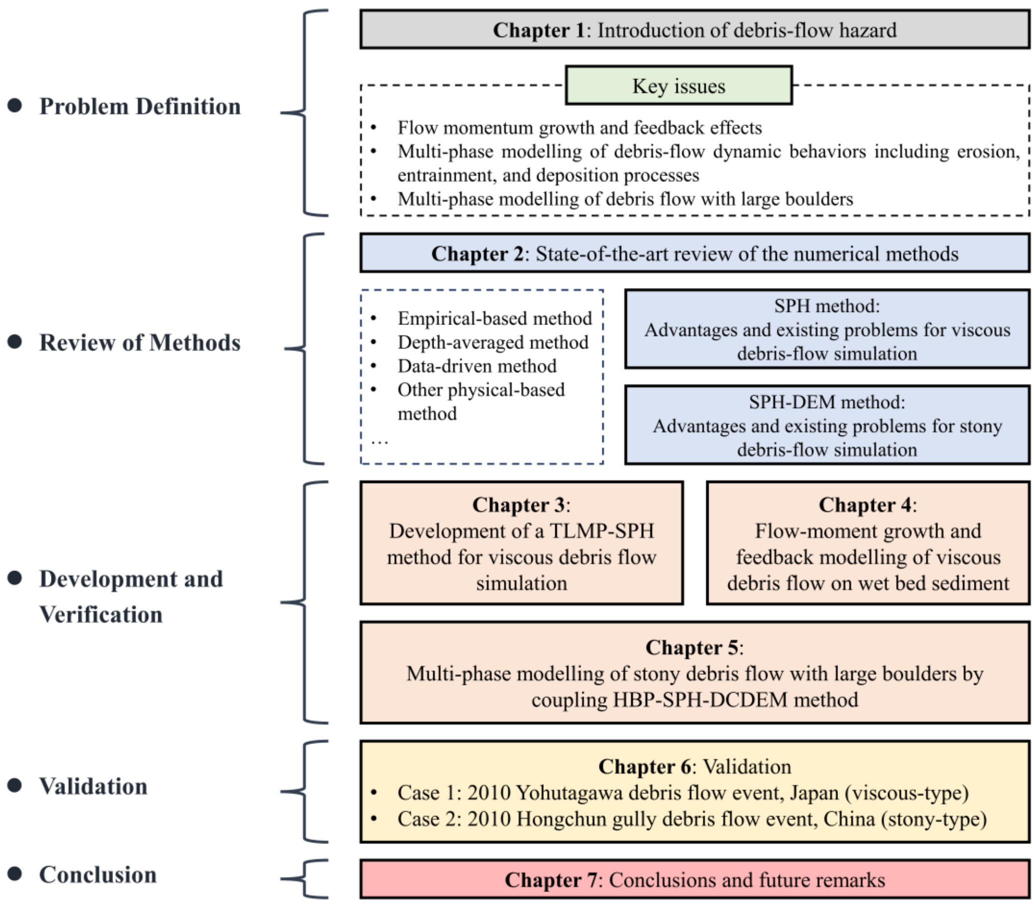

Figure 1.11 Framework of the thesis.

The thesis consists of the following chapters.

Chapter 1 first provides an overview of the background of this study, including several significant debris flow disaster events in recent decades, the triggers and classifications of debris flows, and the disaster chains associated with debris flows. It then presents the key issues addressed in this study, followed by a brief review and summary of the commonly used methods in current debris flow research. Finally, it outlines the research objectives and scope of this study.

Chapter 2 provides a detailed review of debris flow prediction and numerical simulation methods, including empirical, physics-based, and probabilistic and data-driven methods. It then focuses on reviewing and summarizing the current development, advantages, and existing issues of particle-based methods (SPH, DEM). Additionally, it offers a detailed comparison of the applicability and limitations of various current numerical methods.

Chapter 3 develops a Two-Layer, Multi-Phase Smooth Particle Hydrodynamics (TLMP-SPH) model to simulate the rheological characteristics and dynamic processes of viscous debris flows. First, it provides a detailed introduction to the basic framework and principles of the SPH method, as well as various rheological models of debris flows. On this basis, various yield criteria are integrated into the HBP nonlinear rheological model to achieve complex processes such as erosion and entrainment. To achieve stable phase transitions on steep terrains, a stable phase transition model is further developed. Finally, several numerical tests are conducted for verification.

Chapter 4 builds on the above TLMP method by further developing a hydro-poro-mechanisms-based pore water pressure response model and integrating it into the SPH framework. This model successfully reproduces debris flow mass and momentum growth on sediments with varying wetness, and analyzes their feedback effects. To overcome the scale effects on pore pressure dissipation, this method undergoes rigorous testing and validation in a series of large-scale flume experiments conducted by the United States Geological Survey (USGS).

Chapter 5 develops an HBP-SPH-DCDEM-based coupled method to simulate debris flow scenarios involving the transport of large boulders. First, it introduces the basic framework and principles of DEM and conducts numerical tests for modeling large boulders using DEM. Then, it constructs an SPH-DEM coupled numerical framework, which is also verified through a series of numerical tests.

Chapter 6 applies the proposed methods to two case studies: (1) the 2010

Yohutagawa debris flow event in Japan and (2) the 2010 Hongchun Gully debris flow event in China. Based on the material composition characteristics obtained from field investigations, these correspond to viscous and viscous-stony debris flow scenarios, respectively. The proposed methods were successfully applied in both scenarios, generating millions of particles with highlighted visualization effects and yielding conclusions beneficial for engineering applications.

Chapter 7 summarizes the results and major contributions of the study, and also makes recommendations for future research.

References

Armanini, A., Fraccarollo, L. & Rosatti, G. 2009. Two-dimensional simulation of debris flows in erodible channels. Computers & Geosciences 35(5), 993-1006.

Avolio, M., Di Gregorio, S., Mantovani, F., Pasuto, A., Rongo, R., Silvano, S. & Spataro, W. 2000. Simulation of the 1992 Tessina landslide by a cellular automata model and future hazard scenarios. International Journal of Applied Earth Observation and Geoinformation 2(1), 41-50.

Avolio, M.V., Di Gregorio, S., Lupiano, V. & Mazzanti, P. 2013. SCIDDICA-SS 3: a new version of cellular automata model for simulating fast moving landslides. The Journal of Supercomputing 65, 682-696.

Bagnold, R.A. 1954. Experiments on a gravity-free dispersion of large solid spheres in a Newtonian fluid under shear. Proceedings of the Royal Society of London. Series A, Mathematical and Physical Sciences 225(1160), 49-63.

Berger, C., McArdell, B. & Schlunegger, F. 2011a. Direct measurement of channel erosion by debris flows, Illgraben, Switzerland. Journal of Geophysical Research: Earth Surface 116(F1), F01002.

Berger, C., McArdell, B.W. & Schlunegger, F. 2011b. Sediment transfer patterns at the Illgraben catchment, Switzerland: Implications for the time scales of debris flow activities. Geomorphology 125(3), 421-432.

Bilham, R. 2009. The seismic future of cities. Bulletin of earthquake engineering 7, 839-887.

Bower, R., Rogers, B.D. & Schaller, M. 2021. Massively Parallel Particle Hydrodynamics at Exascale. Computing in Science & Engineering 24(1), 14-25.

Campbell, C.S. 1990. Rapid granular flows. Annual Review of Fluid Mechanics 22(1), 57-90.

Cannon, S.H. & DeGraff, J. 2009. The increasing wildfire and post-fire debris-flow threat in western USA, and implications for consequences of climate change. Landslides–disaster risk reduction, 177-190.

Cas, R.A., Wright, H.M., Folkes, C.B., Lesti, C., Porreca, M., Giordano, G. & Viramonte, J.G. 2011. The flow dynamics of an extremely large volume pyroclastic flow, the 2.08-Ma Cerro Galán Ignimbrite, NW Argentina, and comparison with other flow types. Bulletin of volcanology 73, 1583-1609.

Cavalli, M., Crema, S., Trevisani, S. & Marchi, L. 2017. GIS tools for preliminary debris-flow assessment at regional scale. Journal of Mountain Science 14(12), 2498-2510.

Chen, C.-Y. & Yu, F.-C. 2011. Morphometric analysis of debris flows and their source areas using GIS. Geomorphology 129(3-4), 387-397.

Chen, H., Ruan, H., Chen, J., Li, X. & Yu, Y. 2022. Review of investigations on hazard chains triggered by river-blocking debris flows and dam-break floods. Frontiers in Earth Science 10, 830044.

Chen, M., Tang, C., Zhang, X., Xiong, J., Chang, M., Shi, Q., Wang, F. & Li, M. 2021. Quantitative assessment of physical fragility of buildings to the debris flow on 20 August 2019 in the Cutou gully, Wenchuan, southwestern China. Engineering Geology 293, 106319.

Chiarle, M., Geertsema, M., Mortara, G. & Clague, J.J. 2021. Relations between climate change and mass movement: Perspectives from the Canadian Cordillera and the European Alps. Global and Planetary Change 202, 103499.

Clague, J.J., Evans, S. & Blown, I.G. 1985. A debris flow triggered by the breaching of a moraine-dammed lake, Klattasine Creek, British Columbia. Canadian Journal of Earth Sciences 22(10), 1492-1502.

Coulthard, T., Hicks, D. & Van De Wiel, M.J. 2007. Cellular modelling of river catchments and reaches: advantages, limitations and prospects. Geomorphology 90(3-4), 192-207.

Coulthard, T.J., Neal, J.C., Bates, P.D., Ramirez, J., de Almeida, G.A. & Hancock, G.R. 2013. Integrating the LISFLOOD-FP 2D hydrodynamic model with the CAESAR model: implications for modelling landscape evolution. Earth Surface Processes and Landforms 38(15), 1897-1906.

Crespo, A.J., Domínguez, J.M., Rogers, B.D., Gómez-Gesteira, M., Longshaw, S., Canelas, R., Vacondio, R., Barreiro, A. & García-Feal, O. 2015. DualSPHysics: Open-source parallel CFD solver based on Smoothed Particle Hydrodynamics (SPH). Computer Physics Communications 187, 204-216.

Cruden, D.M. 1996. Cruden, dm, varnes, dj, 1996, landslide types and processes, transportation research board, us national academy of sciences, special report, 247: 36-75. Transp Res Board 247, 36-57.

Cui, P., Chen, X.-Q., Zhu, Y.-Y., Su, F.-H., Wei, F.-Q., Han, Y.-S., Liu, H.-J. & Zhuang, J.-Q.J.N.H. 2011. The Wenchuan earthquake (May 12, 2008), Sichuan province, China, and resulting geohazards. Natural Hazards 56, 19-36.

D'Ambrosio, D., Di Gregorio, S. & Iovine, G. 2003. Simulating debris flows through a hexagonal cellular automata model: sciddica s 3–hex. Natural Hazards and Earth System Sciences 3(6), 545-559.

De Haas, T., Nijland, W., De Jong, S. & McArdell, B. 2020. How memory effects, check dams, and channel geometry control erosion and deposition by debris flows. Scientific reports 10(1), 14024.

Deguchi, S. & Asai, M. 2023. Dynamic & norm-based weights to normalize imbalance in back-propagated gradients of physics-informed neural networks. Journal of Physics Communications 7(7), 075005.

Delannay, R., Valance, A., Mangeney, A., Roche, O. & Richard, P. 2017. Granular and particle-laden flows: from laboratory experiments to field observations. Journal of Physics D: Applied Physics 50(5), 053001.

Delmonaco, G., Margottini, C. & Spizzichino, D. 2006. ARMONIA methodology for multi-risk assessment and the harmonisation of different natural risk maps. Deliverable 3.1. 1, ARMONIA.

Di, B., Chen, N., Cui, P., Li, Z., He, Y. & Gao, Y. 2008. GIS-based risk analysis of debris flow: an application in Sichuan, southwest China. International Journal of Sediment Research 23(2), 138-148.

Dowling, C.A. & Santi, P.M. 2014. Debris flows and their toll on human life: a global analysis of debris-flow fatalities from 1950 to 2011. Natural hazards 71, 203-227.

Félix, G. & Thomas, N. 2004. Relation between dry granular flow regimes and morphology of deposits: formation of levées in pyroclastic deposits. Earth and Planetary Science Letters 221(1-4), 197-213.

Gamma, P. 2000. dfwalk-Ein Murgang-Simulationsprogramm zur Gefahrenzonierung. Geographisches Institut der Universität Bern Verlag des Geogr, Switzerland.

Gariano, S.L. & Guzzetti, F. 2016. Landslides in a changing climate. Earth-Science Reviews 162, 227-252.

Gassen, W.V. & Cruden, D. 1989. Momentum transfer and friction in the debris of rock avalanches. Canadian Geotechnical Journal 26(4), 623-628.

Gomez, C. 2024. The January 1 st 2024 Noto Peninsula Co-seismic Landslides Hazards: Preliminary Results, 31 January 2024, PREPRINT (Version 1) available at Research Square [https://doi.org/10.21203/rs.3.rs-3904468/v1].

Gregoretti, C., Stancanelli, L.M., Bernard, M., Boreggio, M., Degetto, M. & Lanzoni, S. 2019. Relevance of erosion processes when modelling in-channel gravel debris flows for efficient hazard assessment. Journal of Hydrology 568, 575-591.

Guidolin, M., Chen, A.S., Ghimire, B., Keedwell, E.C., Djordjević, S. & Savić, D.A. 2016. A weighted cellular automata 2D inundation model for rapid flood analysis. Environmental Modelling & Software 84, 378-394.

Guo, X., Cui, P., Li, Y., Zhang, J., Ma, L. & Mahoney, W.B. 2016. Spatial features of debris flows and their rainfall thresholds in the Wenchuan earthquake-affected area. Landslides 13, 1215-1229.

Haas, T.d. & Woerkom, T.v. 2016. Bed scour by debris flows: experimental investigation of effects of debris-flow composition. Earth Surface Processes and Landforms 41(13), 1951-1966.

Han, X., Yin, Y., Wu, Y. & Wu, S. 2021a. Risk assessment of population loss posed by earthquake-landslide-debris flow disaster chain: a case study in Wenchuan, China. ISPRS International Journal of Geo-Information 10(6), 363.

Han, Z. 2015. DEVELOPMENT OF A COMPREHENSIVE METHOD FOR DEBRIS-FLOW ANALYSIS OVER COMPLEX TOPOGRAPHY CONSIDERING NONUNIFORM VELOCITY DISTRIBUTION AND BED-SEDIMENT EROSION. PhD thesis, 九州大学.

Han, Z., Chen, G., Li, Y., Wang, W. & Zhang, H. 2015. Exploring the velocity distribution of debris flows: an iteration algorithm based approach for complex cross-sections. Geomorphology 241, 72-82.

Han, Z., Fu, Q., Jiang, N., Ma, Y., Zhang, X. & Li, Y. 2024. Optimizing the Numerical Simulation of Debris Flows: A New Exploration of the Hexagonal Cellular Automaton Method. Water 16(11), 1536.

Han, Z., Li, Y., Huang, J., Chen, G., Xu, L., Tang, C., Zhang, H. & Shang, Y. 2017. Numerical simulation for run-out extent of debris flows using an improved cellular automaton model. Bulletin of Engineering Geology and the Environment 76, 961-974.

Han, Z., Ma, Y., Li, Y., Zhang, H., Chen, N., Hu, G. & Chen, G. 2021b. Hydrodynamic and topography based cellular automaton model for simulating debris flow run-out extent and entrainment behavior. Water Research 193, 116872.

Han, Z., Su, B., Li, Y., Wang, W., Wang, W., Huang, J. & Chen, G. 2019. Numerical simulation of debris-flow behavior based on the SPH method incorporating the Herschel-Bulkley-Papanastasiou rheology model. Engineering Geology 255, 26-36.

Hibert, C., Mangeney, A., Grandjean, G., Baillard, C., Rivet, D., Shapiro, N.M., Satriano, C., Maggi, A., Boissier, P. & Ferrazzini, V. 2014. Automated identification, location, and volume estimation of rockfalls at Piton de la Fournaise volcano. Journal of Geophysical Research: Earth Surface 119(5), 1082-1105.

Hibert, C., Mangeney, A., Grandjean, G. & Shapiro, N. 2011. Slope instabilities in Dolomieu crater, Réunion Island: From seismic signals to rockfall characteristics. Journal of Geophysical Research: Earth Surface 116(F4).

Horton, P., Jaboyedoff, M., Rudaz, B.e., al & Zimmermann, M. 2013. Flow-R, a model for susceptibility mapping of debris flows and other gravitational hazards at a regional scale. Natural hazards and earth system sciences 13(4), 869-885.

Huang, R. & Fan, X. 2013. The landslide story. Nature Geoscience 6(5), 325-326.

Hübl, J. & Steinwendtner, H. 2001. Two-dimensional simulation of two viscous debris flows in Austria. Physics and Chemistry of the Earth, Part C: Solar, Terrestrial & Planetary Science 26(9), 639-644.

Hungr, O., Yau, H., Tse, C., Cheng, L. & Cheng, L. 1999. Natural slope hazard and risk assessment framework. *Urban ground engineering*. Thomas Telford Publishing, 332-353.

Hürlimann, M., Coviello, V., Bel, C., Guo, X., Berti, M., Graf, C., Hübl, J., Miyata, S., Smith, J.B. & Yin, H.-Y. 2019. Debris-flow monitoring and warning: Review and examples. Earth-Science Reviews 199, 102981.

Hürlimann, M., Rickenmann, D., Medina, V. & Bateman, A. 2008. Evaluation of approaches to calculate debris-flow parameters for hazard assessment. Engineering Geology 102(3-4), 152-163.

Iovine, G., D'Ambrosio, D. & Di Gregorio, S. 2005. Applying genetic algorithms for calibrating a hexagonal cellular automata model for the simulation of debris flows characterised by strong inertial effects. Geomorphology 66(1-4), 287-303.

Issler, D. 2014. Dynamically consistent entrainment laws for depth-averaged avalanche models. Journal of Fluid Mechanics 759, 701-738.

Iverson, R.M. 1997. The physics of debris flows. Reviews of geophysics 35(3), 245-296.

Iverson, R.M. 2012. Elementary theory of bed-sediment entrainment by debris flows and avalanches. Journal of Geophysical Research: Earth Surface 117(F3), F03006.

Iverson, R.M. 2015. Scaling and design of landslide and debris-flow experiments. Geomorphology 244, 9-20.

Iverson, R.M., Logan, M., LaHusen, R.G. & Berti, M. 2010. The perfect debris flow? Aggregated results from 28 large-scale experiments. Journal of Geophysical Research: Earth Surface 115(F3).

Iverson, R.M., Reid, M.E. & LaHusen, R.G. 1997. Debris-flow mobilization from landslides. Annual Review of Earth and Planetary Sciences 25(1), 85-138.

Iverson, R.M., Reid, M.E., Logan, M., LaHusen, R.G., Godt, J.W. & Griswold, J.P. 2011. Positive feedback and momentum growth during debris-flow entrainment of wet bed sediment. Nature Geoscience 4(2), 116-121.

Jacobs, W., Le Hir, P., Van Kesteren, W. & Cann, P. 2011. Erosion threshold of sand–mud mixtures. Continental Shelf Research 31(10), S14-S25.

Jakob, M., Hungr, O., Cannon, S.H. & Gartner, J.E. 2005a. Wildfire-related debris flow from a hazards perspective. Debris-flow hazards and related phenomena, 363-385.

Jakob, M., Hungr, O., Cui, P., Chen, X., Waqng, Y., Hu, K. & Li, Y. 2005b. Jiangjia Ravine debris flows in south-western China. Debris-flow hazards and related phenomena, 565-594.

Jakob, M., Hungr, O. & Jakob, D.M. 2005c. Debris-flow hazards and related phenomena. Berlin: Springer.

Jia, G., Alvioli, M., Gariano, S.L., Marchesini, I., Guzzetti, F. & Tang, Q. 2021. A global landslide non-susceptibility map. Geomorphology 389, 107804.

Johnson, A.M. 1984. Debris flows. Slope instability, 257-361.

Johnson, C., Kokelaar, B., Iverson, R.M., Logan, M., LaHusen, R. & Gray, J. 2012. Grain-size segregation and levee formation in geophysical mass flows. Journal of Geophysical Research: Earth Surface 117(F1), F01032.

Kang, S. & Lee, S.-R. 2018. Debris flow susceptibility assessment based on an empirical approach in the central region of South Korea. Geomorphology 308, 1-12.

Kawamura, S., Kawajiri, S., Hirose, W. & Watanabe, T. 2019. Slope failures/landslides over a wide area in the 2018 Hokkaido Eastern Iburi earthquake. Soils and Foundations 59(6), 2376-2395.

Kokelaar, B., Graham, R., Gray, J. & Vallance, J.W. 2014. Fine-grained linings of leveed channels facilitate runout of granular flows. Earth and Planetary Science Letters 385, 172-180.

Kurilla, L.J. & Fubelli, G. 2022. Global debris flow susceptibility based on a comparative analysis of a single global model versus a continent-by-continent approach. Natural Hazards 113(1), 527-546.

Larsen, M.C., Wieczorek, G.F. & Latrubesse, E. 2006. Geomorphic effects of large debris flows and flash floods, northern Venezuela, 1999. Zeitschrift für Geomorphologie Neue Folge, Supplementband 145, 147-175.

Lee, D.-H., Cheon, E., Lim, H.-H., Choi, S.-K., Kim, Y.-T. & Lee, S.-R. 2021. An artificial neural network model to predict debris-flow volumes caused by extreme rainfall in the central region of South Korea. Engineering Geology 281, 105979.

Li, C., Han, Z., Li, Y., Li, M., Wang, W., Dou, J., Xu, L. & Chen, G. 2023. Physical information-fused deep learning model ensembled with a subregion-specific sampling method for predicting flood dynamics. Journal of Hydrology 620, 129465.

Li, M.-H., Sung, R.-T., Dong, J.-J., Lee, C.-T. & Chen, C.-C. 2011. The formation and breaching of a short-lived landslide dam at Hsiaolin Village, Taiwan—Part II: Simulation of debris flow with landslide dam breach. Engineering Geology 123(1-2), 60-71.

Linardos, V., Drakaki, M., Tzionas, P. & Karnavas, Y.L. 2022. Machine learning in disaster management: recent developments in methods and applications. Machine Learning and Knowledge Extraction 4(2), 446.

Logan, M. & Iverson, R.M. 2007. Video documentation of experiments at the USGS debris-flow flume 1992–2017 (ver 1.4, January 2018). US Geological Survey Open-File Report Report 2007-1335.

Lube, G., Breard, E.C., Esposti-Ongaro, T., Dufek, J. & Brand, B. 2020. Multiphase flow behaviour and hazard prediction of pyroclastic density currents. Nature Reviews Earth & Environment 1(7), 348-365.

Ma, S. & Xu, C. 2019. Assessment of co-seismic landslide hazard using the Newmark model and statistical analyses: a case study of the 2013 Lushan, China, Mw6. 6 earthquake. Natural Hazards 96, 389-412.

Ma, Y., Han, Z., Li, Y., Chen, G., Wang, W., Chen, N., Hu, G., Zhao, L. & Dou, J. 2023. Robustness evaluation of the probability-based HTCA model for simulating debris-flow run-out extent: Case study of the 2010 Hongchun event, China. Engineering Geology 312, 106918.

Major, J.J. & Pierson, T.C. 1992. Debris flow rheology: Experimental analysis of fine-grained slurries. Water resources research 28(3), 841-857.

Mangeney, A. 2011. Landslide boost from entrainment. Nature Geoscience 4(2), 77-78.

Mangeney, A., Bouchut, F., Thomas, N., Vilotte, J.-P. & Bristeau, M.-O. 2007. Numerical modeling of self-channeling granular flows and of their levee-channel deposits. Journal of Geophysical Research: Earth Surface 112(F2).

Mangeney, A., Roche, O., Hungr, O., Mangold, N., Faccanoni, G. & Lucas, A. 2010. Erosion and mobility in granular collapse over sloping beds. Journal of Geophysical Research: Earth Surface 115(F3).

Martha, T.R., Kerle, N., Jetten, V., van Westen, C.J. & Kumar, K.V. 2010. Characterising spectral, spatial and morphometric properties of landslides for semi-automatic detection using object-oriented methods. Geomorphology 116(1-2), 24-36.

Marzocchi, W., Mastellone, M., Di Ruocco, A., Novelli, P., Romeo, E. & Gasparini, P. 2009. Principles of multi-risk assessment: Interaction amongst natural and man-induced risks. Project Report EUR 23615.

McCave, I. 2006. Introduction to the Physics of Cohesive Sediment in the Marine Environment. Geological Magazine 143(1), 137.

McCoy, S., Kean, J.W., Coe, J.A., Tucker, G., Staley, D.M. & Wasklewicz, T. 2012. Sediment entrainment by debris flows: In situ measurements from the headwaters of a steep catchment. Journal of Geophysical Research: Earth Surface 117(F3), F03016.

McDougall, S. & Hungr, O. 2005. Dynamic modelling of entrainment in rapid landslides. Canadian Geotechnical Journal 42(5), 1437-1448.

Mergili, M., Krenn, J. & Chu, H.-J. 2015. r. randomwalk v1, a multi-functional conceptual tool for mass movement routing. Geoscientific Model Development 8(12), 4027-4043.

Mniszewski, S.M., Belak, J., Fattebert, J.-L., Negre, C.F., Slattery, S.R., Adedoyin, A.A., Bird, R.F., Chang, C., Chen, G. & Ethier, S. 2021. Enabling particle applications for exascale computing platforms. The International Journal of High Performance Computing Applications 35(6), 572-597.

Mondini, A.C., Guzzetti, F. & Melillo, M. 2023. Deep learning forecast of rainfall-induced shallow landslides. Nature communications 14(1), 2466.

Nagl, G., Hübl, J. & Kaitna, R. 2020. Velocity profiles and basal stresses in natural debris flows. Earth Surface Processes and Landforms 45(8), 1764-1776.

Niethammer, U., James, M., Rothmund, S., Travelletti, J. & Joswig, M. 2012. UAV-based remote sensing of the Super-Sauze landslide: Evaluation and results. Engineering Geology 128, 2-11.

O'Callaghan, J.F. & Mark, D.M. 1984. The extraction of drainage networks from digital elevation data. Computer vision, graphics, and image processing 28(3), 323-344.

Parsons, J.D., Whipple, K.X. & Simoni, A. 2001. Experimental study of the grain-flow, fluid-mud transition in debris flows. The Journal of Geology 109(4), 427-447.

Pasculli, A. & Audisio, C. 2015. Cellular automata modelling of fluvial evolution: real and parametric numerical results comparison along River Pellice (NW Italy). Environmental Modeling & Assessment 20, 425-441.

Pastor, M., Tayyebi, S.M., Hernandez, A., Gao, L., Stickle, M.M. & Lin, C. 2023. A new two-layer two-phase depth-integrated SPH model implementing dewatering: Application to debris flows. Computers and Geotechnics 153, 105099.

Perron, J.T. 2017. Climate and the pace of erosional landscape evolution. Annual Review of Earth and Planetary Sciences 45, 561-591.

Pierson, T.C. 1980. Erosion and deposition by debris flows at Mt Thomas, north Canterbury, New Zealand. Earth Surface Processes 5(3), 227-247.

Pierson, T.C. 2020. Flow behavior of channelized debris flows, Mount St. Helens, Washington. *Hillslope processes*. Routledge, 269-296.

Pierson, T.C. & Costa, J.E. 1987. A rheologic classification of subaerial sediment-water flows. Reviews in engineering geology 7, 1-12.

Pudasaini, S.P. 2012. A general two-phase debris flow model. Journal of Geophysical Research: Earth Surface 117(F3), F03010.

Pudasaini, S.P. & Fischer, J.-T. 2020. A mechanical erosion model for two-phase mass flows. International Journal of Multiphase Flow 132, 103416.

Pudasaini, S.P. & Hutter, K. 2007. Avalanche dynamics: dynamics of rapid flows of dense granular avalanches. Springer Science & Business Media.

Pudasaini, S.P. & Krautblatter, M. 2021. The mechanics of landslide mobility with erosion. Nature communications 12(1), 6793.

Pudasaini, S.P. & Mergili, M. 2019. A multi-phase mass flow model. Journal of Geophysical Research: Earth Surface 124(12), 2920-2942.

Quinn, P., Beven, K., Chevallier, P. & Planchon, O. 1991. The prediction of hillslope flow paths for distributed hydrological modelling using digital terrain models. Hydrological processes 5(1), 59-79.

Raymond, C.A., McGuire, L.A., Youberg, A.M., Staley, D.M. & Kean, J.W. 2020. Thresholds for post-wildfire debris flows: Insights from the Pinal Fire, Arizona, USA. Earth Surface Processes and Landforms 45(6), 1349-1360.

Rickenmann, D. 1999. Empirical relationships for debris flows. Natural hazards 19, 47-77.

Scheidl, C. & Rickenmann, D. 2010. Empirical prediction of debris-flow mobility and deposition on fans. Earth Surface Processes and Landforms: The Journal of the British Geomorphological Research Group 35(2), 157-173.

Scheild, C. & Rickenmann, D. 2011. TopFlowDF-A simple GIS based model to simulate debris-flow runout on the fan. Italian journal of engineering geology and environment, 253-262.

Schofield, A. & Wroth, P. 1968. Critical State Soil Mechanics (Mcgrau-Hill, London, 1968). Engineering Properties of Soil 1st edn (Hydroelectricity Publishing, Beijing, 1983)(in Chinese).

Scott, W.E., Hoblitt, R.P., Torres, R.C., Self, S., Martinez, M.M.L. & Nillos, T. 1996. Pyroclastic flows of the June 15, 1991, climactic eruption of Mount Pinatubo. Fire and mud: Eruptions and lahars of Mount Pinatubo, Philippines, 545-570.

Shinohara, Y. & Kume, T. 2022. Changes in the factors contributing to the reduction of landslide fatalities between 1945 and 2019 in Japan. Science of The Total Environment 827, 154392.

Si, G.-W., Chen, X.-Q., Chen, J.-G., Tang, J.-B., Zhao, W.-Y. & Jin, K. 2022. The Impact Force of Large Boulders with Irregular Shape in Flash Flood and Debris Flow. Journal of Civil Engineering 26(10), 4276-4289.

Stock, J. & Dietrich, W.E. 2003. Valley incision by debris flows: Evidence of a topographic signature. Water Resources Research 39(4)(4).

Suwa, H., Okano, K. & Kanno, T. 2009. Behavior of debris flows monitored on test slopes of Kamikamihorizawa Creek, Mount Yakedake, Japan. International Journal of Erosion Control Engineering 2(2), 33-45.

Syvitski, J., Ángel, J.R., Saito, Y., Overeem, I., Vörösmarty, C.J., Wang, H. & Olago, D. 2022. Earth's sediment cycle during the Anthropocene. Nature Reviews Earth & Environment 3(3), 179-196.

Takahashi, T. 1981. Debris flow. Annual review of fluid mechanics 13(1), 57-77.

Takahashi, T. 2007. Debris flow: mechanics, prediction and countermeasures. Taylor & Francis.

Takahashi, T.J.I.J.o.E.C.E. 2009. A review of Japanese debris flow research. International Journal of Erosion Control Engineering 2(1), 1-14.

Tang, C., Rengers, N.v., Van Asch, T.W., Yang, Y. & Wang, G. 2011a. Triggering conditions and depositional characteristics of a disastrous debris flow event in Zhouqu city, Gansu Province, northwestern China. Natural Hazards and Earth System Sciences 11(11), 2903-2912.

Tang, C., van Asch, T.W., Chang, M., Chen, G.Q., Zhao, X.H. & Huang, X.C. 2012. Catastrophic debris flows on 13 August 2010 in the Qingping area, southwestern China: the combined effects of a strong earthquake and subsequent rainstorms. Geomorphology 139, 559-576.

Tang, C., Zhu, J., Ding, J., Cui, X.F., Chen, L. & Zhang, J.S. 2011b. Catastrophic debris flows triggered by a 14 August 2010 rainfall at the epicenter of the Wenchuan earthquake. Landslides 8, 485-497.

Tang, C., Zhu, J., Li, W. & Liang, J. 2009. Rainfall-triggered debris flows following the Wenchuan earthquake. Bulletin of Engineering Geology and the Environment 68, 187-194.

Tarvainen, T., Jarva, J. & Greiving, S. 2006. Spatial pattern of hazards and hazard interactions in Europe. Special Paper-Geological Survey of Finland 42, 83.

Theule, J., Liébault, F., Laigle, D., Loye, A. & Jaboyedoff, M. 2015. Channel scour and fill by debris flows and bedload transport. Geomorphology 243, 92-105.

Tofani, V., Segoni, S., Agostini, A., Catani, F. & Casagli, N. 2013. Use of remote sensing for landslide studies in Europe. Natural Hazards and Earth System Sciences 13(2), 299-309.

Vicari, H., Ng, C.W., Nordal, S., Thakur, V., De Silva, W.R.K., Liu, H. & Choi, C.E. 2022a. The effects of upstream flexible barrier on the debris flow entrainment and impact dynamics on a terminal barrier. Canadian Geotechnical Journal 59(6), 1007-1019.

Vicari, H., Nordal, S. & Thakur, V. Year. The significance of entrainment on debris flow modelling: the case of Hunnedalen, Norway. In: Challenges and Innovations in Geomechanics: Proceedings of the 16th International Conference of IACMAG-Volume 2 16, 507-514.

Vicari, H., Tran, Q.A., Nordal, S. & Thakur, V. 2022b. MPM modelling of debris flow entrainment and interaction with an upstream flexible barrier. Landslides 19(9), 2101-2115.

Walter, F., Amann, F., Kos, A., Kenner, R., Phillips, M., de Preux, A., Huss, M., Tognacca, C., Clinton, J. & Diehl, T. 2020. Direct observations of a three million cubic meter rock-slope collapse with almost immediate initiation of ensuing debris flows. Geomorphology 351, 106933.

Wang, F., Wang, J., Chen, X., Zhang, S., Qiu, H. & Lou, C. 2022. Numerical Simulation of Boulder Fluid–Solid Coupling in Debris Flow: A Case Study in Zhouqu County, Gansu Province, China. Water 14(23), 3884.

Wang, Z.-Y., Wang, G.-Q. & Liu, C. 2005. Viscous and two-phase debris flows in southern China's Yunnan Plateau. Water international 30(1), 14-23.

Winter, M., Macgregor, F. & Shackman, L. 2005. Scottish road network landslides study.

Winterwerp, J., Van Kesteren, W., Van Prooijen, B. & Jacobs, W. 2012. A conceptual framework for shear flow–induced erosion of soft cohesive sediment beds. Journal of Geophysical Research: Oceans 117(C10), C10020.

Wong, H., Ho, K. & Chan, Y. 2018. Assessment of consequence of landslides. *Landslide risk assessment*. Routledge, 111-149.

Xiong, J., Tang, C., Chen, M., Zhang, X., Shi, Q., Gong, L.J.B.o.E.G. & Environment, t. 2021. Activity characteristics and enlightenment of the debris flow triggered by the rainstorm on 20 August 2019 in Wenchuan County, China. Bulletin of Engineering Geology and the Environment 80, 873-888.

Xu, Q., Zhang, S., Li, W. & Van Asch, T.W. 2012. The 13 August 2010 catastrophic debris flows after the 2008 Wenchuan earthquake, China. Natural Hazards and Earth System Sciences 12(1), 201-216.

Yang, Y., Tang, C., Tang, C., Chen, M., Cai, Y., Bu, X. & Liu, C. 2023. Spatial and temporal evolution of long-term debris flow activity and the dynamic influence of condition factors in the Wenchuan earthquake-affected area, Sichuan, China. Geomorphology 435, 108755.

Yu, B., Ma, Y. & Wu, Y. 2013. Case study of a giant debris flow in the Wenjia Gully, Sichuan Province, China. Natural Hazards 65, 835-849.

Yu, P., Peng, X., Chen, G., Fu, H., Zhang, Y., Han, Z. & Zhang, H. 2023. A new coupled depth-integrated model incorporating 3D DDA on debris flow with large boulders. International Journal of Rock Mechanics and Mining Sciences 170, 105496.

Zhang, S., Wang, F. & Li, R. 2022. First insight into the catastrophic Atami debris flow induced by a rain gush on 3 July 2021 in Shizuoka, Japan. Springer.

Zhang, S. & Zhang, L. 2017. Impact of the 2008 Wenchuan earthquake in China on subsequent long-term debris flow activities in the epicentral area. Geomorphology 276, 86-103.

Zheng, H., Deng, Z., Guo, L., Liu, J., Liu, L., Li, T., Zheng, H. & Zheng, T. 2023a. Assessment of Building Physical Vulnerability in Earthquake-Debris Flow Disaster Chain. International Journal of Disaster Risk Science 14(4), 666-679.

Zheng, H., Shi, Z., Hanley, K.J., Zhou, Y. & Hu, X. 2023b. Pore pressure evolution in bed sediment overridden by debris flow: A general formulation. Earth Surface Processes and Landforms 48(6), 1188-1201.

Zheng, H., Shi, Z., Yu, S., Fan, X., Hanley, K.J. & Feng, S. 2021. Erosion mechanisms of debris flow on the sediment bed. Water Resources Research 57(12), e2021WR030707.

Zhou, W., Qiu, H., Wang, L., Pei, Y., Tang, B., Ma, S., Yang, D. & Cao, M. 2022. Combining rainfall-induced shallow landslides and subsequent debris flows for hazard chain prediction. Catena 213, 106199.

Zhu, L., He, S., Qin, H., He, W., Zhang, H., Zhang, Y., Jian, J., Li, J. & Su, P. 2021. Analyzing the multi-hazard chain induced by a debris flow in Xiaojinchuan River, Sichuan, China. Engineering Geology 293, 106280.

CHAPTER 2

STATE-OF-THE-ART REVIEW OF DEBRIS-FLOW PREDICTION METHOD

2.1. INTRODUCTION

This chapter provides an overall review of numerical simulation methods for debris flows, focusing on the basic methodology, latest advancements, application scenarios, and existing issues of two particle-based numerical methods: Smoothed Particle Hydrodynamics (SPH) method, and the Discrete Element Method (DEM). It also reviews other numerical simulation methods for debris flows, including empirical methods, depth-averaged (Shallow Water Equations (SWEs)) methods, and probabilistic and data-driven methods, comparing these with the particle-based methods under study. Finally, it offers insights into future directions for numerical modeling of debris flows and draws conclusions. Before conducting a detailed review, we first introduce the basic concepts of particle methods and how they address various challenges in engineering and applied sciences.

The term "Particle-Based Methods" encompasses two distinct computational approaches in hydrodynamics and geotechnical engineering. Firstly, it refers to discretization techniques where the continuum's response is represented by “particles” that carry mechanical deformation during the process. Typical representatives include Meshless Methods, Smoothed Particle Hydrodynamics (SPH), Moving Particle Simulation (MPS), Particle Finite Element Method

(PFEM), Material Point Method (MPM), and Lattice-Boltzmann Method (LBM). Secondly, it pertains to the computational modeling of physical particles at various scales. Classical methods include Molecular Dynamics (MD) and the Discrete (Distinct) Element Method (DEM). In these models, particles either pre-exist, as in granular materials, or emerge during the loading process. Sometimes, these two approaches of discretization and physical particle modeling are interconnected.

2.2. THE SMOOTHED PARTICLES HYDRODYNAMICS METHOD

2.2.1. STATE-OF-THE-ART OF SPH METHOD AND ITS APPLICATION IN DEBRIS-FLOW SIMULATION

Among the various particle-based methods, the Smoothed Particle Hydrodynamics (SPH) method is one of the earliest continuum approaches that is entirely mesh-free and does not rely on a background mesh to solve partial differential equations (PDEs) (Koshizuka and Oka 1996; Liu et al. 2005; Bui and Nguyen 2021). This method was first introduced by Lucy (1977) and subsequently advanced by Gingold and Monaghan (1977) for applications in astrophysics. Owing to its exceptional ability in handling large deformations, free surface flow, and post-failure issues, the method has become popular and is widely applied in hydrodynamics to address fluid-like phenomena (e.g., Hu and Adams 2006; Bui et al. 2007; Pastor et al. 2009; Pudasaini 2012; Wang et al. 2016; Xu and Deng 2016; Nguyen et al. 2017; Han et al. 2019; Morikawa et al. 2019; Nikooei and Manzari 2020; Yang et al. 2020; Zhou et al. 2024), as well as in geotechnical engineering, focusing on solid-like phenomena (e.g., Libersky and Petschek 2005; Bui et al. 2008; Bui et al. 2011; Bui et al. 2014; Wang and Chan 2014; Peng et al. 2015; Douillet-Grellier et al. 2016; Islam and Peng 2019; Ma et al. 2022; Morikawa and Asai 2022). Furthermore, SPH has been utilized in various engineering applications, including geohazard simulation (e.g., landslides and debris flows) (e.g., Pudasaini 2012), marine and offshore engineering (effects of waves on coasts, ships, and marine structures) (e.g., Ulrich et al. 2013), environmental engineering (e.g., water cycle and pollutant dispersion) (e.g., Aristodemo et al. 2010), and biomedical engineering (e.g., Mao et al. 2017).

Table 2.1 An overview of the SPH code & software.

Code/Software	Reference	SPH scheme	Acceleration
AQUAgpusph	Cercos-Pita (2015)	WCSPH	OpenCL[1]
DualSPHysics	Crespo et al. (2015)	WCSPH	OpenMP[2], CUDA[3]
GADGET-2	Springel (2005)	WCSPH	/
GPUSPH	Bilotta et al. (2016)	WCSPH	CUDA
Ndspmhd	Price (2012)	WCSPH	/
Neutrino	Akinci (2014)	ISPH	Multi-GPU
PersianSPH	Korzani (2017)	WCSPH	/
PreonLab	FIFTY2 PreonLab	ISPH	CPU, GPU
PySPH	Ramachandran et al. (2021)	WCSPH	OpenMP, OpenCL
SPHERA	Amicarelli et al. (2020)	WCSPH	OpenMP
SPHinXsys	Zhang et al. (2021)	WCSPH	/
SPHysics	Gomez-Gesteira et al. (2012)	WCSPH	/
SPLASH	Arnold et al. (1992)	WCSPH	/
SPlisHSPlasH	Bender (2019)	WCSPH/ ISPH	OpenMP, AVX[4], CUDA
SWIFT	Schaller et al. (2018)	WCSPH	MPI[5], SIMD[6]

[1] OpenCL (Open Computing Language) is a framework that enables code to be executed in parallel across various heterogeneous computing platforms, significantly accelerating computation-intensive tasks.
[2] OpenMP (Open Multi-Processing) is an API that supports multi-platform shared memory multiprocessing programming in C, C++, and Fortran, enabling the parallel execution of code to improve performance on multi-core processors.
[3] CUDA (Compute Unified Device Architecture) is a parallel computing platform and API developed by NVIDIA, allowing developers to use NVIDIA GPUs for general-purpose processing to accelerate computation-intensive tasks.
[4] AVX (Advanced Vector Extensions) is an extension to the x86 instruction set architecture, providing SIMD (Single Instruction, Multiple Data) capabilities to significantly speed up data parallel processing on compatible CPUs.
[5] MPI (Message Passing Interface) is a standardized and portable message-passing system designed to function on parallel computing architectures, enabling processes to communicate with each other for efficient parallel computing.
[6] SIMD (Single Instruction, Multiple Data) is a parallel computing architecture that allows a single instruction to process multiple data points simultaneously, enhancing performance for data-parallel

tasks in applications such as multimedia, scientific computing, and machine learning.

SPH stands out from other particle-based methods due to its direct approach in solving the governing PDEs through approximations of their strong forms. In contrast, other particle-based methods tackle the weak forms of PDEs (Bui and Nguyen 2021). Bypassing the requirement to navigate through the weak form formula, integrating the SPH approximation of a fresh PDE, which delineates a novel physical phenomenon, into an existing SPH framework becomes a more direct process. Currently, SPH shows promise as a numerical method but struggles with a lack of widespread recognition in the scientific community as a viable candidate for becoming a prominent numerical tool in the future. Despite recent advancements, significant work remains to address these challenges. The SPHERIC Grand Challenge Working Group (GCWG) has identified several remaining grand challenges, including (1) convergence, consistency, and stability; (2) boundary conditions; (3) adaptivity; (4) coupling with other models, and (5) applicability to industry (Vacondio et al. 2021). To overcome these issues, various powerful open-source or commercial SPH software and codes have been developed. Table 2.1 summarizes several current advanced SPH open-source and commercial programs. These codes often utilize advanced parallel particle acceleration technology and are increasingly being applied to various complex engineering problems, including multi-physics and multi-phase flows. This study focuses on the innovations and applications of SPH in engineering geology, particularly in the simulation of geophysical flows and sediment transport processes on the Earth's surface.

The earliest application of the SPH method in simulating geophysical flow is documented by Hungr (1995). Initial uses of the SPH method often employed depth-integrated simplifications (e.g., Ata and Soulaïmani 2005; Pastor et al. 2009; Pastor et al. 2014; Shen et al. 2019; Pastor et al. 2022). Given that the vertical depth of most geophysical flows is much smaller than their horizontal dimensions, the shallow water assumption serves as a reasonable approximation in many real-world scenarios, significantly reducing computational costs and complexities (Domnik and Pudasaini 2012; Pudasaini and Mergili 2019). However, as previously mentioned, for debris flows with diverse material compositions, the significant non-uniformity and heterogeneity in the vertical direction render the depth-averaged assumption invalid. Accordingly, research into full form, three-dimensional Navier-Stokes computation framework has surged recently. The shift has resulted in an exponential increase in computational demand, accompanied by the challenges in complex boundary treatments. As such, previous SPH-based methods are generally limited to single-layer frameworks or small-scale applications (e.g., Peng et al. 2015; Wang et al. 2016; Han et al. 2019; Han et al. 2020; Nikooei and Manzari 2020).

To achieve unified modeling of the heterogeneous material composition of debris flows, there are two strategies corresponding to two typical schemes in the SPH method: the so-called Weakly Compressible SPH (WCSPH) scheme (Gingold and Monaghan 1977; Monaghan 1992) and the Incompressible SPH (ISPH) scheme (Cummins and Rudman 1999; Ellero et al. 2007). The WCSPH scheme treats the mixed material of debris flows, comprising soil, rock, and water, as a compressible entity, specifically a particle-fluid mixture with variable density, approximating the relationship between pressure and density through an equation of state (Batchelor 1967). By eliminating the need to solve the Pressure Poisson Equation (PPE), it employs an explicit time integration method to simulate the dynamic process of compressible fluids, making it relatively simple to implement. However, density fluctuations also introduce numerical noise and stability issues (Lee et al. 2008). Alternatively, the ISPH scheme requires separate modeling of the soil, rock particles, and fluid in debris flows, treating all entities as incompressible and with constant density. Pressure at each time step is obtained by solving the PPE. Since it uses an implicit integration method, the time step can be relatively large and is not strictly limited by the CFL condition. Comparative studies of the WCSPH and ISPH methods for free-surface flows have indicated that the ISPH method provides enhanced accuracy in both velocity and pressure fields (Lee et al. 2008; Xu et al. 2009; Lee et al. 2010; Ran et al. 2015; Ghaïtanellis et al. 2018; Asai et al. 2023). However, separate modeling of each phase also necessitates considering the strong coupling effects between multi-scale, multi-phase particles, significantly increasing the complexity and computational cost of simulation. More importantly, the acquisition of mesoscopic parameters such as hydraulic and pore forces required for ISPH modeling and computation is significantly more difficult and costly than obtaining the parameters for the particle-fluid mixture required by WCSPH, particularly in field-scale cases (Delannay et al. 2017). The reasons mentioned above lead to the current preference for the WCSPH scheme in geological disaster simulations. However, with the recent proliferation of multi-core GPUs (Valdez-Balderas et al. 2013; Morikawa et al. 2021; Zhao et al. 2023) and massively parallel particle hydrodynamics technology, as well as a deeper understanding of strong coupling interactions in multi-phase media (e.g., Pudasaini and Mergili 2019; Pudasaini and Fischer 2020a, b; Morikawa and Asai 2021; Ma et al. 2022), the ISPH scheme is increasingly being applied to the prediction of large-scale natural disasters (Morikawa et al. 2020; Morikawa and Asai 2022). In summary, the debate over the two SPH schemes has been ongoing for decades and will continue. However, this study employs the WCSPH scheme, based on the particle-fluid mixture, for experiments and cases approximating field-scale scenarios. A discussion on the more refined, strongly coupled ISPH scheme and its integration with other methods will be provided in Chapter 7.

2.2.2. Fundamentals of SPH

The literature presents several different manners of deducing the fundamentals of SPH, often describing it as an interpolation technique used to approximate field quantities or their spatial derivatives. Bui and Nguyen (2021) argue that SPH is not just a numerical method, but a general approach for solving complex systems and engineering physics problems. In this section, we briefly review the fundamental principles of SPH, focusing primarily on the WCSPH scheme, and introduce its state-of-the-art research advancements. Vectors and tensors are referenced using Cartesian coordinates, with Greek superscripts α, β, and γ indicating the Cartesian tensor coordinate directions, and Latin subscripts i and j designating particle locations. The Einstein summation convention is applied to repeated Greek superscripts.

The SPH method is a Lagrangian, mesh-free method for modeling continuous media, where the domain is discretized into particles that carry physical quantities. The fundamental is the integral representation of a function *f*, which can represent a numerical or physical variable, defined over a domain of interest Ω at a point *x*. the integral representation of a field function states:

$$f(x)=\int_{\Omega} f(x')\delta(x-x')dx', \tag{2.1}$$

$$\delta(x-x')=\begin{cases}0 & x\neq x' \\ 1 & x=x'\end{cases}, \tag{2.2}$$

where $\delta(x-x')$ refers to the Dirac delta function. Mathematically, the Dirac delta function can be approximated by a smoothing kernel function (weight function), and the primordial SPH kernel approximation (Gingold and Monaghan 1977) can be denoted as:

$$f(x)\approx\langle f(x)\rangle=\int_{\Omega} f(x')W(x-x',\ h)dx', \tag{2.3}$$

where *h* is the smoothing length defining the size of the kernel's support domain in which neighboring particles are considered, and *W* represents the weighting or kernel function. The symbol <…> denotes an SPH interpolation and will be omitted for simplicity in the remainder of the paper.

The kernel function is selected to be smooth, isotropic, and even, with compact support (i.e., it has a finite radius of influence around *x*), specified as follows, respectively:

$$\begin{cases}\int_{\Omega} W(x-x',\ h)dx'=1 \\ \lim_{h\to 0} W(x-x',\ h)=\delta(x-x') \\ W(x-x',\ h)=0,\ if\ \ |x-x'|>\kappa h\end{cases}, \tag{2.4}$$

where *k* is a constant that defines the effective area or support domain of the smoothing kernel function at point *x*. Due to the compact condition, the integration over the entire problem domain is localized to the support domain of the smoothing kernel function, allowing the integral domain Ω to match the support domain.

The performance of an SPH model is highly dependent on the choice of the smoothing kernel, and the selection will directly affect the accuracy, efficiency and stability of SPH algorithms (Dehnen and Aly 2012). Kernels are expressed as a function of the non-dimensional distance between particles, R, defined as $R=\left|x_i-x_j\right|/h$. The two most popular kernel functions are the cubic spline function and the quintic function. The cubic spline kernel function is defined as follows (Monaghan and Lattanzio 1985):

$$W(R,\ h)=\alpha_d\begin{cases}1-\frac{3}{2}R^2+\frac{3}{4}R^3 & 0\le R\le 1\\ \frac{1}{4}(2-R)^3 & 1\le R\le 2\\ 0 & R\ge 2\end{cases}, \tag{2.5}$$

where α_d denotes the dimensional normalizing factor, defined as $\alpha_d=[2/3h,\ 10/7\pi h^2,\ 1/\pi h^3]$ for one-, two- and three-dimensions, respectively. The tensile correction method proposed by Monaghan (2000) is only used when the kernel's first derivative approaches zero as the particle distance R increases. The fifth-order quintic Wendland kernel with compact support of $2h$ takes the following form (Wendland 1995):

$$W(R,\ h)=\alpha_D\begin{cases}(1-\frac{R}{2})^4(2R+1) & 0\le R\le 2\\ 0 & 2<R\end{cases}, \tag{2.6}$$

where α_d also indicates normalization constant, defined as $\alpha_d=[7/4\pi h^2,\ 21/16\pi h^3]$ for two- and three-dimensions, respectively. In addition, various other kernel functions are available for different applications (e.g., Morris et al. 1997; Liu and Liu 2003; Monaghan 2005; Farhadi et al. 2016). For example, the Gaussian kernel function (Monaghan 2005) lacks a compact domain, causing all particles to contribute to the SPH approximation and resulting in unnecessarily high computational costs. In contrast, the Cubic-spline function rapidly decreases and approaches zero at $R=2$, restricting the calculation to nearby particles and significantly reducing computational costs.

To derive the final SPH approximation for a function, Equation (2.3) must be discretized onto a set of particles representing a continuous field. This is achieved by replacing the integral in Equation (2.3) with a summation over a set of particles, each with a volume $V_j=m_j/\rho_j$, the particle approximation is obtained by:

$$\left\langle f(x_i)\right\rangle=\sum_{j=1}^{N}f(x_j)W(x_i-x_j,\ h)V_j, \tag{2.7}$$

$$W_{ij} = W\left(x_i - x_j,\ h\right) = W\left(\left|x - x'\right|,\ h\right), \tag{2.8}$$

Equation (2.7) depicts that the value of a scalar function $f(x_i)$ at particle i can be approximated by the weighted average of its values at neighboring particles within the influence domain of the kernel function, characterized by the length h. As such, the gradient of function $f(x)$, hereafter referred to as ∇f, can be directly obtained by differentiating Equation (2.3), resulting in:

$$\nabla f\left(x_i\right) \approx \left\langle \nabla f\left(x_i\right)\right\rangle = \sum_{j=1}^{N} f\left(x_j\right) \nabla_i W\left(x_i - x_j,\ h\right) V_j, \tag{2.9}$$

$$\nabla W_{ij} = \nabla_i W\left(x_i - x_j,\ h\right) = \frac{x_i - x_j}{r_{ij}} \frac{\partial W_{ij}}{\partial r_{ij}} = \frac{x_{ij}}{h r_{ij}} \frac{\partial W_{ij}}{\partial R}, \tag{2.10}$$

Where r_{ij} refers to the distance between particles i and j, and $\nabla = (\partial/\partial x,\ \partial/\partial y,\ \partial/\partial z)$ indicates the gradient (nabla) operator. Likewise, the SPH approximation of a vector quantity **f(x)** and its divergence $(\nabla \cdot \mathbf{f})$ can be directly obtained using the same approach and are expressed as follows:

$$\mathbf{f}\left(\mathbf{x_i}\right) \approx \left\langle \mathbf{f}\left(\mathbf{x_i}\right)\right\rangle = \sum_{j=1}^{N} \mathbf{f}\left(\mathbf{x_j}\right) W\left(x_i - x_j,\ h\right) V_j, \tag{2.11}$$

$$\nabla \cdot \mathbf{f}\left(\mathbf{x_i}\right) \approx \left\langle \nabla \cdot \mathbf{f}\left(\mathbf{x_i}\right)\right\rangle = \sum_{j=1}^{N} \mathbf{f}\left(\mathbf{x_j}\right) \cdot \nabla_i W\left(x_i - x_j,\ h\right) V_j. \tag{2.12}$$

The divergence $\nabla \cdot \mathbf{f} = \partial f_x/\partial x + \partial f_y/\partial y + \partial f_z/\partial z$ is a scalar that represents the magnitude of a field's source or sink at a given point. It is noted that the consistency of the kernel approximation does not always yield satisfactory results and often breaks down in the boundary regions without special treatments. A simple way to satisfy the unity conditions is to add a constant coefficient to the discrete form, known as kernel correction (Randles and Libersky 1996; Bonet and Lok 1999). This correction can be defined as follows:

$$\tilde{W}\left(r_{ij},\ h\right) = \frac{W_{ij}}{\int_{S^i} W\left(x_i - x_k,\ h\right)}, \tag{2.13}$$

$$\nabla \tilde{W}\left(r_{ij},\ h\right) = L^{-1} \nabla W_{ij}, \tag{2.14}$$

$$L_i = \sum_{j=1}^{N} \frac{m_j}{\rho_j} \nabla W_{ij} \otimes r_{ij}, \tag{2.15}$$

where S^i represents the region of interior particles truncated by the boundary, $\nabla \tilde{W}(r_{ij}, h)$ denote the correction gradient operator, which is defined by the correction matrix L_i. For an in-depth exploration of the derivations of the SPH approximations, we refer readers to Monaghan (1992), as well as more recent contributions by Bui and Nguyen (2021) and Asai et al. (2023).

2.2.3. Gradient and Laplacian models in SPH

One of the core numerical challenges in applying SPH to solve governing equations in practical problems is the discretization of first and second-order derivatives. Nevertheless, the derivative used in Equations (2.9) and (2.11) does not guarantee the vanishing of gradient for a constant field function. This is problematic when estimating the strain rate or the gradient of a velocity field in computational fluid or solid mechanics. The inaccuracies arising from the SPH approximation for the gradient of a scalar function can be assessed using a Taylor series expansion, as follows:

$$\nabla^{\beta} f_i \approx \sum_{j=1}^{N} V_j f_j \nabla_i^{\beta} W_{ij} = \sum_{j=1}^{N} V_j \left[f_i + \frac{\partial f_i}{\partial x^{\alpha}} \left(x_j - x_i \right)^{\alpha} + o\left(h^2\right) \right] \nabla_i^{\beta} W_{ij}, \tag{2.16}$$

$$\sum_{j=1}^{N} V_j f_j \nabla_i^{\beta} W_{ij} \approx f_i \sum_{j=1}^{N} V_j \nabla_i^{\beta} W_{ij} + \frac{\partial f_i}{\partial x^{\alpha}} \sum_{j=1}^{N} V_j \left(x_j - x_i \right)^{\alpha} \nabla_i^{\beta} W_{ij} + o\left(h^2\right), \tag{2.17}$$

where $\nabla^{\beta} \equiv \partial / \partial x^{\beta}$. The above formulas indicate that the errors arise from the first and second terms on the right-hand side (RHS) of Eq. (2.17). By subtracting the first term of Eq. (2.17) from Eq. (2.9), commonly represented by $\nabla f = \nabla f - f(\nabla 1)$, we obtain the following alternative SPH approximation for the gradient of the function:

$$\nabla f_i \approx \sum_{j=1}^{N} V_j \left(f_j - f_i \right) \nabla_i W_{ij}. \tag{2.18}$$

Another SPH operator for the gradient of a function at particle i can be derived using the following forms:

$$\nabla f_i = \frac{\left[\nabla(\rho_i f_i) - f_i \nabla \rho_i\right]}{\rho_i} = \frac{1}{\rho_i}\sum_{j=1}^{N} m_j \left[f_j - f_i \right] \nabla_i W_{ij}, \tag{2.19}$$

where ρ and m refer to the density and mass, respectively. Similar to the SPH operator in Eq. (2.9), this formulation is used to evaluate the gradient terms. The following well-known SPH gradient operators, commonly used to evaluate the stress or pressure gradient in the momentum equation, will be discussed later along with the general SPH governing equations. These SPH gradient operators can be derived from the following principles:

$$\nabla f(x_i) \approx \left\langle \nabla f(x_i) \right\rangle_{(0)} = \sum_{j=1}^{N} \frac{m_j}{\rho_j} \left[f(x_j) - f(x_i) \right] \nabla W_{ij} \quad \text{and} \tag{2.20}$$

$$\left\langle \nabla f(x_i) \right\rangle_{(0)} = \rho_i \sum_{j=1}^{N} m_j \left[\frac{f(x_i)}{\rho_i^2} + \frac{f(x_j)}{\rho_j^2} \right] \nabla W_{ij}, \tag{2.21}$$

where the subscript (0) indicates the 0^{th}-order accuracy SPH model, as its numerical errors are still controlled by the errors associated with the second term in Eq. (2.17). To fully eliminate these inaccuracies up to 2^{nd}-order accuracy, one can normalize Eq. (2.7), resulting in the following corrected SPH formulation for the kernel derivative (Randles and Libersky 1996; Chen and Beraun 2000):

$$\nabla f(x_i) \approx \left\langle \nabla f(x_i) \right\rangle_{(1)} = \sum_{j=1}^{N} \frac{m_j}{\rho_j} \left[f(x_j) - f(x_i) \right] L^{-1} \nabla W_{ij}. \tag{2.22}$$

The normalized gradient operator is defined as $<\nabla f(x_i)>_{(1)}$ to emphasize that it achieves 1^{st}-order accuracy in the Taylor series expansion after particle discretization. The detailed accuracy comparative analysis of different SPH gradient model, i.e. Eqs (2.20) to (2.22), can be found in previous studies (e.g., Vaughan et al. 2008; Bui and Nguyen 2021; Asai et al. 2023).

The SPH approximation of the Laplacian, involving second derivatives of a scalar or vector field, can be obtained similarly to the SPH approximation for first derivatives. By differentiating Eq. (2.3) and using a Taylor series expansion up to 3^{rd}-order accuracy, the following SPH operator for second derivatives can be derived:

$$\nabla^2 f = \sum_{j=1}^{N} \frac{m_j}{\rho_j}\left(f_j - f_i\right)\nabla_i^2 W_{ij} + \frac{\partial f_i}{\partial x^\alpha}\sum_{j=1}^{N}\frac{m_j}{\rho_j} x_{ji}^\alpha \nabla_i^2 W_{ij} + \frac{1}{2}\frac{\partial}{\partial x^\alpha}\left(\frac{\partial f_i}{\partial x^\beta}\right)\sum_{j=1}^{N}\frac{m_j}{\rho_j} x_{ji}^\alpha x_{ji}^\beta \nabla_i^2 W_{ij} + o\left(h^3\right), \tag{2.23}$$

This formulation depends on the accuracy of the SPH approximations for the terms below:

$$\sum_{j=1}^{N}\frac{m_j}{\rho_j}\nabla_i^2 W_{ij} \approx 0 \;\text{ and }\; \sum_{j=1}^{N}\frac{m_j}{\rho_j} x_{ji}^\alpha x_{ji}^\beta \nabla_i^2 W_{ij} \approx \delta^{\alpha\beta}. \tag{2.24}$$

However, for most existing kernel functions, their second derivatives change sign within the kernel influence domain. This makes the Eq. (2.24) difficult to satisfy, as it requires a highly symmetric particle distribution in all directions. Brookshaw (1985) first introduce a straightforward method to derive the SPH approximation for the Laplacian model. To begin, present the following 3rd-order Taylor series expansion:

$$f_j = f_i + \frac{\partial f_i}{\partial x^\alpha} x_{ji}^\alpha + \frac{1}{2}\frac{\partial^2 f_i}{\partial x^\alpha \partial x^\beta} x_{ji}^\alpha x_{ji}^\beta + o\left(h^3\right), \tag{2.25}$$

Afterwards, multiply both sides of Eq. (2.25) by $x_{ji} \cdot \nabla_i W_{ij} / |x_{ji}|^2$ and integrate respectively to obtain:

$$\int\left(f_j - f_i\right)\frac{x_{ji}\cdot\nabla_i W_{ij}}{\left|x_{ji}\right|^2} dx_j = \frac{\partial f_i}{\partial x^\alpha}\int x_{ji}^\alpha \frac{x_{ji}\cdot\nabla_i W_{ij}}{\left|x_{ji}\right|^2} dx_j + \frac{1}{2}\frac{\partial^2 f_i}{\partial x^\alpha \partial x^\beta}\int x_{ji}^\alpha x_{ji}^\beta \frac{x_{ji}\cdot\nabla_i W_{ij}}{\left|x_{ji}\right|^2} dx_j, \tag{2.26}$$

Based on integral theory, the integral of the first term on the RHS of Eq. (2.26) vanishes for a symmetric kernel function *W*. The second term, however, yields a delta function $\delta^{\alpha\beta}$, ultimately resulting in $\nabla^2 f / 2$. After rearranging Eq. (2.26) and ignored the integral errors associated with these operations, we obtain:

$$\nabla^2 f_i \approx \left\langle \nabla^2 f \right\rangle_{(0)} = 2\sum_{j=1}^{N}\frac{m_j}{\rho_j}\left(f_j - f_i\right)\frac{x_{ji}\cdot\nabla_i W_{ij}}{\left|x_{ji}\right|^2 + \eta^2}, \tag{2.27}$$

where $\eta = 0.0001(h/2)^2$ is defined to avoid numerical dispersion. This formula resembles the SPH approximation for the Laplacian derived by Monaghan (2005) and, like the primitive gradient operator in Eq. (2.20), can only guarantee 0th-order accuracy because it avoids the use of the second derivatives of the kernel function.

The primitive Laplacian model has been successfully applied to modelling the radiative heat diffusion (Brookshaw 1985), seepage force (Fourtakas and Rogers 2016), pore water pressure response (Chen et al. 2024), the viscosity term (Morris et al. 1997; Dalrymple and Rogers 2006) and the density diffusion term (Molteni and Colagrossi 2009; Fourtakas et al. 2020) in weakly compressed fluid. However, the primitive Laplacian model is often criticized for its low accuracy and sensitivity to particle disorder, as well as issues related to kernel truncation at the boundaries (Randles and Libersky 1996; Bonet and Lok 1999; Heydari et al. 2020; Bui and Nguyen 2021; Asai et al. 2023). To minimize these errors, many high-order gradient and Laplacian models have been proposed and applied to practical SPH applications in recent years (e.g., Schwaiger 2008; Basic et al. 2018; Lian et al. 2021; Bašić et al. 2022; Asai et al. 2023).

Despite these efforts, improving the accuracy of the Laplacian model while ensuring efficiency remains extremely challenging. This difficulty arises not only from the need to satisfy the conditions of Eq. (2.24) but also from the significant increase in computational cost due to the cross-derivative matrix involved in 2nd-order derivative approximations. The derivation and comparative analysis of high-order Laplacian models are beyond the scope of this study. This topic is a classic problem in computational mechanics and numerical analysis, requiring separate dedicated research papers. Considering the trade-off between efficiency and accuracy in large-scale applications of geological hazards, this study approximates the second SPH derivatives using a Laplacian model with 1st-order accuracy. This aspect will be elaborated upon in Chapter 4.

2.2.4. SPH GOVERNING EQUATIONS AND SUB-CLOSURE MODELS FOR FLUID

2.2.4.1. SPH approximation of Navier Stokes equations:

The Navier Stokes (NS) equations for solving general geomechanics and geotechnical problems include the mass (or continuity) and momentum equations. The mass equation describes the variation in material density, and thus porosity or void ratio, during deformation. The momentum equation explains how materials deform under external loads. These equations, in Lagrangian form, can be written as follows, respectively:

$$\frac{d\rho}{dt} + \rho \nabla \cdot \mathbf{v} = 0, \tag{2.28}$$

$$\frac{d\mathbf{v}}{dt} = \frac{1}{\rho} \nabla \cdot \boldsymbol{\sigma} + \mathbf{g} + \Gamma, \tag{2.29}$$

where $\mathbf{v}$, $\boldsymbol{\sigma}$, and $\mathbf{g}$ refer to the velocity, stress, and gravity vectors, respectively, and Γ indicates the dissipated term. Another common simplified form of the NS equations is based on Einstein summation notation, using Greek superscripts to represent coordinate directions, as shown below:

$$\frac{d\rho}{dt} + \rho \frac{\partial \mathbf{v}^{\alpha}}{\partial x^{\alpha}} = 0, \tag{2.30}$$

$$\frac{d\mathbf{v}^{\alpha}}{dt} = \frac{1}{\rho} \frac{\partial \boldsymbol{\sigma}^{\alpha\beta}}{\partial x^{\beta}} + \mathbf{g}^{\alpha} + \Gamma^{\alpha}. \tag{2.31}$$

Following the standard computational fluid mechanics (CFD) approach, the total stress tensor is decomposed into the isotropic pressure and the deviatoric stress. For geomechanics applications, most studies follow the classical elastic-plastic soil constitutive model proposed by Bui et al. (Bui et al. 2006; Bui et al. 2008), in which the isotropic pressure is directly computed from the soil constitutive equation based on plasticity theory. However, in this thesis, debris flows are regarded as particle-fluid mixtures characterized by shear rate dependency and the inertial effects of granular materials in the dense flow regime. In a fluidic approach, the total stress tensor $\boldsymbol{\sigma}$ can be written as the sum of the isotropic pressure p and the viscous stresses $\boldsymbol{\tau}$:

$$\boldsymbol{\sigma}^{\alpha\beta} = -p\delta^{\alpha\beta} + \boldsymbol{\tau}^{\alpha\beta}, \tag{2.32}$$

where $\delta^{\alpha\beta}$ is Kronecker delta function, which equals 1 for $\alpha = \beta$ and 0 otherwise. To relate pressure with density, the particle-fluid mixture is assumed to be weakly compressible, and Tait's equation of state is employed to complete the system of equations (Batchelor 1967), as follows:

$$p_i = \frac{\rho_0 c_s^2}{\gamma}\left[\left(\frac{\rho_i}{\rho_o}\right)^{\gamma} - 1\right], \tag{2.33}$$

where ρ_0 denotes the reference density of the material, γ is an isentropic coefficient with values between 1 to 7, c_s is the numerical speed of sound, usually calculated by $c_s = \xi(gh_{\max})^{1/2}$, and ξ is a speed coefficient with a suggested value of 10 (Monaghan 2000; Marrone et al. 2013). It should be emphasized that the pressure treatment in the weakly-compressible model is more of a numerical convenience than a physical representation. The key is to permit density variations due to the Lagrangian motion of particles while keeping compressibility minimal by using a sufficiently high speed of sound. Since it lacks physical meaning, the same equation of state can be applied to different phases with appropriate values of ρ_0 and v_s (Ghaïtanellis et al. 2018).

To solve the governing equations in SPH, the spatial derivative terms must be approximated using a set of SPH particles to discretize the continuum domain. The transient evolution of particle density and momentum in an SPH approximation is described by (Violeau 2012):

$$\frac{d\rho_i}{dt} = \rho_i \sum_{j=1}^{N} V_j \left(\mathbf{v}_i^{\alpha} - \mathbf{v}_j^{\alpha}\right)\frac{\partial W_{ij}}{\partial x^{\alpha}}, \tag{2.34}$$

or

$$\frac{d\rho_i}{dt} = \sum_{j=1}^{N} m_j \left(v_i^{\alpha} - v_j^{\alpha}\right)\frac{\partial W_{ij}}{\partial x^{\alpha}}, \tag{2.35}$$

$$\begin{aligned}\frac{d\mathbf{v}_i^{\alpha}}{dt} &= \sum_{j=1}^{N} m_j \left(\frac{\boldsymbol{\sigma}_i^{\alpha\beta} + \boldsymbol{\sigma}_j^{\alpha\beta}}{\rho_i \rho_j}\right)\frac{\partial W_{ij}}{\partial x^{\beta}} + \mathbf{g}_i^{\alpha} \\ &= -\sum_{j=1}^{N} m_j \left(\frac{p_i + p_j}{\rho_i \rho_j}\right)\frac{\partial W_{ij}}{\partial x^{\alpha}} + \sum_{j=1}^{N} m_j \left(\frac{\boldsymbol{\tau}_i^{\alpha\beta} + \boldsymbol{\tau}_j^{\alpha\beta}}{\rho_i \rho_j}\right)\frac{\partial W_{ij}}{\partial x^{\beta}} + g_i^{\alpha}.\end{aligned} \tag{2.36}$$

or

$$\frac{d\mathbf{v}_i^{\alpha}}{dt} = \sum_{j=1}^{N} m_j \left(\frac{\boldsymbol{\sigma}_i^{\alpha\beta}}{\rho_i^2} + \frac{\boldsymbol{\sigma}_j^{\alpha\beta}}{\rho_j^2} \right) \frac{\partial W_{ij}}{\partial x^{\beta}} + \mathbf{g}_i^{\alpha}$$
$$= -\sum_{j=1}^{N} m_j \left(\frac{p_i}{\rho_i^2} + \frac{p_j}{\rho_j^2} \right) \frac{\partial W_{ij}}{\partial x^{\alpha}} + \sum_{j=1}^{N} m_j \left(\frac{\boldsymbol{\tau}_i^{\alpha\beta}}{\rho_i^2} + \frac{\boldsymbol{\tau}_j^{\alpha\beta}}{\rho_j^2} \right) \frac{\partial W_{ij}}{\partial x^{\beta}} + g_i^{\alpha}. \quad (2.37)$$

Both of the above SPH approximations are commonly used in the literature to evaluate density variation (Eqs. (2.34) and (2.35)) and particle deformation (Eqs. (2.36) and (2.37)). However, a fundamental difference exists between continuity equations. Eq. (2.35) employs the mass of neighboring particles m_j to approximate the velocity divergence, while Eq. (2.34) utilizes the volume of neighboring particles and the particle's own density ρ_i. This means that Eq. (2.34) is more suitable for problems with high density discontinuities, as its approximation involves only the volume of neighboring particles and its own density (Bui and Nguyen 2021). Therefore, Eq. (2.34) is recommended for use in multi-layer, multiphase flow problems.

2.2.4.2. Newtonian viscous formulation and dissipation terms:

The constitutive model is a fundamental component of a computational framework that describes how a material responds to external loads. Here, we present the general expression for the generalized viscous term $\boldsymbol{\tau}$, and the derivation formula for Newtonian fluids, which form the basis of the constitutive model for viscous debris flows. A specific description of the debris flow constitutive model is provided in Chapter 3.

For an isotropic material with a linear deformation rate, such as water, the fluid is called Newtonian. The viscous stress tensor can be calculated from the Newtonian constitutive equation, which relates the strain rates to the viscous stresses, using the following expression:

$$\boldsymbol{\tau}^{\alpha\beta} = 2\mu_w \dot{\boldsymbol{\varepsilon}}^{\alpha\beta}, \quad (2.38)$$

$$\dot{\boldsymbol{\varepsilon}}^{\alpha\beta} = \frac{1}{2}\left[\frac{\partial v^{\alpha}}{\partial x^{\beta}} + \frac{\partial v^{\beta}}{\partial x^{\alpha}} \right] - \frac{1}{3}\left[\frac{\partial v^{\gamma}}{\partial x^{\gamma}} \right] \delta^{\alpha\beta}, \quad (2.39)$$

where μ_w is the total viscosity of water, consisting of the dynamic viscosity and the eddy viscosity obtained through the Smagorinsky algebraic eddy viscosity model. $\dot{\boldsymbol{\varepsilon}}^{\alpha\beta}$ is the deviatoric strain rate.

For 3-D simulations, a Large Eddy Simulation (LES) model, specifically the standard Smagorinsky algebraic eddy viscosity model as described by Dalrymple and Rogers (2006) for Newtonian fluids in a WCSPH framework, captures turbulent characteristics of multi-phase flow. In 2-D simulations, it reduces to a mixing length model and to a laminar viscosity model at low-velocity flow regimes. Although this study does not assess the resolution of turbulence, it is a crucial aspect of the liquid-sediment flow field and requires further investigation.

Eqs. (2.29) and (2.31) highlight that the SPH motion equation is fully dynamic. To prevent SPH particles from oscillating due to small unbalanced forces, a common issue in various numerical methods, an artificial viscosity term (Monaghan and Gingold 1983; Monaghan 1992) is typically introduced to mitigate these oscillations. In SPH notation, Eq. (2.31) can be written as:

$$\frac{d\mathbf{v}_i^\alpha}{dt} = -\sum_{j=1}^{N} m_j \left[\frac{p_i + p_j}{\rho_i \rho_j} + \Pi_{ij} \right] \frac{\partial W_{ij}}{\partial x^\alpha} + \mathbf{g}_i^\alpha, \tag{2.40}$$

$$\Pi_{ij} = \begin{cases} \dfrac{-a_{bd}\bar{c}_{ij}\varphi_{ij}}{\bar{\rho}_{ij}} & \mathbf{v}_{ij} \cdot \mathbf{r}_{ij} < 0 \\ 0 & \mathbf{v}_{ij} \cdot \mathbf{r}_{ij} > 0 \end{cases} \tag{2.41}$$

$$\varphi_{ij} = \frac{\bar{h}_{ij}\mathbf{v}_{ij} \cdot \mathbf{r}_{ij}}{r_{ij}^2 + (0.01h)^2}, \tag{2.42}$$

where Π_{ij} indicates the artificial viscosity term, $\mathbf{v}_{ij} = \mathbf{v}_i - \mathbf{v}_i$ is the difference in velocity vectors of the corresponding particles. $\bar{c}_{ij}$, $\bar{\rho}_{ij}$, and $\bar{h}_{ij}$ are the mean speed of sound, density, and smoothing length, respectively. a_{bd} is a coefficient that needs to be tuned to introduce the proper dissipation, with a recommended value of 0.01 for the study of wave propagation (Altomare et al. 2015) and a suggested value of 0.1 for granular materials (Bui et al. 2008).

Artificial viscosity is a purely numerical technique aimed at stabilizing the simulation, crucial for avoiding unphysical oscillations and effectively managing shock waves. To address the fluid's resistance to deformation in smooth, orderly flow and to model the effects of turbulence at scales smaller than the particle resolution in SPH simulations, laminar viscosity and Sub-Particle Scale (SPS) turbulence are introduced in the SPH scheme. In SPH scheme, Laminar viscous stresses can be formulated as (Lo and Shao 2002):

$$\begin{aligned}\frac{d\mathbf{v}_i^\alpha}{dt} &= -\sum_{j=1}^{N} m_j \left(\frac{p_i + p_j}{\rho_i \rho_j} \right) \nabla_\alpha W_{ij} + \mathbf{g}_i^\alpha \\ &+ \sum_{j=1}^{N} m_j \left[\frac{4\upsilon_k \mathbf{r}_{ij} \cdot \nabla_\alpha W_{ij}}{\left(\rho_i + \rho_j\right)\left(r_{ij}^2 + 0.0001h^2\right)} \right] \mathbf{v}_{ab},\end{aligned} \tag{2.43}$$

where υ_k denotes the kinematic viscosity with a suggested value of 10^{-6} for water. Laminar viscosity dominates at low Reynolds numbers, where the flow is stable and layer-like, providing a straightforward way to simulate the physical viscosity of flows where turbulence is minimal or absent.

The SPS turbulence model captures turbulence effects below the particle resolution in simulations. It uses approaches similar to Large Eddy Simulation (LES), resolving large-scale turbulent motions explicitly, while modeling smaller, sub-grid scales with models like the Smagorinsky model to account for dissipative effects. The concept of SPS was first introduced by Gotoh et al. (2002) to represent turbulence effects in the Moving Particle Semi-implicit (MPS) model. In SPH notation, Eq. (2.43) can be reconstructed by involving the SPS term:

$$\begin{aligned}\frac{d\mathbf{v}_i^\alpha}{dt} &= -\sum_{j=1}^{N} m_j \left(\frac{p_i + p_j}{\rho_i \rho_j} \right) \nabla_\alpha W_{ij} + \mathbf{g}_i^\alpha \\ &+ \sum_{j=1}^{N} m_j \left[\frac{4\upsilon_0 \mathbf{r}_{ij} \cdot \nabla_\alpha W_{ij}}{\left(\rho_i + \rho_j\right)\left(r_{ij}^2 + 0.0001h^2\right)} \right] \mathbf{v}_{ab} \\ &+ \sum_{j=1}^{N} m_j \left(\frac{\vec{\tau}_{ij}^{\beta}}{\rho_j^2} + \frac{\vec{\tau}_{ij}^{\alpha}}{\rho_i^2} \right) \nabla_\alpha W_{ij},\end{aligned} \tag{2.44}$$

$$\frac{\vec{\tau}_{ij}}{\rho} = v_t \left(2S_{ij} - \frac{2}{3} k_{sps} \delta_{ij} \right) - \frac{2}{3} C_I \Delta^2 \delta_{ij} \left| S_{ij} \right|^2, \tag{2.45}$$

where $\vec{\tau}_{ij}$ denotes the sub-particle stress tensor, $v_t = (C_s \Delta l)^2 |S|$ refers to the turbulent eddy viscosity, Δl the particle space, k_{sps} the SPS turbulence kinetic energy. C_s Indicates the Smagorinsky constant with a suggested value of 0.12, and

C_I is assume to equal 0.0066. At last, $|S| = (2S_{ij}S_{ij})^{1/2}$, where S_{ij} represents an element of the SPS strain tensor (Dalrymple and Rogers 2006).

2.2.4.3. Density diffusion in WCSPH scheme:

In the WCSPH scheme, the Density Diffusion Term (DDT) is introduced to enhance the stability and accuracy of simulations, particularly when dealing with high-density gradients or large deformation problems, where density fluctuations and numerical noise can easily occur (Molteni and Colagrossi 2009; Antuono et al. 2010; Marrone et al. 2011). In details, the state equation results in a very stiff density field, and combined with the natural disordering of particles, it leads to high-frequency, low-amplitude oscillations in the density scalar field (Verbrugghe et al. 2018). The DDT can effectively reduce these fluctuations and help prevent particle interpenetration. The general form of the density diffusion formulation in the continuity equation can be written as:

$$\frac{d\rho_i}{dt} = \rho_i \sum_{j=1}^{N} \frac{m_j}{\rho_j}\left(v_i^\alpha - v_j^\alpha\right)\frac{\partial W_{ij}}{\partial x_i^\alpha} + \delta_d h c_s \sum_{j=1}^{n} \frac{m_j}{\rho_j}\psi_{ij}^\alpha \frac{\partial W_{ij}}{\partial x_i^\alpha}, \tag{2.46}$$

where δ_d denotes a dimensionless coefficient, recommended to be set at 0.1 for most applications (Marrone et al. 2011), and ψ_{ij}^α represent the bulk viscosity diffusion operator. Molteni and Colagrossi (2009) first defined the DDT, also known as δ-SPH, by adding the Laplacian of the density field to the continuity equation, now written as:

$$\psi_{ij}^\alpha = 2\left(\rho_j - \rho_i\right)\frac{x_{ij}^\alpha}{\left|x_{ij}^\alpha\right|^2 + 0.0001h^2}. \tag{2.47}$$

Antuono et al. (2012) analyzed this term by decomposing the Laplacian operator, observing operator convergence, and performing linear stability analysis to inspect the impact of the diffusive coefficient. This term acts as a diffusive element in the domain bulk but changes near open boundaries due to kernel truncation, resulting in a net force on particles (Antuono et al. 2010). However, this effect is negligible in nonhydrostatic situations because this force is many orders of magnitude smaller than other forces in such cases. proposed corrections for this effect, but these require solving a renormalization problem for the density gradient, which incurs significant computational cost. Antuono et al. (2010) proposed corrections for this effect, but these require solving a renormalization problem for the density gradient, which incurs significant computational cost.

Another efficient correction proposed by Fourtakas et al. (2020) adopts the same formulation as δ-SPH but substitutes the dynamic density with the total density. Thus, the corrected DDT can be formulated as:

$$\psi_{ij}^{\alpha} = 2\left(\rho_{ij} - \rho_{ij}^{H}\right)\frac{x_{ij}^{\alpha}}{\left|x_{ij}^{\alpha}\right|^{2} + 0.0001h^{2}}, \tag{2.48}$$

with

$$\rho_{ij}^{H} = \rho_0\left(\sqrt{\frac{\gamma\left(\rho_0 g z_{ij} + 1\right)}{\rho_0 c_s^2}} - 1\right), \tag{2.49}$$

where ρ_{ij}^{H} denotes the hydrostatic pressure difference between particle pairs, z_{ij} is the vertical distance between particles. Compared with the primitive δ-SPH, the corrected DDT enhances pressure behavior near wall boundaries by eliminating troublesome dynamic pressure and avoiding solving the normalized density gradient. It is important to note that the formulation by Antuono et al. (2010) is consistent and applicable to various flow types. In contrast, using the corrected DDT is expected to perform better than Eq. (2.47), mostly for gravity-driven flows. In the absence of a gravity force, Eq. (2.48) collapses to the original formulation of δ-SPH. More details about the corrected DDT can be found in Fourtakas et al. (2020), and a similar treatment was adopted for stress field diffusion by Feng et al. (2021).

2.2.4.4. Boundary conditions:

Another widely recognized issue within SPH is the truncation of kernel interpolation support for particles located near the boundary (Vacondio et al. 2021). Addressing boundary conditions in SPH is essential for its application across various engineering problems. For debris-flow simulation, the description of the interaction with the basal boundary, which is often simplified by assuming a no-slip boundary condition (e.g., Moriguchi et al. 2005; Jop et al. 2006; Moriguchi et al.

2009; Han et al. 2019). However, both field and laboratory studies indicate that during rapid granular flow down slopes, even the particle layer in contact with the bottom boundary exhibits a non-zero, non-trivial velocity (Massoudi and Phuoc 2000; Pudasaini et al. 2005; Platzer et al. 2007a; Platzer et al. 2007b; Pudasaini and Hutter 2007; Domnik et al. 2013). Despite many partial-slip boundary methods proposed in recent years (e.g., Domnik et al. 2013; Morikawa et al. 2019; Nikooei and Manzari 2020; English et al. 2022), a complex treatment of boundary projection is still necessary. This significantly increases computational load and relies on subjective judgments regarding the degree of slip.

This study employs the Dynamic boundary conditions (DBC) (Cabrera Crespo et al. 2007) and approximate the no-slip condition by setting the boundary velocity to zero. In DBC, boundary particles satisfy the same equations as fluid particles but do not move according to the forces exerted on them. Instead, they remain fixed or follow an imposed motion function. As a fluid particle approaches a boundary and the distance falls below twice the smoothing length, the boundary density increases, leading to a pressure rise, which in turn exerts a repulsive force on the fluid particle due to the pressure term in the momentum equation. Despite some drawbacks, such as over dissipation, unphysical values of density and pressure in the fixed boundary particles, and unphysically large boundary layers, DBC has a remarkable capacity for discretizing complex 3D geometries without the need to implement complex mirroring techniques or semi-analytical wall boundary conditions. This approach has been preliminarily applied in debris-flow SPH simulation (e.g., Wang et al. 2016; Han et al. 2019; Han et al. 2020). However, In DBC, the presence of unphysical gaps between the boundary and fluid particles results in an inconsistency between the actual surface and the numerical boundary. Consequently, the no-slip boundary conditions cannot be accurately enforced, and partial slip may occur. To sum up, the boundary treatment of DBC, based on the zero-velocity wall particle setting, is a compromise to manage the computational load of debris flow within a large-scale 3-D scheme.

A recent study (English et al. 2022) has demonstrated the implementation of modified dynamic boundary conditions (mDBC) with the SPH scheme. The field variables of the boundary particles are obtained by projecting the ghost nodes located within the fluid domain, utilizing first-order consistent SPH interpolation. A similar attempt was conducted by Feng et al. (2021) regarding rainfall-induced slope collapse. Nevertheless, it is still essential to include a clearly defined partial-slip boundary condition with an acceptable computational cost. Moreover, the degree of slip should dynamically adapt to real-time changes in the spatial distribution of channel roughness as well as the loading conditions of the materials.

2.2.4.5. Explicit time integration scheme:

The SPH governing equations, expressed as time-dependent ordinary differential equations, can be integrated using standard numerical techniques like the second-order leapfrog (LF), predictor-corrector (Diethelm et al. 2002), and Runge-Kutta (RK) schemes (Butcher 1987). The leapfrog algorithm is particularly popular due to its low memory requirements and efficiency in computing one force per step. In this thesis, two computationally simple and numerically stable explicit time integration schemes are implemented, i.e., the Verlet scheme (Verlet 1967), and the Symplectic position Verlet time integrator scheme (Leimkuhler et al. 2016).

The Verlet scheme, known for its low computational cost and efficiency while maintaining 2nd-order accuracy, is commonly used in molecular dynamics because it avoids multiple calculation steps within each iteration interval. Consequently, WCSPH variables are computed as follows:

$$\begin{cases} \mathbf{v}_i^{n+1} = \mathbf{v}_i^{n-1} + 2\Delta t \mathbf{F}_i^n \\ \mathbf{r}_i^{n+1} = \mathbf{r}_i^n + \Delta t \mathbf{v}_i^n + \dfrac{\Delta t^2}{2}\mathbf{F}_i^n \\ \rho_i^{n+1} = \rho_i^{n-1} + 2\Delta t R_i^n \end{cases}, \tag{2.50}$$

with

$$\mathbf{F}_i = \frac{d\mathbf{v}_i}{dt};\ \mathbf{v}_i = \frac{d\mathbf{r}_i}{dt};\ R_i = \frac{d\rho_i}{dt}, \tag{2.51}$$

where $\mathbf{F}_i$ and R_i denote the instantaneous change of velocity and density, respectively, and the subscript n denotes the time step. Since integration occurs over a staggered time interval, the equations for density and velocity are decoupled, potentially causing divergence in the integrated values. To prevent this, an intermediate step is required every Ns steps (with Ns =40 recommended), as follows:

$$\begin{cases} \mathbf{v}_i^{n+1} = \mathbf{v}_i^n + \Delta t \mathbf{F}_i^n \\ \mathbf{r}_i^{n+1} = \mathbf{r}_i^n + \Delta t \mathbf{v}_i^n + \dfrac{\Delta t^2}{2} \mathbf{F}_i^n \\ \rho_i^{n+1} = \rho_i^n + \Delta t R_i^n \end{cases} . \tag{2.52}$$

Verlet scheme offers a good balance between computational cost and accuracy, particularly for long-term simulations where energy conservation is crucial. However, it is less flexible for systems requiring adaptive time steps or dealing with varying conditions and has inconvenient handling of velocity variables.

The Symplectic position Verlet time integrator scheme, on the other hand, is better suited for more complex simulations requiring direct velocity computation due to its time reversibility and symmetry, particularly in the absence of diffusive terms, which helps preserve geometric features. It offers a more numerically stable and energy-conserving solution but is computationally intensive. It is noted that the velocity is required at half-step in the presence of viscous forces and density evolution. As such, the explicit second-order predictor-corrector integrator implemented in WCSPH scheme reads (Parshikov et al. 2000; Leimkuhler et al. 2016):

$$\textbf{Predictor} \begin{cases} \mathbf{r}_i^{n+1/2} = \mathbf{r}_i^n + \dfrac{\Delta t}{2} \mathbf{v}_i^n \\ \mathbf{v}_i^{n+1} = \mathbf{v}_i^n + \Delta t \mathbf{F}_i^{n+1/2} \\ \mathbf{r}_i^{n+1} = \mathbf{r}_i^{n+1/2} + \dfrac{\Delta t}{2} \mathbf{v}_i^{n+1} \end{cases} \quad \textbf{Corrector} \begin{cases} \mathbf{r}_i^{n+1/2} = \mathbf{r}_i^n + \dfrac{\Delta t}{2} \mathbf{v}_i^n \\ \mathbf{v}_i^{n+1/2} = \mathbf{v}_i^n + \dfrac{\Delta t}{2} \mathbf{F}_i^n \\ \mathbf{v}_i^{n+1} = \mathbf{v}_i^n + \Delta t \mathbf{F}_i^{n+1/2} \\ \mathbf{r}_i^{n+1} = \mathbf{r}_i^n + \Delta t \dfrac{\left(\mathbf{v}_i^{n+1} + \mathbf{v}_i^n\right)}{2} \end{cases}$$

(2.53)

with

$$\begin{cases} \rho_i^{n+1/2} = \rho_i^n + \dfrac{\Delta t}{2} R_i^n \\ \rho_i^{n+1} = \rho_i^n \dfrac{2 - \varepsilon_i^{n+1/2}}{2 + \varepsilon_i^{n+1/2}} \\ \varepsilon_i^{n+1/2} = -\left(\dfrac{R_i^{n+1/2}}{\rho_i^{n+1/2}}\right) \Delta t \end{cases} . \tag{2.54}$$

The Symplectic scheme predicts evolution of field variables in time at half time steps, then corrects them using the forces at half time steps, followed by the evaluation of the values at the end time step (Gomez-Gesteira et al. 2012).

The stability of the explicit time integration scheme is governed by the CFL (Courant-Friedrichs-Levy) condition, the maximum force term, and the numerical speed of sound, as shown by Monaghan (1989). Additionally, a further restriction is applied due to the viscous forces (Fourtakas and Rogers 2016). The variable time-step condition reads:

$$\Delta t = Co \min\left(\min_i \sqrt{\frac{h}{|f_i|}}, \frac{h}{c_s}, \frac{h^2}{\upsilon} \right), \tag{2.55}$$

where Co denotes the Courant number with a suggested value of 0.3 by Fourtakas and Rogers (2016), and f_i indicates per unit mass of the particle. The same time-step restriction condition is applied for both schemes mentioned above.

2.2.4.6. Particle shifting algorithm:

Anisotropic particle spacing presents a major stability challenge in SPH, especially in turbulent and multi-phase flows where particles fail to maintain uniform distribution. This instability can lead to noise in the velocity and pressure fields and cause voids in the water flow in some scenarios. To address this issue, Xu et al. (2009) proposed a particle shifting algorithm to prevent instabilities in the ISPH scheme, and this algorithm was later extended to the WCSPH scheme (Vacondio et al. 2013). Manenti et al. (2012) applied the XSPH approach (Monaghan 1994) with an additional smoothing to particle positions using a smoothed velocity. This algorithm has also been applied to pressure smoothing in large-scale dynamic flows (Ulrich et al. 2013). Furthermore, a recent study by Morikawa et al. (2023) proposed a density-based particle shifting technique (PST), specifically designed to deal with incompressible fluids.

In this thesis, we adopt the stable particle shifting algorithm proposed by Lind et al. (2012) to deal with anisotropy and clustering of particles in multiphase flows, in which the shifting magnitude and direction are based on Fick's first law. The shifting algorithm moves particles toward areas with lower concentration, maintaining a uniform distribution and eliminating voids caused by interpolation noise. The connects between the diffusion flux and the concentration gradient can be expressed as:

$$\delta \mathbf{Fr}_i^a = -D'\left(\frac{\partial C_i}{\partial \mathbf{s}}\mathbf{s}_i^\alpha + \frac{\partial C_i}{\partial \mathbf{b}}\mathbf{b}_i^\alpha + \frac{\partial C_i}{\partial \mathbf{n}}\mathbf{n}_i^\alpha\right), \tag{2.56}$$

with

$$D_i' = Ah\left|\mathbf{v}_i\right|\Delta t, \tag{2.57}$$

where D' denotes the diffusion coefficient, which is determined through a von Neumann stability analysis, employing a constraint on the particle's velocity magnitude (Skillen et al. 2013). C refers to the particle concentration, $\mathbf{n}$ and $\mathbf{s}$ are the normal and tangent unit vector, respectively. The vector $\mathbf{b}$ represents the bi-tangent unit vector which takes into consideration shifting at 3-D free surfaces and interfacial flows (Mokos 2014).

2.3. The Discrete element method and coupled SPH-DEM

2.3.1. State-of-the-art of SPH-DEM coupled method

The Discrete Element Method (DEM), initially developed by Cundall and Strack (1979), is a widely utilized numerical approach for simulating the solid phase. It offers inimitable insights into the discontinuous and heterogeneous nature of granular materials (Xu et al. 2019). DEM simulates granular materials as individual particles containing information on shape, speed, and location. These particles interact and their motion is tracked using Newton's laws, following a pure Lagrangian approach (Liu and Xu 2023). By monitoring each particle, DEM predicts the movement of the entire cluster. This method accurately measures the mechanical behavior of complex-shaped particles at the particle scale (Govender et al. 2018) and has become the leading numerical method for simulating particle interactions.

Practical need for computational models in scientific and engineering research has spurred the creation of numerous coupled frameworks for simulating various multi-phase, and multi-physical systems. For instance, both SPH and DEM methods, which are fully Lagrangian and homogeneous frameworks, can effectively handle significant displacements from their initial configurations (Martínez-Estévez et al. 2023). To data, the coupled SPH-DEM method has been applied to a variety of geotechnical and geohazard issues involving multi-physics fields and fluid-solid coupling interactions, such as debris-flow impacting solid structure (e.g., check dam, building) (e.g., Dai et al. 2017; Liu et al. 2021), landslide-generated waves (e.g., Tan and Chen 2017; Bu et al. 2022), rapid flow scour (e.g., Tang et al. 2018; Yeganeh-Bakhtiary et al. 2020), and dammed lakes (e.g., Zhu et al. 2023). Previous studies have shown that SPH-DEM coupling effectively describes fluid-solid interactions. With GPU parallel acceleration, it is particularly suitable for large-scale simulations of geophysical flows process characterized by multi-scale and multi-phase composition.

Currently, the coupling schemes of SPH-DEM methods are classified into resolved, unresolved, and hybrid-resolved approaches based on the method of modeling fluid-particle interaction (Lin et al. 2022; Tsuji et al. 2023). More specifically, the unresolved approach calculates the fluid-particle force primarily using the relative velocity and local solid volume fraction from empirical formulas. The force calculation does not depend on the details of single particles but is based on statistical properties, making it suitable for scenarios with a large number of particles and high computational demands. Such efforts are documented in the literatures (e.g., Tang et al. 2018; Bu et al. 2022; Yu et al. 2023). For instance, the first class of SPH-DEM coupled models (Markauskas and Kruggel-Emden 2019; Jo et al. 2022; Zou et al. 2022) are designed to study granular systems where interactions with fluid phases, typically liquids, are significant. In contrast, the resolved approach offers higher fluid resolution, allowing for the direct calculation of interaction forces between the fluid and each particle, thus avoiding the use of empirical formulas (Lin et al. 2022; Sun et al. 2023). In such cases, particles act as moving boundaries within the fluid domain, and the hydrodynamic forces on these particles are determined by integrating forces over their surfaces. To accurately delineate the fluid dynamics and its interaction with complex boundaries, the resolved approach necessitates a smaller distance between SPH particles, and the characteristic size of discrete grid d should fulfil the following criteria $L > 5d$, where L denotes the characteristic length of the solid (Apte et al. 2009). This also implies that the resolved approach necessitates more nodes to satisfy the resolution requirement compared to the unresolved scheme (Vångö et al. 2018). Additionally, the hybrid resolved approach combines the advantages of the aforementioned methods, allowing different strategies to be used for particles and objects of varying scales based on the requirements. Thus, it is suitable for complex scenarios involving multi-scale flows and particle behaviors that require high precision. Several recent findings have also demonstrated its ability to deal with complex multi-scale, physical problems (e.g., Cheng et al. 2018; K. Tsuji et al. 2023).

In the resolved scheme, a two-way Distributed Contact DEM (DCDEM) formulation (Canelas et al. 2016) is coupled with a WCSPH solver, and successfully applied to a complex stony debris flow case, demonstrating well consistency with the experimental data (Silva et al. 2016; Canelas et al. 2017). Afterward, Peng et al. (2021) adopted an SMR-DEM (Zhan et al. 2021) for more realistic solid grain modelling and improved the coupling algorithm by introducing a unified hybrid contact model, yielding satisfactory results in debris-flow simulations. Asai et al. (2021) introduced an energy-tracking impulse method in their ISPH-DEM coupling framework, resulting in more accurate and effective friction contact resolution. Despite some advancements in modeling non-spherical particles, challenges in accurately representing complex natural shapes persist. It is crucial to carefully handle solid-solid and fluid-solid interactions (FSI) while managing the computational load from large-scale engineering applications.

2.3.2. Fundamentals of DEM

To ensure boundary particle mobility and compatibility during fluid-solid phase contact, this study utilizes an explicit integration-based Lagrange coupling method to calculate fluid-solid particle interactions. The fluid forces on the surface of the solid DEM are integrated into the simulation. Conversely, the solid DEM exerts force on the fluid by treating surface particles as neighbors within the fluid's computational domain. To address multi-rigid and particle-rigid contact collision problems in large-scale geohazard simulations, we employ the classical DCDEM within a coupled framework with WCSPH (Canelas et al. 2016). A rigid body is represented by a fixed set of particles with unchanging relative positions. The volume is discretized by this particle set. Unlike regular SPH particles, these follow a distinct set of equations, specifically Newton's equations for rigid body dynamics. Their discretization involves summing the contributions from each particle as:

$$M_I = \frac{d\mathbf{v}_I}{dt} = \sum_{k \in I} m_k \frac{d\mathbf{v}_k}{dt}, \tag{2.58}$$

$$\mathbf{I}_I \frac{d\Omega_I}{dt} = \sum_{k \in I} m_k \left(\mathbf{r}_k - \mathbf{R}_I\right) \times \frac{d\mathbf{v}_k}{dt}, \tag{2.59}$$

where subscript I denotes the body of particle set, M_I is mass, and $\mathbf{v}_I$, $\mathbf{I}_I$, Ω_I, and $\mathbf{R}_I$ are velocity, inertial tensor, angular velocity, and center of gravity, respectively. The vector quantities are calculated at each time step, and the term within the summation symbol on the RHS of Eq. (2.58) represents the force per unit mass applied to particle k, which correspond to body I. This force includes body forces (such as gravity), fluid interactions, and contacts with other rigid solids. This imply that the term $m_k d\mathbf{v}_k / dt$ should be consist of: (i) fluid force arising from SPH particles by solving the Eq. (2.44), and (ii) solid forces come from rigid collision, which will be elaborated on next.

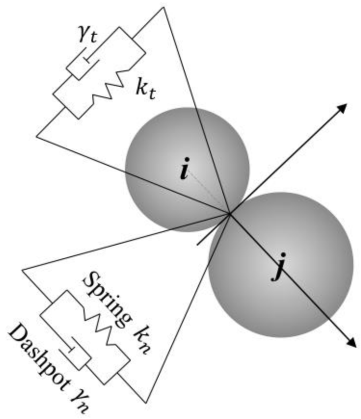

Figure 2.1 Schematic diagram of the DCDEM model.

The calculation of local contributions using kernel interpolation for fluid and solid interactions incorporates the viscous formulation, providing an effective viscous drag closure (Crespo et al. 2015). Moreover, this approach can be seen as an extend of the DBC, merely additionally follows Eqs. (2.58) and (2.59). However, these formulations may overestimate density due to the discontinuity in entropy at the interface (Canelas et al. 2016), leading to an increased gap between fluid and solid particles. Fortunately, the introduction of DDT can mitigate this issue to some extent.

In solid-solid collisions, the contact force decomposes into normal ($\mathbf{F}_n$) and tangential ($\mathbf{F}_t$) components, both involving viscous dissipation effects due to the deformation ranging between perfectly inelastic and perfectly elastic, as shown in Figure 2.1. The degree of dissipation is simply quantified by:

$$e_n = -\frac{v_n \mid_{t=t^n}}{v_n \mid_{t=0}}, \ e \in [0,\ 1]. \tag{2.60}$$

The normal forces are described by a modified Hertzian model, utilizing a spring-damper system, which reads (Kuwabara and Kono 1987; Lemieux et al. 2008):

$$\mathbf{F}_{n,ij} = \mathbf{F}_n^r + \mathbf{F}_n^d = k_{n,ij}\delta_{ij}^{3/2}\mathbf{e}_{ij} - \gamma_{n,ij}\delta_{ij}^{1/4}\dot{\delta}_{ij}\mathbf{e}_{ij}, \tag{2.61}$$

with (Lemieux et al. 2008)

$$k_{n,ij} = \frac{4}{3}E^*\sqrt{R^*}; \ \ \gamma_{n,ij} = C_n\sqrt{6M^*E^*\sqrt{R^*}}, \tag{2.62}$$

where $k_{n,ij}$ denotes the stiffness constant of particles pair i and j, and $\delta_{ij} = \max(0,\ (d_i + d_j)/2 - |\mathbf{r}_{ij}|)$ refers to the particle overlap, $\mathbf{e}_{ij}$ is the unit vector directed from one mass center to the other, $\gamma_{n,ij}$ represents damping constant, and $\dot{\delta}_{ij} = \mathbf{v}_{ij} \cdot \mathbf{e}_{ij}$ the rate of normal deformation. C_n is an empirical tuning parameter with a suggested order of 10^{-5} (Lemieux et al. 2008). These nonlinear formulations mitigate the limitations of constant restitution coefficients and fixed contact durations between particle pairs, resulting in a more accurate representation of physical contact behaviors (Kruggel-Emden et al. 2007). The other material parameters are concluded as follows:

$$\frac{1}{E^*} = \frac{1-\upsilon_I^2}{E_I} + \frac{1-\upsilon_I^2}{E_J}; \ \ R^* = \frac{r_i r_j}{r_i + r_j}; \ \ M^* = \frac{m_I m_J}{m_I + m_J}, \tag{2.63}$$

where E and υ denote Young modulus and Poisson ratio, respectively. The material parameters are defined using the corresponding values for the desired material.

Tangential contacts model the complex mechanism of friction with a linear dashpot, constrained by the Coulomb friction law. This law is adjusted with a sigmoidal function to ensure continuity around the origin concerning tangential velocity. Friction is modelled below:

$$\mathbf{F}_{t,ij} = \min\left(\mu_{f,IJ}\mathbf{F}_{n,ij}\tanh\left(8\dot{\delta}_{ij}^{t}\right)\mathbf{e}_{ij}^{t};\ \mathbf{F}_{t}^{r}+\mathbf{F}_{t}^{d}\right), \tag{2.64}$$

with

$$\mathbf{F}_{t}^{r}+\mathbf{F}_{t}^{d} = k_{t,ij}\delta_{ij}^{t}\mathbf{e}_{ij}^{t} - \gamma_{t,ij}\dot{\delta}_{ij}^{t}\mathbf{e}_{ij}^{t}, \tag{2.65}$$

$$k_{t,ij} = \frac{2}{7k_{n,ij}};\ \gamma_{t,ij} = \frac{2}{7\gamma_{n,ij}}, \tag{2.66}$$

where $\mu_{f,IJ}$ denotes the friction coefficient between *I* and *J*, which is assigned as the average of the two friction coefficients of correspond material. Additional time-step restriction should be included in the existing CFL restrictions to ensure stability in rigid contact, which reads:

$$\Delta t_{DEM} = \min_{i}\left(\frac{\pi}{50}\sqrt{\frac{k_{n,ij}}{m_{IJ}}}\right). \tag{2.67}$$

This class of DEM model, known as the 'soft sphere' approach, uses a penalty method based on particle overlap to deform the spring-damper system. It estimates forces for each particle and, combined with rigid body principles, generalizes geometry without requiring normal directions or topology details, thus effectively handles complex geometries by resolving local interactions (Canelas et al. 2016).

2.4. CONCLUSIONS

This chapter provides a detailed review of numerical simulation methods for debris flows based on the Lagrangian particle framework. Specifically, it covers the latest advancements and current applications of Smoothed Particle Hydrodynamics (SPH), the Discrete Element Method (DEM), and their coupled method (SPH-DEM) in debris flow numerical analysis. Combined with other previously mentioned numerical analysis methods for debris flows, this chapter arrives at the following conclusions:

(1) This section provides a comprehensive review of the development status of the SPH method and its application in numerical analysis of debris flows. It then details the implementation process of the basic principles of the SPH method. Specifically, it focuses on the latest technologies of the WCSPH method, exploring improvements in numerical stability and accuracy. Additionally, it introduces the solution process for first-order (gradient model) and second-order derivatives (Laplacian model) approximations in SPH, laying the theoretical foundation for subsequently solving the second-order pore pressure derivative terms.

(2) The state-of-the-art of the DEM method is reviewed, followed by an introduction to its basic methods and theoretical framework. This discussion leads to the introduction of the SPH-DEM coupling method and its current application in the numerical simulation analysis of debris flows. By exploring the fundamental principles of the coupling method, a foundation is laid for the subsequent construction of multiscale coupled two-way resolved modeling for debris flows.

REFERENCES

Akinci, N. 2014. Interface handling in smoothed particle hydrodynamics. P.h. D thesis, Albert-Ludwigs-Universität.

Altomare, C., Crespo, A.J., Domínguez, J.M., Gómez-Gesteira, M., Suzuki, T. & Verwaest, T. 2015. Applicability of Smoothed Particle Hydrodynamics for estimation of sea wave impact on coastal structures. Coastal Engineering 96, 1-12.

Amicarelli, A., Manenti, S., Albano, R., Agate, G., Paggi, M., Longoni, L., Mirauda, D., Ziane, L., Viccione, G., Todeschini, S., Sole, A., Baldini, L.M., Brambilla, D., Papini, M., Khellaf, M.C., Tagliafierro, B., Sarno, L. & Pirovano, G. 2020. SPHERA v.9.0.0: A Computational Fluid Dynamics research code, based on the Smoothed Particle Hydrodynamics mesh-less method. Computer Physics Communications 250, 107157.

Antuono, M., Colagrossi, A. & Marrone, S. 2012. Numerical diffusive terms in weakly-compressible SPH schemes. Computer Physics Communications 183(12), 2570-2580.

Antuono, M., Colagrossi, A., Marrone, S. & Molteni, D. 2010. Free-surface flows solved by means of SPH schemes with numerical diffusive terms. Computer Physics Communications 181(3), 532-549.

Apte, S.V., Martin, M. & Patankar, N.A. 2009. A numerical method for fully resolved simulation (FRS) of rigid particle–flow interactions in complex flows. Journal of Computational Physics 228(8), 2712-2738.

Aristodemo, F., Federico, I., Veltri, P. & Panizzo, A. 2010. Two-phase SPH modelling of advective diffusion processes. Environmental Fluid Mechanics 10, 451-470.

Arnold, J.M., Buell, D.A. & Davis, E.G. Year. Splash 2. In: Proceedings of the fourth annual ACM symposium on Parallel algorithms and architectures, 316-322.

Asai, M., Fujioka, S., Saeki, Y., Morikawa, D.S., Tsuji, K.J.C.M.i.A.M. & Engineering. 2023. A class of second-derivatives in the Smoothed Particle

Hydrodynamics with 2nd-order accuracy and its application to incompressible flow simulations. Computer Methods in Applied Mechanics and Engineering 415, 116203.

Asai, M., Li, Y., Chandra, B. & Takase, S. 2021. Fluid–rigid-body interaction simulations and validations using a coupled stabilized ISPH–DEM incorporated with the energy-tracking impulse method for multiple-body contacts. Computer Methods in Applied Mechanics and Engineering 377, 113681.

Ata, R. & Soulaïmani, A. 2005. A stabilized SPH method for inviscid shallow water flows. International journal for numerical methods in fluids 47(2), 139-159.

Basic, J., Degiuli, N. & Ban, D. 2018. A class of renormalised meshless Laplacians for boundary value problems. Journal of computational physics 354, 269-287.

Bašić, J., Degiuli, N., Blagojević, B. & Ban, D. 2022. Lagrangian differencing dynamics for incompressible flows. Journal of Computational Physics 462, 111198.

Batchelor, G.K. 1967. An introduction to fluid dynamics. Cambridge university press.

Bender, J. 2019. SPlisHSPlasH Library.

Bilotta, G., Hérault, A., Cappello, A., Ganci, G. & Del Negro, C. 2016. GPUSPH: a Smoothed Particle Hydrodynamics model for the thermal and rheological evolution of lava flows. Geological Society, London, Special Publications 426(1), 387-408.

Bonet, J. & Lok, T.-S. 1999. Variational and momentum preservation aspects of smooth particle hydrodynamic formulations. Computer Methods in applied mechanics and engineering 180(1-2), 97-115.

Brookshaw, L. 1985. A method of calculating radiative heat diffusion in particle simulations. Publications of the Astronomical Society of Australia 6(2), 207-210.

Bu, S., Li, D., Chen, S., Xiao, C. & Li, Y. 2022. Numerical simulation of landslide-generated waves using a SPH-DEM coupling model. Ocean Engineering

258, 111826.

Bui, H., Fukagawa, R. & Sato, K. 2006. Smoothed particle hydrodynamics for soil mechanics. Numerical Methods in Geotechnical Engineering, 275-281.

Bui, H.H., Fukagawa, R., Sako, K. & Ohno, S. 2008. Lagrangian meshfree particles method (SPH) for large deformation and failure flows of geomaterial using elastic–plastic soil constitutive model. International journal for numerical and analytical methods in geomechanics 32(12), 1537-1570.

Bui, H.H., Fukagawa, R., Sako, K. & Wells, J.C. 2011. Slope stability analysis and discontinuous slope failure simulation by elasto-plastic smoothed particle hydrodynamics (SPH). Géotechnique 61(7), 565-574.

Bui, H.H., Kodikara, J.K., Bouazza, A., Haque, A. & Ranjith, P.G. 2014. A novel computational approach for large deformation and post-failure analyses of segmental retaining wall systems. International Journal for Numerical and Analytical Methods in Geomechanics 38(13), 1321-1340.

Bui, H.H. & Nguyen, G.D. 2021. Smoothed particle hydrodynamics (SPH) and its applications in geomechanics: From solid fracture to granular behaviour and multiphase flows in porous media. Computers and Geotechnics 138, 104315.

Bui, H.H., Sako, K. & Fukagawa, R. 2007. Numerical simulation of soil–water interaction using smoothed particle hydrodynamics (SPH) method. Journal of Terramechanics 44(5), 339-346.

Butcher, J.C. 1987. The numerical analysis of ordinary differential equations: Runge-Kutta and general linear methods. Wiley-Interscience.

Cabrera Crespo, A.J., Gómez Gesteira, R. & Dalrymple, R.A. 2007. Boundary conditions generated by dynamic particles in SPH methods. Computers, Materials, & Continua 5(3), 173-184.

Canelas, R., Domínguez, J., Crespo, A., Gómez-Gesteira, M. & Ferreira, R. 2017. Resolved simulation of a granular-fluid flow with a coupled SPH-DCDEM model. Journal of Hydraulic Engineering 143(9), 06017012.

Canelas, R.B., Crespo, A.J., Domínguez, J.M., Ferreira, R.M. & Gómez-Gesteira, M. 2016. SPH–DCDEM model for arbitrary geometries in free surface solid–fluid flows. Computer Physics Communications 202, 131-140.

Cercos-Pita, J.L. 2015. AQUAgpusph, a new free 3D SPH solver accelerated with OpenCL. Computer Physics Communications 192, 295-312.

Chen, J. & Beraun, J. 2000. A generalized smoothed particle hydrodynamics method for nonlinear dynamic problems. Computer Methods in Applied Mechanics and Engineering 190(1-2), 225-239.

Chen, X., Leung, Y.F., Mori, H., Uchida, S. & Takumi, K. 2024. Single-layer soil-water coupled SPH method and its application to sinkhole simulation. Acta Geotechnica 19(2), 991-1018.

Cheng, K., Wang, Y., Yang, Q.J.C. & Geotechnics. 2018. A semi-resolved CFD-DEM model for seepage-induced fine particle migration in gap-graded soils. Computers and Geotechnics 100, 30-51.

Crespo, A.J., Domínguez, J.M., Rogers, B.D., Gómez-Gesteira, M., Longshaw, S., Canelas, R., Vacondio, R., Barreiro, A. & García-Feal, O. 2015. DualSPHysics: Open-source parallel CFD solver based on Smoothed Particle Hydrodynamics (SPH). Computer Physics Communications 187, 204-216.

Cummins, S.J. & Rudman, M. 1999. An SPH projection method. Journal of computational physics 152(2), 584-607.

Cundall, P.A. & Strack, O.D. 1979. A discrete numerical model for granular assemblies. geotechnique 29(1), 47-65.

Dai, Z., Huang, Y., Cheng, H. & Xu, Q. 2017. SPH model for fluid–structure interaction and its application to debris flow impact estimation. Landslides 14, 917-928.

Dalrymple, R.A. & Rogers, B.D. 2006. Numerical modeling of water waves with the SPH method. Coastal engineering 53(2-3), 141-147.

Dehnen, W. & Aly, H. 2012. Improving convergence in smoothed particle hydrodynamics simulations without pairing instability. Monthly Notices of the Royal Astronomical Society 425(2), 1068-1082.

Delannay, R., Valance, A., Mangeney, A., Roche, O. & Richard, P. 2017. Granular and particle-laden flows: from laboratory experiments to field observations. Journal of Physics D: Applied Physics 50(5), 053001.

Diethelm, K., Ford, N.J. & Freed, A.D. 2002. A predictor-corrector approach for the numerical solution of fractional differential equations. Nonlinear Dynamics 29, 3-22.

Domnik, B. & Pudasaini, S.P. 2012. Full two-dimensional rapid chute flows of simple viscoplastic granular materials with a pressure-dependent dynamic slip-velocity and their numerical simulations. Journal of Non-Newtonian Fluid Mechanics 173, 72-86.

Domnik, B., Pudasaini, S.P., Katzenbach, R. & Miller, S.A. 2013. Coupling of full two-dimensional and depth-averaged models for granular flows. Journal of Non-Newtonian Fluid Mechanics 201, 56-68.

Douillet-Grellier, T., Jones, B.D., Pramanik, R., Pan, K., Albaiz, A. & Williams, J.R. 2016. Mixed-mode fracture modeling with smoothed particle hydrodynamics. Computers and Geotechnics 79, 73-85.

Ellero, M., Serrano, M. & Espanol, P. 2007. Incompressible smoothed particle hydrodynamics. Journal of Computational Physics 226(2), 1731-1752.

English, A., Domínguez, J., Vacondio, R., Crespo, A., Stansby, P., Lind, S., Chiapponi, L. & Gómez-Gesteira, M. 2022. Modified dynamic boundary conditions (mDBC) for general-purpose smoothed particle hydrodynamics (SPH): application to tank sloshing, dam break and fish pass problems. Computational Particle Mechanics 9(5), 1-15.

Farhadi, A., Emdad, H. & Rad, E.G. 2016. Incompressible SPH simulation of landslide impulse-generated water waves. Natural Hazards 82, 1779-1802.

Feng, R., Fourtakas, G., Rogers, B.D., Lombardi, D.J.C. & Geotechnics. 2021. Large deformation analysis of granular materials with stabilized and noise-free stress treatment in smoothed particle hydrodynamics (SPH). Computers and Geotechnics 138, 104356.

Fourtakas, G. & Rogers, B. 2016. Modelling multi-phase liquid-sediment scour and resuspension induced by rapid flows using Smoothed Particle Hydrodynamics (SPH) accelerated with a Graphics Processing Unit (GPU). Advances in water resources 92, 186-199.

Fourtakas, G., Vacondio, R., Alonso, J.D. & Rogers, B.D. Year. Improved density diffusion term for long duration wave propagation. In: 2020 SPHERIC Harbin International Workshop.

Ghaïtanellis, A., Violeau, D., Ferrand, M., Abderrezzak, K.E.K., Leroy, A. & Joly, A. 2018. A SPH elastic-viscoplastic model for granular flows and bed-load transport. Advances in Water Resources 111, 156-173.

Gingold, R.A. & Monaghan, J.J. 1977. Smoothed particle hydrodynamics: theory and application to non-spherical stars. Monthly notices of the royal astronomical society 181(3), 375-389.

Gomez-Gesteira, M., Rogers, B.D., Crespo, A.J.C., Dalrymple, R.A., Narayanaswamy, M. & Dominguez, J.M. 2012. SPHysics – development of a free-surface fluid solver – Part 1: Theory and formulations. Computers & Geosciences 48, 289-299.

Gotoh, T., Fukayama, D. & Nakano, T. 2002. Velocity field statistics in homogeneous steady turbulence obtained using a high-resolution direct numerical simulation. Physics of Fluids 14(3), 1065-1081.

Govender, N., Wilke, D.N., Pizette, P. & Abriak, N.-E. 2018. A study of shape non-uniformity and poly-dispersity in hopper discharge of spherical and polyhedral particle systems using the Blaze-DEM GPU code. Applied Mathematics and Computation 319, 318-336.

Han, Z., Su, B., Li, Y., Dou, J., Wang, W. & Zhao, L. 2020. Modeling the progressive entrainment of bed sediment by viscous debris flows using the three-dimensional SC-HBP-SPH method. Water Research 182, 116031.

Han, Z., Su, B., Li, Y., Wang, W., Wang, W., Huang, J. & Chen, G. 2019. Numerical simulation of debris-flow behavior based on the SPH method incorporating the Herschel-Bulkley-Papanastasiou rheology model. Engineering Geology 255, 26-36.

Heydari, Z., Shobeyri, G. & Ghoreishi Najafabadi, S.H. 2020. Accuracy analysis of different higher-order Laplacian models of Incompressible SPH method. Engineering Computations 37(1), 181-202.

Hu, X.Y. & Adams, N.A. 2006. A multi-phase SPH method for macroscopic and mesoscopic flows. Journal of Computational Physics 213(2), 844-861.

Hungr, O. 1995. A model for the runout analysis of rapid flow slides, debris flows, and avalanches. Canadian geotechnical journal 32(4), 610-623.

Islam, M.R.I. & Peng, C. 2019. A total Lagrangian SPH method for modelling damage and failure in solids. International Journal of Mechanical Sciences 157, 498-511.

Jo, Y.B., Park, S.-H., Yoo, H.S. & Kim, E.S. 2022. GPU-based SPH-DEM method to examine the three-phase hydrodynamic interactions between multiphase flow and solid particles. International Journal of Multiphase Flow 153, 104125.

Jop, P., Forterre, Y. & Pouliquen, O. 2006. A constitutive law for dense granular flows. Nature 441(7094), 727-730.

K. Tsuji, Asai, M. & Kasama, K. 2023. Particle-based Semi-resolved Coupling Model for the Simulation of Internal Erosion in soil structures. In: particles2023.

Korzani, M.G. 2017. A new approach in Smoothed Particle Hydrodynamics to simulate hydraulically induced deformation processes in Geomechanics. PhD Thesis, The University of Queensland.

Koshizuka, S. & Oka, Y. 1996. Moving-particle semi-implicit method for fragmentation of incompressible fluid. Nuclear science and engineering 123(3), 421-434.

Kruggel-Emden, H., Simsek, E., Rickelt, S., Wirtz, S. & Scherer, V. 2007. Review and extension of normal force models for the discrete element method. Powder Technology 171(3), 157-173.

Kuwabara, G. & Kono, K. 1987. Restitution coefficient in a collision between two spheres. Japanese journal of applied physics 26(8R), 1230.

Lee, E.-S., Moulinec, C., Xu, R., Violeau, D., Laurence, D. & Stansby, P. 2008. Comparisons of weakly compressible and truly incompressible algorithms for the SPH mesh free particle method. Journal of computational Physics 227(18), 8417-8436.

Lee, E.-S., Violeau, D., Issa, R. & Ploix, S.J.J.o.H.r. 2010. Application of weakly compressible and truly incompressible SPH to 3-D water collapse in waterworks. Journal of Hydraulic research 48(sup1), 50-60.

Leimkuhler, B., Matthews, C. & Stoltz, G. 2016. The computation of averages from equilibrium and nonequilibrium Langevin molecular dynamics. IMA Journal of Numerical Analysis 36(1), 13-79.

Lemieux, M., Léonard, G., Doucet, J., Leclaire, L.-A., Viens, F., Chaouki, J. & Bertrand, F. 2008. Large-scale numerical investigation of solids mixing in a V-blender using the discrete element method. Powder Technology 181(2), 205-216.

Lian, Y., Bui, H.H., Nguyen, G.D., Tran, H.T. & Haque, A. 2021. A general SPH framework for transient seepage flows through unsaturated porous media considering anisotropic diffusion. Computer Methods in Applied Mechanics and Engineering 387, 114169.

Libersky, L.D. & Petschek, A.G. Year. Smooth particle hydrodynamics with strength of materials. In: Advances in the Free-Lagrange Method Including Contributions on Adaptive Gridding and the Smooth Particle Hydrodynamics Method: Proceedings of the Next Free-Lagrange Conference Held at Jackson Lake Lodge, Moran, WY, USA 3–7 June 1990, 248-257.

Lin, X., Li, G., Xu, F., Zeng, K., Xue, J., Yang, W. & Wang, F. 2022. A coupled SPH-DEM approach for modeling of free-surface debris flows. AIP Advances 12(12), 125018.

Lind, S.J., Xu, R., Stansby, P.K. & Rogers, B.D. 2012. Incompressible smoothed particle hydrodynamics for free-surface flows: A generalised diffusion-based algorithm for stability and validations for impulsive flows and propagating waves. Journal of Computational Physics 231(4), 1499-1523.

Liu, C., Yu, Z. & Zhao, S. 2021. A coupled SPH-DEM-FEM model for fluid-particle-structure interaction and a case study of Wenjia gully debris flow impact estimation. Landslides 18(7), 2403-2425.

Liu, G.-R. & Liu, M.B. 2003. Smoothed particle hydrodynamics: a meshfree particle method. World scientific.

Liu, G.-Y. & Xu, W.-J. 2023. A GPU-based DEM framework for simulation of

polyhedral particulate system. Granular Matter 25(2), 27.
Liu, M., Xie, W. & Liu, G. 2005. Modeling incompressible flows using a finite particle method. Applied mathematical modelling 29(12), 1252-1270.
Lo, E.Y. & Shao, S. 2002. Simulation of near-shore solitary wave mechanics by an incompressible SPH method. Applied Ocean Research 24(5), 275-286.
Lucy, L.B. 1977. A numerical approach to the testing of the fission hypothesis. Astronomical Journal 82, 1013-1024.
Ma, G., Bui, H.H., Lian, Y., Tran, K.M. & Nguyen, G.D. 2022. A five-phase approach, SPH framework and applications for predictions of seepage-induced internal erosion and failure in unsaturated/saturated porous media. Computer Methods in Applied Mechanics and Engineering 401, 115614.
Manenti, S., Sibilla, S., Gallati, M., Agate, G. & Guandalini, R. 2012. SPH simulation of sediment flushing induced by a rapid water flow. Journal of Hydraulic Engineering 138(3), 272-284.
Mao, W., Caballero, A., McKay, R., Primiano, C. & Sun, W. 2017. Fully-coupled fluid-structure interaction simulation of the aortic and mitral valves in a realistic 3D left ventricle model. PloS one 12(9), e0184729.
Markauskas, D. & Kruggel-Emden, H. 2019. Coupled DEM-SPH simulations of wet continuous screening. Advanced Powder Technology 30(12), 2997-3009.
Marrone, S., Antuono, M., Colagrossi, A., Colicchio, G., Le Touzé, D. & Graziani, G. 2011. δ-SPH model for simulating violent impact flows. Computer Methods in Applied Mechanics and Engineering 200(13-16), 1526-1542.
Marrone, S., Colagrossi, A., Antuono, M., Colicchio, G. & Graziani, G. 2013. An accurate SPH modeling of viscous flows around bodies at low and moderate Reynolds numbers. Journal of Computational Physics 245, 456-475.
Martínez-Estévez, I., Domínguez, J.M., Tagliafierro, B., Canelas, R.B., García-Feal, O., Crespo, A.J. & Gómez-Gesteira, M. 2023. Coupling of an SPH-based solver with a multiphysics library. Computer Physics Communications 283, 108581.
Massoudi, M. & Phuoc, T.X. 2000. The effect of slip boundary condition on the

flow of granular materials: a continuum approach. International Journal of Non-Linear Mechanics 35(4), 745-761.

Mokos, A. 2014. Multi-phase modelling of violent hydrodynamics using smoothed particle hydrodynamics (sph) on graphics processing units (gpus). The University of Manchester (United Kingdom).

Molteni, D. & Colagrossi, A. 2009. A simple procedure to improve the pressure evaluation in hydrodynamic context using the SPH. Computer Physics Communications 180(6), 861-872.

Monaghan, J. 1989. On the problem of penetration in particle methods. Journal of Computational physics 82(1), 1-15.

Monaghan, J.J. 1992. Smoothed particle hydrodynamics. Annual review of astronomy and astrophysics 30, 543-574.

Monaghan, J.J. 1994. Simulating free surface flows with SPH. Journal of computational physics 110(2), 399-406.

Monaghan, J.J. 2000. SPH without a tensile instability. Journal of computational physics 159(2), 290-311.

Monaghan, J.J. 2005. Smoothed particle hydrodynamics. Reports on progress in physics 68(8), 1703.

Monaghan, J.J. & Gingold, R.A. 1983. Shock simulation by the particle method SPH. Journal of computational physics 52(2), 374-389.

Monaghan, J.J. & Lattanzio, J.C. 1985. A refined particle method for astrophysical problems. Astronomy and Astrophysics (ISSN 0004-6361) 149, 135-143.

Moriguchi, S., Borja, R.I., Yashima, A. & Sawada, K. 2009. Estimating the impact force generated by granular flow on a rigid obstruction. Acta Geotechnica 4, 57-71.

Moriguchi, S., Yashima, A., Sawada, K., Uzuoka, R. & Ito, M. 2005. Numerical simulation of flow failure of geomaterials based on fluid dynamics. Soils and Foundations 45(2), 155-165.

Morikawa, D., Asai, M., Idris, N.A., Imoto, Y. & Isshiki, M. 2019. Improvements in highly viscous fluid simulation using a fully implicit SPH method. Computational Particle Mechanics 6, 529-544.

Morikawa, D., Senadheera, H. & Asai, M. 2020. Explicit incompressible smoothed particle hydrodynamics in a multi-GPU environment for large-scale simulations. Comput Particle Mech.

Morikawa, D., Senadheera, H. & Asai, M. 2021. Explicit incompressible smoothed particle hydrodynamics in a multi-GPU environment for large-scale simulations. Computational Particle Mechanics 8(3), 493-510.

Morikawa, D.S. & Asai, M. 2021. Coupling total Lagrangian SPH–EISPH for fluid–structure interaction with large deformed hyperelastic solid bodies. Computer Methods in Applied Mechanics and Engineering 381, 113832.

Morikawa, D.S. & Asai, M. 2022. A phase-change approach to landslide simulations: Coupling finite strain elastoplastic TLSPH with non-Newtonian IISPH. Computers and Geotechnics 148, 104815.

Morikawa, D.S., Tsuji, K. & Asai, M. 2023. Corrected ALE-ISPH with novel Neumann boundary condition and density-based particle shifting technique. Journal of Computational Physics: X 17, 100125.

Morris, J.P., Fox, P.J. & Zhu, Y. 1997. Modeling low Reynolds number incompressible flows using SPH. Journal of computational physics 136(1), 214-226.

Nguyen, C.T., Nguyen, C.T., Bui, H.H., Nguyen, G.D. & Fukagawa, R. 2017. A new SPH-based approach to simulation of granular flows using viscous damping and stress regularisation. Landslides 14, 69-81.

Nikooei, M. & Manzari, M.T. 2020. Studying effect of entrainment on dynamics of debris flows using numerical simulation. Computers & geosciences 134, 104337.

Parshikov, A.N., Medin, S.A., Loukashenko, I.I. & Milekhin, V.A. 2000. Improvements in SPH method by means of interparticle contact algorithm and analysis of perforation tests at moderate projectile velocities. International Journal of Impact Engineering 24(8), 779-796.

Pastor, M., Blanc, T., Haddad, B., Petrone, S., Sanchez Morles, M., Drempetic, V., Issler, D., Crosta, G., Cascini, L. & Sorbino, G. 2014. Application of a SPH depth-integrated model to landslide run-out analysis. Landslides 11, 793-

812.

Pastor, M., Haddad, B., Sorbino, G., Cuomo, S. & Drempetic, V. 2009. A depth-integrated, coupled SPH model for flow-like landslides and related phenomena. International Journal for numerical and analytical methods in geomechanics 33(2), 143-172.

Pastor, M., Tayyebi, S.M., Stickle, M.M., Molinos, M., Yague, A., Manzanal, D. & Navas, P. 2022. An Arbitrary Lagrangian Eulerian (ALE) finite difference (FD)-SPH depth integrated model for pore pressure evolution on landslides over erodible terrains. International Journal for Numerical and Analytical Methods in Geomechanics 46(6), 1127-1153.

Peng, C., Wu, W., Yu, H.-s. & Wang, C. 2015. A SPH approach for large deformation analysis with hypoplastic constitutive model. Acta Geotechnica 10, 703-717.

Peng, C., Zhan, L., Wu, W. & Zhang, B. 2021. A fully resolved SPH-DEM method for heterogeneous suspensions with arbitrary particle shape. Powder Technology 387, 509-526.

Platzer, K., Bartelt, P. & Jaedicke, C. 2007a. Basal shear and normal stresses of dry and wet snow avalanches after a slope deviation. Cold regions science and technology 49(1), 11-25.

Platzer, K., Bartelt, P. & Kern, M. 2007b. Measurements of dense snow avalanche basal shear to normal stress ratios (S/N). Geophysical Research Letters 34(7), L07501.

Price, D.J. 2012. Smoothed particle hydrodynamics and magnetohydrodynamics. Journal of Computational Physics 231(3), 759-794.

Pudasaini, S.P. 2012. A general two-phase debris flow model. Journal of Geophysical Research: Earth Surface 117(F3), F03010.

Pudasaini, S.P. & Fischer, J.-T. 2020a. A mechanical erosion model for two-phase mass flows. International Journal of Multiphase Flow 132, 103416.

Pudasaini, S.P. & Fischer, J.-T. 2020b. A mechanical model for phase separation in debris flow. International Journal of Multiphase Flow 129, 103292.

Pudasaini, S.P., Hsiau, S.-S., Wang, Y. & Hutter, K. 2005. Velocity measurements

in dry granular avalanches using particle image velocimetry technique and comparison with theoretical predictions. Physics of Fluids 17(9).
Pudasaini, S.P. & Hutter, K. 2007. Avalanche dynamics: dynamics of rapid flows of dense granular avalanches. Springer Science & Business Media.
Pudasaini, S.P. & Mergili, M. 2019. A multi-phase mass flow model. Journal of Geophysical Research: Earth Surface 124(12), 2920-2942.
Ramachandran, P., Bhosale, A., Puri, K., Negi, P., Muta, A., Dinesh, A., Menon, D., Govind, R., Sanka, S. & Sebastian, A.S. 2021. PySPH: a Python-based framework for smoothed particle hydrodynamics. ACM Transactions on Mathematical Software
47(4), 1-38.
Ran, Q., Tong, J., Shao, S., Fu, X. & Xu, Y. 2015. Incompressible SPH scour model for movable bed dam break flows. Advances in Water Resources 82, 39-50.
Randles, P. & Libersky, L.D. 1996. Smoothed particle hydrodynamics: some recent improvements and applications. Computer methods in applied mechanics and engineering 139(1-4), 375-408.
Schaller, M., Gonnet, P., Draper, P.W., Chalk, A.B., Bower, R.G., Willis, J. & Hausammann, L. 2018. SWIFT: SPH with inter-dependent fine-grained tasking. Astrophysics source code library, ascl: 1805.1020.
Schwaiger, H.F. 2008. An implicit corrected SPH formulation for thermal diffusion with linear free surface boundary conditions. International journal for numerical methods in engineering 75(6), 647-671.
Shen, W., Li, T., Li, P., Shen, Y., Lei, Y., Guo, J.J.B.o.E.G. & Environment, t. 2019. The influence of the bed entrainment-induced rheology and topography changes on the propagation of flow-like landslides: a numerical investigation. Engineering Geology and the Environment 78, 4771-4785.
Silva, M., Costa, S., Canelas, R., Pinheiro, A. & Cardoso, A. 2016. Experimental and numerical study of slit-check dams. International Journal of Sustainable Development and Planning 11(2), 107-118.
Skillen, A., Lind, S., Stansby, P.K. & Rogers, B.D. 2013. Incompressible smoothed particle hydrodynamics (SPH) with reduced temporal noise and generalised

Fickian smoothing applied to body–water slam and efficient wave–body interaction. Computer Methods in Applied Mechanics and Engineering 265, 163-173.

Springel, V. 2005. The cosmological simulation code GADGET-2. Monthly notices of the royal astronomical society 364(4), 1105-1134.

Sun, J., Zou, L., Govender, N., Martínez-Estévez, I., Crespo, A.J., Sun, Z. & Domínguez, J.M. 2023. A resolved SPH-DEM coupling method for analysing the interaction of polyhedral granular materials with fluid. Ocean Engineering 287, 115938.

Tan, H. & Chen, S. 2017. A hybrid DEM-SPH model for deformable landslide and its generated surge waves. Advances in water resources 108, 256-276.

Tang, Y., Jiang, Q. & Zhou, C. 2018. A Lagrangian-based SPH-DEM model for fluid–solid interaction with free surface flow in two dimensions. Applied Mathematical Modelling 62, 436-460.

Tsuji, K., Asai, M. & Kasama, K. 2023. Seepage failure prediction of breakwater using an unresolved ISPH-DEM coupling method enriched with Terzaghi's critical hydraulic gradient. Advanced Modeling and Simulation in Engineering Sciences 10(1), 1.

Ulrich, C., Leonardi, M. & Rung, T. 2013. Multi-physics SPH simulation of complex marine-engineering hydrodynamic problems. Ocean Engineering 64, 109-121.

Vacondio, R., Altomare, C., De Leffe, M., Hu, X., Le Touzé, D., Lind, S., Marongiu, J.-C., Marrone, S., Rogers, B.D. & Souto-Iglesias, A. 2021. Grand challenges for smoothed particle hydrodynamics numerical schemes. Computational Particle Mechanics 8, 575-588.

Vacondio, R., Rogers, B.D., Stansby, P.K., Mignosa, P. & Feldman, J. 2013. Variable resolution for SPH: a dynamic particle coalescing and splitting scheme. Computer Methods in Applied Mechanics and Engineering 256, 132-148.

Valdez-Balderas, D., Domínguez, J.M., Rogers, B.D. & Crespo, A.J. 2013. Towards accelerating smoothed particle hydrodynamics simulations for free-surface flows on multi-GPU clusters. Journal of Parallel Distributed Computing 73(11), 1483-1493.

Vångö, M., Pirker, S. & Lichtenegger, T. 2018. Unresolved CFD–DEM modeling of multiphase flow in densely packed particle beds. Applied Mathematical Modelling 56, 501-516.

Vaughan, G., Healy, T.R., Bryan, K.R., Sneyd, A.D. & Gorman, R. 2008. Completeness, conservation and error in SPH for fluids. International journal for numerical methods in fluids 56(1), 37-62.

Verbrugghe, T., Domínguez, J.M., Crespo, A.J., Altomare, C., Stratigaki, V., Troch, P. & Kortenhaus, A. 2018. Coupling methodology for smoothed particle hydrodynamics modelling of non-linear wave-structure interactions. Coastal Engineering 138, 184-198.

Verlet, L. 1967. Computer" experiments" on classical fluids. I. Thermodynamical properties of Lennard-Jones molecules. Physical review 159(1), 98.

Violeau, D. 2012. Fluid mechanics and the SPH method: theory and applications. Oxford University Press.

Wang, J. & Chan, D. 2014. Frictional contact algorithms in SPH for the simulation of soil–structure interaction. International Journal for Numerical and Analytical Methods in Geomechanics 38(7), 747-770.

Wang, W., Chen, G., Han, Z., Zhou, S., Zhang, H. & Jing, P. 2016. 3D numerical simulation of debris-flow motion using SPH method incorporating non-Newtonian fluid behavior. Natural Hazards 81, 1981-1998.

Wendland, H. 1995. Piecewise polynomial, positive definite and compactly supported radial functions of minimal degree. Advances in computational Mathematics 4, 389-396.

Xu, R., Stansby, P. & Laurence, D. 2009. Accuracy and stability in incompressible SPH (ISPH) based on the projection method and a new approach. Journal of computational Physics 228(18), 6703-6725.

Xu, W.-J., Dong, X.-Y. & Ding, W.-T. 2019. Analysis of fluid-particle interaction in granular materials using coupled SPH-DEM method. Powder Technology 353, 459-472.

Xu, X. & Deng, X.-L. 2016. An improved weakly compressible SPH method for simulating free surface flows of viscous and viscoelastic fluids. Computer Physics Communications 201, 43-62.

Yang, E., Bui, H.H., De Sterck, H., Nguyen, G.D. & Bouazza, A. 2020. A scalable parallel computing SPH framework for predictions of geophysical granular flows. Computers and Geotechnics 121, 103474.

Yeganeh-Bakhtiary, A., Houshangi, H. & Abolfathi, S. 2020. Lagrangian two-phase flow modeling of scour in front of vertical breakwater. Coastal Engineering Journal 62(2), 252-266.

Yu, R., Dong, X., Li, Z. & Fan, M. 2023. A coupled SPH–DEM model for erosion process of solid surface by abrasive water-jet impact. Computational Particle Mechanics 10(5), 1093-1112.

Zhan, L., Peng, C., Zhang, B. & Wu, W. 2021. A surface mesh represented discrete element method (SMR-DEM) for particles of arbitrary shape. Powder technology 377, 760-779.

Zhang, C., Rezavand, M., Zhu, Y., Yu, Y., Wu, D., Zhang, W., Wang, J. & Hu, X. 2021. SPHinXsys: An open-source multi-physics and multi-resolution library based on smoothed particle hydrodynamics. Computer Physics Communications 267, 108066.

Zhao, Z.-X., Bilotta, G., Yuan, Q.-E., Gong, Z.-X. & Liu, H. 2023. Multi-GPU multi-resolution SPH framework towards massive hydrodynamics simulations and its applications in high-speed water entry. Journal of Computational Physics 490, 112339.

Zhou, M., Shi, Z., Peng, C., Peng, M., Cui, K.F.E., Li, B., Zhang, L. & Zhou, G.G. 2024. Two-phase modelling of erosion and deposition process during overtopping failure of landslide dams using GPU-accelerated ED-SPH. Computers and Geotechnics 166, 105944.

Zhu, Q.-y., Jiang, N., Chen, Q., Hu, Y.-x. & Zhou, J.-w. 2023. DEM-SPH simulation for the formation and breaching of a landslide-dammed lake triggered by the 2022 Lushan earthquake. Landslides 20(9), 1925-1941.

Zou, L., Sun, J.Z., Sun, Z., Yu, Z.B. & Zhao, H.B. 2022. Study of two free-falling spheres interaction by coupled SPH–DEM method. European Journal of Mechanics-B/Fluids 92, 49-64.

CHAPTER 3

DEVELOPMENT OF A TWO-LAYER MULTI-PHASE SPH MODEL FOR VISCOUS DEBRIS-FLOWS SIMULATION

3.1. INTRODUCTION

As described in chapter 1, the magnitude and destructive potential of debris flows can increase dramatically by side collapse and entraining bed materials as they traverse steep slopes and channels (Jakob et al. 2005; Takahashi 2007; Armanini et al. 2009; Mangeney et al. 2010; Iverson et al. 2011; Iverson 2012; Han et al. 2015; Theule et al. 2015; Haas and Woerkom 2016; Shen et al. 2019; Han et al. 2020; Nikooei and Manzari 2020; Pudasaini and Krautblatter 2021). In some cases, the bulk scale-up can amount to dozens of times the original size. An illustrative example is the 1990 Tsing Shan debris-flow event in Hong Kong (King 1996). Initially, a small slip of 400 m^3 grew to a final volume of 20,000 m^3 by entraining colluvium along its trajectory. Recently, another catastrophic event occurred in Hunnedalen, Norway, in June 2016 likewise created an exaggerated increase from initially 2,000 m^3 to approximately 19000 m^3 (Vicari et al. 2021). Therefore, it is crucial to collectively describe and study the invasive overlying flow, the underlying bed sediment, and the associated geological conditions (e.g., triggering liquid discharge, watershed terrain) (Zheng et al. 2021; Zheng et al. 2023).

To study the mechanisms of EEDPs and their effect on flow mobility and volume changes, a reasonable modelling strategy is the so-called two-layer flows architecture, as proposed by Iverson (2012). As mentioned previously, in the field of geohazard modeling and simulation, existing particle-based models are still mostly confined to the framework of single-layer, single-phase flow frameworks. Despite numerous similar studies in river engineering applications involving rapid flow scouring using a multi-phase approach (e.g., Manenti et al. 2012; Fourtakas and Rogers 2016; Ghaïtanellis et al. 2018; Zubeldia et al. 2018), significant differences exist between the mechanisms of pure water scouring and debris-flow erosion. These differences are mainly reflected in: (i) the dominant force controlling sediment removal and entrainment by flow, and (ii) the evolution pattern of pore water pressure. Although both are sediment transport processes, debris flows typically have higher viscosity and are less influenced by turbulent forces. Frequent inter-particle contact dominates the friction behavior of debris flows, known as the grain-inertia regime (Bagnold 1954), where mass erosion is the primary erosion mode, and the viscosity of the interstitial fluid has a negligible effect. In this scenario, the momentum exchange is significantly greater than in pure water scouring. This intense exchange generates dispersive pressure, leading to grain separation and the generation of shear stresses that constrain the flow (Armanini et al. 2009). Consequently, the erosive behavior of two-phase viscous flows in their initial motion stages frequently yields substantial mutual squeezing and excavation effects. Nevertheless, intense particle collisions and friction significantly decrease the velocity of the mixed fluid. This conclusion is further supported by comparing erodible dam-break tests: the Louvain experiments (Fraccarollo and Capart 2002; Spinewine and Zech 2007) and the granular step collapse (Crosta et al. 2009), which highlight the differences between the two modes, and this section will be covered in detailed later.

However, the grain inertia mechanism alone is inadequate to explain the partial entrainment of the bed layer, despite its higher mechanical strength compared to the fluid. Additionally, there is concern regarding the observed variation in flow momentum within the erodible bed layer during a series of flume experiments (e.g., Iverson et al. 2010; Iverson et al. 2011; Johnson et al. 2012; Zheng et al. 2021; Vicari et al. 2022a). The mechanisms of flow momentum growth and feedback, regulated by the pore water pressure response in wet bed sediment, will be elaborated in Chapter 4. This chapter establishes a fully three-dimensional, two-layer, multi-phase SPH model based on the ideal conditions of saturated sediments to simulate the dynamic behaviors of debris flows, including erosion, entrainment, and deposition processes. Several erosional dam-break tests are conducted to verify its performance. This chapter establishes a two-layer, multi-phase SPH model based on the ideal conditions of saturated sediments to simulate the dynamic behaviors of debris flows, including erosion, entrainment, and deposition. Both the overlying saturated debris and underlying bed sediment are modelled as viscoplastic, dense granular flows governed by the Herschel-Bulkley-Papanastasiou (HBP) rheology and the Drucker-Prager (DP) yield criterion. Initially inspired by the "Multi-phase Liquid-Sediment Model" proposed by Fourtakas and Rogers (2016), this chapter addresses the phase-transition issue associated with erodible beds on steep slopes, and further extends the analysis from pure water scouring schemes to scenarios involving dense flow erosion. Several erosional dam-break tests are conducted to verify the model's performance.

3.2. MODELLING OF THE TWO-LAYER, MULTI-PHASE (TLMP) DEBRIS FLOWS

The modelling architecture utilized in this study closely mirrors the two-layer, depth-averaged entrainment model proposed by Iverson (2012). The key distinction lies in the computational domain of the granular flows, which is discretized into a series of mixture-flow particles, each carrying field variables. Figure 3.1 outlines the proposed TLMP model for debris flow. In this system, a gravity-driven, two-layered dam collapse structure, consisting of an overlying layer of saturated source materials and underlying erodible sediments, undergoes violent interactions across steep slopes or channels. These interactions initiate a series of phase transitions (e.g., phase change (Morikawa and Asai 2022), particle sorting, dewatering (Pastor et al. 2023)), further evolving the bilayer structure into a multi-phase state. This multi-phase framework is characterized, from top to bottom, by saturated debris, an erodible bed, an un-yield region, and a substrate (representing an undrained boundary). Figure 3.1b illustrates the *L*-*L'* cross-section of the TLMP model, demonstrating that the flow depth and erosion depth are determined by the vertical distance from the yield surface (v=0) to the free surface and to the bed sediment surface, respectively. At the undrained boundary, the flow flux k, induced by gravity, has the same magnitude but acts in opposite directions across the domain.

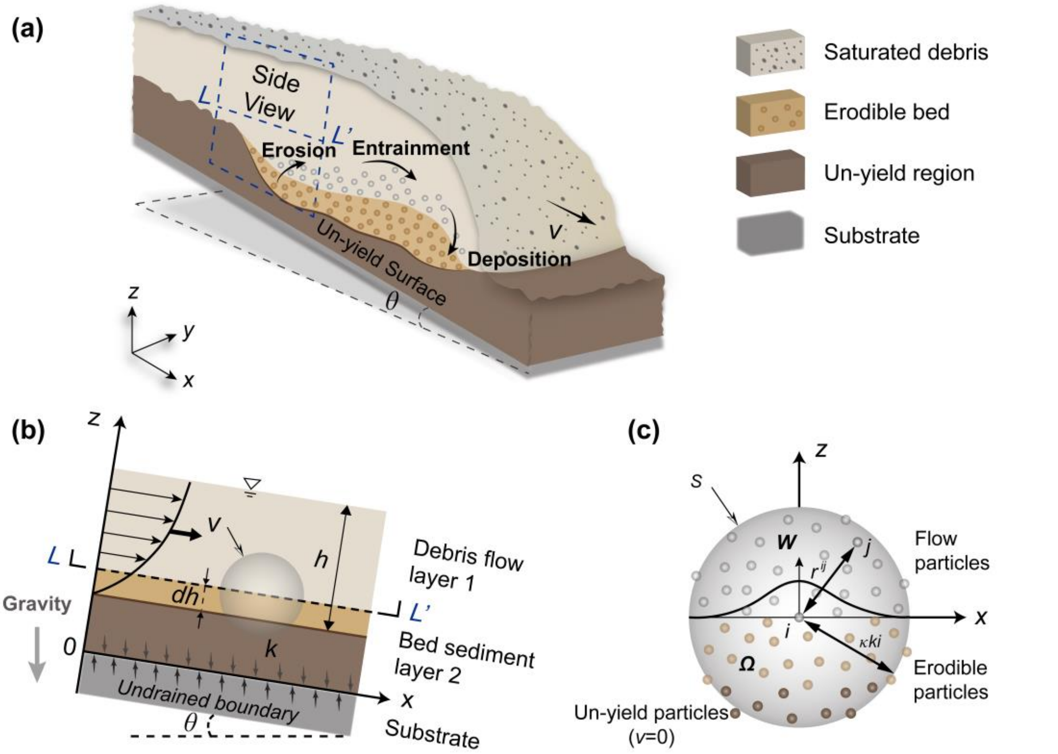

Figure 3.1 Schematic illustration of the TLMP-SPH model. (a) Cutaway view of the debris-flow model, (b) side view of the L-L' cross section, (c) discretization of the multi-phase particles within support domain.

Note that the TLMP model detailed in this paper is predicated on the mechanical properties of debris flow (e.g., density, viscosity, internal friction angle), encompassing dynamic processes, and distinguishing between flow states (either flow-like or solid-like materials), as illustrated in the flow chart (Figure 3.2). In contrast, truly strong coupling necessitates an integrated consideration of interactions among multi-scale grains and interstitial fluids. Currently, such integration can only be partially achieved through miniaturized tests (Bui and Nguyen 2021), or within depth-averaged two-dimensional models (e.g., Pudasaini 2012; Pastor et al. 2018; Pudasaini and Mergili 2019; Pudasaini and Fischer 2020a, b; Pudasaini and Krautblatter 2021; Pastor et al. 2023; Zhou et al. 2024), owing to the contentious nature of the mechanism and the high computational costs involved. Our objective is to examine the dynamic behaviours of debris flows in a hierarchical and state-by-state manner from the perspective of particulate mixtures. Next, a detailed description of the computational model including the numerical scheme, rheological model and multi-phase features, is elaborated.

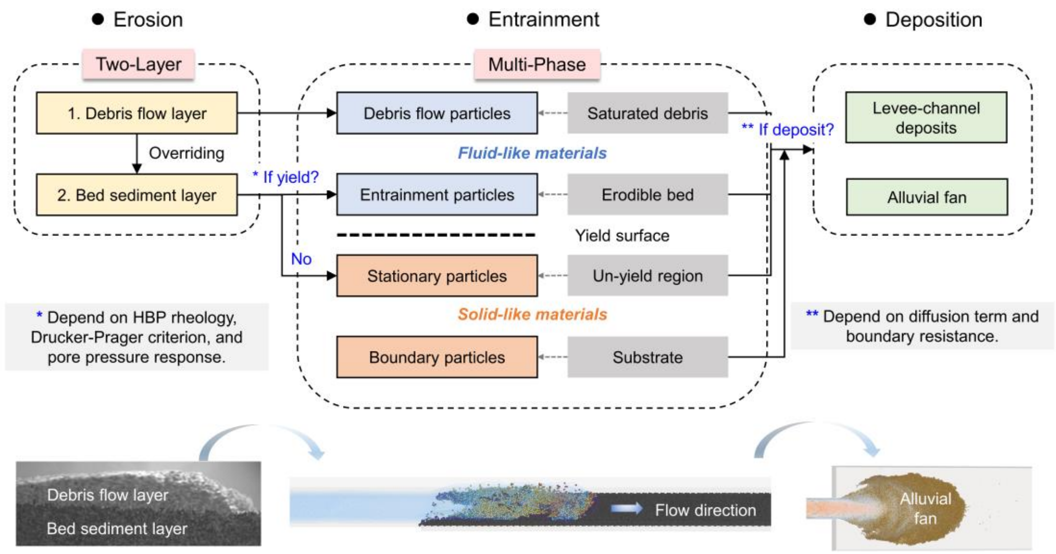

Figure 3.2 Flow chart of the erosion, entrainment and deposition process (EEDPs) in the proposed TLMP-SPH method.

3.2.1. Debris flow rheological model: non-Newtonian Bingham-type family

The debris flow mass is regarded as a variable-density, multi-grain mixture over a non-uniform, erodible bed in this study. As illustrated in Figure. 3.1c, rapid wet granular flows are modelled as a collection of discretized particles, each carrying field variables and physical properties, moving along with the material.

The debris flow rheology (or constitutive) model reflects the interrelationship between normal stress, shear stress, and deformation, wherein the pressure is calculated by Eq. (2.33). The selection of the rheological model directly impacts the ability of the numerical model to accurately depict the complex rheological characteristics of debris flows. To accurately describe the nonlinear relationship between shear stress and shear strain of debris flow under large deformation, we first review the shear stress formula in Eq. (2.38) within the context of SPH:

$$\boldsymbol{\tau}^{\alpha\beta} = 2\mu_{\text{eff}}\dot{\boldsymbol{\varepsilon}}^{\alpha\beta}, \tag{3.1}$$

where μ_{eff} denotes the effective viscosity term, which varies according to rheological model. In the literature, a series of non-Newtonian Bingham-type models have been widely used and integrated into the SPH framework. These include the Bingham model (e.g., Dai et al. 2014; Huang and Dai 2014), the Cross model (e.g., Wang et al. 2016), the Herschel-Bulkley (HB) model (e.g., Nikooei and Manzari 2020), and the Herschel-Bulkley-Papanastasiou (HBP) model (e.g., Han et al. 2019; Han et al. 2020). The detailed comparison and limitations of these rheological models have been thoroughly discussed in previous studies (Fourtakas and Rogers 2016; Han et al. 2019). Similar to the Newtonian viscous formulation, we convert them to their equivalent Newtonian fluid forms, as listed below:

$$\text{Bingham: } \boldsymbol{\tau}^{\alpha\beta} = 2\mu_{\text{Bingham}}\boldsymbol{\varepsilon}^{\alpha\beta} = 2\left(\mu + \frac{\tau_y}{2\dot{\boldsymbol{\gamma}}}\right)\boldsymbol{\varepsilon}^{\alpha\beta}, \tag{3.2}$$

$$\text{Cross: } \boldsymbol{\tau}^{\alpha\beta} = 2\mu_{\text{Cross}}\boldsymbol{\varepsilon}^{\alpha\beta} = 2\frac{\mu_0 + \left(K\dot{\boldsymbol{\gamma}}\right)^m \mu_\infty}{1+\left(K\dot{\boldsymbol{\gamma}}\right)^m}\boldsymbol{\varepsilon}^{\alpha\beta};\ K = \frac{\mu_0}{\tau_y}, \tag{3.3}$$

$$\text{HB: } \boldsymbol{\tau}^{\alpha\beta} = \tau_y + \mu_{\text{HB}}\dot{\boldsymbol{\gamma}}^n = 2^{n-1}\cdot\mu\left(\dot{\boldsymbol{\gamma}}\right)^{n-1} + \frac{\tau_y}{2\dot{\boldsymbol{\gamma}}}, \tag{3.4}$$

$$\text{HBP: } \boldsymbol{\tau}^{\alpha\beta} = \tau_y + \mu_{\text{HBP}}\dot{\boldsymbol{\gamma}}^n = 2^{n-1}\cdot\mu\left(\dot{\boldsymbol{\gamma}}\right)^{n-1} + \frac{\tau_y}{2\dot{\boldsymbol{\gamma}}}\left(1-e^{-2m\dot{\gamma}}\right), \tag{3.5}$$

with

$$\dot{\boldsymbol{\gamma}} = \sqrt{\frac{1}{2}\boldsymbol{\varepsilon}^{\alpha\beta}\boldsymbol{\varepsilon}^{\alpha\beta}} \text{ and } \boldsymbol{\varepsilon}^{\alpha\beta} = \frac{1}{2}\left[\frac{\partial \mathbf{v}^\alpha}{\partial x^\beta} + \frac{\partial \mathbf{v}^\beta}{\partial x^\alpha}\right], \tag{3.6}$$

where μ_{Bingham}, μ_{Cross}, μ_{HB}, and μ_{HBP} are the equivalent effective viscosity corresponding to the rheological model, respectively, μ denotes the apparent dynamic viscosity, τ_y is the is the yield stress. In the Cross mode, μ_0 and μ_∞ signify the fluid viscosities at low and high shear rates, respectively. In the HBP model, m governs the exponential growth of stress, and n is the power law index that facilitates the simulation of dilatant and pseudoplastic fluids.

The primary Bingham model, which uses an equivalent viscosity coefficient, encounters numerical divergence when the shear strain rate $\dot{\boldsymbol{\gamma}}$ approaches zero, causing the effective viscosity coefficient μ_{eff} to approach infinity. Physically, this implies that the debris flow slurry would completely freeze in low strain rate regions, which is unrealistic. Cross model addresses this issue by introducing viscosity coefficients for high and low shear strain rates. However, the value of μ_0 still needs to be determined empirically, and both models exhibit a linear stress-strain relationship under large deformation.

Debris flow mixtures exhibit both dilatant and pseudoplastic behaviors with varying proportions of soil, water, and gravel, as observed in the experiment by Major and Pierson (1992) and Parsons et al. (2001). These nonlinear rheological relationships are commonly referred to as "shear thickening" and "shear thinning." The HB model successfully replicates nonlinear rheological relationships by introducing a power-law term. By adjusting the *n* value, it can simulate both the dilatant and pseudoplastic behaviors of debris flows. However, the HB model still exhibits numerical divergence issues at low shear strain rates. In this context, a more generalized model, known as the Herschel-Bulkley-Papanastasiou (HBP) model (Papanastasiou 1987), is developed and applied to various non-Newtonian and geophysical flow problems (e.g., Domnik and Pudasaini 2012; Domnik et al. 2013; Fourtakas and Rogers 2016; Khattri and Pudasaini 2018; Zubeldia et al. 2018; Han et al. 2019; Han et al. 2020; Zhou et al. 2024). Another commonly employed version of the HBP model in the literature is written as follows:

$$\boldsymbol{\tau}^{\alpha\beta} = 2\mu_{\text{HBP}}\boldsymbol{\varepsilon}^{\alpha\beta}, \tag{3.7}$$

with

$$\mu_{\text{HBP}} = \frac{\left|\tau_y\right|}{\sqrt{\boldsymbol{\Pi}_D}}\left[1-e^{-m\sqrt{\boldsymbol{\Pi}_D}}\right] + 2\mu\left|4\boldsymbol{\Pi}_D\right|^{\frac{n-1}{2}}, \tag{3.8}$$

where Π_D is the second invariant of the strain rate tensor, defined as $\Pi_D = \boldsymbol{\varepsilon}^{\alpha\beta}\boldsymbol{\varepsilon}^{\alpha\beta}/2$. Compared to other Bingham-type rheology models, the HBP model involves two additional parameters, *m* and *n*, which regulate the exponential increase in stress, and the nonlinear power-law growth at low and high shear rates, respectively.

Previous studies have demonstrated the capability of the HBP model in accurately predicting significant features of both overlying debris flows (Han et al. 2019) and underlying bed sediments (Fourtakas and Rogers 2016). Specifically, Han et al. (2019) successfully applied a single-layer HBP-SPH model to simulate a real debris flow event, and rigorously analyzed the essential parameters (τ_y, μ, m, and n) of the HBP model, focusing on their sensitivity and data fitting capabilities. Fourtakas and Rogers (2016) combined the HBP model with the Drucker-Prager (DP) yield criterion, successfully capturing the erosion patterns of sediments in a pure water environment. However, the task of establishing the yield criterion for particles in erodible bed sediments, in relation to yield stress τ_y, continues to provoke debate. Next, we will establish the physical connections between debris-flow erosion, entrainment, particle yield, and phase transition mechanisms within the SPH framework.

3.3. EROSION AND ENTRAINMENT IMPLEMENTATION

3.3.1. YIELD CRITERIONS

In the three-dimensional SPH framework, erosion and entrainment behaviours are evaluated through the analysis of bed failure and the subsequent particle transport by the flow, as opposed to depth-averaged methods that assess entrainment rates on a per-grid basis (Vicari et al. 2022b). The transition between stationary and flowing regions is frequently modelled using various approaches, such as the Mohr-Coulomb (MC) (e.g., Manenti et al. 2012; Han et al. 2019; Nikooei and Manzari 2020; Vicari et al. 2022b), the Drucker-Prager (DP) (e.g., Bui et al. 2008; Fourtakas and Rogers 2016; Zubeldia et al. 2018; Zhou et al. 2024), and the Shields criterion (e.g., Zubeldia et al. 2018; Martínez-Aranda et al. 2022). Specifically, the Shields criteria are primarily utilized for analyzing pure water scour in the fields of hydrology and river engineering. Compared to the MC approach, the DP criterion yields a better approximation for continuous media subjected to dynamic high-pressure loads, owing to its smoother yield surface and mathematical consistency (Jiang and Xie 2011). Further study (Fourtakas et al. 2013) indicates that the MC criterion adopts a more conservative stance with respect to particle yielding. Given the available evidence, the MC criterion appears to be more suitable for addressing low moisture content dry landslide issues, whereas the DP criterion is more appropriate for dealing with multiphase erosion problems associated with debris flows. To determine the yield term of the HBP rheology, it is straightforward to apply the following formulas:

$$\text{MC Criterion: } \tau_y = c + \left(p - p_w\right)\tan\varphi, \tag{3.9}$$

$$\text{DP Criterion: } \tau_y = -\alpha_\varphi\left(p - p_w\right) + \kappa_c, \tag{3.10}$$

with

$$\text{2-D: } \alpha_\varphi = \frac{\tan\varphi}{\sqrt{9+12\tan^2\varphi}};\ \kappa_c = \frac{3c}{\sqrt{9+12\tan^2\varphi}}, \tag{3.11}$$

and

$$\text{3-D: } \alpha_\varphi = -\frac{2\sqrt{3}\sin\varphi}{3-\sin\varphi};\ \kappa_c = \frac{2\sqrt{3}c\cos\varphi}{3-\sin\varphi}, \tag{3.12}$$

where c and φ denote the cohesion and internal friction angle, respectively, and p_w refers to the pore water pressure. The coefficients α_φ and κ_c are determined by mapping the DP onto the MC yield criterion within the deviatoric plane. Generally, the yield surface of the bed sediment layer can be characterized based on the state of stress and mechanical properties (Fourtakas et al. 2013), i.e.

$$f = \alpha_\varphi\left(p - p_w\right) + \sqrt{J_2} - \kappa_c \begin{cases} < 0, & \text{unyield} \\ \geq 0, & \text{yield} \end{cases}, \tag{3.13}$$

where J_2 is the second invariant of the deviatoric shear stress tensor defined as $J_2 = \tau^{\alpha\beta}\tau^{\alpha\beta}/2$. This method facilitates a natural transition between stationary and flowing sediment regions by incorporating the increase in stress with depth through a pressure-dependent yield criterion. As a result, particles exhibit a higher effective viscosity μ_{HBP} and tend to be stationary as the critical shear stress τ_y increases.

3.3.2. Phase transition on steep terrain

The pressure-dependent criteria exhibit acceptable stability in gentle terrain but tend to fail in steep slope scenarios. As depicted in Figure 3.3, even on flat ground, sediment particles can be disturbed by stress waves, which is reasonable in the context of movable riverbeds. However, this does not apply to the scenarios of debris flow on mountain slopes and channels. In these cases, the slopes can remain relatively stable before erosion occurs, and the impact of stress waves is relatively minor. This difficulty partly stems from the lack of an elastic branch within the HBP rheology and the direct dependence of flow dynamics on the strain rate tensor. Such a configuration renders the sediment system unable to withstand perturbations from gravitational force in steep terrain, thereby making it highly susceptible to particle collapse (Ma et al. 2023). The key to solving this problem lies in the two-stage nature of the HBP model (Fourtakas and Rogers 2016; Han et al. 2019). As demonstrated in Eq. (3.8), when the shearing rate approaches zero, the effective viscosity of the HBP model satisfies:

$$\lim_{\dot{\varepsilon}\to 0}\left\{\frac{\left|\tau_y\right|}{\sqrt{\Pi_D}}\left[1-e^{-m\sqrt{\Pi_D}}\right]+2\mu\left|4\sqrt{\Pi_D}\right|^{\frac{n-1}{2}}\right\}=m\left|\tau_y\right| \tag{3.14}$$

This suggests that the Papanastasiou term significantly influences the exponential increase in stress at low shear rates. As shear rates continue to increase, the effective viscosity decreases markedly, transitioning into a stage governed by the Herschel-Bulkley (HB) term. Herein, we incorporate an additional constraint into the DP criterion, utilizing the two-stage features of effective viscosity to determine the onset state of sediment particles, as:

$$\begin{cases} -\alpha_\varphi\left(p-p_w\right)+\kappa_c<0 \cup \mu_{\mathrm{HBP}}>m\left|\tau_y\right|, \text{ unyield} \\ \text{else, yield} \end{cases}, \tag{3.15}$$

The proposed phase transition model identifies the pre-distortion state of effective viscosity as an un-yielded phase, aim at enhancing the resistance of sediment particles to perturbations in complex terrains. In addition, it eliminates the need for extra artificial parameters to establish the critical state.

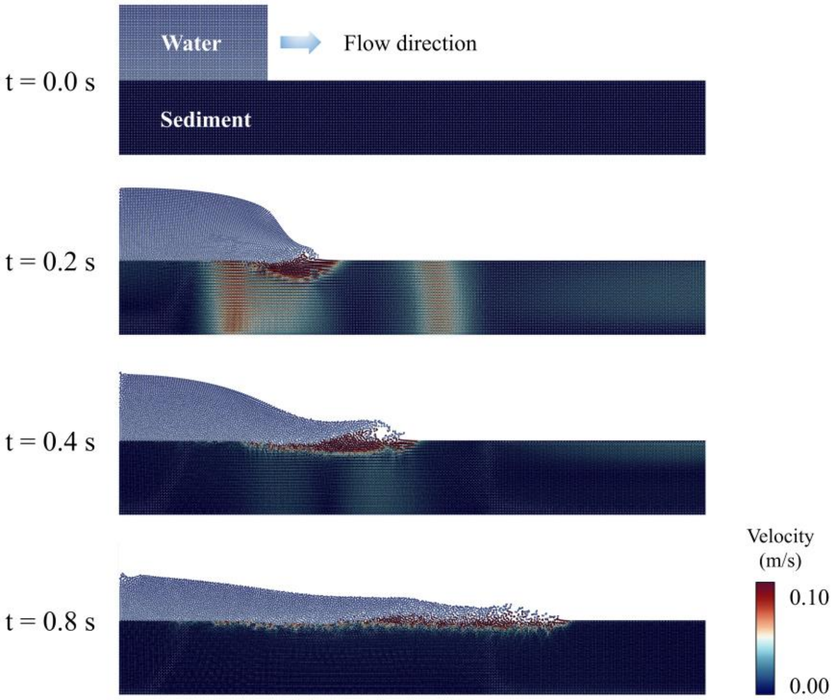

Figure 3.3 Snapshots illustrating the numerical results of liquid-sediment scouring simulations, derived from the "Multi-phase Liquid-Sediment Model" proposed by Fourtakas and Rogers (2016).

Typically, measuring pore water pressure necessitates detecting the soil-water interface and the free surface to determine the hydraulic head pressure difference. Manenti et al. (2012) demonstrated that this process is computationally expensive and yields inaccurate results due to significant interface deformation. For saturated sediments, Fourtakas and Rogers (2016) proposed a low-cost method that establishes a connection between pore water pressure and the pressure exerted by the saturated sediment, as follows:

$$p_{i,w} = \frac{\rho_{0,w} C_{s0,w}^2}{\gamma}\left[\left(\frac{\rho_{i,sat}}{\rho_{0,sat}}\right)^{\gamma} - 1\right], \tag{3.16}$$

where subscripts w and sat refer to the water and saturated sediment phase respectively. Finally, the skeleton pressure can be determined by calculating the difference between the total pressure and the pore water pressures. For unsaturated condition, the pore water pressure response pattern is more complex and will be elaborated upon in Chapter 4.

3.4. Verification examples

In this section, we compare the numerical simulation results with model experiment results to highlight the characteristics and differences between pure water scouring and dense granular flow mass erosion. The two-layer water scouring on saturated beds is qualitatively validated using the Louvain erosional dam-break tests (Fraccarollo and Capart 2002), while the dense flow erosion is tested using a granular step collapse (Crosta et al. 2009).

3.4.1. Example 1: Dam-break wave on movable beds

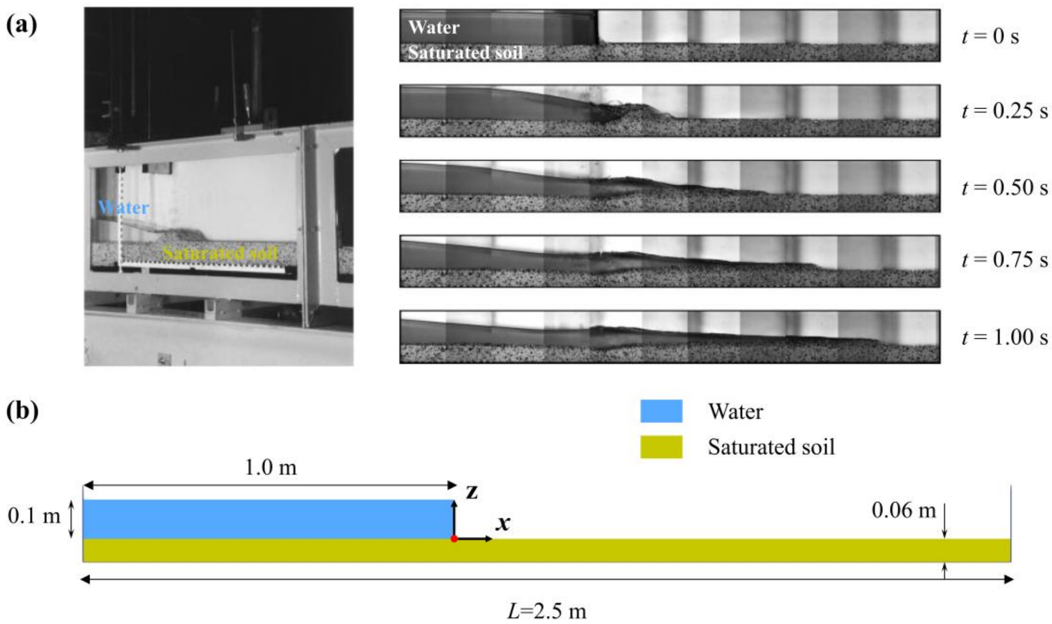

Figure 3.4 (a) Side view of the Louvain laboratory configuration and snapshots of the erosional dam-break wave. Images modified from Fraccarollo and Capart (2002). (b) Numerical modeling of the dam-break wave on saturated beds – experiment set-up.

The Louvain erosional dam-break laboratory is one of the widely recognized tests for liquid-sediment scouring, with well-documented results, and has been used as a benchmark for sediment transfer and water-soil interactions by various researchers (e.g., Ulrich et al. 2013; Fourtakas and Rogers 2016; Zubeldia et al. 2018). The original tests are conducted in horizontal prismatic flumes with a rectangular cross-section, measuring 2.5 m in length, 0.1 m in width, and 0.35 m in height, as illustrated in Figure 3.4a. Before each test, the granular material is spread into a consistent layer 5-6 cm thick within the test area. A watertight sluice gate is lowered to the flume bottom at the center of the test area to represent the idealized dam. Water is then introduced downstream of the gate to fully saturate the sediment bed. Subsequently, the water level is increased to 0.1 m above the surface of the granular bed. Upon releasing the water column, hydrodynamic stress at the interface triggers yielding and scouring at the sediment boundary. This creates a shear layer that extends to a depth where viscosity, density, and pressure continuously change.

Table 3.1 Rheological and SPH parameters in the Louvain experiment.

Parameter	Notation	Unit	Value
Water Density	ρ_w	kg/m^3	1000
Soil Density	ρ_s	kg/m^3	1560
Kinematic viscosity (Water)	υ_w	m^2/s	0.001
Kinematic viscosity (Soil)	υ_s	m^2/s	0.002
Particle distance	d_p	m	0.002
Number of fluid particles	N_w	/	25,000
Number of soil particles	N_s	/	37,470
Number of boundary particles	N_b	/	1,451
Cohesion	c	Pa	0
Internal friction angle	φ	°	31
Exponential index	m	/	10
Power law index	n	/	1.2
Sound speed coefficient	ξ	/	20
EoS constant	γ	/	7
Density diffusion coefficient	δ_d	/	0.1
CFL coefficient	CFL	/	0.1

The bed was constructed using cylindrical PVC pellets with an equivalent spherical diameter of 3.5 mm and a density of 1560 kg/m^3 when saturated. In the numerical setup, the geometric model is designed to replicate the experimental configuration, featuring a 0.1 m high water column and a 0.06 m fully saturated soil bed, as shown in Figure 3.4b. Based on the equivalent diameter of the sediment particles and for comparison with the results of Fourtakas and Rogers (2016), we used a particle spacing of $dp = 0.002$ m. This setup generated a total of 25,000 water particles (N_w) and 37,470 soil particles (N_s) within the computational domain. For the mechanical properties of the saturated soil under the Drucker-Prager criterion, we follow the methods of Fourtakas and Rogers (2016) and Zubeldia et al. (2018), setting $c = 0$ and $\varphi = 31°$ to reproduce the properties of a cohesionless material, similar to those of PVC pellets. The HBP parameters of exponential and power law coefficients are set to $m = 10$ and $n = 1.2$, respectively, to delineate the shear-thinning flow behavior observed in the experiment. Detailed numerical modeling parameters for the Louvain dam-break test are provided in Table 3.1.

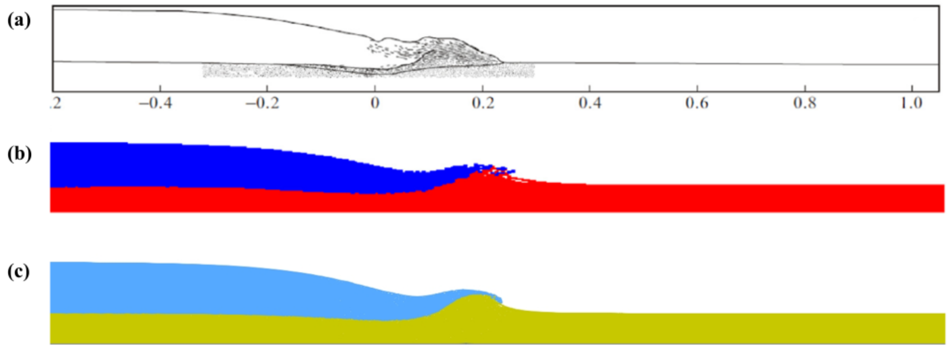

Figure 3.5 Qualitative comparison of simulation and experimental data. (a) Particles displacement tracked at t = 0.25 s; (b) numerical results of Fourtakas and Rogers (2016); (c) numerical results from the current model.

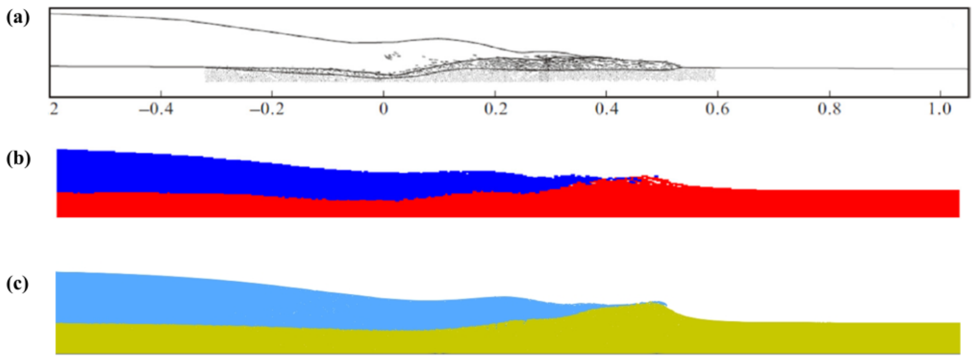

Figure 3.6 Qualitative comparison of simulation and experimental data. (a)

Particles displacement tracked at t = 0.50 s; (b) numerical results of Fourtakas and Rogers (2016); (c) numerical results from the current model.

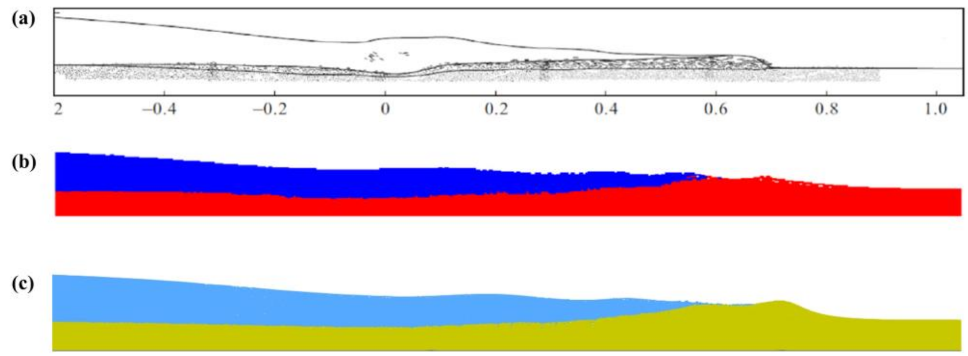

Figure 3.7 Qualitative comparison of simulation and experimental data. (a) Particles displacement tracked at t = 0.75 s; (b) numerical results of Fourtakas and Rogers (2016); (c) numerical results from the current model.

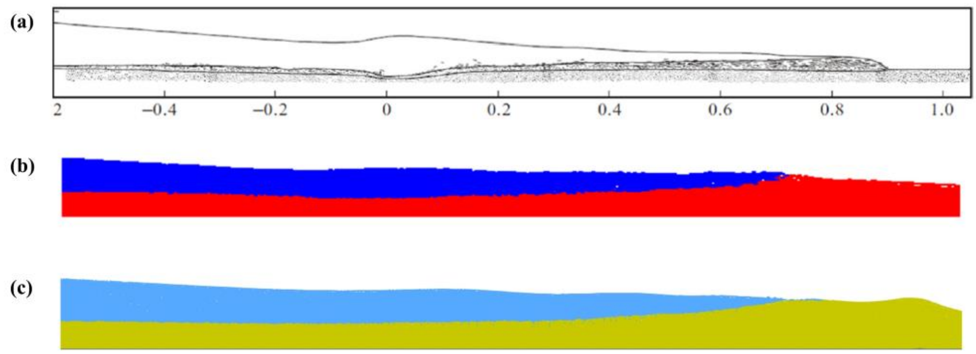

Figure 3.8 Qualitative comparison of simulation and experimental data. (a) Particles displacement tracked at t = 1.00 s; (b) numerical results of Fourtakas and Rogers (2016); (c) numerical results from the current model.

Figures 3.5-3.8 illustrate a qualitative comparison of the particle displacement profile from Fraccarollo and Capart (2002) with the SPH numerical results obtained from the proposed method and those from Fourtakas and Rogers (2016) at different instant. These demonstrate that the flow dynamics are well reproduced by the current model. The main difference from the model of Fourtakas and Rogers (2016) lies in our use of a more consistent density diffusion term (Fourtakas et al. 2020) and particle shifting algorithm, as well as the consideration of the two-phase transition in HBP rheology. It is evident that in the control experiments at various time points, the existing model consistently achieved results closer to experimental observations. Additionally, the water-sediment interface profiles are smoother and more continuous, better reflecting real-world conditions.

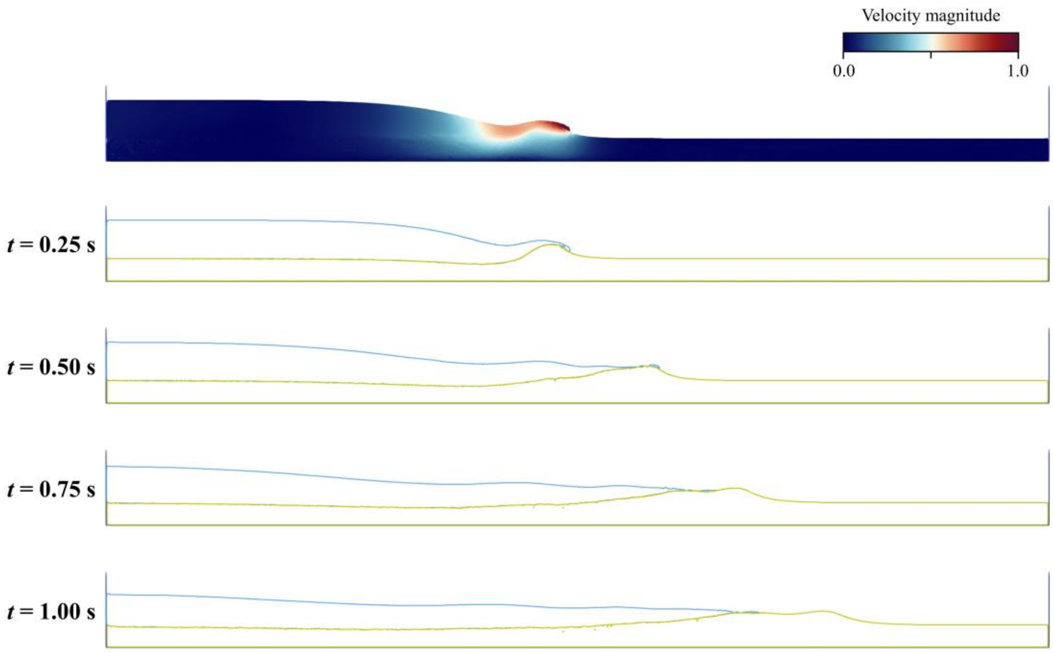

Figure 3.9 Snapshots of the Louvain liquid-sediment dam-break profiles and velocity cloud diagram.

Figure 3.5 shows that at the initial moment of t = 0.25 s, the release of the water column immediately exerted compression and excavation on the riverbed, forming a typical dam-break shape. At the interface between the front end of the water column and the sediment, the scoured sediment was partially pushed to the upper layer, forming an elliptical flow front. The improved SPH-HBP-DP model used in this study accurately reproduced this flow pattern, generating a greater excavation effect compared to previous SPH simulation results, while the upper water column maintained a smooth dam-collapse shape. The improved method also exhibits closer agreement with experimental data for both the scour profiles and the liquid surface profiles. However, in the control groups at t = 0.75 s and beyond (Figures 3.7 and 3.8), the SPH simulations produced excessive scouring volume compared to the experimental data, and the flow front decelerated more rapidly. This discrepancy can be partially attributed to the pore water pressure algorithm based on Equation 3.16, which may overestimate the pore water pressure, as noted in the report by Ghaïtanellis et al. (2018). Additionally, simplifications in turbulence effects and the yield criterion, as well as modeling within a weakly compressible framework, may have contributed to deviations in flow velocity and pressure fields.

Figure. 3.9 illustrates the snapshots of the erosional dam-break tests and the velocity cloud diagram at t = 0.25 s. From this, the spatiotemporal characteristics of the water column and scouring surface profiles can be obtained. The experiment demonstrates that the improved SPH-HBP-DP model can effectively depict the morphological variations of the sediment interface during the scouring process, highlighting its potential for further simulation of debris flow erosion, entrainment, and deposition.

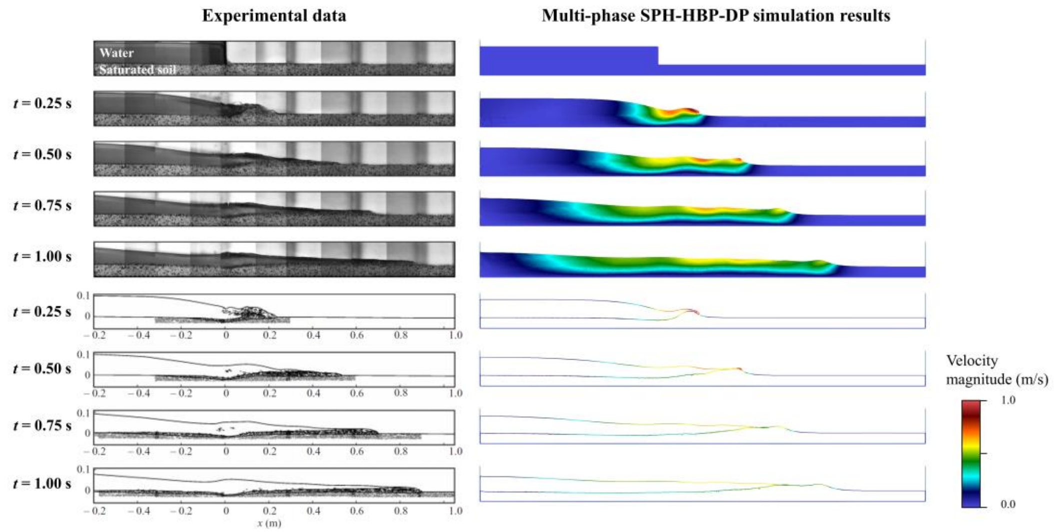

Figure 3.10 Comparative analysis of the Louvain erosional dam-break tests and SPH-HBP-DP simulation results.

The comparative analysis in Figure 3.10 demonstrates the effectiveness of experimental observations and SPH-HBP-DP-based numerical simulations, including time series flow velocity distribution maps and the developmental process of water-sediment profile characteristics. Our model successfully reproduces and captures the hydrodynamic characteristics of water-sediment flow. The purpose of this numerical experiment is to validate whether the HBP-DP model can capture the transition process from solid sediment to fluid phase, as saturated sediment is eroded from the riverbed, thereby laying the foundation for understanding the dynamic characteristics of debris flows on unsaturated sediment in the next chapter.

3.4.2. Example 2: Granular step collapse

In rapid granular flows with dense particles and greater density such as debris flows and avalanches, the dynamic behavior and flow state of the mass flow may differ significantly from those in scenarios involving pure water scouring. As we discussed earlier, an increase in viscosity usually indicates a low Reynolds number flow, where the effects of turbulence become minimal. In this scenario, inertial-dominated particle collision forces or viscous forces become predominant. This implies that the compression, excavation, and energy dissipation caused by particle collisions may far exceed the scouring effect of water on saturated sediment. At this stage, both upper and lower layers of material are modeled using the HBP constitutive model to simulate the flow characteristics of the particles.

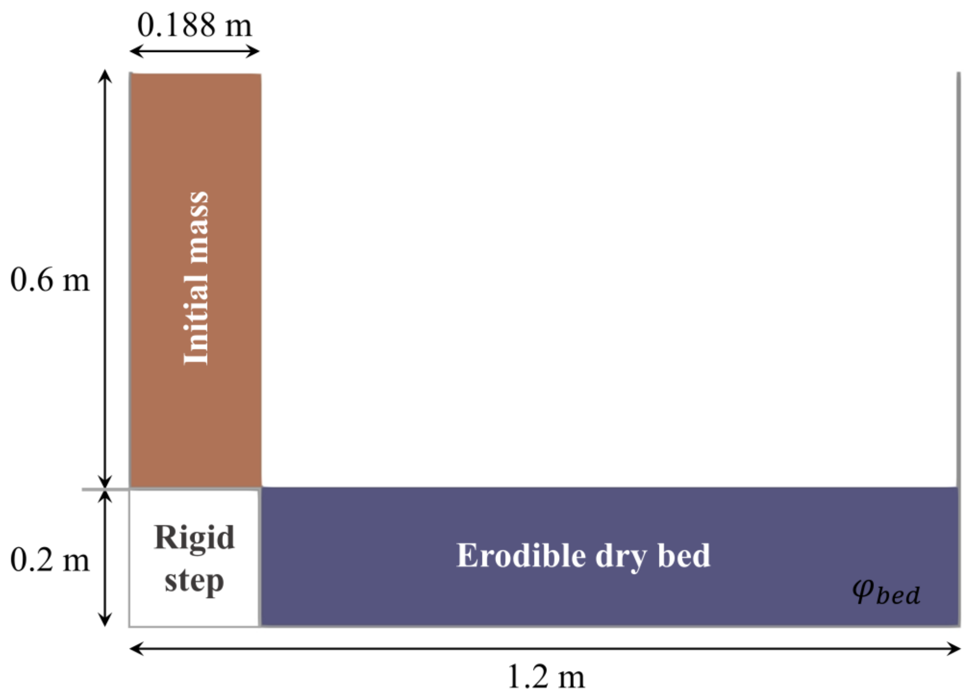

Figure 3.11 Schematic diagram of the granular step collapse.

Based on the granular step collapse experiment initially introduced by Crosta et al. (2009) and later validated using FEM and SPH methods (Nikooei and Manzari 2020), we conduct verification and dense flow erosion analysis. In the previous work, the non-cohesion granular flow was described as an elastoplastic model based on Geomechanically model. Given the relatively dry material used in this test, we adopt the SPH-HBP-based Lagrangian framework combined with the Mohr-Coulomb (MC) yield criterion to simulate the mass erosion behavior of granular flows.

Figure 3.11 illustrates the experimental setup for granular step collapse. An initial granular column with a high aspect ratio is positioned on a rigid step. Due to gravity, the column collapses and slides onto an erodible bed composed of the same material on the right side of the step. This process exerts compression, collision, and excavation forces on the bed. The only difference between the upper- and lower-layer materials is the internal friction angle. The experiment manipulates the internal friction angle of the bed layer φ_{bed} to alter the strength of the materials, thereby observing the changes in erosion effects and flow dynamics. Table 3.2 lists the materials and simulation parameters for the granular step collapse test.

Table 3.2 Modelling and materials parameters used in the granular step collapse.

Material	Parameter	Notation	Unit	Value
Initial mass	Bulk density	ρ_s	kg/m^3	1550
	Cohesion coefficient	c_s	Pa	0
	Internal Friction angle	φ_s	°	30
	Dynamic viscosity	μ_s [1]	Pa·s	0.1
	Exponential index	/	/	100
	Power law index	/	/	1.2
Erodible bed	Bulk density	ρ_{bed}	kg/m^3	1550
	Cohesion coefficient	c_{bed}	Pa	0
	Internal Friction angle	φ_{bed}	°	10-30
	Dynamic viscosity	μ_{bed}	Pa·s	0.1
	Exponential index	/	/	100
	Power law index	/	/	1.2

[1] The values for dynamic viscosity are referenced from the report by Nikooei and Manzari (2020)

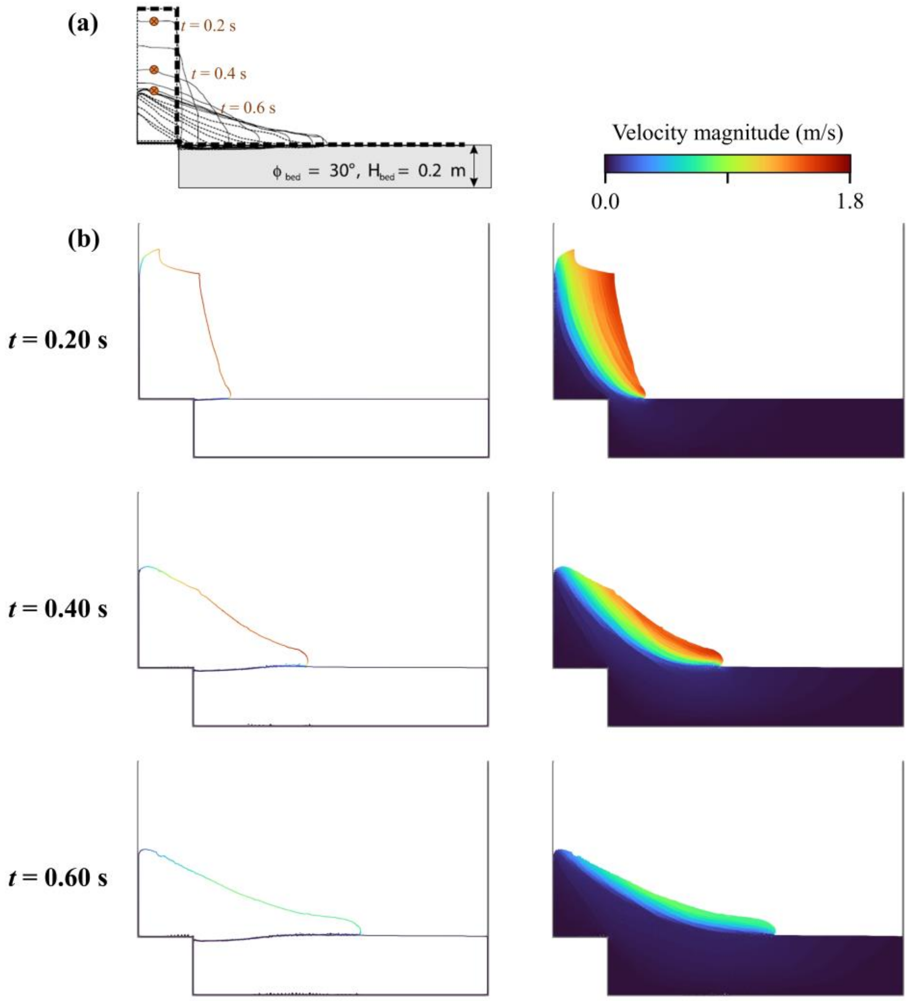

Figure 3.12 (a) Granular step collapse conducted with an internal friction angle of 30°. (b) Different stages of an entraining granular flow obtained by the SPH-HBP-MC method.

In the numerical setup, the particle distance is set to $dp = 0.002\ \text{m}$, generating 28,200 initial mass particles and 50,500 bed particles. The parameters for numerical sound speed and dissipation coefficients are identical to those used in the Louvain erosion dam-break test. Figures 3.12 and 3.13 show the simulation results for bed layer materials with internal friction angles of $\varphi_{\text{bed}} = 30°$ and $10°$, respectively. It is evident that the particle erosion pattern and the morphology of the interface are highly dependent on the strength of the bed layer. For the scenario with $\varphi_{\text{bed}} = 30°$, the sliding granular column causes almost no effective erosion of the bed layer material. There is negligible displacement and deformation of the bed materials, and the flow pattern resembles non-entraining flow over a completely rigid interface (Lube et al. 2005; Lube et al. 2007). As such, deposition occurs at a relatively early stage.

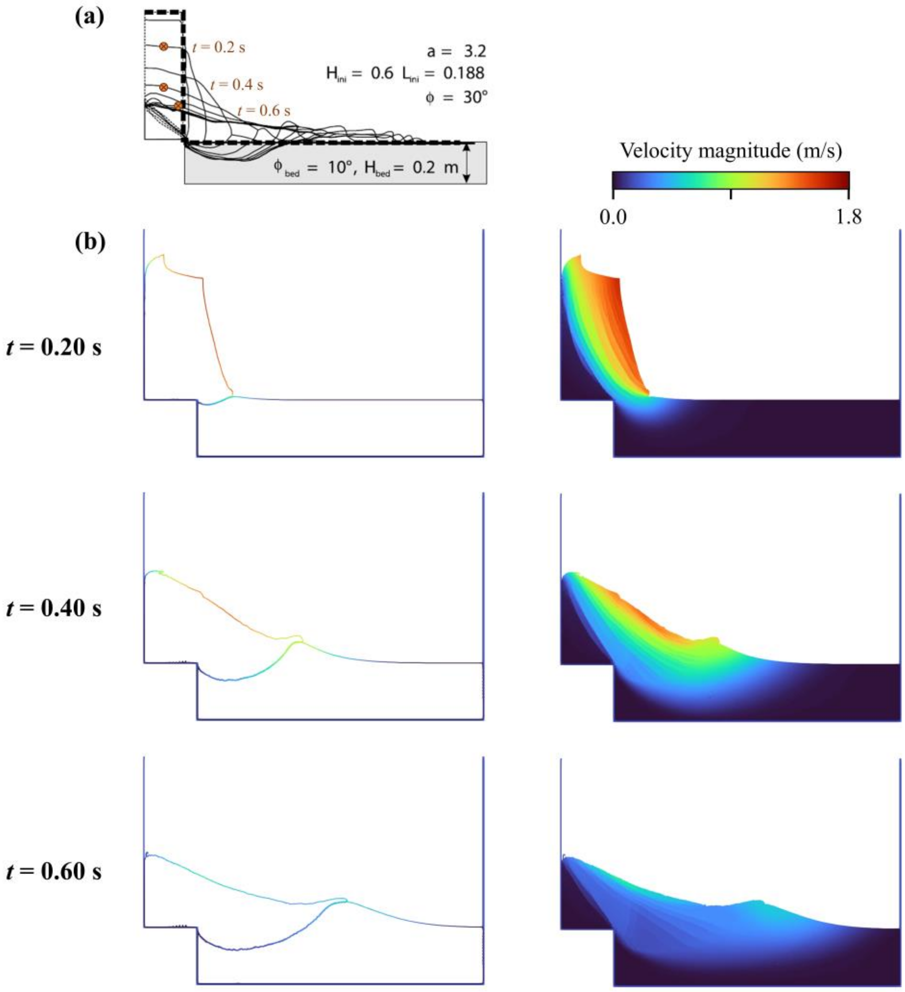

Figure 3.13 (a) Granular step collapse conducted with an internal friction angle of 10°. (b) Different stages of an entraining granular flow obtained by the SPH-HBP-MC method.

However, as the strength of the bed layer material decreases ($\varphi_{bed} = 10°$), the sediment particles cannot remain stable under the compression and scouring of the granular column, resulting in significant displacement and deformation. At this point, the bed layer material interface is pushed forward by compression and plowing, leading to delayed deposition. By comparing with experimental data (Figures 3.12a and 3.13a), it can be seen that the erosion and non-erosion flow patterns of granular materials obtained using the viscoplastic SPH-HBP-DC model closely match the results simulated using the elastoplastic FEM model. This alignment holds true even during the initial stages of granular collapse, where some materials exhibit curling similar to a viscous flow.

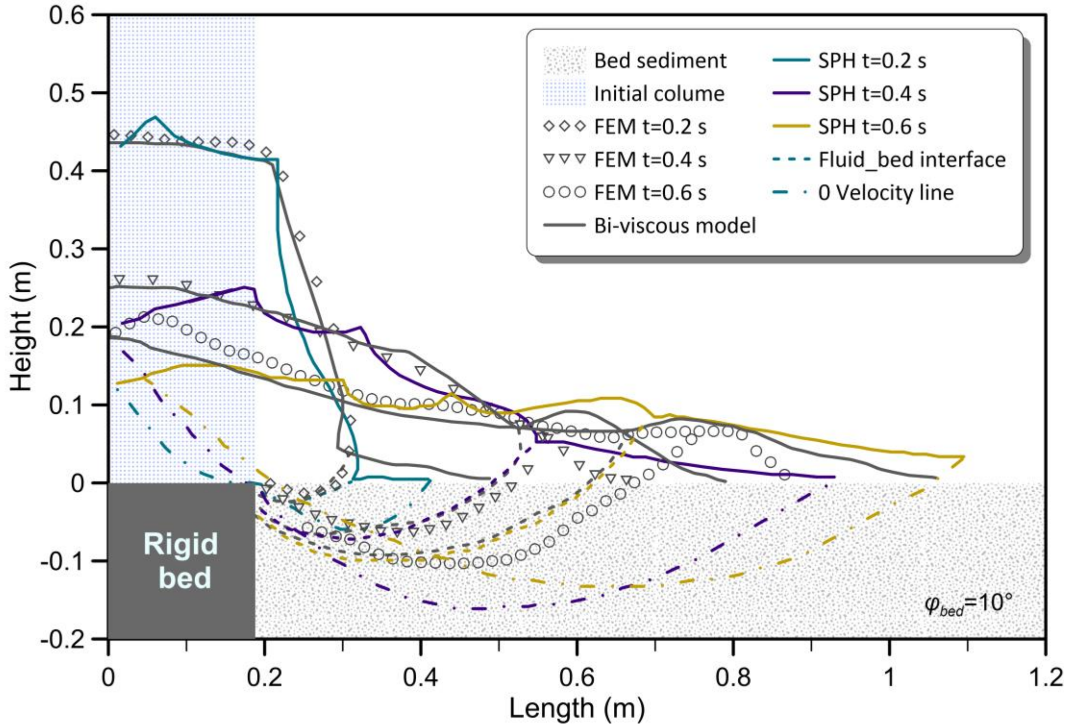

Figure 3.14 Comparative analysis of profiles of the granular step collapse on an entrained bed with $\varphi_{bed} = 10°$. Successive curves are plotted at 0.2 s intervals.

Figure 3.14 shows the comparative profiles of granular step collapse at different time intervals. It can be observed that our model accurately reproduces the surface and interface morphology development characteristics seen in both the experimental and FEM simulation results. Notably, the dashed line represents the critical interface ($v = 0$), above which all particles have yielded and displaced.

3.5. CONCLUSIONS

In this chapter, an advanced Two-Layer Multi-phase SPH (TLMP-SPH) model is introduced to simulate the complex rheological behavior and flow dynamics of debris flows, encompassing processes such as erosion, entrainment, and deposition (EEDPs). We begin by reviewing the current state of debris flow rheological models, emphasizing the evolution of models based on non-Newtonian fluid dynamics. The chapter details the application of the HBP model, integrated with suitable yield criteria and phase transition models, to simulate the dynamic processes of debris flows, including the overlying intrusive flow and underlying erodible beds. Subsequently, we discuss several commonly used yield criteria and their integration within the SPH Lagrangian framework, as well as the implementation of phase transitions. Finally, numerical tests and experimental comparisons are presented to validate the capabilities of the proposed model. The specific conclusions are as follows:

(1) Existing numerical models for debris flows, such as SWES, FEM, and FVM, are primarily based on single-phase continuous media approach. These models fail to fully account for the complex interactions between the overlying debris flow and the underlying sediment bed, including dynamic processes such as erosion, entrainment, and deposition. Leveraging the applicability of the Herschel-Bulkley-Papanastasiou (HBP) model for dilatant (shear thickening) and pseudoplastic (shear thinning) flows, we propose combining the HBP model with yield criteria like Drucker-Prager (DP) and Mohr-Coulomb (MC). This approach incorporates the two-phase nature of the HBP model to simulate the phase transition processes of sediment beds under rapid flow erosion, offering a new methodology for the numerical modeling of complex multi-phase geophysical flows.

(2) The proposed SPH-HBP-DP model was compared in detail with the Louvain erosional dam-break laboratory data and the SPH simulation results from Fourtakas and Rogers (2016). Our method integrates a more consistent and stable density dissipation term, a shifting algorithm, and phase transition handling. Comparisons of liquid-sediment erosion profiles, velocity fields, and other metrics indicate that our method accurately reproduces experimental observations, including the morphological characteristics of the erosion interface, the velocity field distribution, and displacement distances. This scouring experiment on saturated sediments establishes a foundation for future studies on the pore water pressure response patterns in unsaturated sediments and the physical mechanisms of debris flow erosion.

(3) To validate the capability of the SPH-HBP model in depicting the erosion patterns of dense granular flows, comparisons were made with granular step collapse experiments and their FEM simulation results. The Mohr-Coulomb yield criterion was integrated into the SPH-HBP framework to model the erosion of dense dry granular flows. Simulation results indicate that our model successfully captures the erosion characteristics of the collapsing granular column on erodible beds with varying shear strengths. When the erodible bed strength is high ($\varphi_{bed} = 30°$), the granular flow behaves almost like a non-entraining flow on a completely rigid boundary, with minimal deformation and displacement of the bed material, rapid reduction in granular flow velocity, and early deposition. As the bed strength decreases ($\varphi_{bed} = 10°$), significant deformation and displacement occur at the interface between the upper and lower layers, with lower layer particles being squeezed, excavated, and pushed to the flow front. The simulation results based on the SPH-HBP-MC model closely match the experimental data and FEM simulation results.

References

Armanini, A., Fraccarollo, L. & Rosatti, G. 2009. Two-dimensional simulation of debris flows in erodible channels. Computers & Geosciences 35(5), 993-1006.

Bagnold, R.A. 1954. Experiments on a gravity-free dispersion of large solid spheres in a Newtonian fluid under shear. Proceedings of the Royal Society of London. Series A, Mathematical and Physical Sciences 225(1160), 49-63.

Bui, H.H., Fukagawa, R., Sako, K. & Ohno, S. 2008. Lagrangian meshfree particles method (SPH) for large deformation and failure flows of geomaterial using elastic–plastic soil constitutive model. International journal for numerical and analytical methods in geomechanics 32(12), 1537-1570.

Bui, H.H. & Nguyen, G.D. 2021. Smoothed particle hydrodynamics (SPH) and its applications in geomechanics: From solid fracture to granular behaviour and multiphase flows in porous media. Computers and Geotechnics 138, 104315.

Crosta, G., Imposimato, S. & Roddeman, D. 2009. Numerical modeling of 2-D granular step collapse on erodible and nonerodible surface. Journal of Geophysical Research: Earth Surface 114(F3).

Dai, Z., Huang, Y., Cheng, H. & Xu, Q. 2014. 3D numerical modeling using smoothed particle hydrodynamics of flow-like landslide propagation triggered by the 2008 Wenchuan earthquake. Engineering Geology 180, 21-33.

Domnik, B. & Pudasaini, S.P. 2012. Full two-dimensional rapid chute flows of simple viscoplastic granular materials with a pressure-dependent dynamic slip-velocity and their numerical simulations. Journal of Non-Newtonian Fluid Mechanics 173, 72-86.

Domnik, B., Pudasaini, S.P., Katzenbach, R. & Miller, S.A. 2013. Coupling of full two-dimensional and depth-averaged models for granular flows. Journal of Non-Newtonian Fluid Mechanics 201, 56-68.

Fourtakas, G. & Rogers, B. 2016. Modelling multi-phase liquid-sediment scour and resuspension induced by rapid flows using Smoothed Particle Hydrodynamics (SPH) accelerated with a Graphics Processing Unit (GPU). Advances in water resources 92, 186-199.

Fourtakas, G., Rogers, B.D. & Laurence, D.R. 2013. Modelling sediment resuspension in industrial tanks using SPH. La Houille Blanche 99(2), 39-45.

Fourtakas, G., Vacondio, R., Alonso, J.D. & Rogers, B.D. Year. Improved density diffusion term for long duration wave propagation. In: 2020 SPHERIC Harbin International Workshop.

Fraccarollo, L. & Capart, H. 2002. Riemann wave description of erosional dam-break flows. Journal of Fluid Mechanics 461, 183-228.

Ghaïtanellis, A., Violeau, D., Ferrand, M., Abderrezzak, K.E.K., Leroy, A. & Joly, A. 2018. A SPH elastic-viscoplastic model for granular flows and bed-load transport. Advances in Water Resources 111, 156-173.

Haas, T.d. & Woerkom, T.v. 2016. Bed scour by debris flows: experimental investigation of effects of debris-flow composition. Earth Surface Processes and Landforms 41(13), 1951-1966.

Han, Z., Chen, G., Li, Y., Wang, W. & Zhang, H. 2015. Exploring the velocity distribution of debris flows: an iteration algorithm based approach for complex cross-sections. Geomorphology 241, 72-82.

Han, Z., Su, B., Li, Y., Dou, J., Wang, W. & Zhao, L. 2020. Modeling the progressive entrainment of bed sediment by viscous debris flows using the three-dimensional SC-HBP-SPH method. Water Research 182, 116031.

Han, Z., Su, B., Li, Y., Wang, W., Wang, W., Huang, J. & Chen, G. 2019. Numerical simulation of debris-flow behavior based on the SPH method incorporating the Herschel-Bulkley-Papanastasiou rheology model. Engineering Geology 255, 26-36.

Huang, Y. & Dai, Z. 2014. Large deformation and failure simulations for geo-disasters using smoothed particle hydrodynamics method. Engineering Geology 168, 86-97.

Iverson, R.M. 2012. Elementary theory of bed-sediment entrainment by debris flows and avalanches. Journal of Geophysical Research: Earth Surface 117(F3), F03006.

Iverson, R.M., Logan, M., LaHusen, R.G. & Berti, M. 2010. The perfect debris flow? Aggregated results from 28 large-scale experiments. Journal of Geophysical Research: Earth Surface 115(F3).

Iverson, R.M., Reid, M.E., Logan, M., LaHusen, R.G., Godt, J.W. & Griswold, J.P. 2011. Positive feedback and momentum growth during debris-flow entrainment of wet bed sediment. Nature Geoscience 4(2), 116-121.

Jakob, M., Hungr, O., Cui, P., Chen, X., Waqng, Y., Hu, K. & Li, Y. 2005. Jiangjia Ravine debris flows in south-western China. Debris-flow hazards and related phenomena, 565-594.

Jiang, H. & Xie, Y. 2011. A note on the Mohr–Coulomb and Drucker–Prager strength criteria. Mechanics Research Communications 38(4), 309-314.

Johnson, C., Kokelaar, B., Iverson, R.M., Logan, M., LaHusen, R. & Gray, J. 2012. Grain-size segregation and levee formation in geophysical mass flows. Journal of Geophysical Research: Earth Surface 117(F1), F01032.

Khattri, K.B. & Pudasaini, S.P. 2018. An extended quasi two-phase mass flow model. International Journal of Non-Linear Mechanics 106, 205-222.

King, J. 1996. Tsing Shan debris flow (Special Project Report SPR 6/96). Geotechnical Engineering Office, Hong Kong Government.

Lube, G., Huppert, H.E., Sparks, R.S.J. & Freundt, A. 2005. Collapses of two-dimensional granular columns. Physical Review E 72(4), 041301.

Lube, G., Huppert, H.E., Sparks, R.S.J. & Freundt, A. 2007. Static and flowing regions in granular collapses down channels. Physics of Fluids 19(4).

Ma, Y., Asia, M., Chen, G. & Han, Z. 2023. Physical Process-Based Entrainment Behaviour Modelling of Diluted Debris Flow Using SPH Incorporated with HBP-DP Approach. In: particles2023. 10.23967/c.particles.2023.029.

Major, J.J. & Pierson, T.C. 1992. Debris flow rheology: Experimental analysis of fine-grained slurries. Water resources research 28(3), 841-857.

Manenti, S., Sibilla, S., Gallati, M., Agate, G. & Guandalini, R. 2012. SPH simulation of sediment flushing induced by a rapid water flow. Journal of Hydraulic Engineering 138(3), 272-284.

Mangeney, A., Roche, O., Hungr, O., Mangold, N., Faccanoni, G. & Lucas, A. 2010. Erosion and mobility in granular collapse over sloping beds. Journal of Geophysical Research: Earth Surface 115(F3).

Martínez-Aranda, S., Murillo, J. & García-Navarro, P. 2022. A GPU-accelerated Efficient Simulation Tool (EST) for 2D variable-density mud/debris flows over non-uniform erodible beds. Engineering Geology 296, 106462.

Morikawa, D.S. & Asai, M. 2022. A phase-change approach to landslide simulations: Coupling finite strain elastoplastic TLSPH with non-Newtonian IISPH. Computers and Geotechnics 148, 104815.

Nikooei, M. & Manzari, M.T. 2020. Studying effect of entrainment on dynamics of debris flows using numerical simulation. Computers & geosciences 134, 104337.

Papanastasiou, T.C. 1987. Flows of materials with yield. Journal of rheology 31(5), 385-404.

Parsons, J.D., Whipple, K.X. & Simoni, A. 2001. Experimental study of the grain-flow, fluid-mud transition in debris flows. The Journal of Geology 109(4), 427-447.

Pastor, M., Tayyebi, S.M., Hernandez, A., Gao, L., Stickle, M.M. & Lin, C. 2023. A new two-layer two-phase depth-integrated SPH model implementing dewatering: Application to debris flows. Computers and Geotechnics 153, 105099.

Pastor, M., Yague, A., Stickle, M., Manzanal, D. & Mira, P. 2018. A two-phase SPH model for debris flow propagation. International Journal for Numerical and Analytical Methods in Geomechanics 42(3), 418-448.

Pudasaini, S.P. 2012. A general two-phase debris flow model. Journal of Geophysical Research: Earth Surface 117(F3), F03010.

Pudasaini, S.P. & Fischer, J.-T. 2020a. A mechanical erosion model for two-phase mass flows. International Journal of Multiphase Flow 132, 103416.

Pudasaini, S.P. & Fischer, J.-T. 2020b. A mechanical model for phase separation in debris flow. International Journal of Multiphase Flow 129, 103292.

Pudasaini, S.P. & Krautblatter, M. 2021. The mechanics of landslide mobility with erosion. Nature communications 12(1), 6793.

Pudasaini, S.P. & Mergili, M. 2019. A multi-phase mass flow model. Journal of Geophysical Research: Earth Surface 124(12), 2920-2942.

Shen, W., Li, T., Li, P., Shen, Y., Lei, Y., Guo, J.J.B.o.E.G. & Environment, t. 2019. The influence of the bed entrainment-induced rheology and topography changes on the propagation of flow-like landslides: a numerical investigation. Engineering Geology and the Environment 78, 4771-4785.

Spinewine, B. & Zech, Y. 2007. Small-scale laboratory dam-break waves on movable beds. Journal of Hydraulic Research 45(sup1), 73-86.

Takahashi, T. 2007. Debris flow: mechanics, prediction and countermeasures. Taylor & Francis.

Theule, J., Liébault, F., Laigle, D., Loye, A. & Jaboyedoff, M. 2015. Channel scour and fill by debris flows and bedload transport. Geomorphology 243, 92-105.

Ulrich, C., Leonardi, M. & Rung, T. 2013. Multi-physics SPH simulation of complex marine-engineering hydrodynamic problems. Ocean Engineering 64, 109-121.

Vicari, H., Ng, C.W., Nordal, S., Thakur, V., De Silva, W.R.K., Liu, H. & Choi, C.E. 2022a. The effects of upstream flexible barrier on the debris flow entrainment and impact dynamics on a terminal barrier. Canadian Geotechnical Journal 59(6), 1007-1019.

Vicari, H., Nordal, S. & Thakur, V. Year. The significance of entrainment on debris flow modelling: the case of Hunnedalen, Norway. In: Challenges and Innovations in Geomechanics: Proceedings of the 16th International Conference of IACMAG-Volume 2 16, 507-514.

Vicari, H., Tran, Q.A., Nordal, S. & Thakur, V. 2022b. MPM modelling of debris flow entrainment and interaction with an upstream flexible barrier. Landslides 19(9), 2101-2115.

Wang, W., Chen, G., Han, Z., Zhou, S., Zhang, H. & Jing, P. 2016. 3D numerical simulation of debris-flow motion using SPH method incorporating non-Newtonian fluid behavior. Natural Hazards 81, 1981-1998.

Zheng, H., Shi, Z., Hanley, K.J., Zhou, Y. & Hu, X. 2023. Pore pressure evolution in bed sediment overridden by debris flow: A general formulation. Earth Surface Processes and Landforms 48(6), 1188-1201.

Zheng, H., Shi, Z., Yu, S., Fan, X., Hanley, K.J. & Feng, S. 2021. Erosion mechanisms of debris flow on the sediment bed. Water Resources Research 57(12), e2021WR030707.

Zhou, M., Shi, Z., Peng, C., Peng, M., Cui, K.F.E., Li, B., Zhang, L. & Zhou, G.G. 2024. Two-phase modelling of erosion and deposition process during overtopping failure of landslide dams using GPU-accelerated ED-SPH. Computers and Geotechnics 166, 105944.

Zubeldia, E.H., Fourtakas, G., Rogers, B.D. & Farias, M.M. 2018. Multi-phase SPH model for simulation of erosion and scouring by means of the shields and Drucker–Prager criteria. Advances in water resources 117, 98-114.

CHAPTER 4

Flow-momentum growth and its feedback in viscous debris flow on wet bed sediment

4.1. Introduction

Flow-momentum growth and resultant feedback from bed-sediment entrainment significantly influence the mobility of debris flows and valley topography. Existing models inadequately capture the mass and momentum growth regulated by scale-sensitive, time-dependent pore water pressure in erodible beds, which exhibit pronounced anisotropy and nonlinearity.

Extensive field and lab studies (e.g., Jakob et al. 2005; McArdell et al. 2007; Iverson et al. 2010; Iverson et al. 2011; Johnson et al. 2012; Haas and Woerkom 2016; Zheng et al. 2021; Vicari et al. 2022a) suggest that the evolving excess pore water pressure significantly contributes to the reduction of shear strength in wet bed sediment. Nevertheless, accurately quantifying the time-space evolution of interstitial pore water pressures, especially those characterized by rapid loading in undrained, quasi-saturated basal sediments, remains a huge challenge. Existing studies, especially the depth-averaged method, tend to adopt a simplified treatment by introducing pore pressure ratio (Iverson and Denlinger 2001) to evaluate the pore pressure response patterns (e.g., Iverson 2012; Han et al. 2015; Han et al. 2020; Vicari et al. 2022b). Another strategy involves employing porous medium mechanics to analyze the interdependence between soil skeleton deformation and pore water pressure (e.g., Pastor et al. 2015; Cascini et al. 2016; Morikawa and Asai 2022). Such methods often rely on fully coupled numerical models and require expensive poro-mechanical parameters. To address this issue, this chapter builds upon the proposed TLMP-SPH model, presenting an efficient hydro-poro-mechanics-based pore water pressure algorithm embedded within the SPH scheme to simulate the pore pressure response and flow-momentum growth of debris flows on wet beds. To address the size effect, the method was rigorously tested through small-scale erosional tests and a series of full-scale, well-documented entrainment experiments.

4.2. Development of a hydro-poro-mechanism-based pore water pressure algorithm

4.2.1. Physics-based pore water pressure response algorithm

The physics-based pore water pressure algorithm applied in the SPH method can be broadly classified into particle-fluid mixture SPH (single-layer) and fluid-grain strong coupling SPH (two-layer). Single-layer SPH utilizes a single type of particle to incorporate data from both the solid grain (soil skeleton) and interstitial fluid (water or viscous fluid) phases. This approach is relatively simple to implement, has low computational costs, and has been used to solve various practical SPH problems (e.g., Bui and Fukagawa 2009; Pastor et al. 2009; Bui and Fukagawa 2013; Pastor et al. 2015; Lian et al. 2022; Morikawa and Asai 2022). By contrast, The two-layer strong coupling SPH approach employs different Lagrangian particles to separately model the fluid and solid phases. The fluid is usually treated as incompressible or weakly compressible, whereas the soil skeleton is modeled using an elastic or elasto-plastic constitutive model. The interaction between these phases is represented by seepage or drag forces. This method can account for relative accelerations between the solid and fluid phases and allows for independent application of hydraulic and mechanical boundary conditions. Some typical examples include (e.g., Huang et al. 2013; Zhang et al. 2016; Pastor et al. 2018; Zhang et al. 2019). Given the particle-fluid mixture modeling framework adopted in this study, and considering the significant computational cost and compromises required for large-scale applications of the strong coupling model, we introduce an efficient pore water pressure physical model based on the single-layer SPH framework. This model, initially proposed by Chen et al. (2024), is derived from volumetric strain and Darcy's law, and will be elaborated upon below.

Let's first review the continuity equation in Eq. (2.18), and consider the mass conservation of the solid and liquid phases separately. The mass conservation of the separate phase within a unit volume can be expressed as follows:

$$\frac{d\left(n_s\rho_s\right)}{dt}+n_s\rho_s\nabla\cdot\mathbf{v}_s=0, \tag{4.1}$$

and

$$\frac{d\left(n_w\rho_w\right)}{dt}+n_w\rho_w\nabla\cdot\mathbf{v}_w=0, \tag{4.2}$$

where the subscripts *s* and *w* denote solid and fluid phases, respectively; n_s and n_w indicate the volume fractions of the corresponding phases; The velocity vector of the solid in the porous medium is denoted as $\mathbf{v}_s$, while the seepage velocity vector, $\mathbf{v}_w$, represents the relative velocity between the water and solid phases. It is important to note that the total volumetric strain increment ($d\varepsilon_t$) is equivalent to the negative change in void volume, following the sign convention where compression is considered positive. Additionally, considering the physical relationship between pore water pressure p_w, its bulk modulus K_w, and density variation, i.e., $K_w=dp_w/(d\rho_w/\rho_w)$, the pore water pressure response can be expressed as follows:

$$\frac{n}{K_w}\frac{dp_w}{dt}=-\nabla\cdot\mathbf{q}_w+\frac{d\varepsilon_t}{dt}, \tag{4.3}$$

with

$$\mathbf{q}_w=n_w\mathbf{v}_w, \tag{4.4}$$

where $\mathbf{q}_w$ denotes the vectors of Darcy velocity. In the SPH model, the velocities of solids are determined using the momentum equation, which incorporates the total stresses and the overall density of the mixture. The overall density is defined as $\rho=n_w\rho_w+(1-n_w)\rho_s$, similar to the method used by Lian et al. (2022):

$$\frac{d\mathbf{v}_s}{dt} = \frac{1}{\rho}\nabla \cdot \boldsymbol{\sigma} + \mathbf{F}, \tag{4.5}$$

where $\mathbf{F}$ represents the vector of external body force. The momentum balance of liquid phase is typically described by the NS equation, which simplifies to Darcy's law for laminar flows. According to Eq. (4.3), the pore water pressure response is influenced by both seepage and soil volumetric strains. In a fully saturated porous material, the increment in pore pressure can be formulated as:

$$\frac{dp_w}{dt} = \frac{K_w}{n}\left(-\nabla \cdot \mathbf{q}_w + \frac{d\varepsilon_t}{dt}\right). \tag{4.6}$$

Following Darcy's law, the flux component $\mathbf{q}_w$ along the direction of gravity (referred to as β in this study) and in other directions can be described as follows:

$$q_w^\beta = -k^\beta i^\beta = -k^\beta\left(\frac{1}{\gamma_w}\frac{\partial p_w}{\partial x^\beta} - \frac{dH_e}{dx^\beta}\right) = -\frac{k^\beta}{\gamma_w}\frac{\partial p_w}{\partial x^\beta} + k^\beta, \tag{4.7}$$

$$q_w^\alpha = -k^\alpha i^\alpha = -\frac{k^\alpha}{\gamma_w}\frac{\partial p_w}{\partial x^\alpha}, \tag{4.8}$$

$$q_w^\gamma = -k^\gamma i^\gamma = -\frac{k^\gamma}{\gamma_w}\frac{\partial p_w}{\partial x^\gamma}, \tag{4.9}$$

where k^α, k^β, and k^γ denote the hydraulic conductivity, and i^α, i^β, and i^γ refer to the hydraulic gradients in each directions. γ_w is the unit weight of water; H_e represents the elevation head, so the difference dH_e between particle pairs corresponds to the particle spacing in the direction of gravity.

In this context, we assume isotropic hydraulic properties (i.e., $k^\alpha = k^\beta = k^\gamma = k$) that remain constant during the simulation. Consequently, the pore pressure increment dp_w / dt can be derived by combining Eqs. (4.6) through (4.9):

$$\frac{dp_w}{dt} = \left(\frac{K_w k}{n_w \gamma_w}\right)\nabla^2 p_w + \frac{K_w}{n}\frac{d\boldsymbol{\varepsilon}_t}{dt}, \tag{4.10}$$

where ∇^2 indicates the Laplace operator, which should be rigorous approximated in the SPH scheme. Therefore, the interaction between soil and water is captured by integrating seepage effects and pore water pressure response into the governing equations.

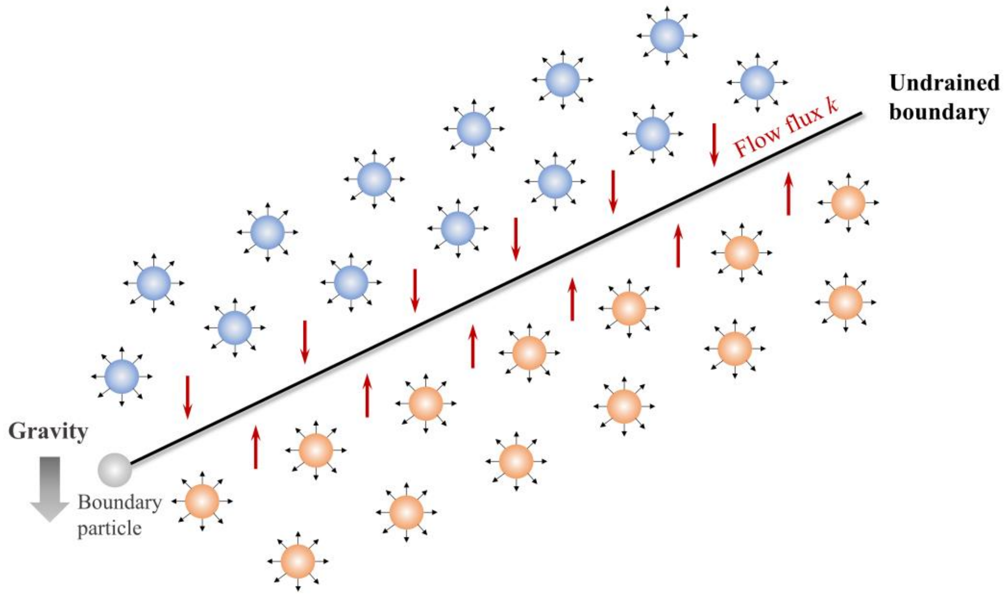

Figure 4.1 Schematic of flow flux at an undrained boundary accounting for gravity effects.

For defining hydraulic conditions, a drained boundary is typically modeled by setting a fixed pore pressure value at the boundary. Conversely, an undrained boundary is simulated using virtual particles that replicate the pore pressure values of the adjacent particles across the boundary. Thus, at the undrained boundaries (Figure. 4.1), the gravity-induced flow flux $q_w^\beta(g) = -k$ exhibits the same magnitude but flows in the opposite direction across the boundary. The change in flow flux due to gravity at these undrained boundaries can be described as:

$$\frac{\partial q_w^\beta(g)}{\partial x^\beta} = -\frac{-k-(k)}{dx^\beta} = \frac{2k}{dx^\beta}. \tag{4.11}$$

As such, taking gravity into account, the derivative of the total flux at the undrained boundary can be expressed as:

$$\frac{\partial q_w^\beta}{\partial x^\beta} = \left(\frac{k}{\gamma_w}\right)\frac{\partial^2 p_w}{\partial\left(x^\beta\right)^2} + \frac{2k}{dx^\beta}. \tag{4.12}$$

Combining Eqs (4.10) and (4.12), the pore pressure increment at the undrained boundary of the particles can be formulated as:

$$\frac{dp_w}{dt} = \left(\frac{K_w k}{n_w \gamma_w} \right) \nabla^2 p_w + \frac{2K_w k}{ndx^\beta} + \frac{K_w}{n} \frac{d\boldsymbol{\varepsilon}_t}{dt}. \tag{4.13}$$

where dx^β denotes the distance separating the bottom boundary and the particle directly above it, aligned with direction of gravity. The three terms on the RHS of Eq. (4.13) correspond, respectively, to the effect of the hydraulic gradient, soil volumetric strains, and the undrained boundary on the pore pressure response. The pore water pressure response is precisely modeled by incorporating both the hydraulic gradient and volumetric strain within a single-layer mixture of SPH particles, achieving a balance between accuracy and computational efficiency.

4.2.2. EXTENSION TO QUASI-SATURATED WET SEDIMENT CONDITIONS

Debris flows commonly occur in conjunction with antecedent precipitation or groundwater recharge, leading to varying degrees of saturation in bed sediments, ranging from unsaturated to quasi-saturated states. Modelling the dynamic response of pore water pressure in this scenario proves to be quite challenging, as it is influenced by a combination of geological conditions, external loads, and material properties. In the previous section, we reviewed a pore water pressure algorithm derived based on volumetric strain rate and Darcy's law, which is used for calculating the pore pressure response in saturated sediments. The consolidation model efficiently captures excess pore pressures, ensuring high accuracy with minimal computational demand. Here, we extend its application to a broader scenario characterized by wet, quasi-saturated conditions, wherein the water content is sufficiently high to generate a conspicuous pore pressure response.

Given the intricate physical mechanisms inherent in the multiphase media of unsaturated soils, the relationship between pore water pressure and water content exhibits pronounced non-linearity. To develop a pore pressure response algorithm for wet sediment, it is essential to adopt several well-founded assumptions:

(i) The soil skeleton is considered incompressible, with total volumetric strain attributed to changes in pore water and air volumes.

(ii) The saturation degree of bed sediment remains constant during the dynamic process.

(iii) The water content in the sediments is sufficiently high to generate a pore pressure that far exceeds the matric suction between pore fluid and air, thereby sustaining the applicability of Terzaghi's effective stress principle.

(iv) The rapid loading of debris flows allows insufficient time for the separation or rearrangement of pore fluid and air, resulting in consistent pressure responses.

Based on assumption (i), the total volumetric strain rate $\boldsymbol{\varepsilon}_t$ can be expressed as a weighted average of each component (Pietruszczak and Pande 1996).

$$\boldsymbol{\varepsilon}_t = n\left[S_r\boldsymbol{\varepsilon}_w + \left(1 - S_r\right)\boldsymbol{\varepsilon}_a\right], \tag{4.14}$$

where $\boldsymbol{\varepsilon}_w$ and $\boldsymbol{\varepsilon}_a$ denote the volumetric strain rate of pore water and air, respectively; S_r is the saturation degree (i.e., $S_r = n_w / n$ where n_w refers to the water content). Applying the constitutive equations for both materials, based on assumption (iv), leads to:

$$\boldsymbol{\varepsilon}_w = -\frac{\Delta p}{K_w}, \tag{4.15}$$

$$\boldsymbol{\varepsilon}_a = -\frac{\Delta p}{K_a}, \tag{4.16}$$

where K_a is the bulk modulus of pore air. Through Eqs. (4.14) to (4.16), the volumetric strain rate of pore water can be derived as:

$$\boldsymbol{\varepsilon}_w = \frac{1}{n_w + \left(n - n_w\right)K_\varepsilon}\boldsymbol{\varepsilon}_t, \tag{4.17}$$

where $K_\varepsilon = K_w / K_a$ represents the ratio of bulk modulus between pore water and air, and *n* refers to the porosity. By substituting the volumetric strain rate in Eq. (4.13) with the portion of pore water, the resultant pressure responses of pore pressure for wet sediment can be derived:

$$\frac{dp_w}{dt} = \left(\frac{K_w k}{n_w \gamma_w}\right)\nabla^2 p_w + \frac{K_w}{n}\boldsymbol{\varepsilon}_w + \frac{2K_w k}{ndz^\beta}, \tag{4.18}$$

Based on the relationship between the volumetric strain and bulk modulus of each phase in porous media materials, Equations (4.17) and (4.18) establish the relationship between pore water pressure response and volumetric water content in unsaturated sediments.

4.3. SPH approximation of the second derivative term of pore water pressure

The diffusion term in Eq. (4.18) involves the second derivatives of p_w, which need to be rigorously approximated within the SPH scheme. As previously mentioned, calculating the second-order derivative of functions using SPH approximation faces numerous challenges, including large computational costs, convergence issues, consistency, and uniform particle distribution. Therefore, it is recommended to avoid using the second-order derivative of the kernel function in practical SPH applications. However, solving many physical problems in engineering involves approximating second-order derivatives. To address this, we introduced a general, 0th-order accurate primitive Laplacian SPH model (Brookshaw 1985) in Chapter 2, which is reviewed here:

$$\nabla^2 f_i \approx \left\langle \nabla^2 f \right\rangle_{(0)} = 2\sum_{j=1}^{N} \frac{m_j}{\rho_j}\left(f_j - f_i \right) \frac{x_{ji} \cdot \nabla_i W_{ij}}{\left| x_{ji} \right|^2 + \eta^2}, \tag{4.19}$$

Applying this to the pore water pressure response algorithm (Eq. (4.18)) yields a 0th-order accuracy SPH approximation formula based on the primitive Laplacian method (Chen et al. 2024):

$$\begin{aligned} \frac{dp_{wi}}{dt} &\approx \left(\frac{2K_w k}{n\gamma_w} \right) \sum_{j=1}^{N} \frac{m_j}{\rho_j} \frac{p_{wji} x_{ji} \cdot \nabla_i W_{ij}}{\left| x_{ji} \right|^2 + \left(0.01h/2 \right)^2} \\ &+ \frac{K_w}{n \cdot \left[n_w + \left(n - n_w \right) K_\varepsilon \right]} \left(\frac{d\varepsilon_i^\alpha}{dt} + \frac{d\varepsilon_i^\beta}{dt} + \frac{d\varepsilon_i^\gamma}{dt} \right) + \frac{2K_w k}{ndz_i^\beta}, \end{aligned} \tag{4.20}$$

The primitive SPH Laplacian model avoids using the second derivative of the kernel function; hence, its accuracy and robustness are often criticized due to the impact of non-uniform particle distribution. In this study, the Naïve model (Asai et al. 2023) is adopted to evaluate the Laplacian operator. Similar to a cross-derivative formulation proposed by Lian et al. (2021), this approach offers enhanced accuracy and convergence relative to the primitive Laplacian model, while obviously reducing computational demand relative to other Laplacian models. This study does not cover the detailed derivation process of the Laplacian model. Instead, we directly present the Naïve form of the Laplacian operator as follows:

$$\nabla^2 f_i \approx \langle \nabla^2 f \rangle_{(NI)} = 2\sum_{j=1}^{N} \frac{m_j}{\rho_j} \frac{r_{ij} \cdot \tilde{\nabla} W(r_{ij},\, h)}{|r_{ij}|^2} \left(f_{ij} - r_{ij} \cdot \langle f_i \rangle_{(1)} \right), \tag{4.21}$$

with

$$\langle f_i \rangle_{(1)} = \sum_{j=1}^{N} \frac{m_j}{\rho_j} (f_j - f_i) \tilde{\nabla} W(r_{ij},\, h), \tag{4.22}$$

$$L_i = \sum_{j=1}^{N} \frac{m_j}{\rho_j} \nabla W_{ij} \otimes r_{ij}, \tag{4.23}$$

where $\langle f_i \rangle_{(1)}$ refers to the kernel gradient correction term (Randles and Libersky 1996), and $\nabla W_c(r_{ij},\, h)$ denote the correction gradient operator, which is defined by the correction matrix L_i. For a comprehensive analysis of the Naïve and other refined Laplacian models, please refer to the work by Asai et al. (2023). Similarly, by applying the Naïve Laplacian operator to the pore water pressure formula, we obtain a 1st-order accurate SPH second derivative approximation, as follows:

$$\begin{aligned} \frac{dp_{wi}}{dt} = & \left(\frac{K_w k}{n_w \gamma_w} \right) \langle \nabla^2 p_{wi} \rangle_{(NI)} \\ & + \frac{K_w}{n \cdot \left[n_w + (n - n_w) K_\varepsilon \right]} \left(\frac{d\varepsilon_i^\alpha}{dt} + \frac{d\varepsilon_i^\beta}{dt} + \frac{d\varepsilon_i^\gamma}{dt} \right) + \frac{2K_w k}{ndz_i^\beta}, \end{aligned} \tag{4.24}$$

$$\langle \nabla^2 p_{wi} \rangle_{(NI)} = 2\sum_{j=1}^{N} \frac{m_j}{\rho_j} \frac{r_{ij} \cdot \nabla \tilde{W}(r_{ij},\, h)}{|r_{ij}|^2} \left(p_{wij} - r_{ij} \cdot \langle \nabla p_{wi} \rangle_{(1)} \right), \tag{4.25}$$

$$\langle \nabla p_{wi} \rangle_{(1)} = \sum_{j=1}^{N} \frac{m_j}{\rho_j} (p_{wj} - p_{wi}) \nabla \tilde{W}(r_{ij},\, h), \tag{4.26}$$

$$\nabla \tilde{W}(r_{ij},\, h) = L^{-1} \nabla W(r_{ij},\, h), \tag{4.27}$$

4.4. VERIFICATION EXAMPLES

4.4.1. EXAMPLE 1: PORE PRESSURE TESTS FOR EROSIONAL DAM-BREAK

Since there are currently no experiments on pore water pressure in erosive structures, we use the Louvain test model framework to test the evolution of pore pressure in a two-layer dam-break model. However, we have increased the initial mass column (water or dense material) and the bed material thickness to 0.5 m to observe the pressure variation along the depth direction, as shown in Figure 4.2.

Table 4.1 Material parameters of the two-layer scouring test.

Material	Parameter	Notation	Unit	Value
Upper-layer initial column	Water density	ρ_w	kg/m^3	1000
	Dense flow density	ρ_m	kg/m^3	2010
	Cohesion coefficient	c_m	Pa	0
	Internal friction angle	φ_m	°	25
	Kinematic viscosity	υ_m	m^2/s	0.01
Underlying Sediment	Bulk density	ρ_s	kg/m^3	1650
	Cohesion coefficient	c_s	Pa	1
	Internal friction angle	φ_s	°	40
	Kinematic viscosity	υ_s	m^2/s	0.02
	Porosity	n	/	0.40
	Volumetric water content	n_W	/	0.25
	Bulk modulus of water	K	Pa	2×10^9
	Hydraulic permeability	k	m^2	10^{-8}

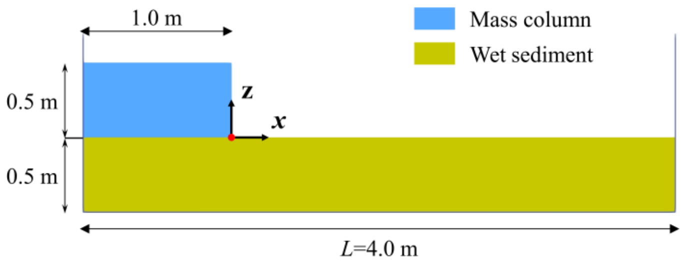

Figure 4.2 Numerical modeling of the pore pressure response on erosional dam break structure–experiment set-up.

A liquid-sediment dam-break scouring experiment on wet bed sediments was conducted. The numerical parameters used in the simulation were consistent with those of the Louvain test. Additionally, other material parameters related to pore water pressure calculations were introduced, including the bulk modulus of pore water, hydraulic conductivity, porosity, and water content. These parameters were referenced from the values reported by Iverson et al. (2010) in their large-scale debris-flow flume experiments, as detailed in Table 4.1.

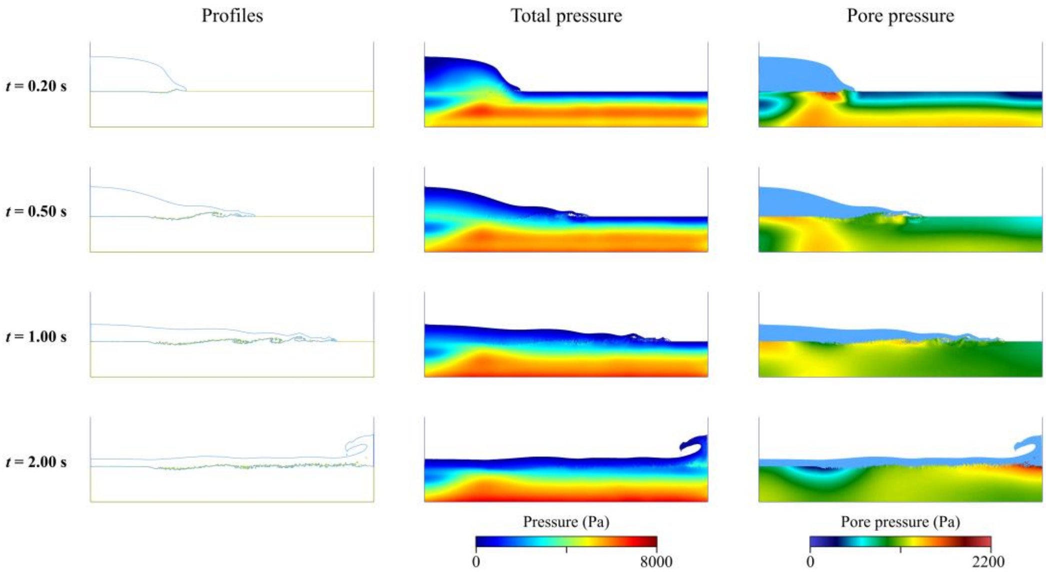

Figure 4.3 Simulation results of the two-layer liquid-sediment dam-break, including surface profiles, total pressure, and pore pressure cloud maps.

Figure 4.3 illustrates the dam-break simulation results under pure water scouring, including the liquid-sediment profile, total pressure, and the time series development characteristics of pore water pressure. It can be observed that with higher sediment strength ($\varphi_s = 40°$), the erosion mode of the sediment under water scouring is a grain-by-grain surface erosion state. At the moment of the dam break (t = 0.2 s), a stress concentration phenomenon occurs directly below the front of the water column, while the total pressure at other locations generally conforms to the hydrostatic pressure distribution pattern, increasing with depth. As the water column continues to scour and move forward, the overall total pressure distribution remains stable, with a more uniform linear distribution from top to bottom. However, the pore water pressure in the sediment bed undergoes significant changes. At the moment of the dam break, a large pore water pressure is generated directly below the water column, which then rapidly dissipates. By 0.5 s, the pore water pressure has almost completely dissipated, with the pressure distribution becoming uniform. A noticeable pore pressure response occurs again only at the impact boundary at the front end of the water flow (t = 2 s). The response of the liquid-sediment pore pressure indicates that the sediment bed cannot sustain a prolonged pore pressure response under scouring conditions.

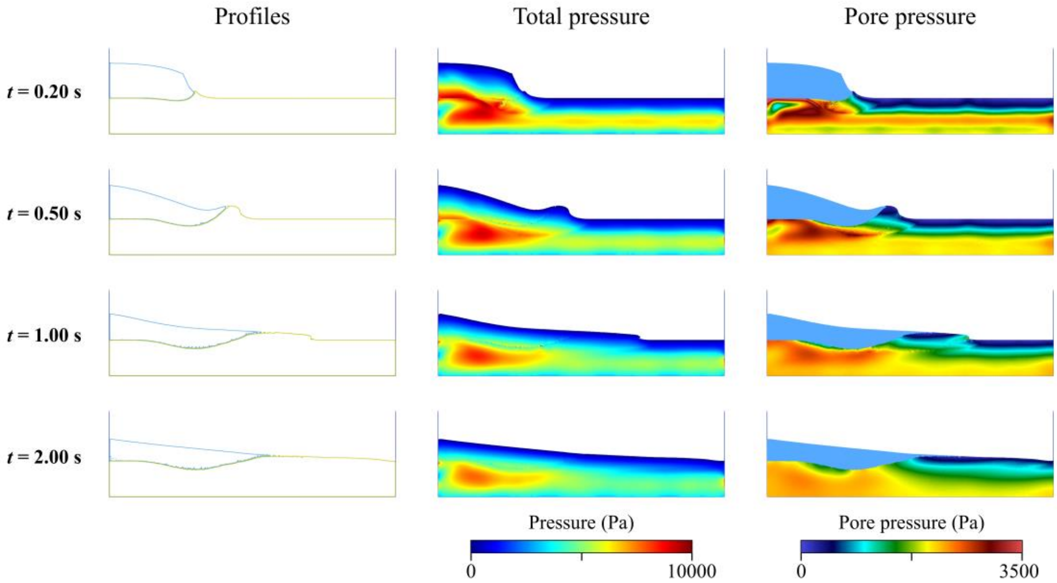

Figure 4.4 Simulation results of the two-layer dense flow collapse, including surface profiles, total pressure, and pore pressure cloud maps.

Subsequently, we conducted an erosive dam-break experiment with dense granular flow, replacing the initial mass column with a granular flow controlled by the HBP constitutive model and the DP yield criterion, as shown in Figure 4.4. The characteristic profile of this scenario differs significantly from that of pure water scouring. The dense flow exerts a more pronounced excavation and compression effect on the sediment bed from the initial stage, resulting in a noticeable displacement at the interface between the upper and lower layers. The total pressure under the erosive action of the dense flow is also significantly higher than that in the liquid-sediment scouring scenario, with a maximum of 10,000 Pa, and is more concentrated directly beneath the mass column. The erosion effect and velocity attenuation are more pronounced in this scenario. Additionally, the pore water pressure response is more intense, with a longer duration and greater concentration under dense flow erosion. This type of erosive effect corresponds to the erosion process of debris flows in an undrained condition, highlighting the interaction characteristics between debris flows and wet sediments.

4.4.2. EXAMPLE 2: LARGE-SCALE DEBRIS FLOWS ENTRAINMENT EXPERIMENTS

4.4.2.1. Configuration and simulation results:

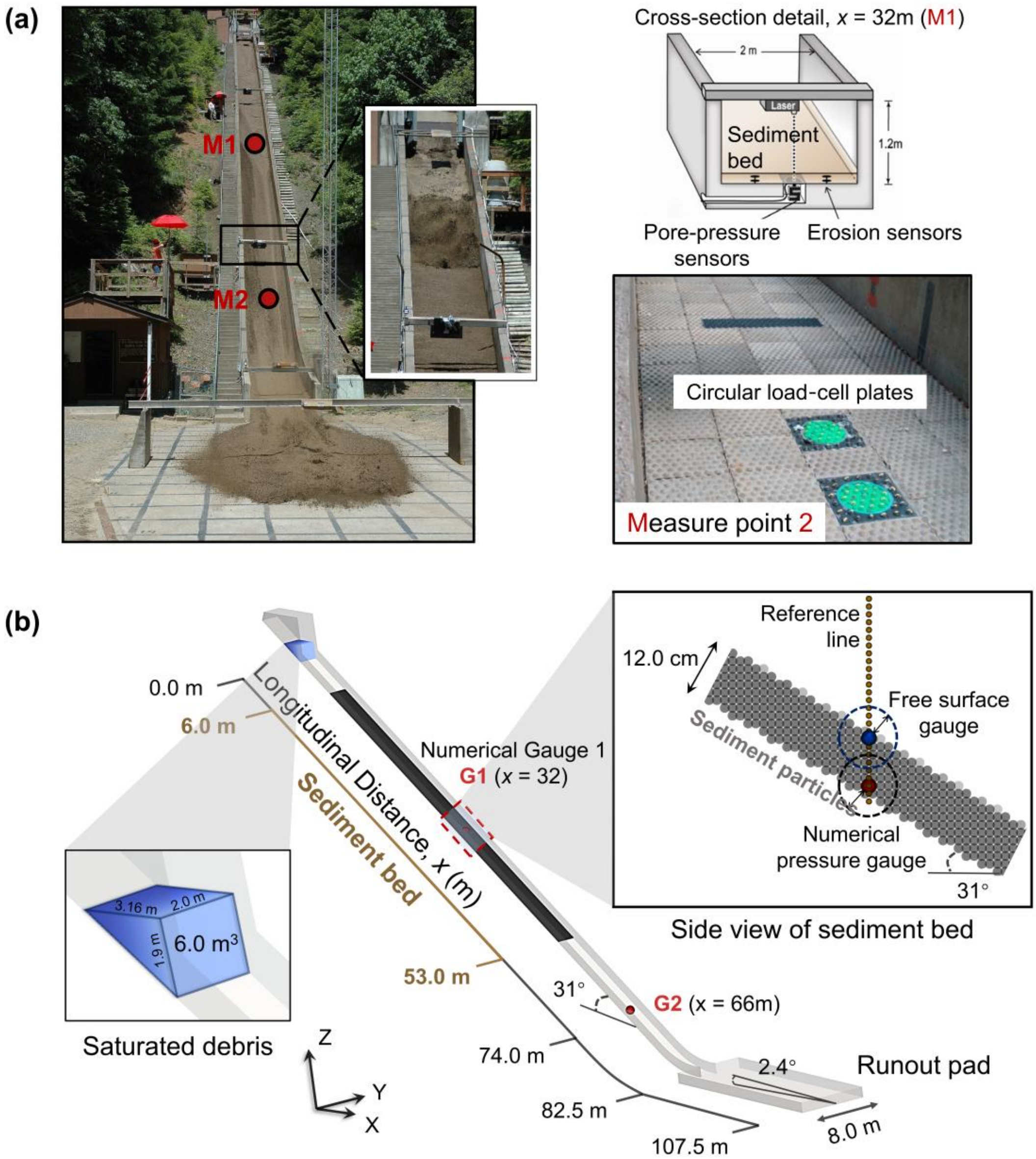

Figure 4.5 (a) Photographs of the USGS debris-flow flume experiment (figure modified from (Iverson et al. 2010) and (Iverson et al. 2011)). (b) Schematic depicting experiment configuration and the gauge system for numerical analysis.

As previously noted, field-scale test facilities are essential to address scaling issues related to pore pressure diffusion in water-laden debris flows (Iverson et al.

2010; Iverson 2015; Delannay et al. 2017; Vicari et al. 2022a). In this context, the large-scale debris-flow entrainment experiments conducted by the United States Geological Survey (USGS) (Iverson et al. 2011) are selected to verify the proposed method. As depicted in Figure 4.5, the substructure comprises a 95-m-long, 2-m-wide and 1.2-m-deep rectangular concrete sloping ($\theta = 31°$) flume and is deployed with arrays of electronic sensors (refer to Iverson et al. (2010) for details). The channel begins to flatten from $x = 74$, following the catenary curve, and extends out of the flume mouth at $x = 82.5$, eventually debouches onto a nearly planar ($\theta = 2.4°$) concrete runout pad.

Table 4.2 Property parameters of debris flow and sediment materials.

SGM[1]	Parameter	Notation	Unit	Value
Water-saturated debris	Bulk density	ρ_s	kg/m^3	2010
	Cohesion coefficient	c_s	Pa	0
	Internal friction angle	φ_s	°	25
	Kinematic viscosity	υ_s	m^2/s	0.001
	Porosity	n_s	/	0.45
Bed sediment	Bulk density	ρ_b	kg/m^3	1650
	Cohesion coefficient	c_b	Pa	1
	Internal friction angle	φ_b	°	40
	Kinematic viscosity	υ_b	m^2/s	0.002
	Porosity[2]	n_b	/	0.40
	Water content	n_w	/	0.15-0.28
	Bulk modulus of water	K	Pa	2×10^9
	Hydraulic permeability	k	m^2	10^{-8}

[1] Both layers are mixture of 56% gravel, 37% sand, 7% mud grains (referred to as SGM) and water, varying in saturation levels (Iverson et al. 2010).

[2] Porosity in the bed-sediment reduced to around 0.4 due to observed settlements during wetting, but instability in the wet beds hindered further resampling after sprinkling (Iverson et al. 2011).

A total of 163 experiments were conducted by the USGS from 1992 to 2017 (Logan and Iverson 2007), of which Iverson et al. (2011) report the notable results with different bed-sediment volumetric water content. In these experiments, 6 m^3

of water-saturated source material is discharged from a headgate and flows across beds that are partially saturated, with an average thickness of 12 cm, extending from $x = 6$ m to 53 m ($x = 0$ refers to the headgate position). As illustrated in Figure. 4.5b, the geometric model, constructed to mirror the experimental setup, includes numerical gauges (Bonallo 2015) at equivalent locations ($x = 32$, 66 m) to capture the instantaneous variations in flow depth and pressure. Table 4.2 presents the property parameters, primarily derived from measurements. The experiments to be verified involve seven control groups: five groups conducted on beds with n_w uniformly ranging from 0.15 to 0.28, and two groups conducted on non-erodible, bare beds. The baseline data for each group utilized in the quantitative analysis are listed in Table 4.3.

Table 4.3 Baseline data for the USGS experiments (Iverson et al. 2011).

Test No.	Sediment water content	Normalized speed (S)[1]	Normalized volume (V)[2]	Flow-front runout (m)	Normalized momentum gain (Γ)[3]
A	0.28±0.041	1.30	3.05	113.5	0.357
C	0.253±0.047	1.16	2.27	107.5	1.121
F	0.220±0.031	0.60	1.52	101.7	0.910
G	0.183±0.026	0.83	1.35	99.2	2.629
H	0.148±0.030	0.23	1.55	83.7	3.965
I	/	/	/	92.9	/
J	/	/	/	93.7	/

[1] The normalized speed is defined as the ratio of the flow-front speed measured between x=60-70 m to the corresponding bare-bed value (9.8 m/s).

[2] The normalized volume, denoted as $V = V_{\text{total}} / V_{\text{initial}}$, is defined where V_{total} and V_{initial} refer to the post-entrainment and source volumes (6 m^3), respectively.

[3] The normalized gain factor is defined as $P = VS$.

In the SPH scheme, source materials and sediments are discretized into a substantial number of particles to ensure a minimal inter-particle distance, which is crucial for capturing the behavior of bed-sediment entrainment. Table 4.4 summarizes the dynamic simulation and rheological parameters involved.

Simulations are conducted on a NVIDIA RTX A6000 device using GPU-based code, while the Intel(R) Xeon(R) W-2225 @ 4.10GHz is employed for the CPU-based algorithm.

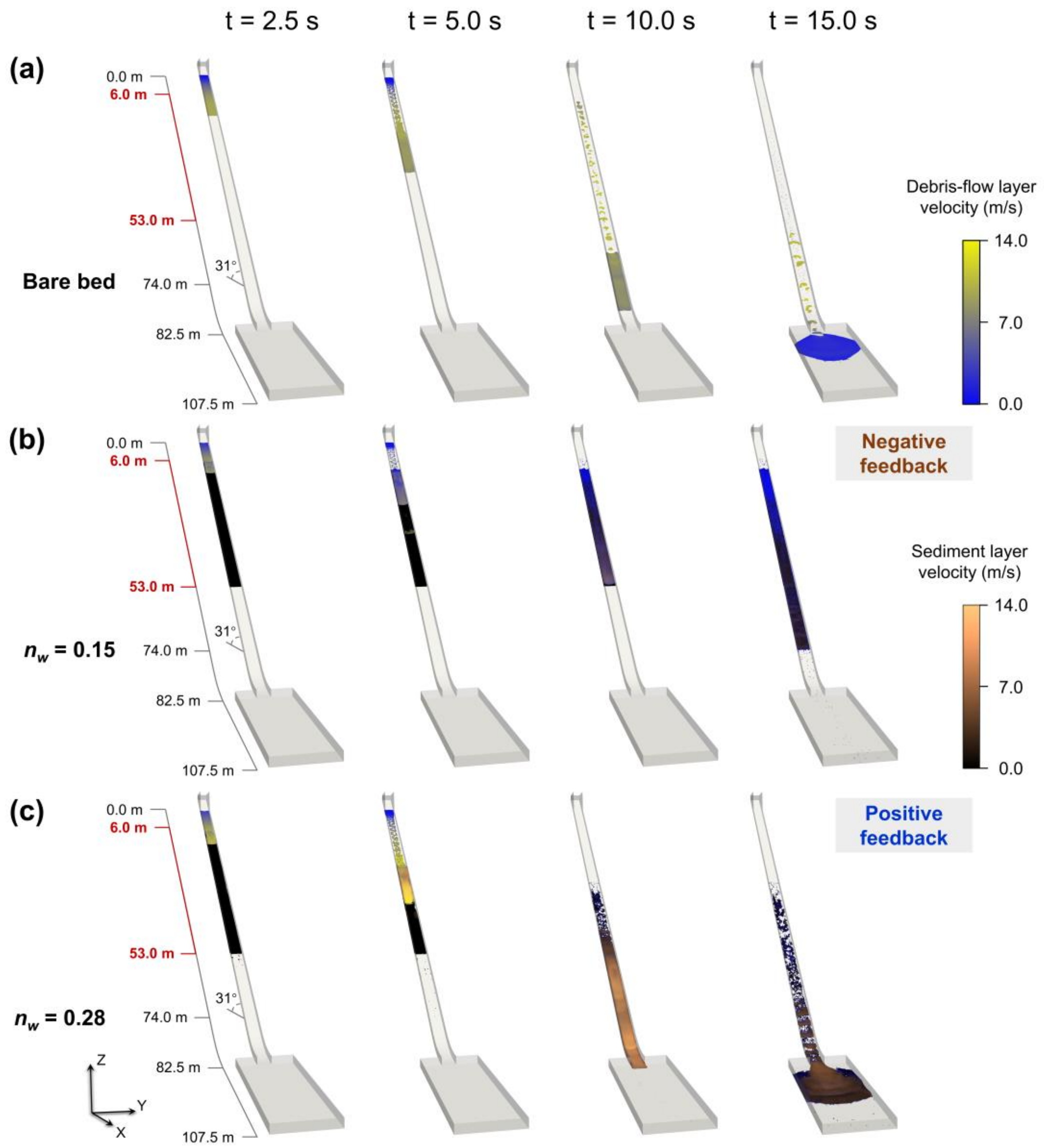

Figure 4.6 Snapshots of the simulated USGS entrainment experiments at different instants. (a) Debris flow on a bare, no-erodible bed; (b) debris flow on an erodible bed with $n_w = 0.15$; (c) debris flow on an erodible bed with $n_w = 0.28$.

A comparative analysis of the time-elapsed simulation results for the bare beds (I, J), the wettest bed (A with $n_w = 0.28$), and the driest bed (H with $n_w = 0.15$) highlights the mechanisms by which n_w influenced mobility and mass change

(Figure 4.6). Compared to the bare-bed cases, both erodible groups gain additional volume from bed-sediment entrainment, with flow A visibly entraining more material and exhibiting higher mobility than flow G. Indeed, as the flow fronts begin to move beyond the sediment beds, their acceleration universally diminishes, and subsequent discrepancies in erosion patterns emerge. Flows encountering the wettest beds behave similarly to mass movements, characterized by progressive slab-by-slab failures (Iverson et al. 2011; Zheng et al. 2021; Zheng et al. 2023), as their depths and levels of agitation rise rapidly. By contrast, in the latter part of the dry-bed flow, the capacity to entrain material significantly weakens, transitioning to progressive grain-by-grain scouring. These findings align with the results and trends observed in the experiments (Logan and Iverson 2007).

Table 4.4 Rheological and SPH parameters in the dynamic simulation.

Parameter	Notation	Unit	Value
Key coefficients of HBP rheology[1]	m	/	100
	n	/	0.95
Particle distance	dp	m	0.025
Number of debris-flow particles	N_f	/	361,040
Number of sediment particles	N_s	/	761,179
Number of boundary particles	N_b	/	1,259,480
Debris-flow duration	t	s	20
Sound speed coefficient	ξ	/	20
EoS constant	γ	/	7
Density diffusion coefficient	δ_d	/	0.1
CFL coefficient[2]	CFL	/	0.1

[1] The values of the rheological coefficients are derived from the fitting results recommended by Han et al. (2020), with the debris-flow mixture being considered as a shear-thinning material.
[2] The Symplectic scheme is utilized for time integration.

Furthermore, the accuracy of the velocity simulation is verified by comparing time series data of the flow-front position. As depicted in Figure 4.7. The simulation results precisely reproduce the propagation data. However, the velocity in the dry-bed group exhibited premature decay within the entrainment section, only to gradually realign upon entering the bare bed section. This discrepancy can be partially attributed to the neglect of matrix suction effects between pore air and pore fluid, potentially leading to an overestimation of pore water pressure in sediments with lower water content.

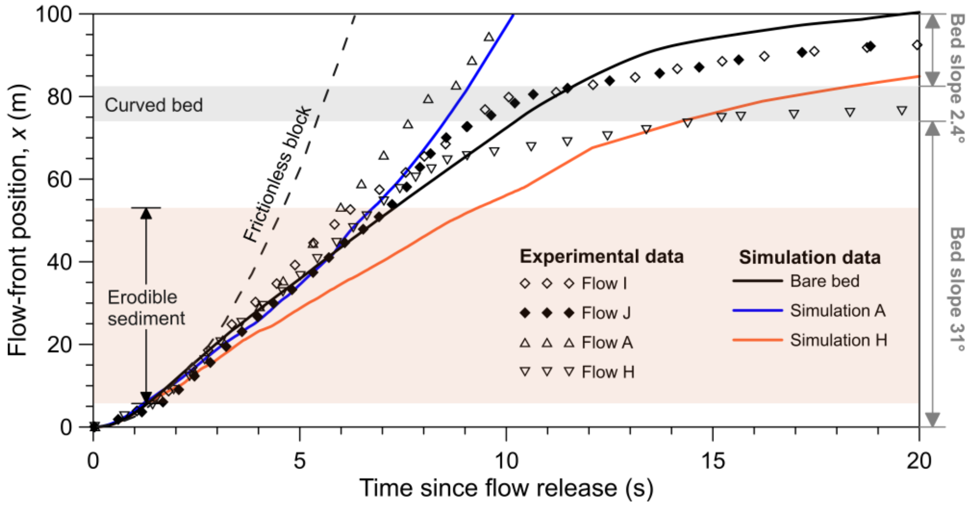

Figure 4.7 Comparison of the flow-front position over time between experimental and simulation results.

4.4.2.2. Momentum growth and feedback analysis:

To characterize the effect of the volumetric water content of bed-sediment on flow momentum, Iverson et al. (2011) introduced three normalized coefficients as proxies for overall flow dynamics, as detailed in Table 4.2. The normalized volume in the SPH simulation is defined as $V = n_{total} / n_{initial}$, where n_{total} denotes the total number of post-entrainment particles, and $n_{initial}$ refers to the source particles. For all simulations, the only variable is the volumetric water content, and the results are rigorously compared with experimental data. As illustrated in Figure 4.8, both experimental and simulation results indicate that the normalized flow-front speed (S), volume (V), and momentum gain (P) generally increase with rising volumetric water content. Compared with the regression curve, the simulated growth of S is slightly smaller than that observed in the experimental results (Figure 4.8a). Examination of the video recordings (Logan and Iverson 2007) reveals that the formation of lateral levees and channelized flow may influence flow dynamics. Specifically, both the run-out distance and speed are enhanced because the coarse-grained borders prevent lateral spreading, and the channel, primarily consisting of finer grains, exhibits lower friction. As such, we speculate that the absence of a polydispersity mechanism is the primary reason for this discrepancy. By contrast, the simulated volume growth is higher than that measured in the field (Figure 4.8b), particularly under wetter bed conditions.

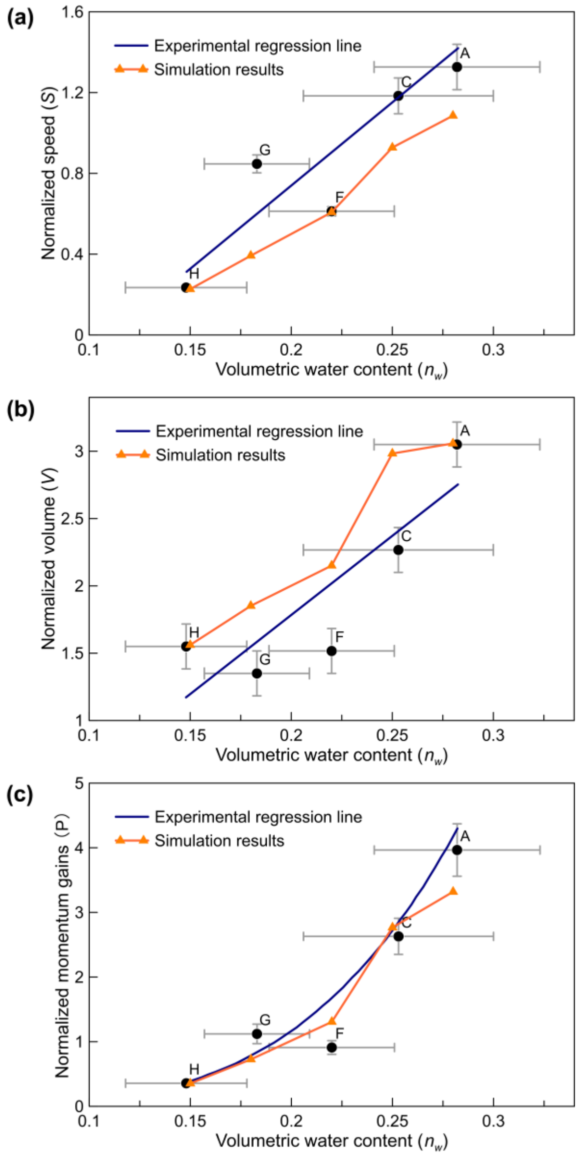

Figure 4.8 Effects of varying bed water content on the normalized values. (a) Normalized flow-front speeds (S), (b) normalized flow volumes (V), (c) normalized momentum gains (P). Error bars represent cumulative measurement uncertainties for V (< 1 m3), S (< 0.06 s transit from *x* = 60 to 70 m), and *P* (determined by propagating errors from *S* and *V*). Further details are available in Iverson et al. (2011).

The momentum growth and feedbacks from entrainment are quantified by the normalized momentum gain factor *P*. This proxy effectively demonstrates the comprehensive impact of bed moisture content on flow mobility and volume expansion. Here *P*>1 indicates a momentum gain, whereas *P*<1 denotes a momentum loss compared to the reference state observed in bare-bed groups (I, J). As depicted in Figure 4.8c, the outcomes of the simulation closely align with the experimental findings. Specifically, the momentum gains are positive in all experiments when $n_w > 0.18$. In contrast, this feedback is negative in the drier groups, where the flows are retarded. Despite the momentum growth in Group A being lower than that observed experimentally, this discrepancy can also be attributed to the propagation of errors in the normalized speed. It is worth noting that although the excessive volume somewhat mitigates the impact of speed errors, our simulation results still numerically confirm the decisive role of pore pressures in reducing shear strength and promoting flow-momentum growth.

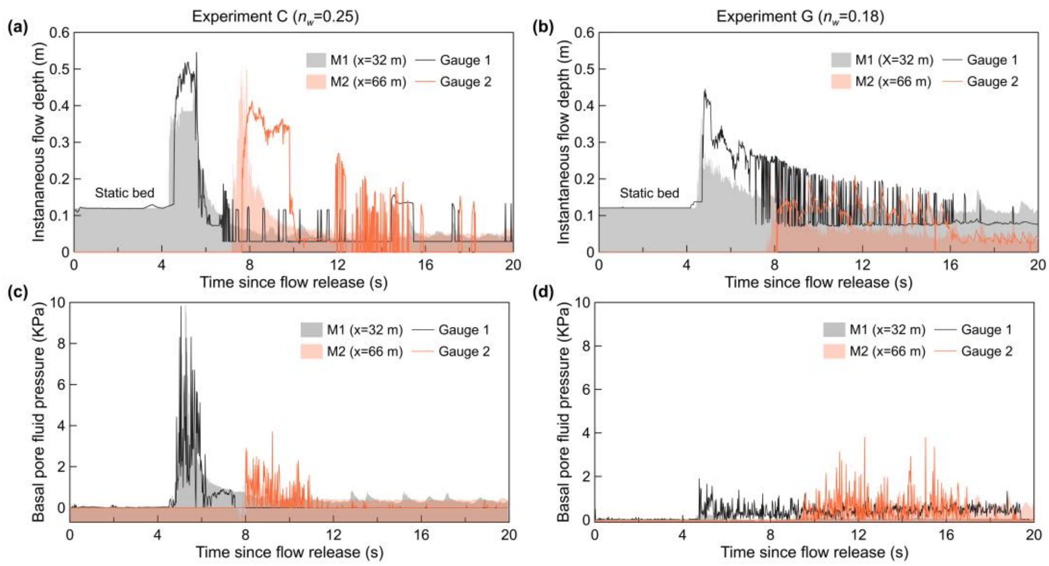

Figure 4.9 Comparison of the time-series data between numerical gauges and experiments (C and G) at x=32 and 66 m. (a)-(b) Variation in the flow thickness, (c)-(d) variation in the basal pore fluid pressure.

Figure 4.9 compares the simulated results and sensor data for relatively wet (C with $n_w = 0.25$) and dry-bed (G with $n_w = 0.18$) conditions. Here, Figures 4.9a and 4.9b demonstrate that our results successfully reproduce the time series evolutions in flow depth at the entrainment section (x=32 m) and bare bed section (x=66 m), where both the measured and simulated data show a deeper and faster flow in wet-bed scenario. Consistent with previous findings, both groups in the SPH simulations eroded more material, resulting in deeper flow thickness. Moreover, the response of basal pore pressure behave sharply as the flow front arrives, and to some extent, it is proportional to the flow depth, as illustrated in Figures 4.9c and 4.9d. We also notice that the simulated pore pressure response in flow G is more pronounced than that observed experimentally. Another discrepancy occurs during the duration of the trailing flow, where the simulated pore pressure response in flow C is consistently smaller than the measured value and approaches nearly zero (Figure 4.9c). It appears that the insufficient material supply is the dominant factor, and reducing the particle distance can partially ameliorate this issue. However, this treatment also necessitates a dramatic increase in computational consumption.

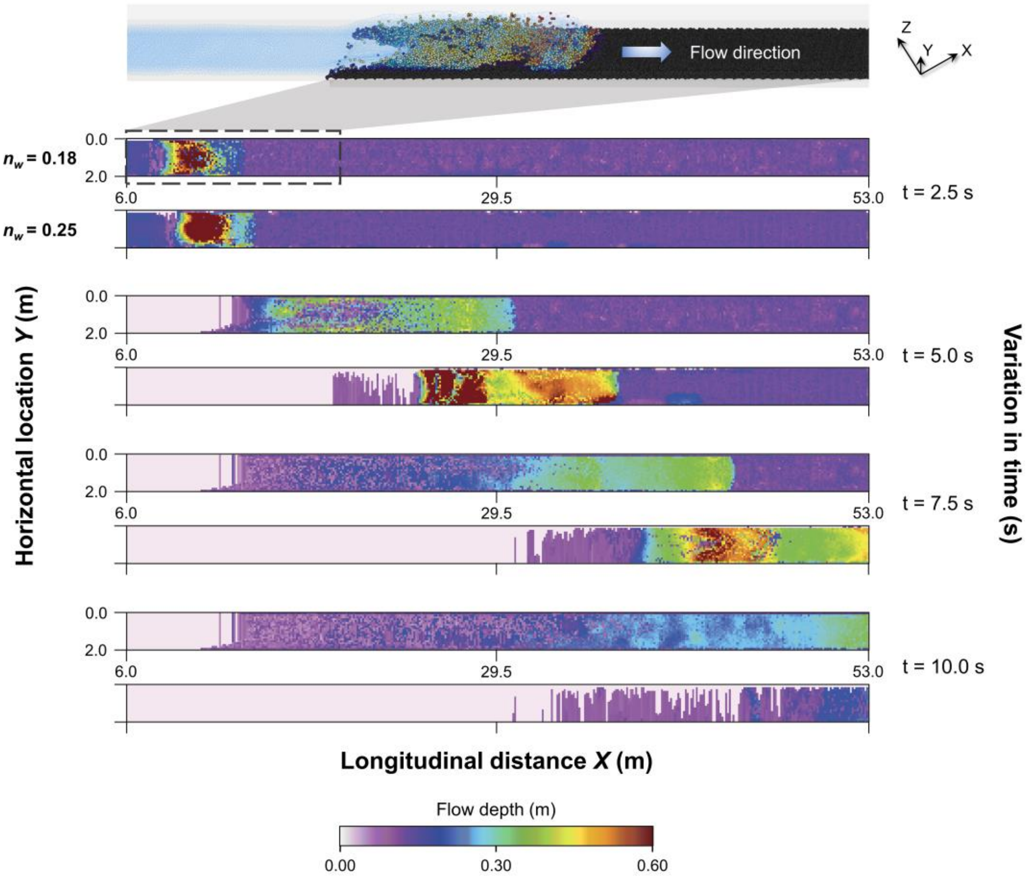

Figure 4.10 Temporal variation in flow depth illustrated through spatial distribution. The resolution of the cloud map is 0.10 m.

A plot of the spatiotemporal evolution of flow depth in the entrainment section is presented in Figure 4.10, where comparisons between flows C and G further highlight that the growth of flow velocity and mass entrainment in debris flows highly depends on the bed-water content. The snapshot from the particle simulation in Figure 4.10 illustrates that the progressive entrainment of sediments initiates in the center of the channel and gradually extends toward the sidewalls with a typically bulbous front forming at the flow head. Five seconds later, the front of flow C, which was flowing through a wetter bed, had evidently surpassed flow G and subsequently scoured away most of the material from the channel bed. Additionally, differences in density and rheological parameters, along with inertia, cause the entrained material to lag behind the wave front at an early stage. For flow C, this resistance effect transforms into a push from behind once the pore pressure rises to levels almost sufficient to liquefy the bed.

4.4.2.3. Depositional morphology:

This study qualitatively reproduces the levee-channel deposits of self-channeling flows without considering the strong coupling effect or polydispersity, as shown in Figure 4.11. Mangeney et al. (2007) also reported similar findings using a depth-averaged model based on the $\mu(I)$ rheology. despite extensive research (e.g., Johnson et al. 2012; Kokelaar et al. 2014; Pudasaini and Mergili 2019; Pudasaini and Fischer 2020) substantiating the significant role of polydispersity-related segregation processes on the depositional morphology of geophysical flows. In the TLMP SPH model, the quasi-static shoulders are generated behind the flow-front by the rotation of the velocity field, which results from the balance between gravity, pressure gradient, and boundary stress. Our results also suggest that variations in pore water content can influence the segregation process, as depicted in Figure 4.11b. Indeed, reduced stability of the lateral levees, along with an increase in the width of the central channel and a decrease in thickness, is evident as excess pore water pressure grows. Additionally, parameters such as particle distance, internal friction angle, and density gradient could affect the levee-channel morphology. On the other hand, the presence of a viscous fluid may decrease the permeability of the inner flow, potentially enhancing the retention of pore pressure and thus increasing flow mobility (Delannay et al. 2017).

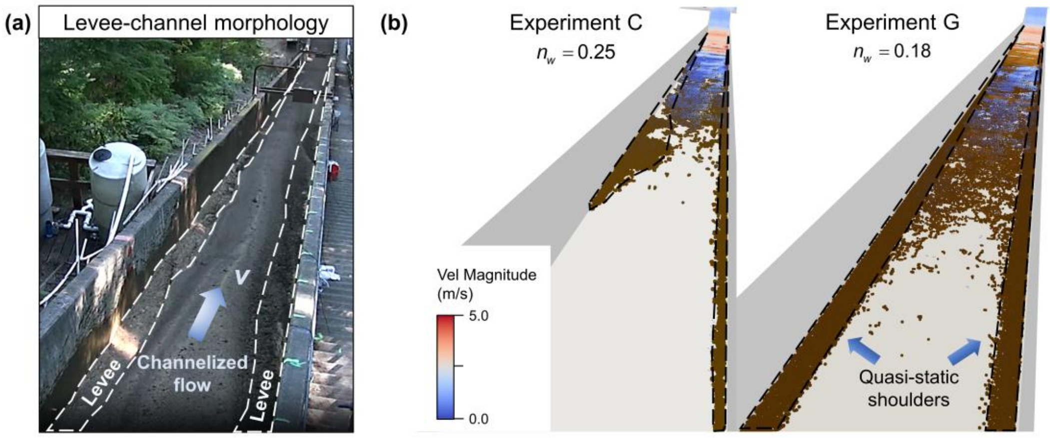

Figure 4.11 Reproduce the lateral levee morphology in the entrainment section of self-channeling flows. (a) On-site channel photo modified from McArdell et al. (2007), (b) the simulated levee-channel deposit with different water content.

The limitations of particle-scale homogenization are clearly evidenced by the deposition patterns observed on the runout pad, as depicted in Figure 4.12. After debouching at the flume mouth, the sediments fail to form effective embankments (Figure 4.12b) necessary to constrain the lateral expansion of channelized flow, due to the absence of sorting and separation mechanisms. A recent study by Pudasaini and Fischer (2020) incorporated a new phase-separation mechanism into their two-phase depth-averaged model, successfully quantifying the solid- and liquid-phase segregation processes. However, in the three-dimensional SPH paradigm, the resolution adaptive adjustment and boundary handling involved in multi-scale modelling significantly increase the computational cost (Violeau and Rogers 2016). Moreover, multi-scale particle coupling encounters numerous challenges, such as numerical stability and physical consistency. Nevertheless, a robust coupling model that integrates multi-scale grains and fluid constituents, as well as their interactions, is essential to further delineate the physical processes and accurately simulate the segregation processes in debris flows.

As outlined earlier, the feasibility of the proposed pore pressure algorithm for a wet erodible bed hinges on the validity of the assumptions made. Notably, disregarding matric suction and capillarity could lead to noticeable errors when the bed-water content is insufficient. In such scenarios, the pore fluid likely becomes disconnected, unable to transmit pressure owing to the significant expulsion of pore air as the sediment is overridden (Iverson et al. 2011; Han et al. 2015). As such, Bishop's effective stress should be adopted in dryer beds to accurately predict the dynamic response and momentum gains. The data presented in Figures 4.9c and 4.9d also indicate partially negative pore pressure values prior to the arrival of the debris-flow front, which our current method cannot reproduce. However, debris-flow paths typically feature wet beds, and sufficient precipitation is the primary trigger for initiating these flows (Mondini et al. 2023). Therefore, the prerequisites of quasi-saturated beds and positive feedback from pore pressures are rational for most practical applications.

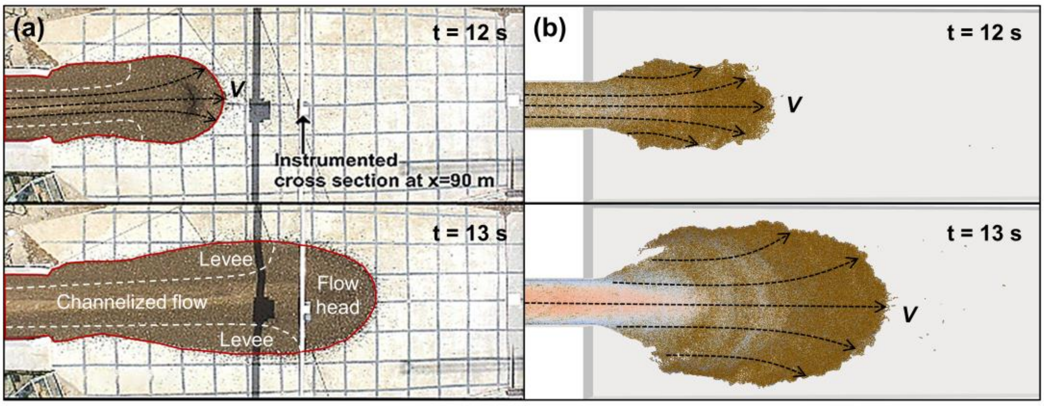

Figure 4.12 Depositional morphology of the USGS flume experiments (background image modified from (Iverson et al. 2010)). (b) The simulated deposits form on runout pad with $n_w = 0.25$.

This work further underscores the significance of bed sediment wetness and establishes a clear link among volumetric water content, the diffusion term, and the pore pressure response. In addition, recent findings suggest that other phenomena such as air pressure, bed permeability (e.g., Zheng et al. 2023), and grain-size sorting (e.g., Pudasaini and Fischer 2020; Zheng et al. 2021) may also contribute to friction reduction during entrainment. Future research is necessary to more thoroughly investigate the effects of flow mass and momentum growth mechanisms and to develop a more refined pore pressure response model.

4.1. CONCLUSIONS

This chapter addresses a typical wet-bed erosional scenario, proposing a full three-dimensional, two-layer, multi-phase Smoothed Particle Hydrodynamics (TIMP-SPH) method to model the momentum growth and feedback effects. It captures the erosion-induced excessive volume and mobility changes during the dynamic process of debris flows. Specifically, an efficient hydro-poro-mechanics-based pore pressure algorithm is developed and integrated into the existing SPH numerical scheme to simulate the response patterns of pore pressure in quasi-saturated sediments. Specific findings are as follows:

(1) First, a pore water pressure response algorithm based on hydraulic and porous media mechanics is introduced. It is derived from the momentum conservation equation and integrated into the existing SPH framework. Furthermore, the algorithm is extended to unsaturated sediments, where the pore water pressure is sufficiently high to neglect the effects of matric suction or capillary forces. By utilizing the relationship between the volumetric strain rate and the bulk modulus of each phase in porous media materials, a relationship between pore water pressure and water content is established. Additionally, an advanced Laplacian model is employed to solve the second-order derivative terms, laying the foundation for understanding the momentum growth and sediment feedback in the dynamic process of debris flow erosion.

(2) To validate the proposed pore water pressure algorithm, we examine the pore pressure evolution in a small-scale two-layer erosive dam-break test. Specifically, we conduct dam-break scouring experiments with both pure water and dense granular flow, comparing the flow interface features of two different two-layer dam-break configurations. We analyze the evolution patterns of total pressure and pore water pressure in the sediment materials under the coverage and scouring of the upper mass column. The simulation results indicate that the pure water scouring mode resembles grain-by-grain surface erosion, with a relatively uniform total pressure distribution and rapid dissipation of pore water pressure. In contrast, the dense granular flow scouring mode is characterized by mass erosion, where the

scouring interface experiences significant compression, collision, and excavation. As a result, the velocity decreases more rapidly, and the pore pressure response is more intense and sustained. This response pattern is similar to the movement of debris flows over wet bed sediments.

(3) Finally, the proposed method is verified through a series of full-scale debris-flow entrainment experiments. Although several numerical studies have investigated these experiments, this research marks the first attempt to model the feedback effects of debris flows on beds of varying wetness within a fully three-dimensional Lagrangian paradigm. The simulation results accurately reproduce the experimental measurements, and the comparative analysis based on beds with varying water contents rigorously confirms the critical role of pore water pressure response. It underscores the positive feedback from EEDPs of debris flows on sufficiently wet beds, as well as the promotional effect of this mechanism on flow mobility and volume expansion. Another highlight of this study is the capability to reproduce levee-channel morphology without the need to consider strong-phase coupling and polydispersity. The presented TLMP-SPH model achieves a paradigm shift to better understand and predict debris-flow hazards from a particulate perspective.

REFERENCES

Asai, M., Fujioka, S., Saeki, Y., Morikawa, D.S., Tsuji, K.J.C.M.i.A.M. & Engineering. 2023. A class of second-derivatives in the Smoothed Particle Hydrodynamics with 2nd-order accuracy and its application to incompressible flow simulations. Computer Methods in Applied Mechanics and Engineering 415, 116203.

Bonallo, R.J.M.s.T., Imperial College London. 2015. Post Processing Techniques for Smoothed Particle Hydrodynamics. Master's Thesis.

Brookshaw, L. 1985. A method of calculating radiative heat diffusion in particle simulations. Publications of the Astronomical Society of Australia 6(2), 207-210.

Bui, H. & Fukagawa, R. 2009. A first attempt to solve soil-water coupled problem by SPH. Terra Mech 29, 33-38.

Bui, H.H. & Fukagawa, R. 2013. An improved SPH method for saturated soils and its application to investigate the mechanisms of embankment failure: Case of hydrostatic pore-water pressure. International Journal for numerical and analytical methods in geomechanics 37(1), 31-50.

Cascini, L., Cuomo, S., Pastor, M. & Rendina, I. 2016. SPH-FDM propagation and pore water pressure modelling for debris flows in flume tests. Engineering Geology 213, 74-83.

Chen, X., Leung, Y.F., Mori, H., Uchida, S. & Takumi, K. 2024. Single-layer soil-water coupled SPH method and its application to sinkhole simulation. Acta Geotechnica 19(2), 991-1018.

Delannay, R., Valance, A., Mangeney, A., Roche, O. & Richard, P. 2017. Granular and particle-laden flows: from laboratory experiments to field observations. Journal of Physics D: Applied Physics 50(5), 053001.

Haas, T.d. & Woerkom, T.v. 2016. Bed scour by debris flows: experimental investigation of effects of debris-flow composition. Earth Surface Processes and Landforms 41(13), 1951-1966.

Han, Z., Chen, G., Li, Y., Tang, C., Xu, L., He, Y., Huang, X. & Wang, W. 2015.

Numerical simulation of debris-flow behavior incorporating a dynamic method for estimating the entrainment. Engineering geology 190, 52-64.

Han, Z., Su, B., Li, Y., Dou, J., Wang, W. & Zhao, L. 2020. Modeling the progressive entrainment of bed sediment by viscous debris flows using the three-dimensional SC-HBP-SPH method. Water Research 182, 116031.

Huang, Y., Zhang, W., Dai, Z. & Xu, Q. 2013. Numerical simulation of flow processes in liquefied soils using a soil–water-coupled smoothed particle hydrodynamics method. Natural Hazards 69, 809-827.

Iverson, R.M. 2012. Elementary theory of bed-sediment entrainment by debris flows and avalanches. Journal of Geophysical Research: Earth Surface 117(F3), F03006.

Iverson, R.M. 2015. Scaling and design of landslide and debris-flow experiments. Geomorphology 244, 9-20.

Iverson, R.M. & Denlinger, R.P. 2001. Flow of variably fluidized granular masses across three-dimensional terrain: 1. Coulomb mixture theory. Journal of Geophysical Research: Solid Earth 106(B1), 537-552.

Iverson, R.M., Logan, M., LaHusen, R.G. & Berti, M. 2010. The perfect debris flow? Aggregated results from 28 large-scale experiments. Journal of Geophysical Research: Earth Surface 115(F3).

Iverson, R.M., Reid, M.E., Logan, M., LaHusen, R.G., Godt, J.W. & Griswold, J.P. 2011. Positive feedback and momentum growth during debris-flow entrainment of wet bed sediment. Nature Geoscience 4(2), 116-121.

Jakob, M., Hungr, O. & Jakob, D.M. 2005. Debris-flow hazards and related phenomena. Berlin: Springer.

Johnson, C., Kokelaar, B., Iverson, R.M., Logan, M., LaHusen, R. & Gray, J. 2012. Grain-size segregation and levee formation in geophysical mass flows. Journal of Geophysical Research: Earth Surface 117(F1), F01032.

Kokelaar, B., Graham, R., Gray, J. & Vallance, J.W. 2014. Fine-grained linings of leveed channels facilitate runout of granular flows. Earth and Planetary Science Letters 385, 172-180.

Lian, Y., Bui, H.H., Nguyen, G.D., Tran, H.T. & Haque, A. 2021. A general SPH framework for transient seepage flows through unsaturated porous media considering anisotropic diffusion. Computer Methods in Applied Mechanics and Engineering 387, 114169.

Lian, Y., Bui, H.H., Nguyen, G.D., Zhao, S. & Haque, A. 2022. A computationally efficient SPH framework for unsaturated soils and its application to predicting the entire rainfall-induced slope failure process. Géotechnique, 1-19.

Logan, M. & Iverson, R.M. 2007. Video documentation of experiments at the USGS debris-flow flume 1992−2017 (ver 1.4, January 2018). US Geological Survey Open-File Report Report 2007-1335.

Mangeney, A., Bouchut, F., Thomas, N., Vilotte, J.-P. & Bristeau, M.-O. 2007. Numerical modeling of self-channeling granular flows and of their levee-channel deposits. Journal of Geophysical Research: Earth Surface 112(F2).

McArdell, B.W., Bartelt, P. & Kowalski, J. 2007. Field observations of basal forces and fluid pore pressure in a debris flow. Geophysical research letters 34(7), L07406.

Mondini, A.C., Guzzetti, F. & Melillo, M. 2023. Deep learning forecast of rainfall-induced shallow landslides. Nature communications 14(1), 2466.

Morikawa, D.S. & Asai, M. 2022. Soil-water strong coupled ISPH based on u− w− p formulation for large deformation problems. Computers and Geotechnics 142, 104570.

Pastor, M., Haddad, B., Sorbino, G., Cuomo, S. & Drempetic, V. 2009. A depth-integrated, coupled SPH model for flow-like landslides and related phenomena. International Journal for numerical and analytical methods in geomechanics 33(2), 143-172.

Pastor, M., Martin Stickle, M., Dutto, P., Mira, P., Fernández Merodo, J., Blanc, T., Sancho, S., Benítez, A.J.C.M. & Thermodynamics. 2015. A viscoplastic approach to the behaviour of fluidized geomaterials with application to fast landslides. Continuum Mechanics and Thermodynamics 27, 21-47.

Pastor, M., Yague, A., Stickle, M., Manzanal, D. & Mira, P. 2018. A two-phase SPH model for debris flow propagation. International Journal for Numerical and Analytical Methods in Geomechanics 42(3), 418-448.

Pietruszczak, S. & Pande, G. 1996. Constitutive relations for partially saturated soils containing gas inclusions. Journal of geotechnical engineering 122(1), 50-59.

Pudasaini, S.P. & Fischer, J.-T. 2020. A mechanical model for phase separation in debris flow. International Journal of Multiphase Flow 129, 103292.

Pudasaini, S.P. & Mergili, M. 2019. A multi-phase mass flow model. Journal of Geophysical Research: Earth Surface 124(12), 2920-2942.

Randles, P. & Libersky, L.D. 1996. Smoothed particle hydrodynamics: some recent improvements and applications. Computer methods in applied mechanics and engineering 139(1-4), 375-408.

Vicari, H., Ng, C.W., Nordal, S., Thakur, V., De Silva, W.R.K., Liu, H. & Choi, C.E. 2022a. The effects of upstream flexible barrier on the debris flow entrainment and impact dynamics on a terminal barrier. Canadian Geotechnical Journal 59(6), 1007-1019.

Vicari, H., Tran, Q.A., Nordal, S. & Thakur, V. 2022b. MPM modelling of debris flow entrainment and interaction with an upstream flexible barrier. Landslides 19(9), 2101-2115.

Violeau, D. & Rogers, B.D. 2016. Smoothed particle hydrodynamics (SPH) for free-surface flows: past, present and future. Journal of Hydraulic Research 54(1), 1-26.

Zhang, W., Maeda, K., Saito, H., Li, Z. & Huang, Y. 2016. Numerical analysis on seepage failures of dike due to water level-up and rainfall using a water–soil-coupled smoothed particle hydrodynamics model. Acta Geotechnica 11, 1401-1418.

Zhang, W., Zheng, H., Jiang, F., Wang, Z. & Gao, Y. 2019. Stability analysis of soil slope based on a water-soil-coupled and parallelized Smoothed Particle Hydrodynamics model. Computers and Geotechnics 108, 212-225.

Zheng, H., Shi, Z., Hanley, K.J., Zhou, Y. & Hu, X. 2023. Pore pressure evolution in bed sediment overridden by debris flow: A general formulation. Earth

Surface Processes and Landforms 48(6), 1188-1201.
Zheng, H., Shi, Z., Yu, S., Fan, X., Hanley, K.J. & Feng, S. 2021. Erosion mechanisms of debris flow on the sediment bed. Water Resources Research 57(12), e2021WR030707.

CHAPTER 5

MULTI-PHASE MODELLING OF DEBRIS FLOWS WITH LARGE BOULDERS BY COULPING HBP-SPH-DCDEM METHOD

5.1. INTRODUCTION

In geophysical flow dynamics simulations, mixed materials are often modeled and analyzed using continuum models such as the finite element method (FEM), finite volume method (FVM), depth-averaged method, and various particle methods. However, in many engineering applications, the solid bodies (i.e., gravel, cobbles, and boulders) are much larger than the smallest flow scales. This implies that the Reynolds numbers involved are very large, thereby allowing the viscous modes of momentum transfer to be neglected (Shu et al. 2011). In the first chapter, we have discussed in detail the material composition and classification of debris flows. To realistically reproduce the dynamic processes of actual disaster occurrences and design effective disaster prevention strategies and facilities, it is evident that relying solely on continuum models is insufficient. These models cannot accurately capture the complex coupling and phase transition mechanisms of multi-scale, multi-phase materials. This is particularly true in cases where debris flows carry large boulders, a common occurrence, where the diameters of these boulders can reach up to tens of meters, as shown in Figure 5.1. The presence of such large boulders significantly alters the flow dynamics of debris flows, greatly increasing their destructiveness and impact range, and thereby posing a tremendous threat to the safety of human lives and property in mountainous areas.

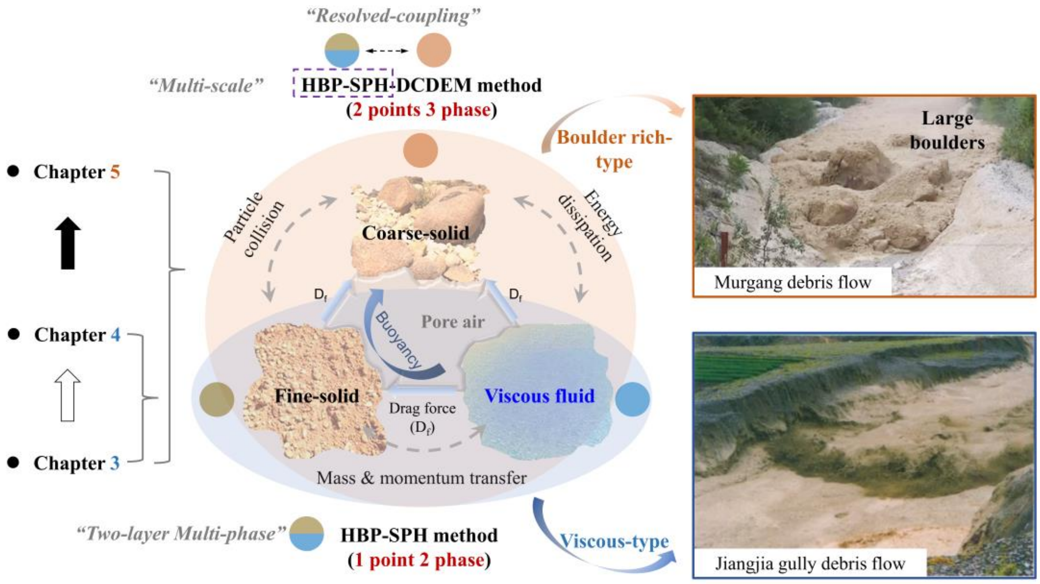

Figure 5.1 The material composition and physical mechanisms of viscous and stony debris flows correspond to the research methods employed in this study. The background figure is modified from Pudasaini and Mergili (2019), and the disaster image is from Zhao et al. (2020).

In the literature, various types of fine-grained sand and liquids are typically modeled using CFD models, which assume a given rheology and treat the solid-fluid mixture as a continuous medium. In contrast, irregular large boulders are usually modeled using discrete media models, with typical examples being the Discrete Element Method (DEM) and the Discontinuous Deformation Analysis (DDA) method (Shi 1992). Both methods are employed to simulate and analyze discontinuous media problems, such as fractured rock masses in geotechnical engineering and granular assemblies. They necessitate managing the contact forces and frictional interactions between blocks or particles. DEM is predicated on a particle model, typically utilizing explicit time-stepping methods to handle particle motion and interactions. Conversely, DDA is based on a block model, employing energy methods and the principle of minimum potential energy to address block motion and deformation. Overall, the advantage of DEM lies in its natural simulation of granular materials and complex contact conditions, making it suitable for studying granular flow and interactions between particles. On the other hand, the strength of DDA is its accurate handling of contact and friction between blocks, making it ideal for large-scale discontinuous deformation and steady-state analysis. Mikola and Sitar (2013) first proposed the coupled modeling method of SPH and DDA, applying it to simulate fluid-rock interactions (Mikola and Sitar 2014). This method has subsequently been widely adopted for analyzing geological hazards, rock mass stability, coastal and offshore engineering, and various other practical applications (e.g., Wang et al. 2019; Peng et al. 2020b; Peng et al. 2021b; Yu et al. 2022; Liang et al. 2023). Despite these advantages, DDA calculations entail complex contact detection and processing algorithms, and the structure of implicit integration results in significantly higher computational costs compared to DEM. This characteristic becomes even more pronounced in large-scale three-dimensional computations and various fluid-solid coupling engineering applications. Additionally, DDA encounters numerous challenges, including issues related to numerical stability and the modeling of complex, irregular blocks (Hatzor et al. 2017). Currently, most applications related to DDA are still confined to two-dimensional, small-scale cases. Although recent research has focused on parallel acceleration of DDA calculations (e.g., Song et al. 2017; Xiao et al. 2017; Peng et al. 2019; Peng et al. 2020a), the number of blocks that can be simultaneously computed still falls short of the magnitude required for some field scale disaster events.

Within particle-based paradigms, significant strides have been made toward the unification of solid and fluid modeling. Recently, attempts to couple SPH and DEM have become a research hotspot in the field of fluid-solid coupling analysis. Due to their complementary mechanisms in fluid-solid interactions (FSI) and the commonality of the particle framework, they can achieve FSI through the exchange of forces and momentum. Additionally, parallelization is highly efficient and easy to implement.

Initially, unresolved, one-way coupled models gained popularity in this area due to their relative ease of implementation and computational efficiency (e.g., Fernandez et al. 2011). Correspondingly, two-way coupling models must account for the mutual influences between fluids and solids. The motion and forces of the fluid affect the movement and deformation of the solid, while the movement and deformation of the solid, in turn, influence the motion and forces of the fluid. In debris flow transport, the significant interaction between solid particles and fluid necessitates two-way coupling models to accurately capture the momentum exchange between both phases. In this chapter, an efficient two-way coupling scheme is introduced to manage the complex interaction between non-Newtonian viscous flow and irregular polyhedral boulders (or debris) within a unified time framework.

5.2. SPH-DCDEM COUPLING METHOD AND BOULDER-RICH GRANULAR FLOW MODELLING

A major challenge in simulating fluid–solid interactions, especially with irregular shapes, lies in accurately monitoring complex interface contacts and efficiently solving multi-body collision forces in rigid body dynamics. Koshizuka et al. (1998) represented rigid bodies as clusters of Moving Particle Simulation (MPS) fluid particles, inherently rigidified. The particles within a rigid body had fixed relative positions and were treated as MPS particles by the fluid. This method has become the standard for resolved models due to its simplicity and elegance. In this regard, the distributed-contact discrete-element method (DCDEM) was introduced by Canelas et al. (2013) as an innovative fluid–solid interaction model, characterized by its reliance on a relatively few set of conceptual assumptions, akin to the approaches utilized by Zhang et al. (2009). Key innovations are introduced in the DualSPHysics code to address solid-fluid and solid-solid interactions by coupling the SPH-DCDEM approach (Crespo et al. 2015). This coupling scheme is a two-way, resolved model that avoids using ad hoc formulations for momentum exchanges between phases. It effectively describes the motion of arbitrarily shaped solids in viscous fluids without requiring special boundary treatments. In this approach, boundaries or particles of a rigid body treat other solid particles as DEM elements, building upon the distributed contacts concept introduced by Cummins and Cleary (2011). Canelas et al. (2016) implemented this method to address the multi-body contact collision problem, which was subsequently validated for granular-fluid flow, demonstrating a strong correlation with experimental data (Canelas et al. 2017). Further, Peng et al. (2021a) improved the SPH-DEM coupling algorithm by introducing a straightforward unified hybrid contact model, which yielded satisfactory results in simulating debris flows. Sun et al. (2023) incorporated an advanced contact collision detection method into the SPH-DCDEM coupling scheme, ensuring shape fidelity and significantly enhancing the accuracy of polyhedral collision simulations.

Previous studies have attempted to simulate geophysical flow consisted of multiphase and multiscale components using the SPH-DEM coupling method. However, these studies often describe the liquid phase simply as water, neglecting the viscous non-Newtonian fluid dynamics caused by the mixture of slurry and fine sand. In this study, we will, for the first time, describe the complex multiphase flow dynamics of debris flows by incorporating viscoplastic flow based on HBP-SPH and solid particle collision mechanisms based on DCDEM. In Chapter 2, we have already detailed the fundamental principles of the SPH and DEM methods. Therefore, here we will directly derive the two-way coupling process for solid-solid and solid-liquid interactions.

During the transport of debris flow and its impact on structures, we use the HBP-SPH-based non-Newtonian fluid model to simulate the behavior of viscous fluid particles and the DCDEM method to simulate the carried debris, boulders, and impacted structures. Based on the differing properties of interacting particle phases, the contact relationships can be categorized into three types: contact between fluid particles, contact between fluid particles and solid particles or boundaries, and contact between solid particles. The explicit integration common to both the SPH and DEM methods effectively ensures the mobility and compatibility of boundaries during fluid-solid interactions. The realized process of DEM-SPH coupling algorithm is illustrated in Figure 5.2. When dealing with irregular polyhedral, the basic theory is to decompose them into multiple simple geometries (e.g., spheres, cubes, ellipsoids). Each decomposed geometry is then used as a unit for searching interaction domains and determining contacts. Finally, the resultant forces on all geometries are integrated into a total force and torque, applied to the centroid of the complex structural block.

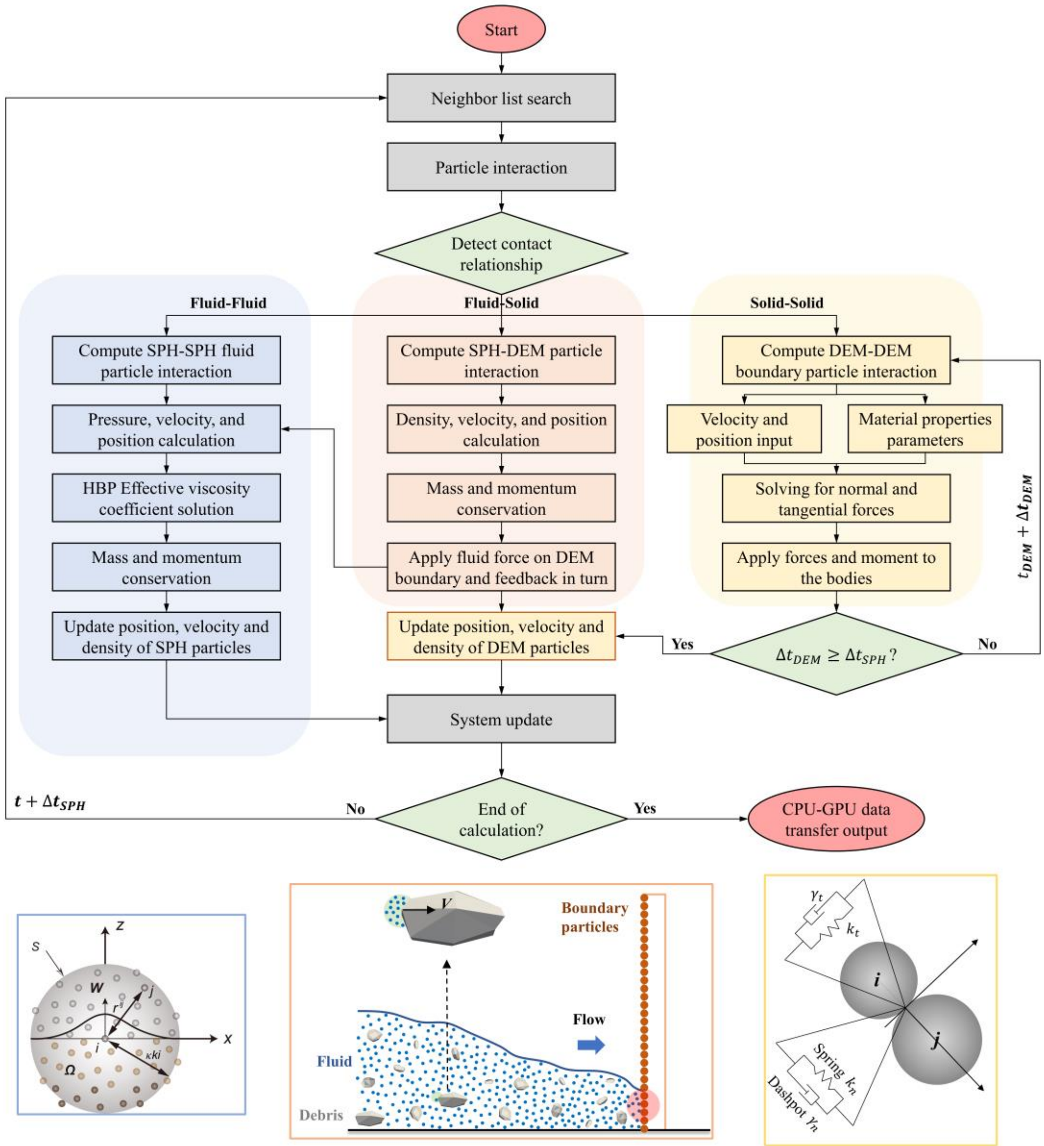

Figure 5.2 Flow chart of the two-way resolved coupling using the HBP-SPH-DCDEM approach.

This approach allows for solving the motion of the structural block and completing the contact interaction using the SPH-DEM method, thereby enabling the analysis of fluid-solid coupling problems. It is also important to note that the time step for the DEM module is typically much smaller than that for the fluid module. Therefore, it is necessary to nest the collision calculations of the solid blocks within each SPH loop until the time steps of both modules are synchronized. Only then can the positions, velocities, and other information of the SPH fluid particles and DEM solids be updated uniformly. Additionally, to maintain consistency between the calculation accuracy of SPH particles and DEM discrete elements, a consistent initial particle spacing value is typically used in the modeling of structural blocks.

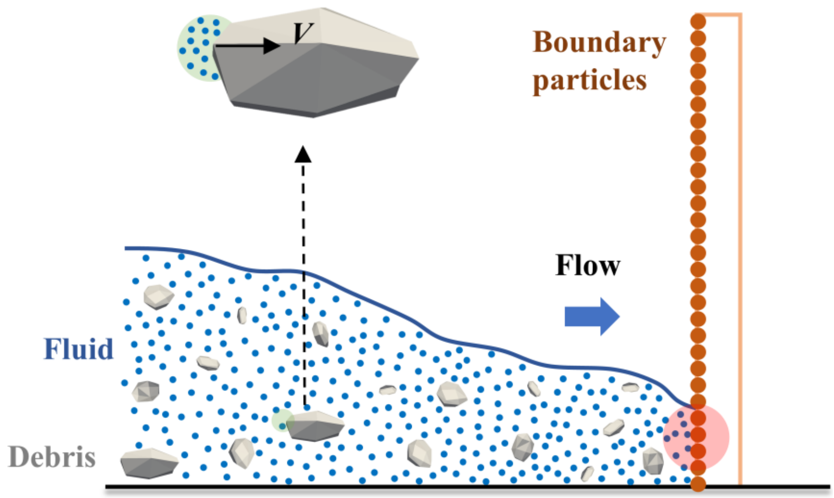

Figure 5.3 Schematic diagram of the multiphase coupling computational domain for debris flow, including fluid SPH particles and solid structure DEM particles.

Building on the fundamental principles of DEM presented in Chapter 2, herein we provide the equations of motion for structural blocks, including boundary DEM structures and debris or boulders carried by the debris flow. According to the Newton-Euler equations, the translational and rotational motion of block i are calculated as follows:

$$M_i \frac{dv_i}{dt} = \sum_{k \in i} m_k \frac{dv_k}{dt}, \tag{5.1}$$

$$I_i \frac{d\Omega_i}{dt} = \sum_{k \in i} m_k \left(r_k - R_i\right) \frac{dv_k}{dt}, \tag{5.2}$$

where M_i indicates the total mass of block i, v_i and I_i refer to the velocity and moment of inertial, respectively; Ω_i and R_i are the angular velocity and radius of the center of gravity, respectively. When particles enter the computational domain, the motion state of block i is determined by calculating the resultant force and resultant inertial torque acting on block i. It should be noted that the Symplectic integration scheme used in this study typically has an increment step size on the order of 10^{-5}, resulting in very small angular increments. For motion processes with relatively small macroscopic angular velocity, the translational motion of the block is updated first. Then, the rotation axis and angular velocity around that axis are calculated to complete the block's motion process.

To prevent SPH particles from penetrating DEM block particles, dynamic boundary conditions (DBC) can be simply applied at the boundaries in fluid-solid coupling to provide sufficient repulsive force. The type of interaction is determined based on the different marker values assigned to solid particles and fluid particles in the modeling process, as illustrated in Figure 5.2. As previously mentioned, the SPH-DCDEM fluid-solid coupling simulation essentially involves integrating the forces exerted by fluid particles on the surfaces of the blocks to represent the interaction between SPH particles and DEM particles. As detailed in Figure 5.3, The force exerted by the solid DEM on fluid particles is equal to inserting the particles on the surface of the solid DEM into the computational domain of the fluid particles as neighboring particles.

According to Newton's third law of motion, equal and opposite interaction forces exist between the SPH fluid particles and the boundary particles on the surface of the DEM block. Based on the control equations of SPH approximation and momentum equations, the interaction force between each phase can be derived as follows:

$$\frac{\partial v_{ib}}{\partial t} = -m_b \left(\frac{p_i^{\alpha\beta}}{\rho_i^2} + \frac{p_b^{\alpha\beta}}{\rho_b^2} \right) \frac{\partial W_{ib}}{\partial x_i^{\beta}} + f^{\alpha}, \tag{5.3}$$

$$F_{bi} = m_i \cdot m_b \left(\frac{p_i^{\alpha\beta}}{\rho_i^2} + \frac{p_b^{\alpha\beta}}{\rho_b^2} \right) \frac{\partial W_{ib}}{\partial x_i^{\beta}} + f^{\alpha}. \tag{5.4}$$

Here, Eq (5.3) represents the momentum equation for fluid particle i under the influence of DEM boundary particle b. Eq (5.4) represents the calculation of the resultant force on boundary particle b due to fluid particle i. Based on Eq (5.4), the resultant force on the boundary particle from the surrounding fluid particles can be expressed as follows:

$$F_b = \sum_{i \in b}^{N} F_{bi} \cdot m_b \left(\frac{p_i^{\alpha\beta}}{\rho_i^2} + \frac{p_b^{\alpha\beta}}{\rho_b^2} \right) \frac{\partial W_{ib}}{\partial x_i^\beta} + f^\alpha. \tag{5.5}$$

In the above equation, N represents the number of particles within the computational domain of boundary particle b. The interaction between the boundary particle and the fluid particles is illustrated in Figure 5.3. Based on the force acting on a single boundary particle, the resultant force and torque on the entire DEM block I can be derived:

$$F_I = \sum_{b \in I}^{M} F_b = \sum_{b \in I}^{M} \sum_{i \in b}^{N} F_{bi} \cdot m_b \left(\frac{p_i^{\alpha\beta}}{\rho_i^2} + \frac{p_b^{\alpha\beta}}{\rho_b^2} \right) \frac{\partial W_{ib}}{\partial x_i^\beta} + f^\alpha, \tag{5.6}$$

$$M_I = \sum_{b \in I}^{M} F_b d_{cb} = \sum_{b \in I}^{M} \left(\sum_{i \in b}^{N} F_{bi} \cdot m_b \left(\frac{p_i^{\alpha\beta}}{\rho_i^2} + \frac{p_b^{\alpha\beta}}{\rho_b^2} \right) \frac{\partial W_{ib}}{\partial x_i^\beta} \right). \tag{5.7}$$

where M represents the number of boundary particles on the surface of the DEM block; d_{cb} refers the vector from the boundary particle to the centroid of block I. It is worth noting that in the process of calculating the resultant torque for interface interactions, body forces do not generate torque.

5.3. Verification of SPH-DCDEM approach

5.3.1. Example 1: Aluminum cylinder collapse

To verify the proposed two-way coupling method, numerical analyses were performed on the collapse of multiple layers of solid aluminum cylinders. The experiment was initially conducted by Zhang et al. (2009) to validate a similar numerical scheme by coupling finite volume particle (FVP) method and DEM. Figure 5.4 illustrates the experimental setup and the corresponding numerical modeling. Solid aluminum cylinders, each with a density of 2.7 × 10^3 kg/m^3, a diameter of 1.0 cm, and a length of 9.9 cm, were initially stacked in multiple layers on the left side of an acrylic resin tank measuring 26 cm in length, 10 cm in width, and 26 cm in height. The layers were held in place by a removable plate located 6 cm from the tank's left wall. The number of layers, serving as an experimental parameter, varied between 6, 8, 10, and 12. Each layer consisted of five or six cylinders, alternately piled up. Upon the plate's rapid vertical removal, the layers began to collapse due to gravity, causing the cylinders to move towards the right wall of the tank. The transient collapse behavior was captured using a high-speed camera.

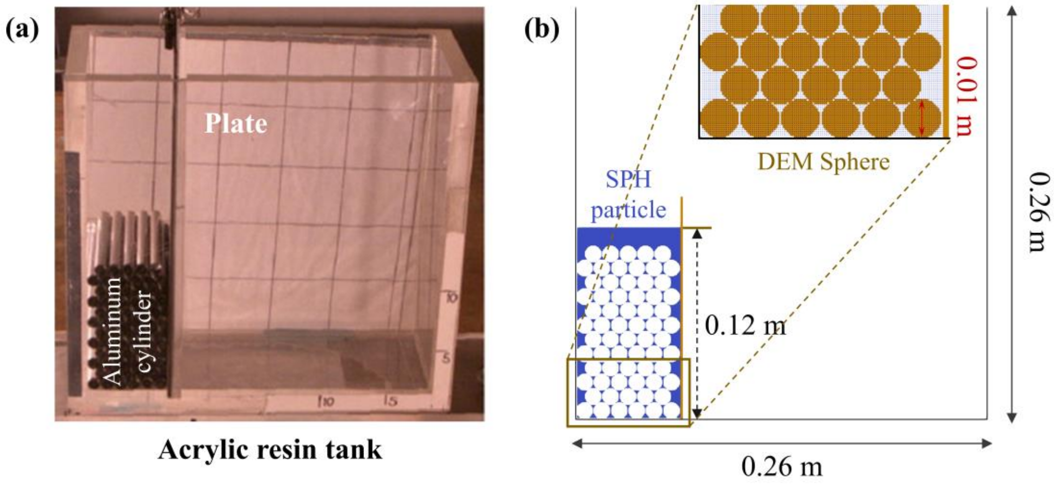

Figure 5.4 (a) The experimental setup for the collapse of aluminum cylinders, with the figure modified from Zhang et al. (2009). (b) SPH-DCDEM modelling of the fluid-cylinder system, which is composed of 12 layers.

The computations utilized aluminum for the cylinders, while PVC was assumed for the tank due to the wide variety of acrylic resin types. The configuration of material properties is based on the work by Canelas et al. (2016), with detailed parameters provided in Table 5.1. Nota that the DEM simulations for the collapse of solid cylinder were carried out in a two-dimensional framework, omitting the influence of the tank's front and back walls.

Table 5.1 Mechanical Characteristics of the aluminum cylinder and the acrylic resin tank.

	Material	E [GN m^{-2}]	υ [-]	μ_f [-]
Cylinders	Aluminum	69	0.30	0.45
Tank	PVC	3	0.30	0.45

Figure 5.5 illustrated the 2D DCDEM simulation results in the case of six-layer aluminum cylinders without fluid, compared with experimental data and FVP-DEM simulation results. To construct a sufficiently detailed model of the aluminum

cylinders, the initial spacing in the simulation was set to *dp*=0.0005 m, ensuring that each cylinder contained at least 20 particles across its diameter. It should be noted that the numerical solution must establish the equilibrium position of the cylinders by balancing gravitational and contact forces. Initially, forces are not included and are computed through small displacements using the DEM soft-body approach. Consequently, *t*=0.5 s marks the gate removal, which happens 1.0 s after the simulation starts.

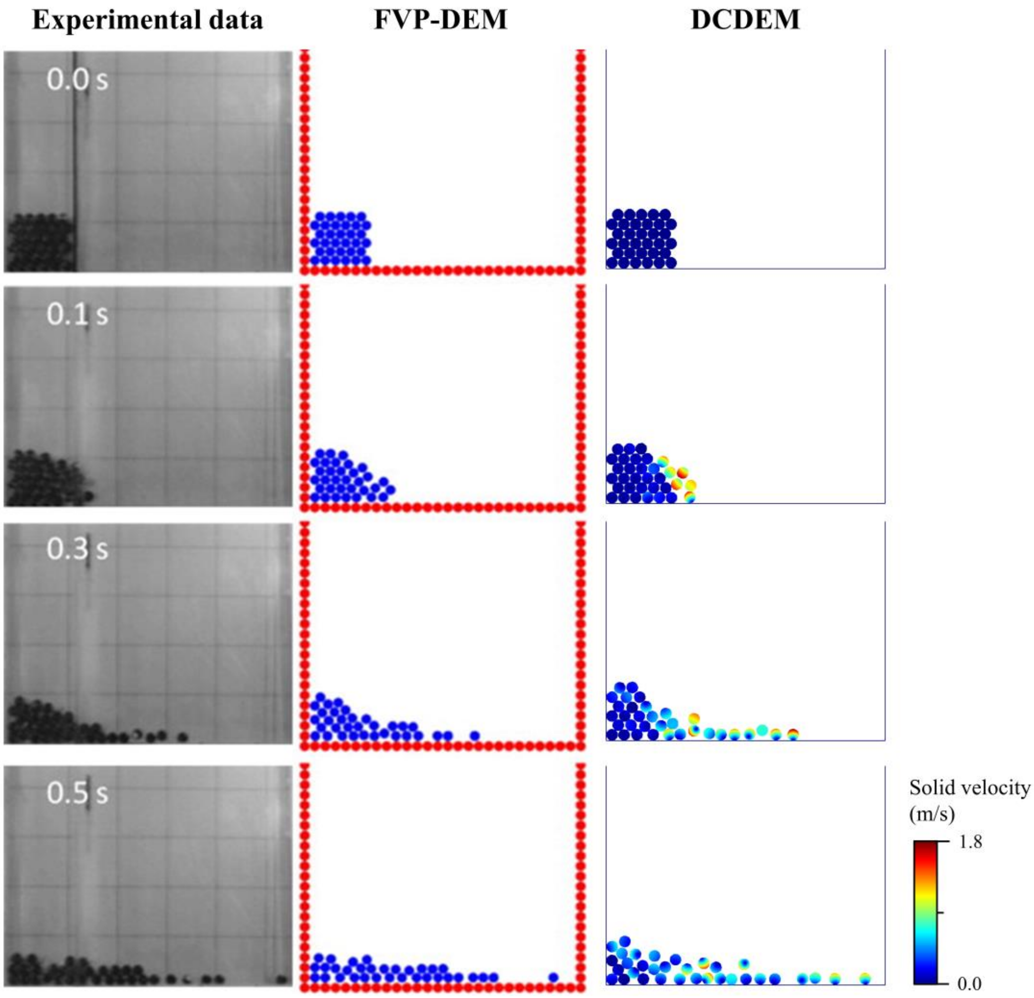

Figure 5.5 Comparison of the time series evolution of the collapse of six-layer aluminum cylinders, including experimental photographs and FVM-DEM simulation results adapted from Zhang et al. (2009).

Figure 5.5 indicates that the DCDEM model successfully reproduced the dynamic collapse process of the five-layer aluminum cylinders, particularly the collision timing of the fastest-moving cylinder with the right wall. Although the final pile shape of the cylinders differs slightly, the DCDEM simulation results show slightly more accumulation against the left wall compared to the experimental results.

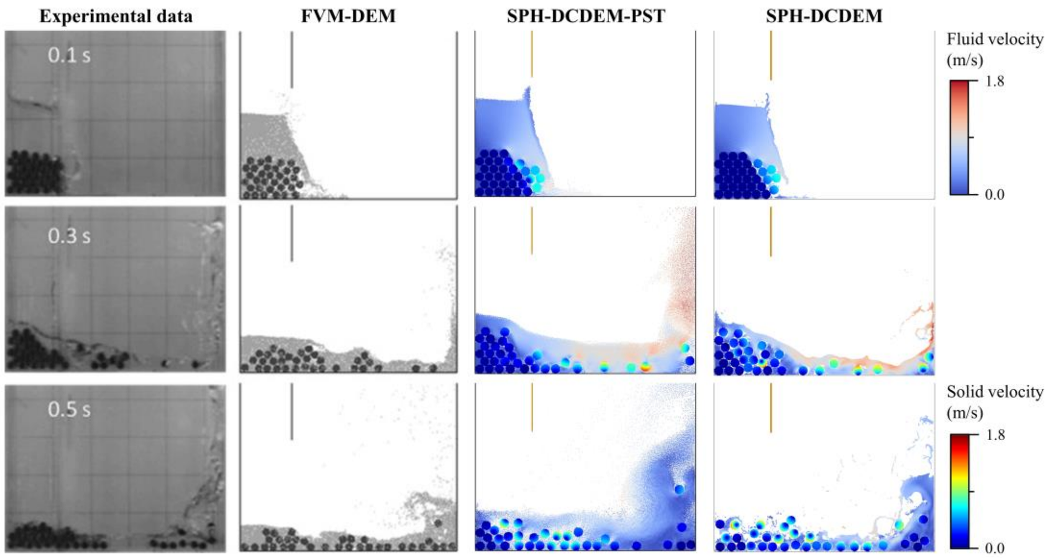

Figure 5.6 Comparison of the time series evolution in the water dam breakage with six-layer solid cylinders. From left to right: experimental results, FVM-DEM simulation results, SPH-DCDEM results with PST, and SPH-DCDEM results without PST.

The proposed two-way SPH-DCDEM coupling algorithm was subsequently validated using a solid-fluid dam break scenario involving multiple layers of solid cylinders. As shown in Figure 5.4b, the cylinder layers were submerged in water with a dam height of 12 cm. The experiment utilized 6, 8, 10, and 12 layers of cylinders. In the present dam-breaking simulations, the fluid is considered Newtonian with a dynamic viscosity of 10^{-3} m^2/s, and the material parameters of the cylinders were consistent with those used in the previous DEM simulation. The plate, modeled as a layer of moving boundary particles, was withdrawn vertically at a speed of 2.0 m/s. After the cylinders had settled in the water dam for 1.0 s, the simulation began to capture the breaking of the water dam involving the solid cylinder layers. In all simulations, we utilized the state-of-the-art density diffusion treatment (Fourtakas et al. 2020) for the weakly compressible SPH scheme applied to the fluid particles. The SPH-DCDEM solutions, both with and without the particle shifting technique (PST), are compared with experimental data and FVM-DEM results to determine the effects of solid-solid and solid-fluid interactions.

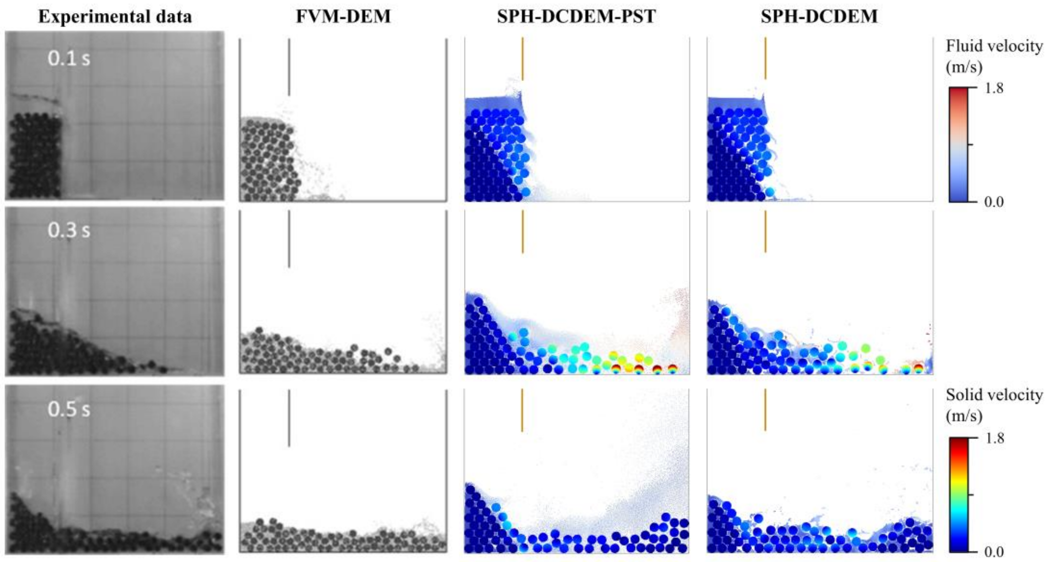

Figure 5.7 Comparison of the time series evolution in the water dam breakage with 12-layer solid cylinders. From left to right: experimental results, FVM-DEM simulation results, SPH-DCDEM results with PST, and SPH-DCDEM results without PST.

Figures 5.6 and 5.7 compare the transient behavior of water dam breakage between the simulation and experiment for cases with six- and twelve-cylinder layers, respectively. Compared with the FVM-DEM model, our model more accurately simulated the transient collision and piling behavior of the aluminum cylinders, especially after 0.5 seconds. The former model could not maintain the stability of the remaining cylinders against the left wall, whereas the SPH-DCDEM model successfully reproduced the trapezoidal piling shape following the dam break. It is evident that the simulations with the PST significantly differ from those without it. This difference seems reasonable because PST tends to move particles from high-concentration areas to low-concentration areas to maintain a relatively uniform particle distribution. In the simulations with PST, the aluminum cylinders are uniformly surrounded by particles, with minimal clustering or voids. However, this also causes PST to replenish particles at the front of the water column ruptured by the dam break, resulting in a cumulative effect over time steps that leads to a significantly higher number of fluid particles at the front edge than observed in the experiment, which is unrealistic. Nonetheless, the model with PST achieved a more stable flow field and piling shape due to the uniform particle distribution. Conversely, the simulation without PST achieved a transient piling shape that more closely matched the experiment.

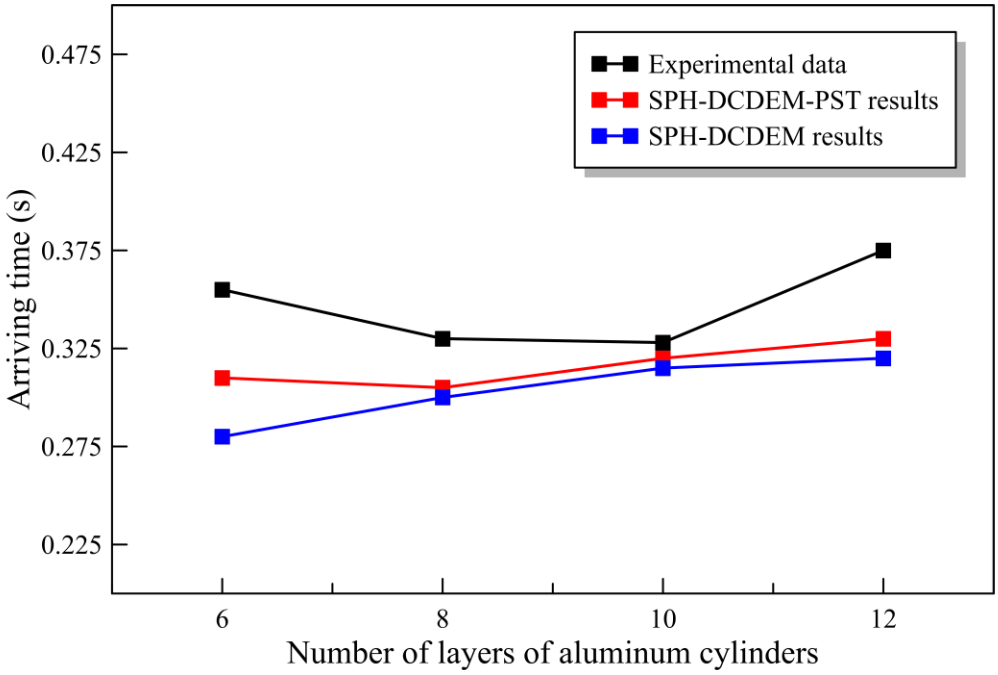

Figure 5.8 Comparison of arriving times between experimental data and SPH-DCDEM simulations with and without PST.

To compare the simulation accuracy, the time at which a cylinder first contacted the right wall of the tank was compared between the simulations and the experiments. As shown in Figure 5.8, the model considering PST achieved simulation results that more closely matched the experimental data. These simulation results suggest that the decision to use PST should depend on the research objective. If the aim is to study dynamic behaviors and variable evolution characteristics within the flow field, PST will evidently yield more accurate results. Additionally, further research should focus on sensitivity analysis of PST, examining how controlling the timestep displacement can better balance simulation accuracy and the true reproduction of dynamic behavior.

5.3.2. EXAMPLE 2: MASSIVE POLYHEDRAL STONE STACKING TEST

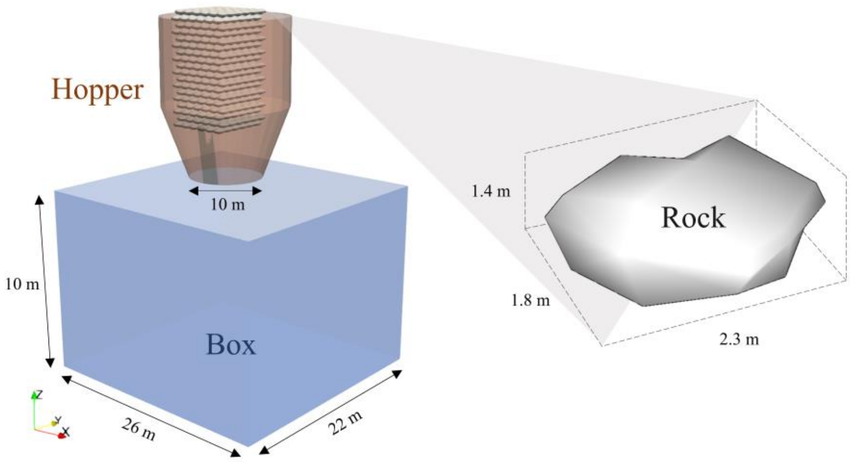

Figure 5.9 Configuration of the polyhedral stone stacking test.

In this section, a polyhedral stone stacking test is conducted to verify the stacking process of irregular DEM blocks and test their stability. As previously mentioned, the key to solving the resolved coupled model lies in how to handle the contact and determination of complex boundaries, as well as balancing simulation accuracy and computational cost. Here we follow the model of Canelas et al. (2017), which introduces a hopper-shaped device to gather and consistently release blocks. The model was initially designed to simulate the flow state of debris carried by floods and the accumulation characteristics under the action of a silt check dam. Thanks to the hopper's collecting effect, each sediment particle may undergo multiple contacts simultaneously. This simulation scenario not only consumes significant computational resources but also requires careful parameter adjustments to prevent system crashes.

Table 5.2 Mechanical Characteristics of the boulder grain and box.

	Material	E [GN m^{-2}]	υ [-]	μ_f [-]
boulder	Limestone	8	0.35	0.35
Tank	PVC	3	0.30	0.45
Hopper	PVC	3	0.3	0.45

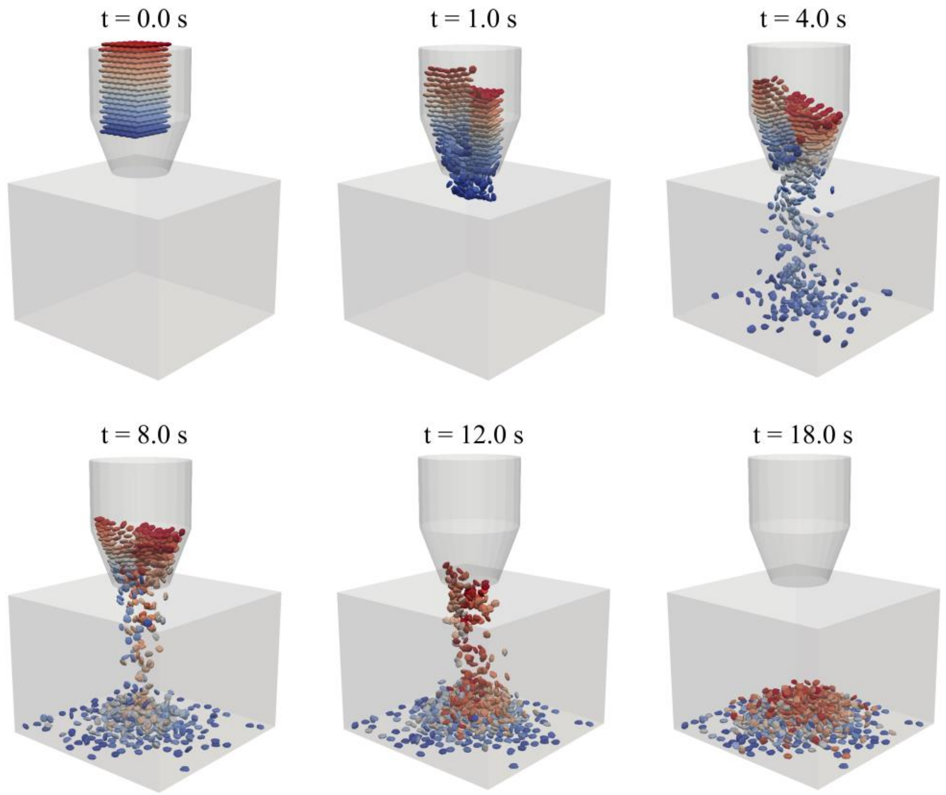

Figure 5.10 Snapshots of polyhedral stone stacking through a hopper device.

Figure 5.9 illustrates the configuration of the polyhedral stone stacking test. To ensure the proper introduction of solid material, a hopper was positioned on top of the box. Its dimensions were heuristically designed to guarantee a constant solid discharge. Compared to the sediment particles in the original experiment, we increased the particle size in the numerical experiment to match the debris flow carrying boulders discussed in Chapter 6. The boulder shape was derived from a three-dimensional model of a rock used in the experiments (Silva et al. 2016), as detailed in Figure 5.9. At the beginning of the simulation, the blocks are dispersed in the hopper and allowed to settle into their natural equilibrium positions. The mechanical properties of the material were based on the values for limestone, as listed in Table 5.2.

Figure 5.10 presents snapshots depicting the stacking of polyhedral stones within a hopper device. This simulation generated a total of 648 polyhedral blocks. Upon release, the stones swiftly congregate at the hopper's opening. The rapid and frequent collisions among the stones markedly reduce their descent speed. As the collisions among the stones and with the hopper boundary reach a critical threshold, the release speed of the stones gradually stabilizes. After 12 seconds, nearly all stones have been discharged into the tank, accumulating centrally to form a small pile. The simulation results demonstrate that this method can efficiently manage the massive collision processes of irregular blocks, establishing a foundation for subsequent field-scale simulations of debris flows containing large stones.

5.3.3. Example 3: Debris-flow impacting experiment

To validate the impact force and deposition morphology in the 3D SPH-HBP and SPH-HBP-DCDEM models, we simulated the laboratory test of debris-flow impact on check dams as conducted by Moriguchi et al. (2009). The experimental material was dry Toyoura fine sand. Specific gravity tests showed that the gravity of the solid phase was 2.65, and the sand grains were almost spherical. The physical laboratory experiments involved simulating debris flows at various slopes to measure the impact force applied to a fixed rigid wall.

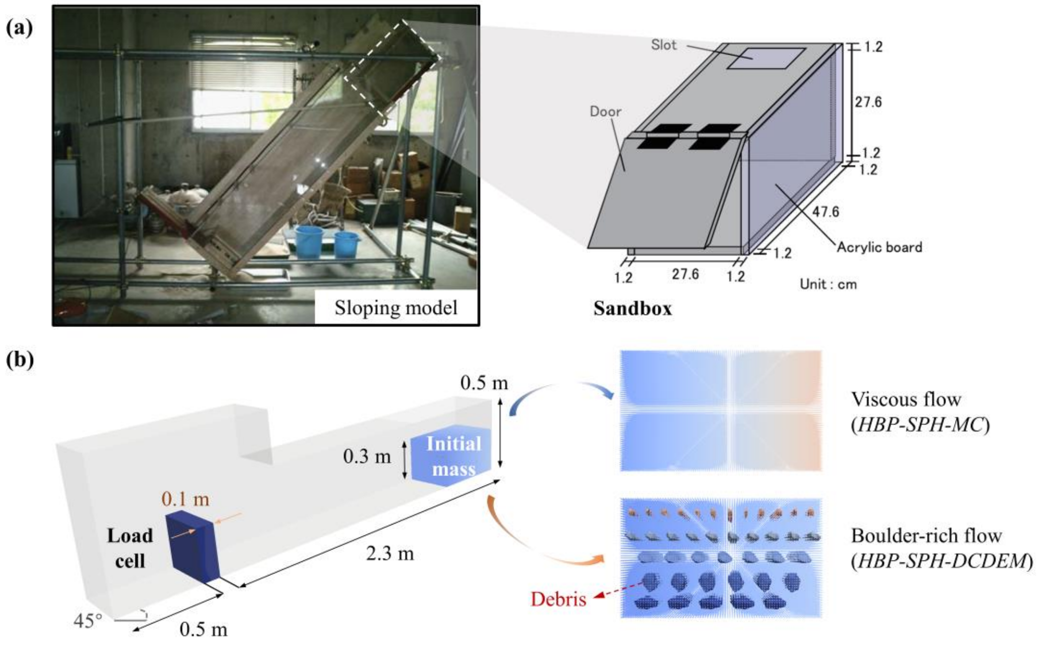

Figure 5.11 (a) Diagram illustrating the debris-flow impact force measurement instrument and the sandbox setup (Moriguchi et al. 2009). (b) Numerical modeling of the sloping system with an initial mass composed of different materials.

Figure 5.11a presents a schematic of the flume, which includes a sand box and an instrument for measuring impact force. The flume's surface was coated with sand to ensure consistent surface friction, whereas the front surface of the wall was considered smooth. The flume itself was 1.8 m long and 0.3 m wide, with an adjustable slope ranging from 45° to 65°. Herein, experiments were conducted at slopes of 45°, 55°, 60°, and 65° to validate the findings. A sand box with a volume of 0.045 m^3 (dimensions 0.3 m × 0.3 m × 0.5 m) was positioned at the top of the flume and filled with sand. The box had a side door that could be opened instantly to initiate the flow, ensuring the process was swift enough to prevent any effects on mass flow initiation. The smooth acrylic plastic side boards of the sand box ensured a two-dimensional initial flow pattern. The sensor timing was not synchronized with the sand release. At steeper inclinations, the sand moved too quickly to record accurate arrival times, so only the 45° inclination was captured accurately on video. A load cell was positioned at the device's base, accompanied by horizontal roller guides to facilitate smooth transmission of impact forces across the instrument's surface. For additional details on the load cell, refer to Moriguchi et al. (2009).

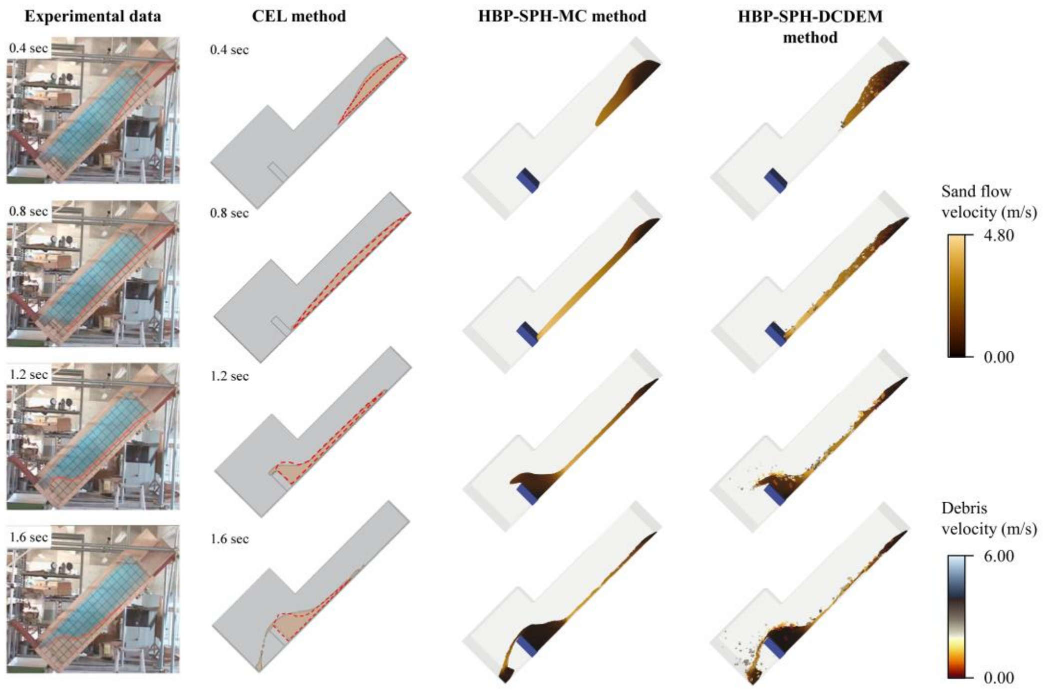

Figure 5.12 Comparison of the deposition morphology and arrival time of the debris flows on a 45° sloping bed. From left to right: snapshots of experimental

observations (Moriguchi et al. 2009), coupled Eulerian-Lagrangian (CEL) simulations (Lee et al. 2019), uniform sand flow simulated with HBP-SPH-MC, and boulder-rich debris flow simulated with HBP-SPH-DCDEM.

Figure 5.11b depicts the experimental setup, including a sloping tank, initial mass materials, and a rigid wall equipped with a numerical gauge. In all simulations, we positioned the tank horizontally to facilitate modeling and simulated the effect of an inclined flume by altering the direction of gravitational acceleration. It should be noted that the original experiment did not include a test group with multi-scale debris; here, the debris flow containing rocks is only compared with the group with uniform particle size. In this analysis, the rheological behavior of sand is modeled using the HBP-SPH model with the Mohr-Coulomb (MC) failure criterion, chosen for its effectiveness in representing the behavior of drying particles. As for the material properties of the rocks, the physical parameters of limestone were referenced. The material properties utilized in the impact force analysis are detailed in Table 5.3.

Table 5.3 Material parameters used in the debris-flow dynamic simulation.

Material	Parameter	Notation	Unit	Value
Dry sand flow	Bulk density	ρ_s	kg/m^3	1379
	Cohesion coefficient	c_s	Pa	0
	Internal friction angle[1]	φ_s	°	35
	Kinematic viscosity	υ_s	m^2/s	0.002
Debris	Bulk density	ρ_b	kg/m^3	2600
	Young's modulus	E	GN m^{-2}	8.0
	Poisson's ratio	υ	/	0.3
	Kinetic friction	μ_f	/	0.35

[1] According to Moriguchi et al. (2009), an internal friction angle of 35° most accurately captured the observed flow behavior.

In the numerical scheme, The initial particle spacing was set to dp = 0.005 m, generating a total of 35,2703 fluid particles and 230,039 boundary particles. The rheological parameters of HBP were set to m = 100 and n = 1.0 to simulate sand flow without significant shear thickening or thinning. Other numerical parameters refer to the values used for viscous debris flows in Chapter 4.

Figure 5.12 shows the instantaneous free surface deposition morphology and impact snapshots of the debris flow observed experimentally and numerically on a 45° sloping flume. From left to right: snapshots of experimental observations, coupled Eulerian-Lagrangian (CEL) simulations, uniform sand flow simulated with HBP-SPH-MC, and boulder-rich debris flow simulated with HBP-SPH-DCDEM. From the figure, it is evident that after the release of the sand in the sandbox, the source material of the debris flow rapidly begins to breach, accelerating and elongating along the slope. At approximately t = 0.8 s, the front of the debris flow reaches the check dam, impacting the wall and accumulating until it overflows the rock barrier. By t = 1.2 s, it has already passed over the rock barrier. Upon reaching the weighing sensor, the debris flow deviates upwards, runs parallel to the wall, forms a bulge, and then decelerates. The simulation results based on the HBP-SPH-MC model successfully captured the velocity and shape of the debris flow at each stage.

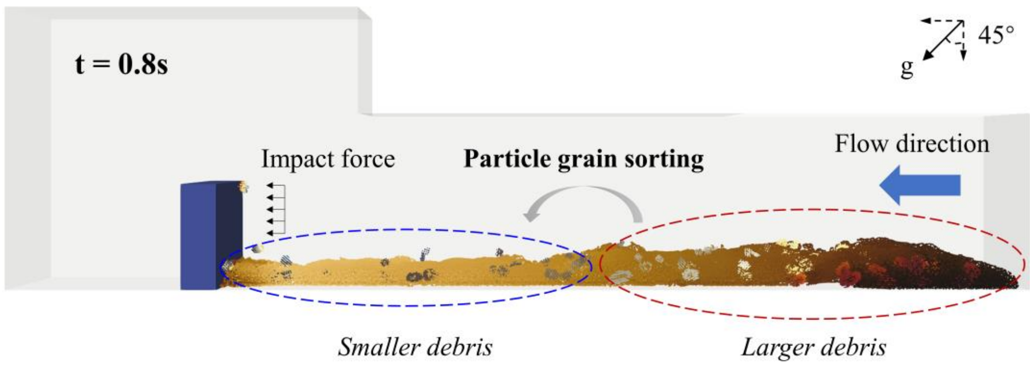

Figure 5.13 The deposition snapshot at t = 0.8 s of the boulder-rich debris flow based on the HBP-SPH-DCDEM model.

The boulder-rich flow generally exhibited similar behavior to the sand flow; however, material transport and interaction with the check dam were more intense, and the flow was more turbulent. It can be seen that some debris was ejected and overflowed the wall after impacting it. Figure 5.13 depicts the instantaneous snapshot at t = 0.8 s when the mixed flow contacts the check dam. Although the debris in the initial state of the mixed flow was uniformly distributed from bottom to top (Figure 5.11b), as the dam breach progressed, the particles naturally sorted themselves, with smaller debris gathering at the flow front and larger particles lagging behind. This behavior is consistent with the dynamics of real geophysical flows, indicating that the two-way resolved coupled model based on HBP-SPH-DCDEM effectively and qualitatively reproduced the transport process of debris-laden flows.

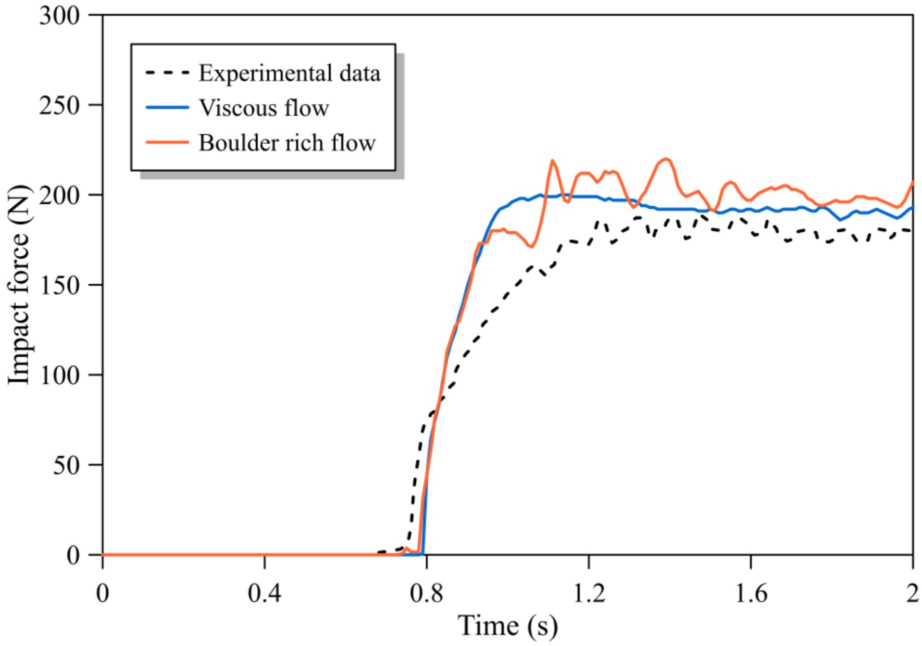

Figure 5.14 Comparison of the experimental and simulated impact forces.

Figure 5.14 presents a comparison between the experimental and numerical results, showing the impact force over time. It can be seen that the impact force begins to increase sharply after the front of the debris flow reaches the wall at t = 0.8 s, reaching a peak around t = 1.0 s and then maintaining a quasi-static value. Overall, the proposed method effectively reproduces the time-varying characteristics of the impact force of the debris flow against the wall. The mixed flow containing debris also exhibited a more turbulent flow state, with a peak slightly higher than that of the sand flow. The simulated impact force values were slightly higher than the experimental observations, which can be attributed to the use of the same mechanical parameters for the PVC material of the tank bottom and sidewalls in the simulation. In the original experiment, the bottom bed was precovered with sand of the same material as the source mass to provide equivalent friction, leading to a slightly higher debris flow transport speed in the simulation and thus a higher measured impact force.

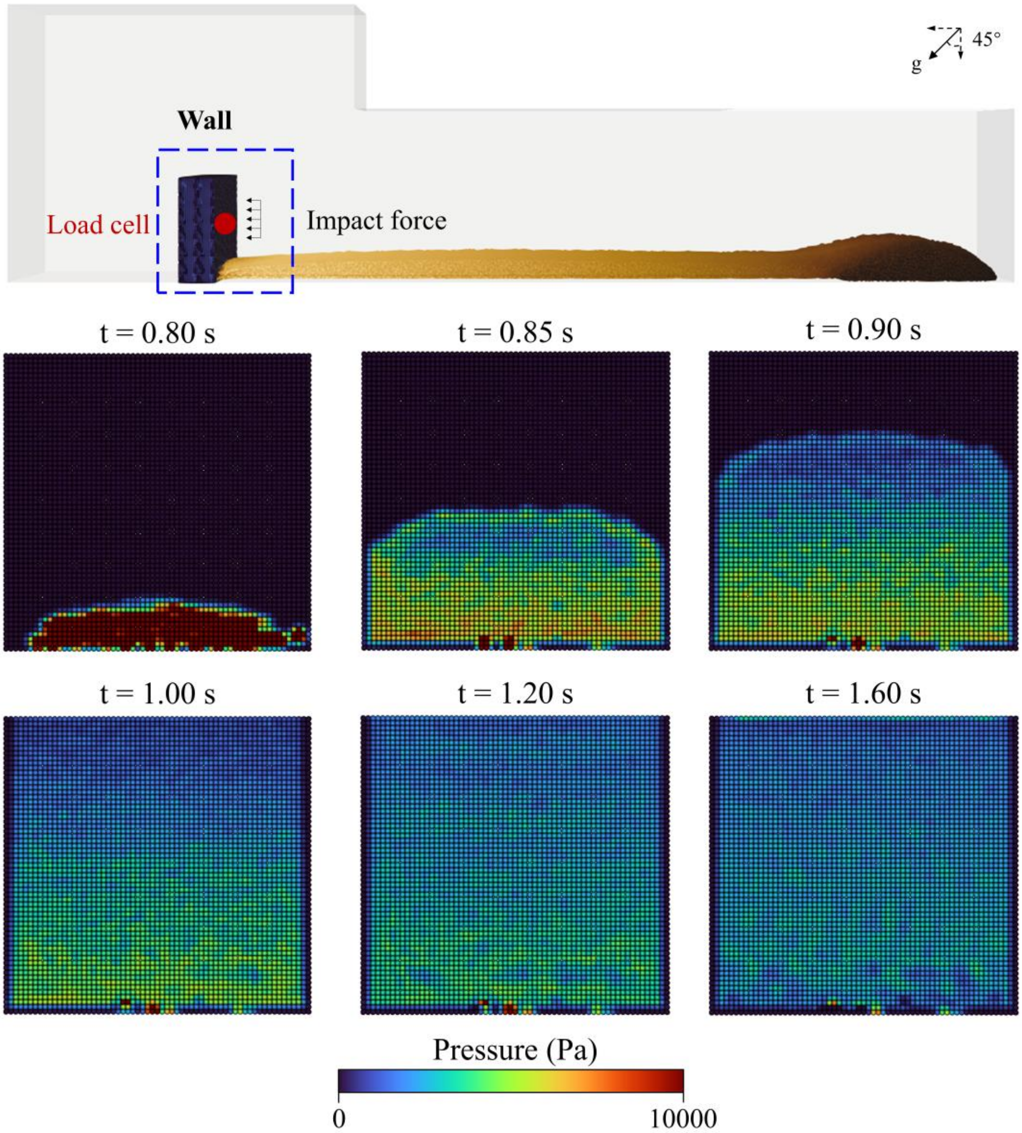

Figure 5.15 The evolution of the pressure contour on the surface of the check dam under the impact of the debris flow on a 45° sloping bed.

The evolution of the pressure on the surface of the check dam is illustrated in Figure 5.15. The numerical measurement principle is also based on SPH kernel function interpolation, calculating the sum of the pressure interpolations generated by fluid particles within the support domain (Figure 5.3). The figure above vividly illustrates the temporal variation characteristics of the wall under pressure. At the moment of debris-flow impact, a pressure distribution contour of the flow front shape forms instantly on the wall surface, with the pressure exceeding 10,000 Pa. As the sediment mass accumulates in front of the dam, the pressure rapidly dissipates, decreasing uniformly along the vertical face of the dam from bottom to top. After t = 1.6 s, the pressure roughly stabilizes around 3,000 Pa.

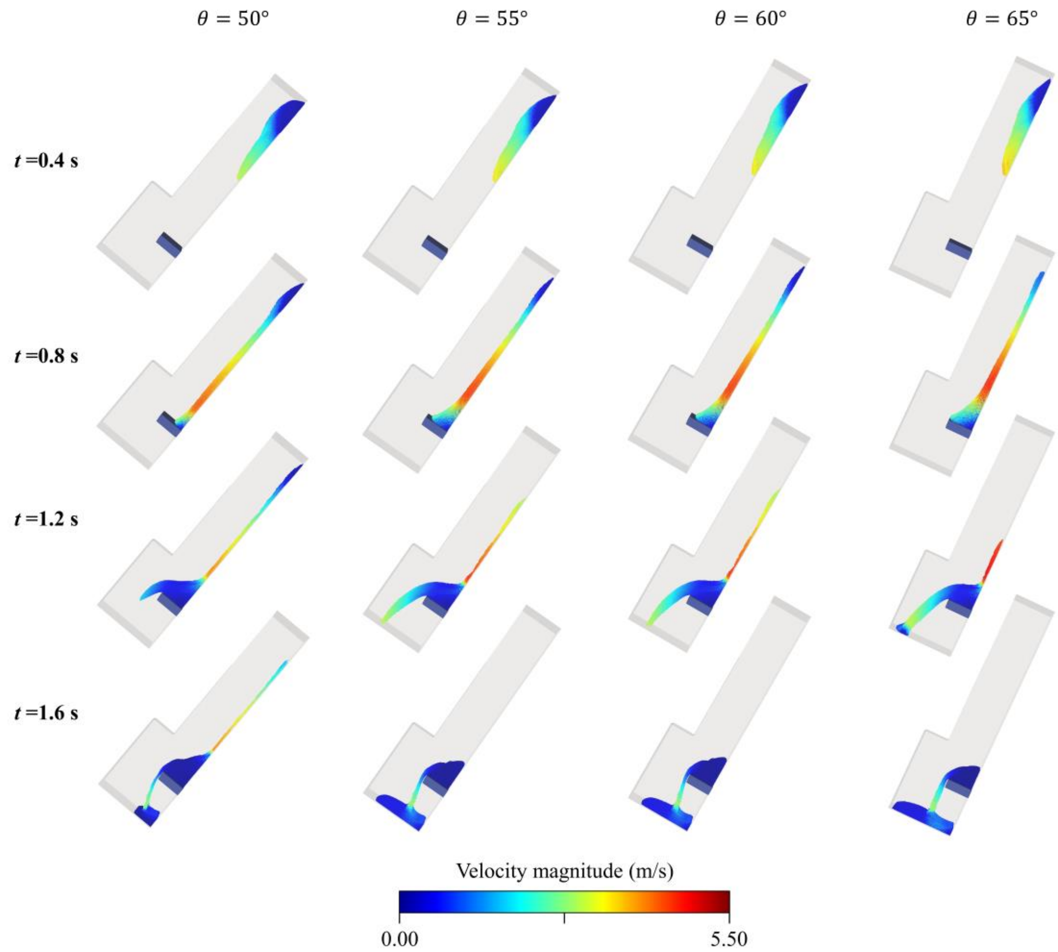

Figure 5.16 Comparison of the deposition morphology and arrival time of the debris flows on various sloping beds, including 50°, 55°, 60°, and 65°.

To study the effect of flume inclination on the impact force and deposition morphology, numerical tests with different slope angles were conducted, as illustrated in Figure 5.16. It is evident that as the slope increases, the flow speed of the debris flow becomes faster, the time to reach the wall is shorter, and the height and distance it travels after surpassing the wall are greater. In the 45° group, the debris flow had just reached the wall at t = 0.8 s, while in the 65° group, it had almost completely surpassed the check dam. Furthermore, on steep slopes, the source material could not be maintained on the tank, with almost all of it either flowing over the wall or accumulating in front of the dam.

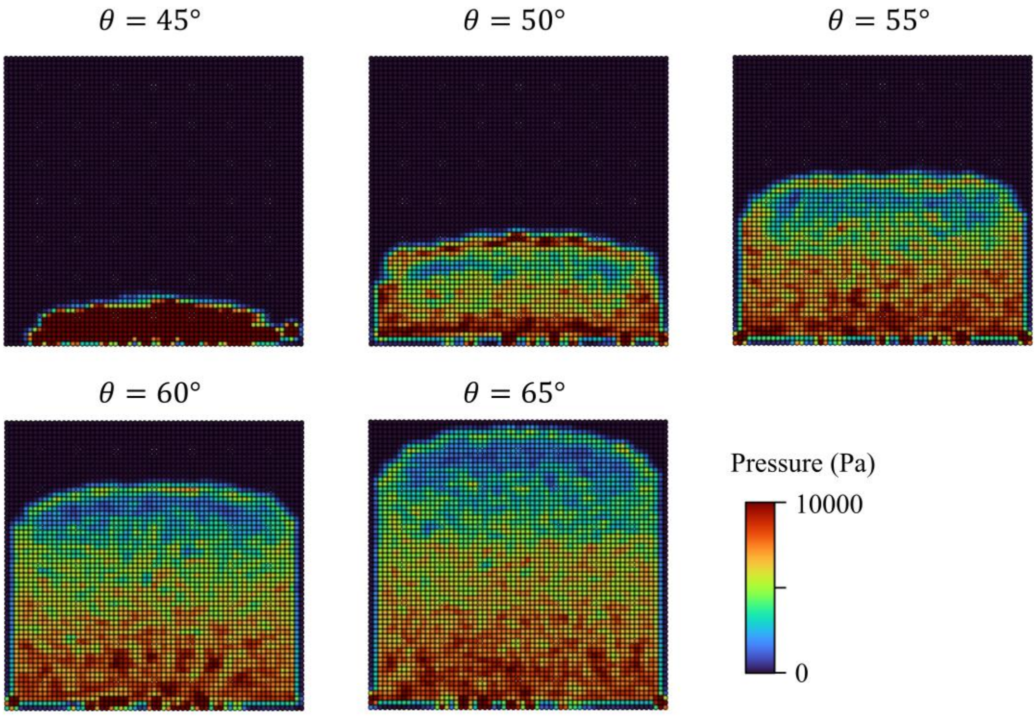

Figure 5.17 Instantaneous pressure distribution contour on the wall surface at t = 0.8 s for each slope simulation group.

Figure 5.17 shows the instantaneous pressure distribution contour on the wall surface at t = 0.8 s resulting from the impact of debris flow in each slope angle experimental group. The simulation results suggest that the steeper slope groups accumulated more source material in front of the dam, with the overall pressure distribution gradually decreasing from bottom to top. This is consistent with previous experimental and simulation results, indicating that the steeper the slope, the shorter the time to reach the dam front, resulting in higher speed and thus greater impact force.

5.4. CONCLUSION

In this chapter, a two-way resolved coupling numerical method is proposed to simulate the dynamic behavior of boulder-rich debris flows. Specifically, based on the material composition and classification of the debris flow, the HBP-SPH method is employed to model fine-grained materials (e.g., clay, silt, and sand) and water as a unified particle-fluid mixture continuum, as detailed in Chapter 4. Building on this, the boulders, which have particle sizes much larger than the fluid, are individually considered and modeled using the Distributed Contact Discrete Element Method (DCDEM). This approach is coupled with the HBP-SPH method to develop a multi-scale, multi-physics, multi-phase flow framework for particle numerical analysis of debris flows. The following conclusions are drawn in this chapter:

(1) A multi-phase, multi-size particle numerical framework for boulder-rich debris flows is constructed. The fine-grained materials and water are collectively simplified into a viscoplastic model following the HBP non-Newtonian fluid constitutive behavior. The DCDEM is used to depict irregular boulders or debris with particle sizes much larger than the fluid, and the interaction forces between fluid and solid, as well as between solids, are explicitly defined.

(2) The aluminum cylinder collapse laboratory is selected to verify the proposed method. We conduct a series of comparative tests on the collapse of multi-layered aluminum columns and the aluminum column-water dam system. The simulation results show that the adopted model can not only capture the dynamic process of the collapse and mutual collision of the multi-layered aluminum cylinders but also achieve satisfactory simulation accuracy for solid-liquid systems. Compared to FVM-DEM simulations, our model produces deposition morphology that closely matches experimental observations. Notably, we compare scenarios using PST and those without PST. The results indicate that the model using PST effectively avoids voids at the solid-liquid contact surface, such as the front end of the water column, thus achieving a more uniform flow field distribution. However, this treatment also results in fluid particles at the collapse front far exceeding experimental observations. This indicates that the use of PST depends more on the specific objectives of the study.

(3) To validate the collision patterns of irregular blocks in debris flows, a stacking numerical test is constructed using a large number of polyhedral materials.

In this test, hundreds of blocks are funneled and continuously discharged into a tank through a hopper device. These blocks gather at the hopper mouth and collide with the hopper walls and with each other multiple times over a short period until they stabilize and gradually accumulate in the tank. This experiment tests the contact and collision stability of the irregular blocks.

(4) The proposed HBP-SPH-DCDEM method is further verified through a debris flow impact laboratory test with different slope angles. First, in the 45° sloping bed group, we compare the experimental data, the simulation results based on the coupled Eulerian-Lagrangian (CEL) method, the simulation results based on the HBP-SPH method and the Mohr-Coulomb (MC) yield criterion, and the simulation results of boulder-rich debris flows using the HBP-SPH-DCDEM method. Comparative analysis shows that the adopted model accurately captures the instantaneous deposition morphology and the impact force on the wall of the debris flow. In particular, the boulder-rich mixed flow exhibits a more turbulent flow state, with boulders traveling further after surpassing the check dam. The simulation results also effectively replicate the pressure variation characteristics of the wall under debris flow impact. Finally, by adjusting the slope angle, we compare the instantaneous deposition morphology and impact force of the debris flows at different angles. The simulation results are consistent with the experimental observations, verifying the feasibility of the proposed model.

References

Canelas, R., Domínguez, J., Crespo, A., Gómez-Gesteira, M. & Ferreira, R. 2017. Resolved simulation of a granular-fluid flow with a coupled SPH-DCDEM model. Journal of Hydraulic Engineering 143(9), 06017012.

Canelas, R., Ferreira, R., Crespo, A. & Domínguez, J. Year. A generalized SPH-DEM discretization for the modelling of complex multiphasic free surface flows. In: Proceedings of the 8th International SPHERIC Workshop, Trondheim, Norway, 4-6.

Canelas, R.B., Crespo, A.J., Domínguez, J.M., Ferreira, R.M. & Gómez-Gesteira, M. 2016. SPH–DCDEM model for arbitrary geometries in free surface solid–fluid flows. Computer Physics Communications 202, 131-140.

Crespo, A.J., Domínguez, J.M., Rogers, B.D., Gómez-Gesteira, M., Longshaw, S., Canelas, R., Vacondio, R., Barreiro, A. & García-Feal, O. 2015. DualSPHysics: Open-source parallel CFD solver based on Smoothed Particle Hydrodynamics (SPH). Computer Physics Communications 187, 204-216.

Cummins, S.J. & Cleary, P.W. 2011. Using distributed contacts in DEM. Applied mathematical modelling 35(4), 1904-1914.

Fernandez, J., Cleary, P., Sinnott, M. & Morrison, R. 2011. Using SPH one-way coupled to DEM to model wet industrial banana screens. Minerals Engineering 24(8), 741-753.

Fourtakas, G., Vacondio, R., Alonso, J.D. & Rogers, B.D. Year. Improved density diffusion term for long duration wave propagation. In: 2020 SPHERIC Harbin International Workshop.

Hatzor, Y.H., Ma, G. & Shi, G.-h. 2017. Discontinuous deformation analysis in rock mechanics practice. CRC Press.

Koshizuka, S., Nobe, A. & Oka, Y. 1998. Numerical analysis of breaking waves using the moving particle semi-implicit method. International journal for numerical methods in fluids 26(7), 751-769.

Lee, K., Kim, Y., Ko, J. & Jeong, S. 2019. A study on the debris flow-induced impact force on check dam with-and without-entrainment. Computers and Geotechnics 113, 103104.

Liang, H., Jiang, Y., Ning, P., Zhu, L.J.C. & Geotechnics. 2023. A modified friction-viscous solid boundary of the SPH method for landslide simulation. Computers and Geotechnics 155, 105238.

Mikola, R. & Sitar, N. 2013. Next generation discontinuous rock mass models: 3-D and rock-fluid interaction. Front Discontin Numer Methods Pract Simul Eng Disaster Prev 12, 81-90.

Mikola, R.G. & Sitar, N. Year. 3D simulation of tsunami wave induced by rock slope failure using coupled DDA-SPH. In: ARMA US Rock Mechanics/Geomechanics Symposium, ARMA-2014-7094.

Moriguchi, S., Borja, R.I., Yashima, A. & Sawada, K. 2009. Estimating the impact force generated by granular flow on a rigid obstruction. Acta Geotechnica 4, 57-71.

Peng, C., Zhan, L., Wu, W. & Zhang, B. 2021a. A fully resolved SPH-DEM method for heterogeneous suspensions with arbitrary particle shape. Powder Technology 387, 509-526.

Peng, X., Chen, G., Fu, H., Yu, P., Zhang, Y., Tang, Z., Zheng, L. & Wang, W. 2021b. Development of coupled DDA-SPH method for dynamic modelling of interaction problems between rock structure and soil. International Journal of Rock Mechanics and Mining Sciences 146, 104890.

Peng, X., Chen, G., Yu, P., Zhang, Y., Guo, L., Wang, C., Cheng, X., Niu, H.J.c. & Geotechnics. 2019. Parallel computing of three-dimensional discontinuous deformation analysis based on OpenMP. Computers and Geotechnics 106, 304-313.

Peng, X., Chen, G., Yu, P., Zhang, Y., Zhang, H. & Guo, L. 2020a. A full-stage parallel architecture of three-dimensional discontinuous deformation analysis using OpenMP. Computers and Geotechnics 118, 103346.

Peng, X., Yu, P., Chen, G., Xia, M. & Zhang, Y. 2020b. Development of a coupled DDA–SPH method and its application to dynamic simulation of landslides involving solid–fluid interaction. Rock Mechanics and Rock Engineering

53, 113-131.

Pudasaini, S.P. & Mergili, M. 2019. A multi-phase mass flow model. Journal of Geophysical Research: Earth Surface 124(12), 2920-2942.

Shi, G.h. 1992. Discontinuous deformation analysis: a new numerical model for the statics and dynamics of deformable block structures. Engineering computations 9(2), 157-168.

Shu, C., Xia, J., Falconer, R.A. & Lin, B. 2011. Incipient velocity for partially submerged vehicles in floodwaters. Journal of hydraulic research 49(6), 709-717.

Silva, M., Costa, S., Canelas, R., Pinheiro, A. & Cardoso, A. 2016. Experimental and numerical study of slit-check dams. International Journal of Sustainable Development and Planning 11(2), 107-118.

Song, Y., Huang, D. & Zeng, B. 2017. GPU-based parallel computation for discontinuous deformation analysis (DDA) method and its application to modelling earthquake-induced landslide. Computers and Geotechnics 86, 80-94.

Sun, J., Zou, L., Govender, N., Martínez-Estévez, I., Crespo, A.J., Sun, Z. & Domínguez, J.M. 2023. A resolved SPH-DEM coupling method for analysing the interaction of polyhedral granular materials with fluid. Ocean Engineering 287, 115938.

Wang, W., Yin, K., Chen, G., Chai, B., Han, Z. & Zhou, J. 2019. Practical application of the coupled DDA-SPH method in dynamic modeling for the formation of landslide dam. Landslides 16, 1021-1032.

Xiao, Y., Miao, Q., Huang, M., Wang, Y. & Xue, J. 2017. Parallel computing of discontinuous deformation analysis based on graphics processing unit. International Journal of Geomechanics 17(5), E4016010.

Yu, P., Peng, X., Hu, B., Cheng, X., Zhang, Y. & Li, D. 2022. Extension of 3-D coupled DDA-SPH method for dynamic analysis of soil-structure interaction problems. Applied Mathematical Modelling 111, 436-453.

Zhang, S., Kuwabara, S., Suzuki, T., Kawano, Y., Morita, K. & Fukuda, K. 2009. Simulation of solid–fluid mixture flow using moving particle methods.

Journal of Computational Physics 228(7), 2552-2565.
Zhao, L., He, J., Yu, Z., Liu, Y., Zhou, Z. & Chan, S. 2020. Coupled numerical simulation of a flexible barrier impacted by debris flow with boulders in front. Landslides 17, 2723-2736.

CHAPTER 6

PRACTICAL APPLICATIONS FOR STUDYING CATASTRAPHE DEBRIS-FLOW EVENTS INCLUDING VISCOUS AND STONY TYPES

6.1. INTRODUCTION

In the previous text, we conducted a series of laboratory-scale numerical simulation tests to verify the accuracy and feasibility of the proposed method. The subjects of these experiments are mostly steady and homogeneous flow configurations. Nevertheless, natural flows are characterized by inhomogeneous and unsteady flow states, which are complex in their spatiotemporal evolution and difficult to reproduce on a laboratory scale. On one hand, scaling issues emerge in small-scale laboratory experiments involving water-saturated granular flows (Iverson et al. 2011; Iverson 2015; Delannay et al. 2017; Vicari et al. 2022). These issues are primarily due to the relatively pronounced effects of surface tension, pore-fluid shear resistance, and cohesion, as well as the faster dissipation of excess pore-fluid pressure compared to real-world conditions (Delannay et al. 2017). Currently, the up-scaling from laboratory to field-scale hazard prediction still encounters various conceptual and technical challenges. For instance, the reduced dissipation responsible for the unexpectedly long run-out of large-scale granular avalanches (e.g., the Donghekou landslide-debris flow in China (Yin et al. 2009)) is not observed in laboratory-scale experiments, and the underlying physical mechanisms remain a topic of debate. On the other hand, small-scale experiments are generally limited by their simple configurations, which provide minimal information for heterogeneous, multiphase geophysical flows. As such, recent experimental research on debris flows has progressively shifted towards scales that approximate real-world conditions, aiming to minimize the impact of scaling effects as much as possible (e.g., Iverson et al. 2010; Iverson et al. 2011; Fávero Neto et al. 2020; Baselt et al. 2022; Vicari et al. 2022). Even so, these large-scale experiments are mostly self-channeling flows, failing to replicate the fan-shaped paths of hillside debris flows. Additionally, the available erodible material on the bed layer is limited, costs are high, and reproducibility is low. These have partly contributed to the persistent underestimation of the actual scale and destructiveness of such disasters.

One approach to bridging the gap between laboratory experiments and field data is through numerical modeling. The goal is to create models that accurately replicate laboratory experiments and then apply these models to natural flows, considering the complex terrain and geological conditions. However, as discussed in Chapter 2, most numerical methods rely on numerous simplifications and assumptions about natural processes, such as the depth-averaged paradigms, single phase flow, isotropic, and non-dispersive. Even if the physical laws governing these processes can be determined, the specific field conditions that define the parameters are rarely known and can vary over the course of an event (e.g., cohesion distribution, water content evolution, and grain size sorting).

This thesis does not aim to address all the aforementioned issues but rather takes a step forward within the existing particle-based framework by extending the single-layer particle-fluid mixture architecture to a multi-scale, multiphase approach that can account for dynamic processes such as erosion, entrainment, and deposition behaviors. Next, we examine a case of a debris flow characterized by a relatively uniform particle size distribution (the 2010 Yohutagawa debris flow event in Japan) and a case involving a boulder-rich debris flow (the 2010 Hongchun gully debris flow event in China). We perform full-size modeling based on Digital Terrain Model (DTM) and field measurements to replicate and qualitatively analyze these two disaster events, thereby validating the feasibility of the method proposed in this thesis. Finally, we endeavor to discuss and draw some meaningful conclusions.

6.2. CASE STUDY 1: 2010 YOHUTAGAWA DEBRIS-FLOW EVENTS, JAPAN

6.2.1. DISASTER BACKGROUND AND MOTIVATION

The 2010 Yohutagawa debris flow event, selected for this case study, offers an insightful analysis of debris flow dynamics triggered by intense rainfall. As shown in Figure 6.1a, this event occurred on October 20, 2010, on Amamioshima Island in South Kyushu, Japan (28°24′ N, 129°32′ E), following Typhoon Megi, which brought a maximum rainfall intensity of 131 mm/h and an accumulated intensity of 601 mm. The catchment area spans 0.24 km^2, with elevations ranging from 20 to 250 m and a channel length of 750 m (as depicted in Figures 6.1b and 6.1c). The region was predominantly forested before the debris flow, and the geological composition mainly consisted of sandstone and mudstone, interspersed with colluvium deposits a few meters thick. These colluvium deposits, lying above the bedrock, were destabilized by the intense rainfall, leading to the initiation of the debris flow.

An investigation by Kokusai Kogyo Co., Ltd., Japan (KKC) revealed that the Yohutagawa torrent's channel has an average slope of about 16°, varying from 33° in the higher parts to 5° on the alluvial fan. The debris flow resulted in a total deposit volume of 8697 m^3, including an initial 5843 m^3 from the source area and an additional 2854 m^3 from along-path entrainment (Figure 6.1a). Clearly observable entrainment depths ranging from 0.5 m to 2.0 m were also recorded along the path (Han et al. 2016). Notably, the existing check dam managed to intercept a significant portion of the debris mass, approximately 5621 m^3 (Figures 6.2a and 6.2d), but some material bypassed the dam, causing damage to two buildings located on the alluvial fan. Despite the severity of the event, no casualties were reported.

Field investigations reveal that although the check dam was designed to be 2 meters high, its actual effective height before the disaster was only 1 meter (Figure 6.2a). The largest grain size in the downstream sediment samples does not exceed 20 cm, with a representative grain size of approximately 3 cm (Figure 6.2c). Overall, the grain size distribution of both the source materials and sediments is uniform, which permits the use of the proposed HBP-based numerical model for analysis. Considering the significant erosion observed in this debris flow event, we develop a numerical analysis model based on field surveys. This model encompasses initiation, erosion, propagation, and deposition areas (Figure 6.1a), integrating the bed sediments and initiation sources into the DTM of the site.

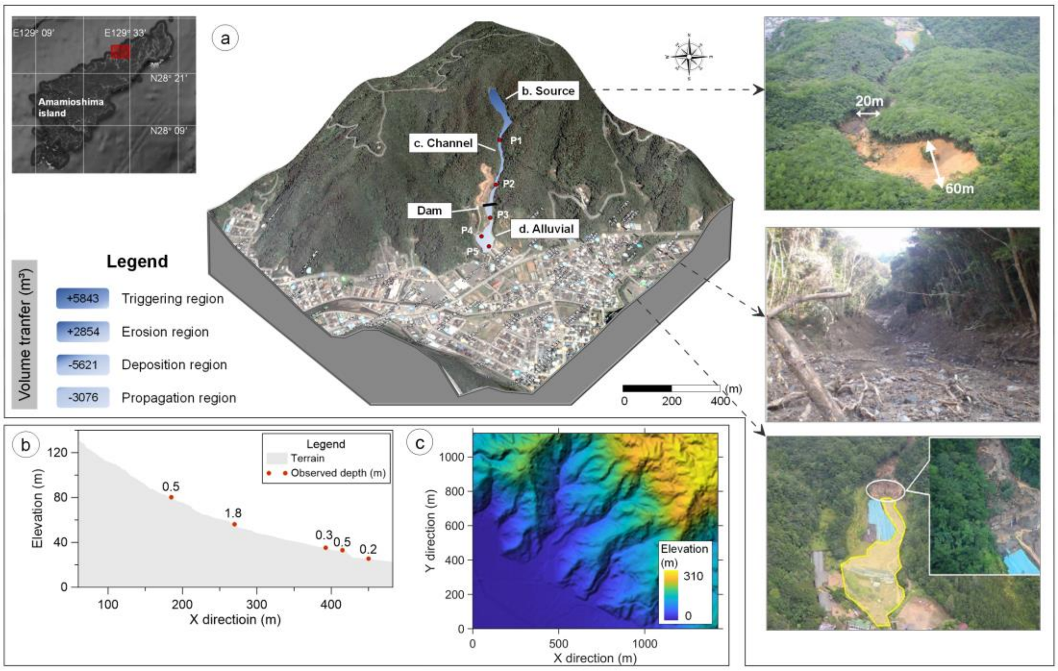

Figure 6.1 Overview of the 2010 Yohutagawa debris-flow event. (a) Morphology and photographs of the event in different sectors. (b) The profile of the terrain and flow depth measurement points along the path. (c) DTM data showing the topography relief of the area.

Figure 6.3 shows the post-disaster sediment distribution pattern inverted by KKC using the New-SASS model, with the results compared to and rigorously corrected against field survey data. Our subsequent numerical simulations will also be validated based on this data. Observing the sediment distribution pattern reveals that the check dam and the structures behind it significantly influenced the final sediment morphology. No damage to the sand-retaining dam is found on-site. Therefore, the numerical calculations do not consider scenarios where the dam is breached but rather treat it as a fixed rigid boundary.

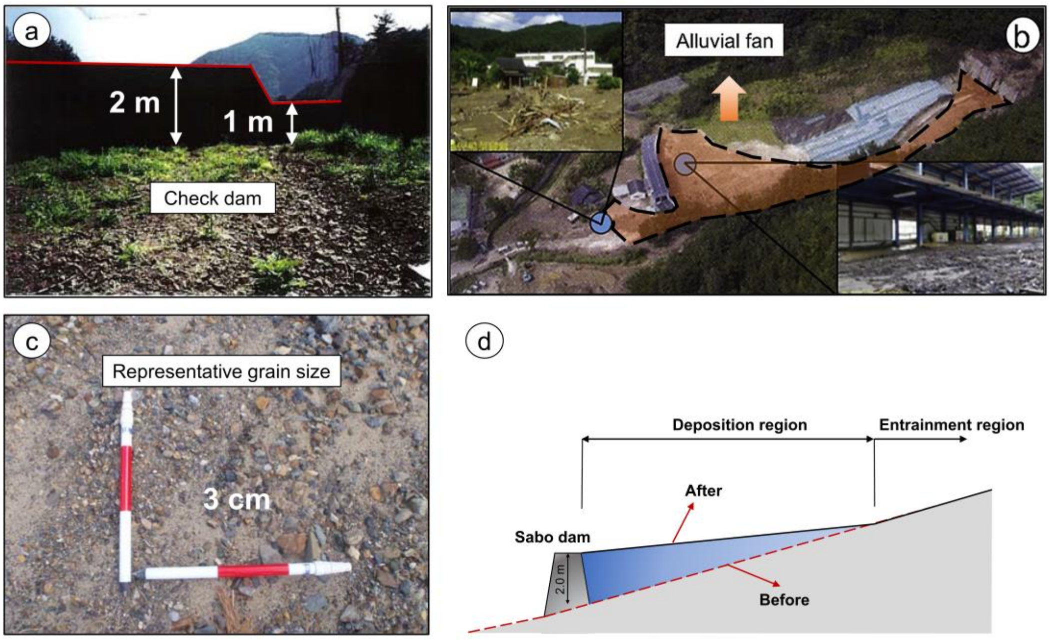

Figure 6.2 (a) The effective height and morphology of check dam. (b) The extent of the alluvial fan downstream of the check dam. (c) The representative grain size obtained from field surveys. (d) schematic illustration of the topography near the check dam.

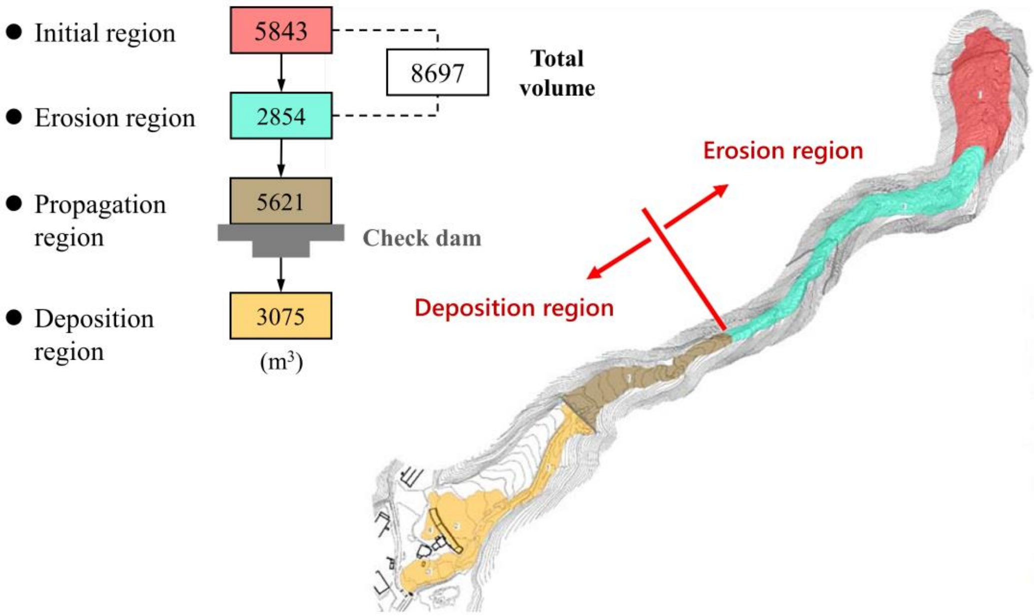

Figure 6.3 Post-disaster sediment distribution inversion diagram, modified from Kokusai Kogyo Co., Ltd., Japan (KKC).

6.2.2. NUMERICAL MODELLING AND SETUP

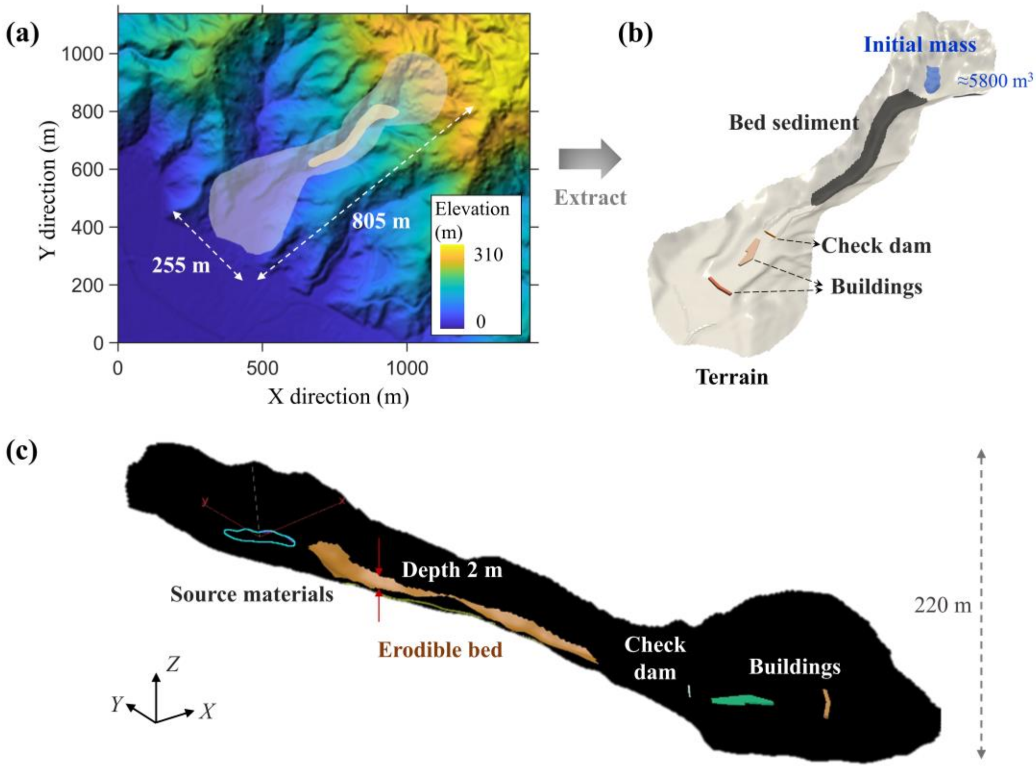

Figure 6.4 (a) Digital Terrain Model (DTM) of the Yohutagawa basin (2.5 m resolution) with delineated computation and erosion regions. (b) 3-D modelling of the Yohutagawa terrain with bed sediment, check dam, and buildings. (c) Side view of the computational model

In the SPH scheme, complex terrain modeling typically relies on DTM, which are discretized into one or more layers of boundary particles to constrain the movement of debris flow particles on the topography. However, only a small portion of these boundary particles are involved in the computation. To reduce computational costs, we delineated the target simulation area using field survey data and aerial photographs on a DTM with 2.5 m resolution, encompassing all potential regions affected by fluid particles, as shown in Figure 6.4a. Moreover, the erosion region is also delineated based on the scope calibrated by KKC, featuring a 2-meter depth sediment bed underlying the terrain (Figure 6.4c). Note that the surface of the erodible bed layer still corresponds to the elevation data of the DTM. Fluid particles interact directly with boundary particles outside the designated sediment region. This design aims to maximize the accuracy of simulating the actual disaster scenario. Since the maximum erosion depth observed in field measurements did not exceed 2 meters, the designed erodible bed layer provides a sufficient source of erosion material. Figure 6.4b shows the extracted target terrain and erosion regions. In addition, the positions of initiation sources, the check dam, and buildings are also determined based on the scope calibrated by KKC and aerial photographs. The initial volume was matched to the field survey data by controlling the generated particles and their spacing.

Table 6.1 Material properties and related values in the Yohutagawa debris-flow event simulation.

Source material	Parameter	Notation	Unit	Value
Initial mass (water saturated)	Bulk density	ρ_i	kg/m^3	1650
	Cohesion coefficient	c_i	Pa	0
	Internal friction angle	φ_i	°	28
	Kinematic viscosity	υ_i	m^2/s	0.001
	Porosity	n_i	/	0.40
	Debris flow concentration	C_d	/	0.44
	Exponential index	m	/	100
	Power law index	n	/	1.0
Bed sediment	Bulk density	ρ_b	kg/m^3	1600
	Cohesion coefficient	c_b	Pa	1
	Internal friction angle	φ_b	°	30
	Kinematic viscosity	υ_b	m^2/s	0.0015
	Porosity	n_b	/	0.40
	Water content	n_w	/	0.15-0.28
	Bulk modulus of water	K	Pa	2×10^9
	Hydraulic permeability[1]	K	m^2	10^{-8}
	Exponential index	m	/	100
	Power law index	n	/	0.95

[1] Field surveys did not provide information on the hydraulic conductivity. Considering the event

occurred after heavy rainfall, leaving the sediments nearly saturated, the coefficient was referenced from values used in USGS large-scale flume experiments (Iverson et al. 2010).

The extracted terrain is characterized by a main gully of 880 m with an elevation difference of approximately 220 m. The proposed HBP-SPH method, combined with the Drucker-Prager (DP) yield criterion, is used to simulate the dynamic behaviors of debris flow over the extracted topography. Additionally, the phase transition treatment and pore pressure response algorithm, detailed in Chapter 4, are implemented in the erodible particles to reproduce the momentum feedback from bed sediment. Regarding the determination of the rheological parameters, most material properties are directly derived from the in-situ survey. The HBP rheological parameters, however, are obtained according to the findings of Han et al. (2019), as summarized in Tables 6.1 and 6.2.

The kinematic viscosity is determined using an empirical equation developed by Komatina and Jovanovic (1997). This equation, based on physical experiments, correlates the dynamic viscosity μ with the material concentration C_d, which reads:

$$\mu = 0.000621\exp\left(0.173C_d\right). \tag{6.1}$$

Table 6.2 Controlling parameters and related numerical setup in the dynamic simulation of the 2010 Yohutagawa debris-flow event.

Parameter	Notation	Unit	Value
Particle distance	dp	m	0.3
Number of initial mass particles	N_f	/	212,228
Number of sediment particles	N_s	/	509,788
Number of boundary particles	N_b	/	1,923,801
Debris-flow duration	t	s	120
Sound speed coefficient	ξ	/	20
EoS constant	γ	/	7
Density diffusion coefficient	δ_d	/	0.1
Verlet steps	S_{verlet}	/	40
CFL coefficient[2]	CFL	/	0.2

For the numerical scheme, the Verlet time-stepping algorithm was adopted to decrease computational cost. The initial particle spacing is set to 0.3 m, resulting in the generation of 212,228 debris flow source material particles, 509,788 erodible bed sediment particles, and 1,923,801 boundary particles. Theoretically, increasing the model resolution (i.e., reducing initial particle distance) facilities improved computational accuracy. However, within the current unified particle size modeling framework, further increasing the resolution would lead to a sharp rise in the number of boundary particles. Therefore, until multi-scale modeling and multi-core GPU parallel processing are implemented, we aim to keep the particle count at the million level. The simulations are performed on a NVIDIA RTX A6000 GPU using GPU-optimized code, while an Intel(R) Xeon(R) W-2225 @ 4.10GHz processor is utilized for running the CPU-based algorithm. Additionally, the total simulation time for this case is 120 seconds, and the visualization of the simulation results is conducted using the open-source toolkit Paraview.

6.2.3. Results analysis and discussion

The time-elapsed simulation results of the Yohutagawa debris flow run-out extent with a 0.28 volumetric water content are illustrated in Figure 6.5. After the simulation begins, the source material starts to collapse and accelerate within the channel with a slope exceeding 30°. The maximum speed exceeds 15 m/s. Simultaneously, the rapid flow erodes the sediment materials on the steep slope, with sediment particles partially scoured and entrained into the debris flow mixture. As the slope becomes gentler and the flow interacts with boundary particles, the velocity at the flow front gradually stabilizes at around 7 m/s. Approximately 70 seconds later, the flow front reaches the check dam. However, after just 4 seconds, the high-speed surging debris flow had already overtopped the dam, despite the dam's capacity limit not yet being exceeded. At t = 100 seconds, the front of the debris flow has reached the downstream buildings of the alluvial fan. By 120 seconds, the deposition flow gradually ceases, and the deposition morphology becomes stable.

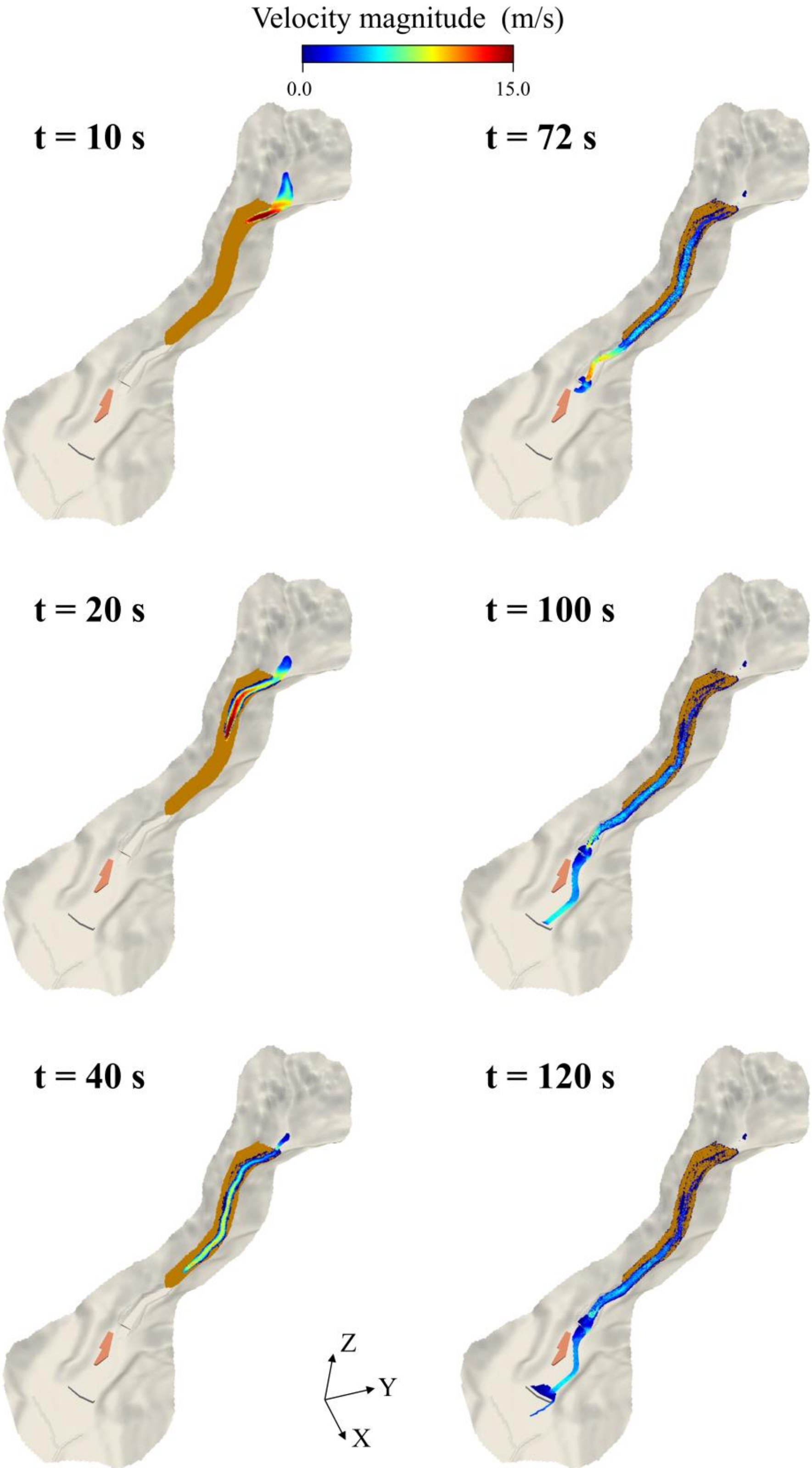

Figure 6.5 Snapshots of the Yohutagawa debris-flow run-out extent.

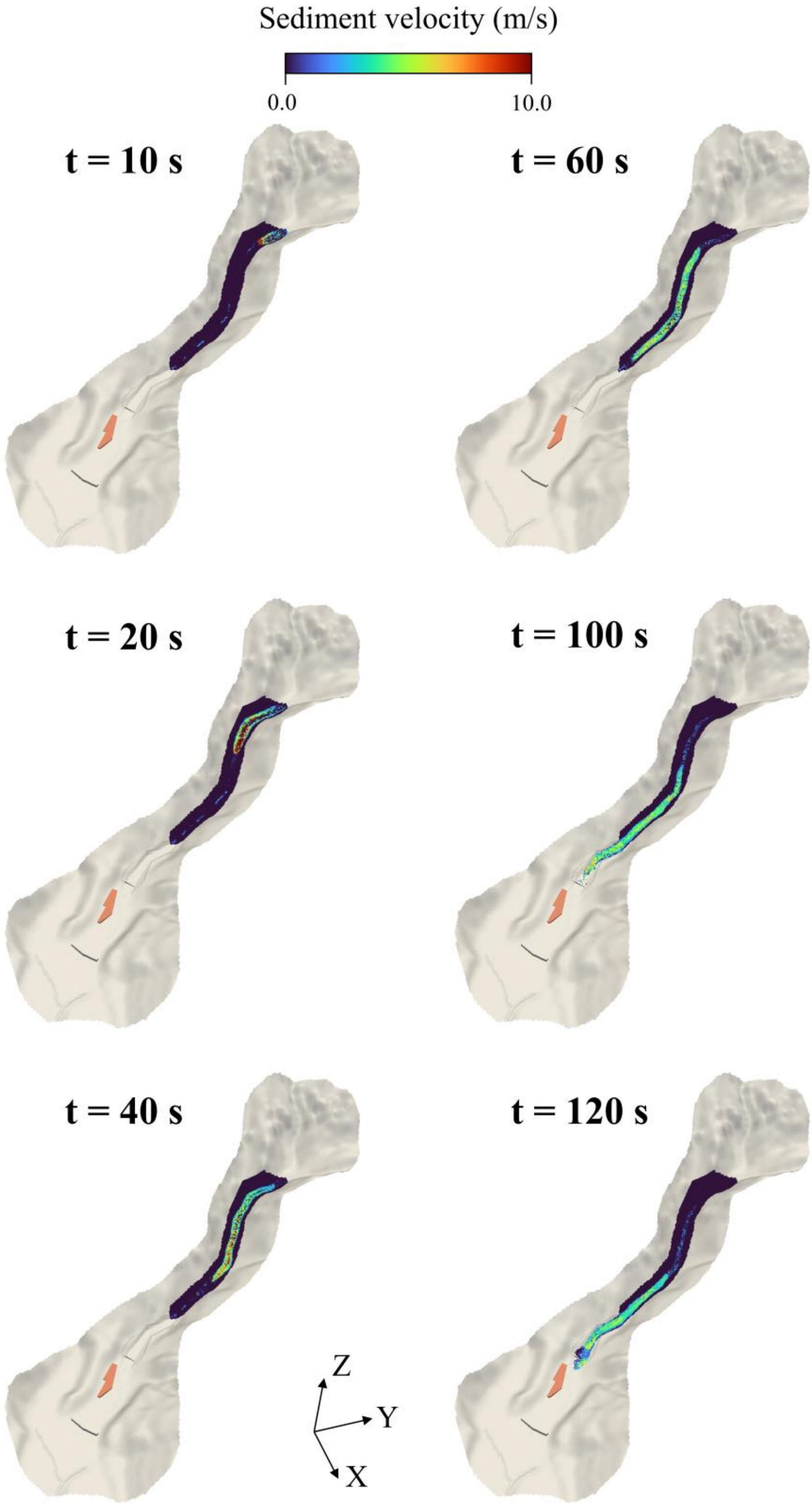

Figure 6.6 Time-elapsed simulation of bed-sediment velocity erosion and entrainment by debris flow.

Figure 6.6 shows a snapshot of the velocity cloud map depicting the erosion and transport of sediment particles by the debris flow on the slope. The transport velocity of sediment particles is evidently influenced by material properties such as yield criteria and internal friction angle, resulting in lower velocities compared to the overlying debris-flow mixture. Over time, this lag effect becomes increasingly apparent. Sediment particles take approximately 100 seconds to reach the vicinity of the check dam, while the debris flow source takes only 70 seconds. Ultimately, most of the bed sediment particles deposit in front of the check dam, with only a small portion of particles overtopping the dam and reaching the alluvial fan.

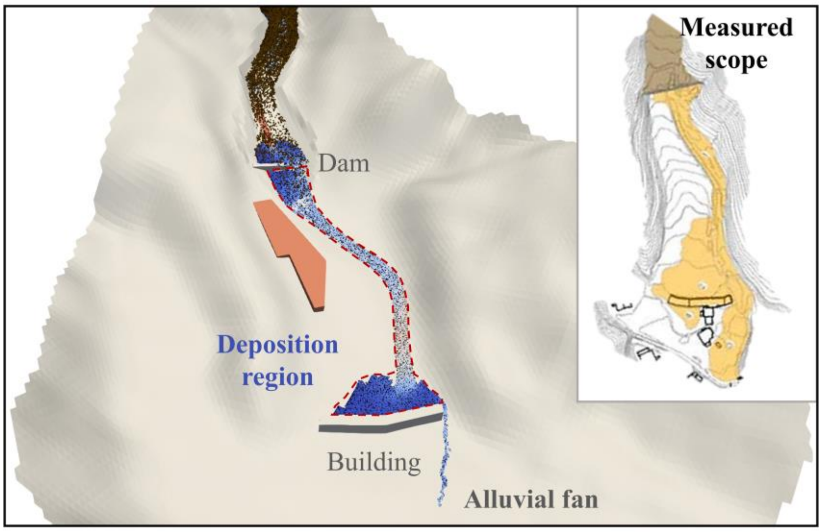

Figure 6.7 Deposition morphology of the Yohutagawa debris-flow event compared with measurement data.

Although this study does not consider the strong coupling and sorting mechanisms of different particles between water and multi-scale grain, the debris flow source and sediment particles exhibit behavior similar to particle separation and premature deposition. This issue has also been discussed in Chapter 4 with the USGS flume experiments. In short, differences in the mechanical properties of materials, phase transition mechanisms, yield criteria, and pressure gradients collectively contribute to the sorting phenomenon between the upper and lower layers of materials.

To validate the feasibility and accuracy of the model, we compared the deposition morphology of the debris flow on the alluvial fan with measured data conducted by KKC, as shown in Figure 6.7. The comparison results indicate that the TLMP-SPH model successfully depicted the deposition morphology of the Yohutagawa debris flow event. The deposition behind the dam was mainly concentrated on the side close to the mountain. Due to the obstruction by downstream buildings on the alluvial fan, the debris flow deposition materials ultimately accumulated near these buildings.

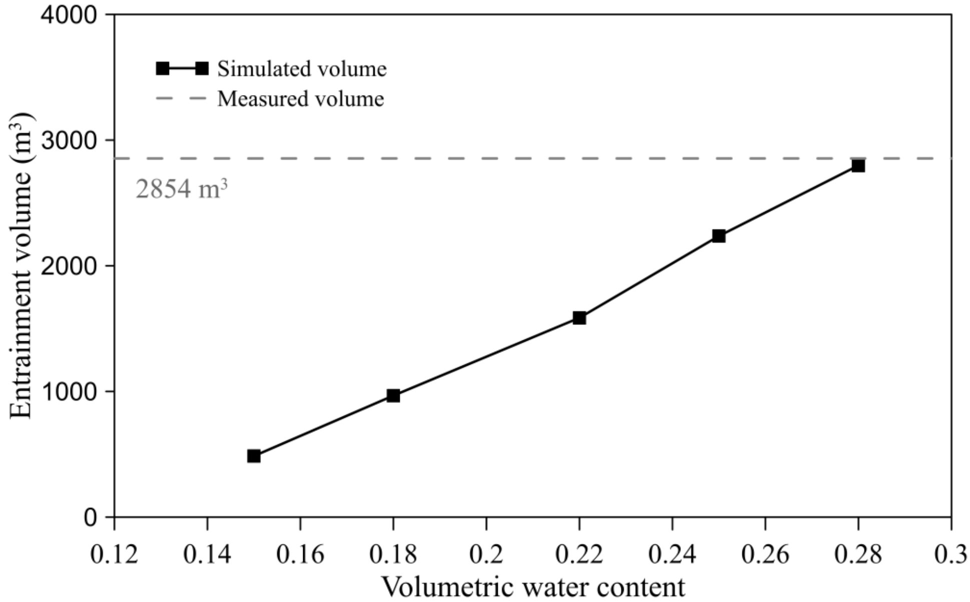

Figure 6.8 Effects of varying bed water content on the entrainment volume.

We also studied the variation characteristics of the entrainment volume under different sediment water contents, as shown in Figure 6.8. It can be observed that the erosion volume increases with the increase in water content. When the water content reaches critical saturation, the sediment transport volume of the sediment bed closely matches the field survey results. Considering that this event was triggered by heavy rainfall, which was preceded by sufficient precipitation replenishment, the calibrated water content aligns with the actual conditions.

6.3. Case study 2: 2010 Hongchun gully debris-flow event, China

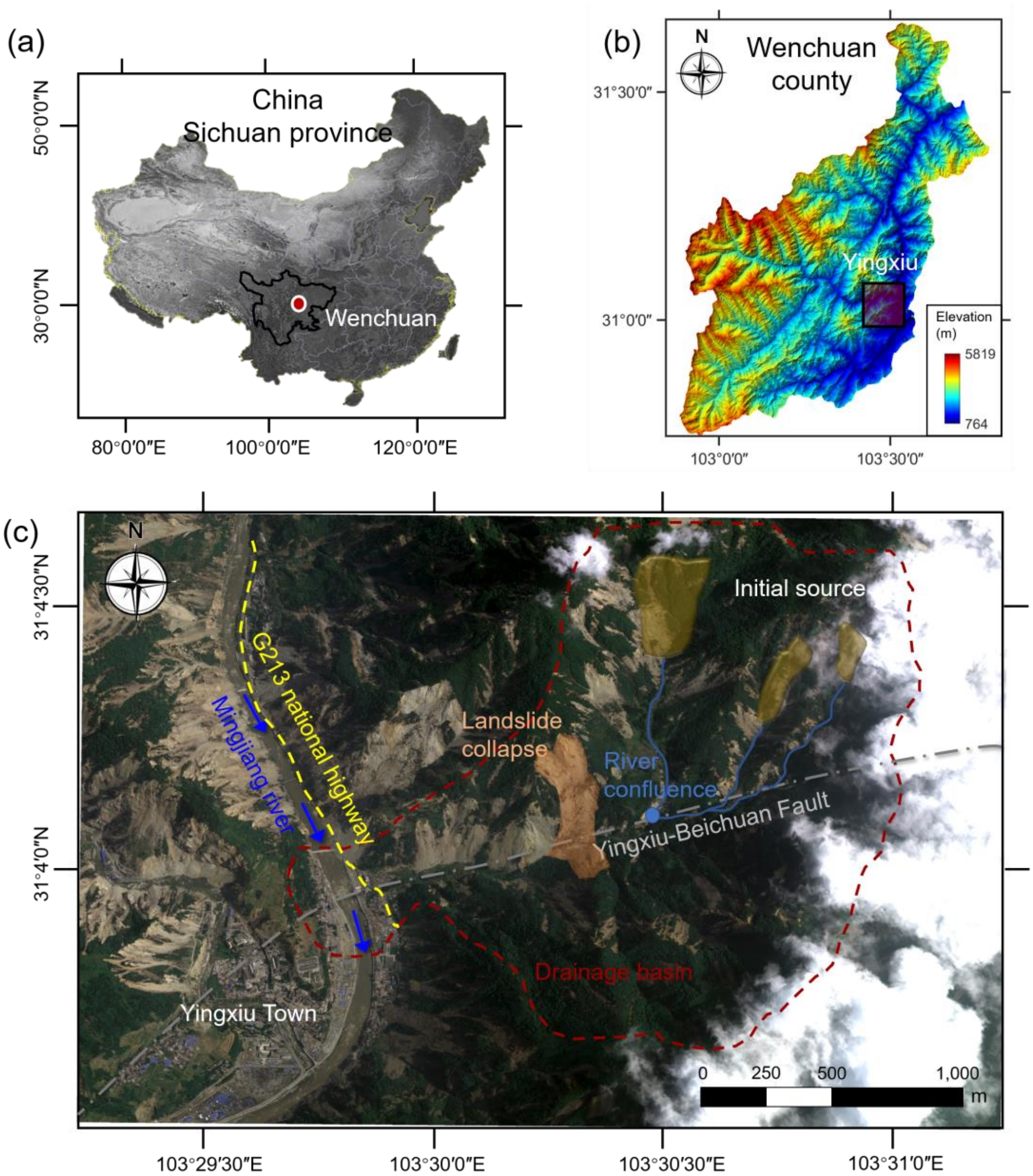

Figure 6.9 (a) Wenchuan Regional map in Sichuan province, China. (b) Local elevation cloud image of Wenchuan region. (c) Overview of the August 14, 2010, debris-flow event in Hongchun catchment.

The catastrophic event that occurred in the Hongchun catchment, Sichuan Province, on August 14, 2010, characterized by boulder-rich debris flow, is selected as a case study to evaluate the capability of the HBP-SPH-DCDEM model. The Hongchun catchment is located in Yingxiu town, Beichuan County of Sichuan

Province, China, approximately 3.0 km northeast of the epicenter of the 2008 Ms 8.0 Wenchuan earthquake. It is characterized by a sector morphology and medium-relief landscapes with craggy mountains (Tang et al. 2012). As shown in Figure 6.9, the Yingxiu-Beichuan fault, which triggered the Wenchuan earthquake, crosses the study area. Although the event contained a large amount of boulders and cobbles, the nature of the sand-fluid mixture remained a viscous debris flow.

6.3.1. Disaster background and motivation

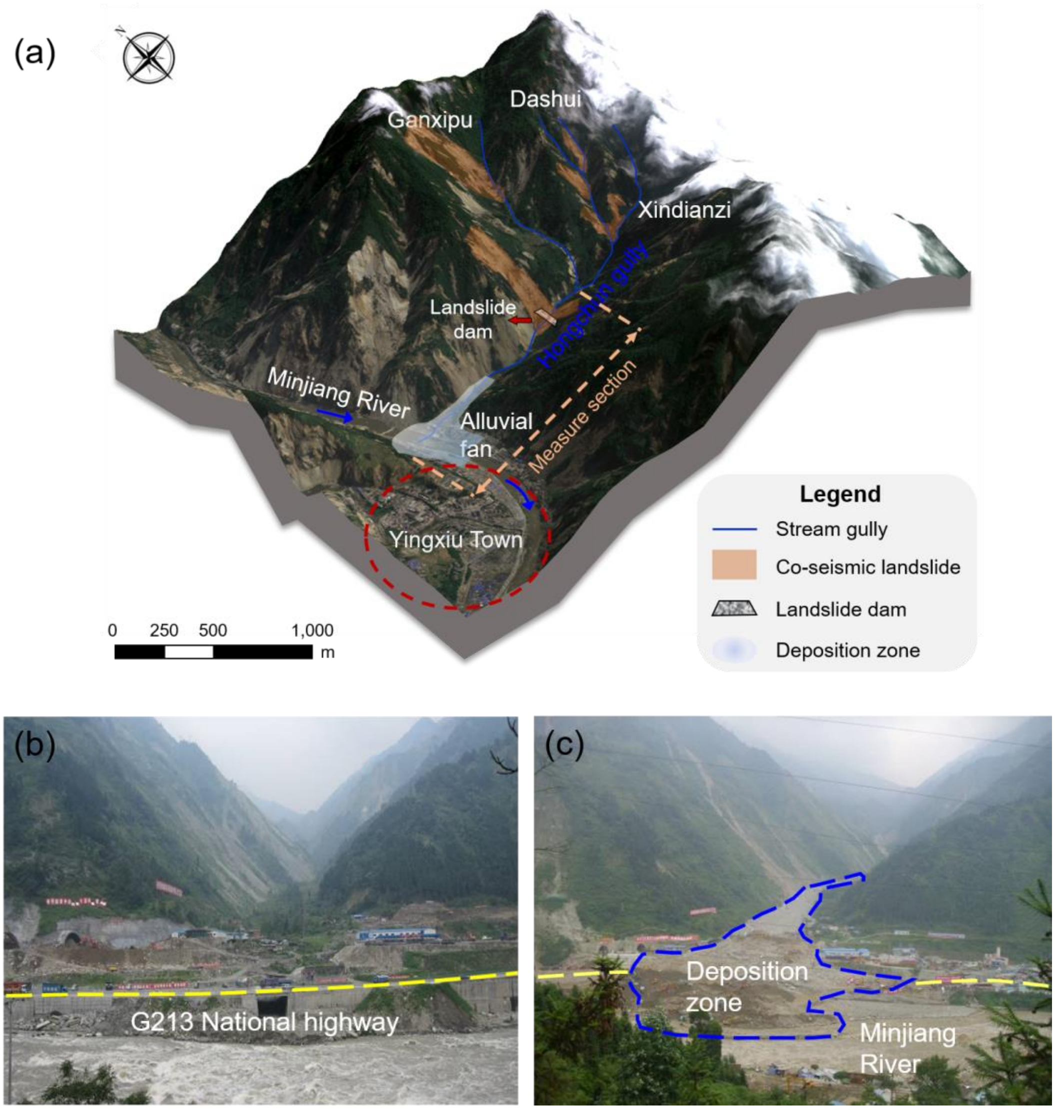

Figure 6.10 Overview of the August 14, 2010, Hongchun debris-flow event. (a) Overall illustration of the debris-flow event. (b) The alluvial fan before the event. (c) The alluvial fan after the event.

The Hongchun catchment area covers 5.35 km^2 and consists of a principal gully on the left bank of the Minjiang River and three upstream branch gullies (Ganxipu, Dashui, and Xindianzi), as shown in Figure 6.10a. The incised V-shaped gully is 3.60 km in length, with elevations ranging from 880 m to 1700 m and an average channel slope of 358‰. The steepest branch, Xindianzi, has the highest gradient of 538‰. The slopes on both sides of the channel are precipitous, with an average slope angle of 35°. Downstream of the junction of the tributaries, alternating steep and gentle spatial variations are observed.

Historically, the Hongchun catchment has been prone to debris flows. Two debris-flow events were reported before the 2008 Ms 8.0 Wenchuan earthquake (Shen et al. 2020). The loosely scattered debris mass was primarily distributed along both sides of the gully. According to a field investigation (Gan et al. 2012), 52 sediment sources with a total mass volume of 3.5814×10^6 m^3 were found within the catchment before the 2010 debris-flow event, among which 1.7890×10^6 m^3 was presumed to be involved in the debris-flow process. Table 6.3 indicates the sources of the loosened materials involved in this event, which were gathered during an in-situ survey (Ma et al. 2023) after the event.

The event was triggered by severe rainfall from August 12 to 14, 2010, resulting in a total precipitation of 162.1 mm in the catchment area (Xu et al. 2012; Shen et al. 2019). The intense rainfall infiltration reduced soil strength and remobilized the co-seismic landslide materials in the three branches, as detailed in Table 6.3. The remobilized material transitioned into a debris-flow mass with a total volume of 80.5×10^4 m^3, half of which was deposited on the alluvial fan. Photographs taken before and after the event illustrate the deposition pattern on the alluvial fan (Figures 6.10b and 6.10c), where the subgrade and the bridge of the G213 national highway crossing the gully were severely damaged (Ouyang et al. 2015; Shen et al. 2019). The event also resulted in a 10 m deep natural debris dam across the Minjiang River (Jiang et al. 2014). Due to its immense magnitude and destructive consequences, the Hongchun debris-flow event was declared the most catastrophic of the 21 debris flows that occurred along the Minjiang River (Tang et al. 2011).

Table 6.3 Distribution of the debris-flow source materials in the 2010 Hongchun catchment.

Tributary gullies in Hongchun catchment	Collapsed sources ($\times 10^4$ m^3)[1]	Channel sources ($\times 10^4$ m^3)[1]	Sum ($\times 10^4$ m^3)
Ganxipu	11.20	10.20	21.40
Dashui	3.90	2.70	6.60
Xindianzi	3.20	2.00	5.20
Upstream[2]	0.30	3.70	4.00
Midstream[2]	30.10	10.70	40.80
Downstream[2]	2.50	2.00	4.50
Total volume	/	/	80.50

[1] The loose sediment from the collapsed area and the channel area is referred to as Collapsed sources and Channel sources, respectively.
[2] These ditch sections refer to the part of the main gully below the junction of tributaries.

According to the investigation, the initiation of the landslide deposits in the mid-section of Ganxipu Gully is one of the significant sources for triggering the Hongchun Gully debris flow. Persistent rainfall before the debris flow had nearly saturated the loose soil layers in the landslide accumulation area. Simultaneously, the rock fissures in the steep rock area at the back of the landslide zone were filled with water, causing the rocks with reduced post-earthquake stability to collapse. The large boulders that collapsed rolled along the upstream side of the landslide accumulation. Due to the saturated loose layers at the lower part of the slope, which had low shear strength, the rolling boulders picked up loose soil from the slope surface, causing intense gully erosion. The large boulders, loose soil, and rainwater converged downstream of Ganxipu Gully, becoming the triggering factors for the debris flow. Furthermore, the debris flow deposits generated after the gully erosion temporarily blocked the gully, causing breaches and resulting in a debris flow of considerable scale and volume.

The source materials of the debris flow event in Hongchun Gully included a large number of boulders and gravel, and particle sorting is poor, as shown in Figure 6.11. Especially in the downstream channel of Ganxipu, the largest boulders deposited had diameters exceeding 5 m, while in other channels, numerous boulders with diameters ranging from 0.6 to 2 m were observed. These massive boulder deposits, along with gravel, sand, clay, and water mixtures, constituted this destructive debris flow disaster.

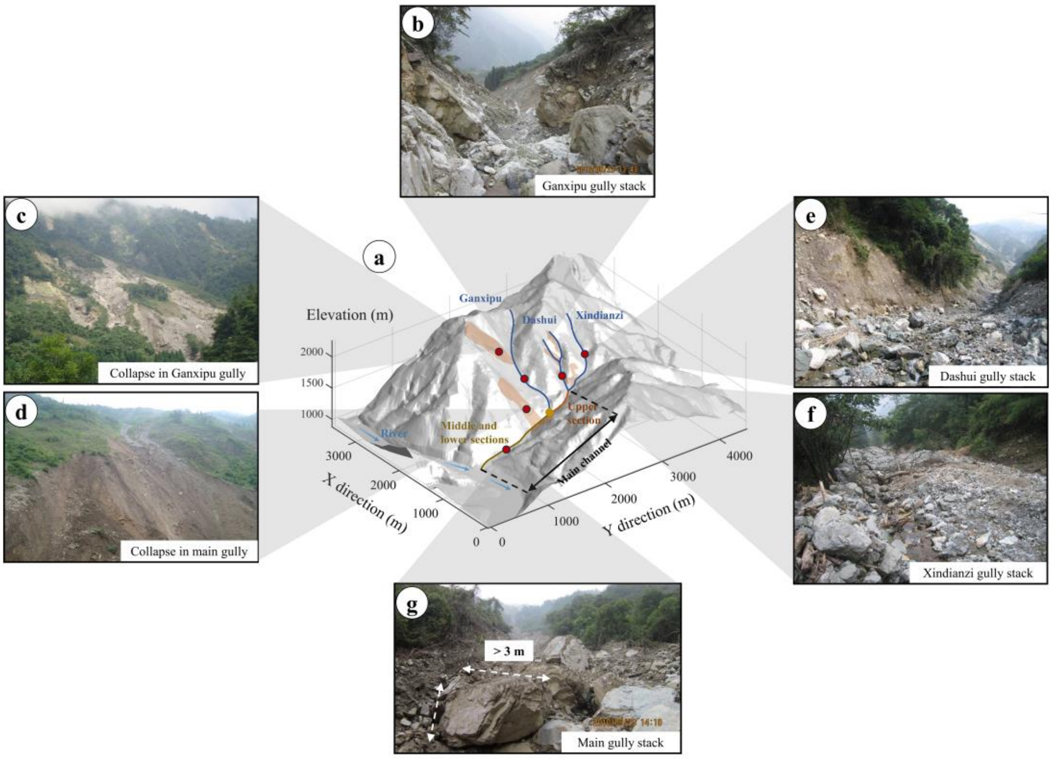

Figure 6.11 (a) The DTM model and gully features of the Hongchun basin. (b) Characteristics of sediment accumulation in the Ganxipu Gully. (c) Collapse source on the right side of Ganxipu. (d) Collapse source on the right side of the main gully. (e) Sediment accumulation in the Dashui Gully. (f) Xindianzi gully stack. (g) Upstream sediments of the main gully deposits.

6.3.2. NUMERICAL MODELLING AND SETUP

Similar to the Yohutagawa case, the three-dimensional numerical modeling of the Hongchun Gully terrain is based on DTM (10 m resolution) and field survey data. As shown in Figure 6.12a, we delineated the entire watershed potentially affected by moving particles, with the main channel extending up to 3350 meters. Given the vast extent of this large-scale case, employing multi-layer modeling of debris flow and sediment beds exceeds our current computational capacity, especially in regions where erosion depth exceeds 10 m. Modeling an erosion bed layer with acceptable accuracy in this range would require a particle scale in the billions. Therefore, in this case, we did not consider the erosion and entrainment effects of the sediment. Instead, the additional material generated by erosion was incorporated into the initial source.

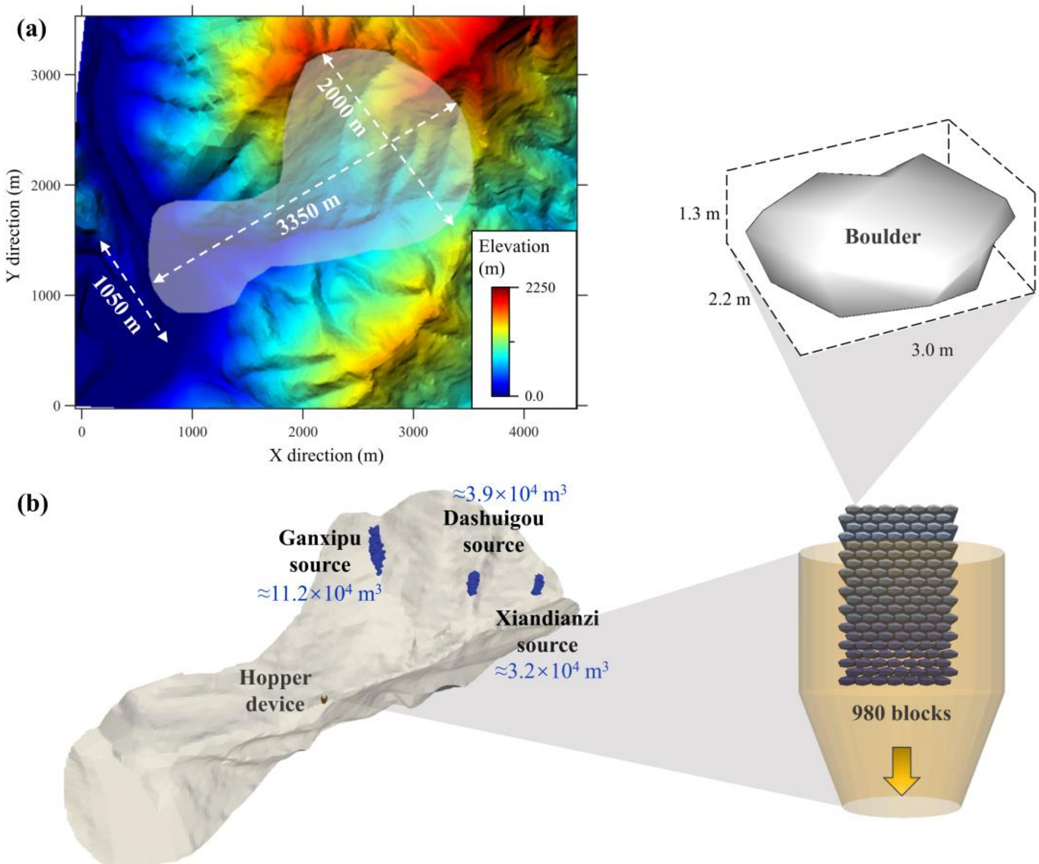

Figure 6.12 (a) The elevation map of the Hongchun Gully basin (10 m resolution) and the delineated simulation area. (b) 3-D modelling of the Hongchun terrain with three initiating sources and hopper device.

Figure 6.12b illustrates the three-dimensional modeling schematic of the Hongchun Gully target area within the SPH environment. Based on field survey data and aerial images, we placed the initial sources at the corresponding locations in Ganxipu, Dashui, and Xiandizi gullies. Additionally, considering that boulders are mostly concentrated downstream of Ganxipu Gully and in the mid to downstream sections of the main channel, we simplified the computational process by using a hopper-stone release device to systematically position thousands of boulders with a maximum diameter of 3 m in the midstream of the main channel, as shown in Figure 6.12b. We calculated the approximate time for the upstream materials to reach the boulder locations and froze the boulders and the interior of the hopper until the debris-flow front reached the area below the hopper. The boulders were then released in batches at a constant rate through the hopper opening and integrated into the debris flow.

Table 6.4 Controlling parameters and related material properties in the dynamic simulation of the 2010 Hongchun gully debris-flow event.

Source material	Parameter	Notation	Unit	Value
Initial mass (water saturated)	Bulk density	ρ_i	kg/m^3	2020
	Cohesion coefficient	c_i	Pa	100
	Internal friction angle	φ_i	°	30
	Kinematic viscosity	υ_i	m^2/s	0.002
	Porosity	n_i	/	0.40
	Debris flow concentration	C_d	/	0.44
	Exponential index	m	/	100
	Power law index	n	/	1.0
Boulders	Bulk density	ρ_b	kg/m^3	2600
	Young's modulus	E	GN m^{-2}	8.0
	Poisson's ratio	υ	/	0.3
	Kinetic friction	μ_f	/	0.35

Table 6.4 listed the controlling parameters and related material properties in the dynamic simulation Hongchun gully debris-flow event. Most of the parameter values are based on field survey data, while the material properties of the boulders are still referenced from limestone. For the numerical scheme, an initial particle distance of 0.65 is set, generating 1,288,565 fluid particles, 83,300 solid particles (comprising 980 blocks), and 9,953,530 boundary particles. Other numerical parameters are referenced from the Yohutagawa case and summarized in Table 6.5.

Table 6.5 Numerical setup and parameters used in the dynamic simulation.

Parameter	Notation	Unit	Value
Particle distance	dp	m	0.65
Number of initial mass particles	N_f	/	1,288,565
Number of solid particles	N_s	/	83,300
Number of boundary particles	N_b	/	9,953,530
Debris-flow duration	t	s	220
Sound speed coefficient	ξ	/	20
EoS constant	γ	/	7
Density diffusion coefficient	δ_d	/	0.1
Verlet steps	S_{verlet}	/	40
CFL coefficient[2]	CFL	/	0.2

6.3.2. RESULTS ANALYSIS AND DISCUSSION

It should be noted that the current program we have developed consumes a significant amount of computational resources for large-scale DEM blocks and fluid-solid systems. Therefore, the increase in mass and momentum is neglected, and there is a limitation on the number of blocks. Consequently, this section aims to qualitatively reproduce and analyze the impact range of the disaster event. As illustrated in Figure 6.13, the time-space evolution of the debris-flow mass in Hongchun Gully is successfully replicated. The initial sources of the three upstream tributaries rapidly extended and accelerated along the channels after the simulation began. Among them, the downstream section of Ganxipu Gully is extremely steep, causing the debris flow to reach a maximum speed of over 30 m/s. After approximately 40 s, the debris flow materials in Dashui and Xiandizi Gullies converged in the upper section of the main channel. About 10 s later, the flowing materials from the three tributaries converged and quickly flowed toward the downstream of the main channel. Although the largest boulders set in the simulation have a diameter of over 3 m, they are still relatively small in the context of the entire Hongchun Gully terrain, making them difficult to distinguish clearly in Figure 6.13. In reality, after approximately 75 s, the debris-flow front reached the area below the

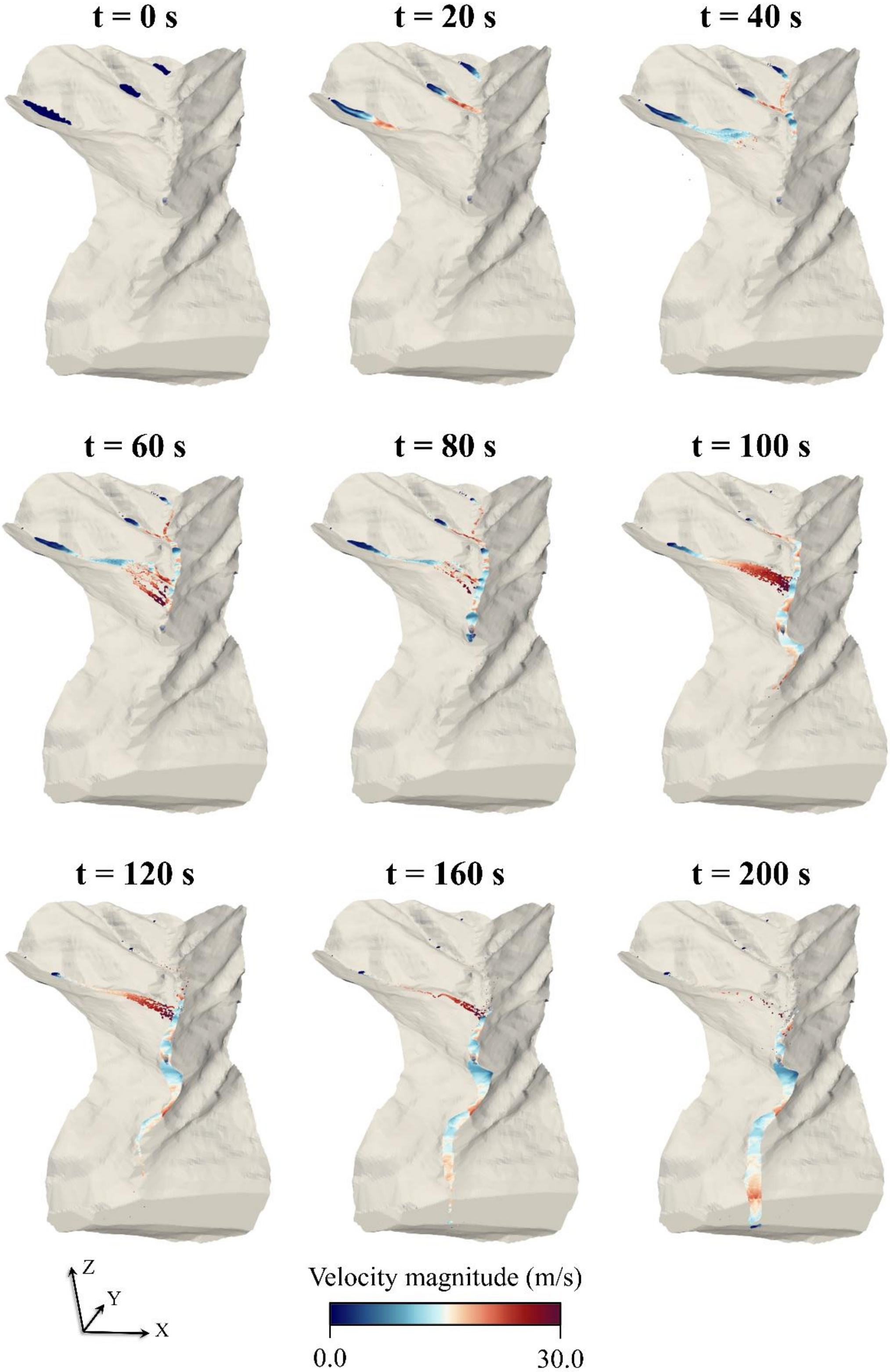

Figure 6.13 Snapshots of the run-out extent of the 2010 Hongchun Gully debris-flow event.

hopper, causing the boulders to be actively released and continuously discharged through the outlet, joining the flowing materials (Figure 6.14a). It should be noted that the impact of the boulders falling from the hopper on the dynamics of the debris flow was not considered here. After approximately 200 s, the debris flow surged into the Minjiang River, with an average flow speed of 20 m/s in this case.

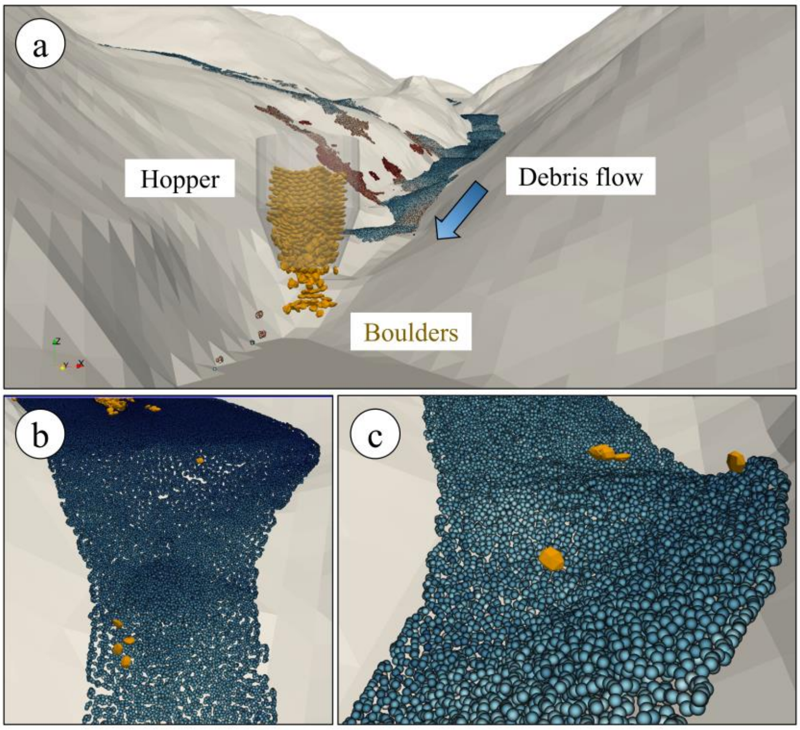

Figure 6.14 (a) Hopper-boulders device set above the terrain. (b)-(c) Particle-boulders moving along the channel.

Figure 6.14 illustrates how the boulders are incorporated into the movement of the debris flow. It can be seen that the boulders exhibit sliding rather than flowing behavior on the terrain, and their movement lags behind the debris flow fluid, as shown in Figure 6.14b. Unfortunately, we are currently unable to generate more boulders to more accurately reflect the dynamic process of such large-scale, boulder-rich debris flows. More detailed quantitative studies require the future development of more efficient multi-physics coupling models.

6.4. CONCLUSIONS

This chapter achieves the up-scaling from laboratory numerical tests to full-scale disaster analysis using the proposed multi-phase particle method discussed earlier. In particular, we select two typical real-world cases, corresponding to two types of debris flows: viscous and boulder-rich. For these cases, we conduct three-dimensional particle modeling, full-scale simulations, and comparative analysis with field survey data. After careful validation and discussion, we reach the following conclusions:

(1) The 2010 Yohutagawa debris flow event originated from a mixture of upstream slope failure and sediment materials triggered by heavy rainfall. During the incident, the channel sediment approached saturation after sufficient rainfall, significantly reducing shear strength. As a result, the debris flow volume increased substantially due to erosion and entrainment. Field surveys indicated that the area contained few large particles. Consequently, this event was classified as a viscous debris flow and used to validate the proposed TLMP-SPH model.

First, three-dimensional modeling of the target watershed was conducted based on digital terrain models (DTM) and field survey data, including elevation models, source material, erodible areas, check dams, and buildings on the alluvial fan. The simulation results successfully reproduced the dynamic process of the Yohutagawa debris-flow event, particularly depicting the deposition morphology on the alluvial fan. By adjusting the water content of the bed sediment, the erosion volume was calibrated. This case study successfully validated the TLMP-SPH model's capability to describe the dynamic behavior of viscous debris flows, particularly the complex processes of erosion, entrainment, and deposition, as well as the resulting mass growth and momentum feedback from the sediment.

(2) Based on the 2010 Hongchun Gully debris flow case, we construct a three-dimensional numerical analysis model and its initial source using DTM. Using the HBP-SPH-DCDEM method, we qualitatively reproduce the dynamic process of debris flow carrying large boulders along complex terrain. In this case, the boulders are also introduced into the debris flow through a hopper device in a constant discharge manner, creating a multi-scale, multi-physics motion field. Although the dynamic process of boulder-rich flow along the channel is qualitatively reproduced, limitations in computational resources prevent the construction of an erodible bed

layer to replicate the key process of mass growth and momentum feedback due to erosion and entrainment in the debris flow, and the number of boulders is also limited. Future research necessitates the development of more efficient and defined multi-physics, multi-scale coupling analysis models.

References

Baselt, I., de Oliveira, G.Q., Fischer, J.-T. & Pudasaini, S.P. 2022. Deposition morphology in large-scale laboratory stony debris flows. Geomorphology 396, 107992.

Delannay, R., Valance, A., Mangeney, A., Roche, O. & Richard, P. 2017. Granular and particle-laden flows: from laboratory experiments to field observations. Journal of Physics D: Applied Physics 50(5), 053001.

Fávero Neto, A.H., Askarinejad, A., Springman, S.M. & Borja, R.I. 2020. Simulation of debris flow on an instrumented test slope using an updated Lagrangian continuum particle method. Acta Geotechnica 15, 2757-2777.

Gan, J., Sun, H., Huang, R., Tan, Y., Fang, C., Li, Q. & Xu, X. 2012. Study on mechanism of formation and river blocking of Hongchuangou giant debris flow at Yingxiu of Wenchuan County. Journal of catastrophology 27(1), 5-9.

Han, Z., Chen, G., Li, Y., Zhang, H. & He, Y. 2016. Elementary analysis on the bed-sediment entrainment by debris flow and its application using the TopFlowDF model. Natural Hazards and Risk 7(2), 764-785.

Han, Z., Su, B., Li, Y., Wang, W., Wang, W., Huang, J. & Chen, G. 2019. Numerical simulation of debris-flow behavior based on the SPH method incorporating the Herschel-Bulkley-Papanastasiou rheology model. Engineering Geology 255, 26-36.

Iverson, R.M. 2015. Scaling and design of landslide and debris-flow experiments. Geomorphology 244, 9-20.

Iverson, R.M., Logan, M., LaHusen, R.G. & Berti, M. 2010. The perfect debris flow? Aggregated results from 28 large-scale experiments. Journal of Geophysical Research: Earth Surface 115(F3).

Iverson, R.M., Reid, M.E., Logan, M., LaHusen, R.G., Godt, J.W. & Griswold, J.P. 2011. Positive feedback and momentum growth during debris-flow entrainment of wet bed sediment. Nature Geoscience 4(2), 116-121.

Jiang, Z., Zhu, J., Chang, M., Tang, D. & Huang, X. 2014. Dynamic evolution characteristics of Hongchun gully source area of debris flow in Wenchuan earthquake region. Mountain Research 32(1), 81-88.

Komatina, D. & Jovanovic, M. 1997. Experimental study of steady and unsteady free surface flows with water-clay mixtures. Journal of Hydraulic Research 35(5), 579-590.

Ma, Y., Han, Z., Li, Y., Chen, G., Wang, W., Chen, N., Hu, G., Zhao, L. & Dou, J. 2023. Robustness evaluation of the probability-based HTCA model for simulating debris-flow run-out extent: Case study of the 2010 Hongchun event, China. Engineering Geology 312, 106918.

Ouyang, C., He, S. & Tang, C. 2015. Numerical analysis of dynamics of debris flow over erodible beds in Wenchuan earthquake-induced area. Engineering Geology 194, 62-72.

Shen, W., Li, T., Li, P., Shen, Y., Lei, Y., Guo, J.J.B.o.E.G. & Environment, t. 2019. The influence of the bed entrainment-induced rheology and topography changes on the propagation of flow-like landslides: a numerical investigation. Engineering Geology and the Environment 78, 4771-4785.

Shen, W., Wang, D., He, S. & Li, T. 2020. Numerical assessment of the impeding effect of check dams in the Hongchun debris flow gully, Sichuan Province, China. Bulletin of Engineering Geology and the Environment 79, 2833-2845.

Tang, C., van Asch, T.W., Chang, M., Chen, G.Q., Zhao, X.H. & Huang, X.C. 2012. Catastrophic debris flows on 13 August 2010 in the Qingping area, southwestern China: the combined effects of a strong earthquake and subsequent rainstorms. Geomorphology 139, 559-576.

Tang, C., Zhu, J., Ding, J., Cui, X.F., Chen, L. & Zhang, J.S. 2011. Catastrophic debris flows triggered by a 14 August 2010 rainfall at the epicenter of the Wenchuan earthquake. Landslides 8, 485-497.

Vicari, H., Ng, C.W., Nordal, S., Thakur, V., De Silva, W.R.K., Liu, H. & Choi, C.E. 2022. The effects of upstream flexible barrier on the debris flow entrainment and impact dynamics on a terminal barrier. Canadian Geotechnical Journal 59(6), 1007-1019.

Xu, Q., Zhang, S., Li, W. & Van Asch, T.W. 2012. The 13 August 2010 catastrophic debris flows after the 2008 Wenchuan earthquake, China. Natural Hazards and Earth System Sciences 12(1), 201-216.

Yin, Y., Wang, F. & Sun, P. 2009. Landslide hazards triggered by the 2008 Wenchuan earthquake, Sichuan, China. Landslides 6, 139-152.

CHAPTER 7

Conclusions and future studies

7.1. Highlights and major conclusions

Research on numerical simulations of debris flows has a long history. Researchers have traditionally idealized this multi-scale (i.e., rock, debris, mud, water, snow, and ice), multi-phase (i.e., solid, fluid, and air), and multi-physics geophysical flow process as a single-layer, single-phase particle-fluid mixture, employing fixed rheological models to describe its dynamic processes. Alternatively, depth-integrated paradigms that ignore vertical flow fields and momentum redirection are used to reduce modeling and computational costs. While these simplifications and assumptions are somewhat valid, they inevitably lead to significant issues. Notably, key physical mechanisms such as non-linear coupling, phase changes, and sorting in the dynamic processes of erosion, entrainment, and deposition of debris flows are inadequately considered and validated. Specifically, the interaction between transported debris flow and underlying erodible bed sediments, which leads to mass growth and momentum feedback from the sediments, is crucial in determining the extent, scale, and destructiveness of debris flows. These issues cannot be sufficiently addressed within the existing models and methodological frameworks.

To address these issues, this thesis develops a high-performance numerical simulation program using advanced Lagrangian particle methods, specifically Smoothed Particle Hydrodynamics (SPH) and the Discrete Element Method (DEM).

This program integrates key physical mechanisms of debris flows into these particle-based methods. Following a framework that includes theoretical analysis, program development, experimental verification, and real-world case validations, a comprehensive method for the numerical simulation and analysis of debris flows is established.

The highlight of this study is its incisive identification and creative resolution of the following key issues in numerical research on debris flows: **(i)** How can the processes of erosion, entrainment, and deposition in debris flows be characterized within a Lagrangian particle framework? **(ii)** Why do some erosive debris flows generate higher mobility and volume, while others experience reduction? What are the mechanisms underlying these variations, and how can they be calculated? **(iii)** How can a coupling model of debris flow containing large boulders be constructed, and how can the interaction between the fluid phase and the irregular blocks be defined? The following are the solutions proposed by the author:

(1) Develop a two-layer, multi-phase SPH (TLMP-SPH) model for debris flow erosion, entrainment, and deposition behaviors.

In the three-dimensional SPH framework, erosion and entrainment behaviors are evaluated through the analysis of bed failure and the subsequent particle transport by the intrusive flow, as opposed to depth-averaged methods that assess entrainment rates on a per-grid basis. It is, therefore, essential to rigorously define the yield criteria for particles, which serve as the phase transition mechanism. Inspired by the liquid-sediment multiphase scouring method, this study proposes a two-layer, multi-phase SPH model based on the non-Newtonian Herschel-Bulkley-Papanastasiou (HBP) model for dilatant (shear thickening) and pseudoplastic (shear thinning) flows. This approach combines the HBP model with yield criteria such as Drucker-Prager (DP) and Mohr-Coulomb (MC). By incorporating the two-phase nature of the HBP model, the proposed methodology simulates the phase transition processes of sediment beds under rapid flow erosion, offering a novel and efficient approach for the numerical modeling of complex geophysical flows.

The TLMP-SPH model is verified through numerical tests, including pure water scour and dense flow erosion. Comparative analyses indicate that this method accurately reproduces experimental observations, encompassing the morphological characteristics of the erosion interface, the velocity field distribution, and displacement distances.

(2) Pioneer a hydro-poro-mechanics-based pore water pressure algorithm embedded within the TLMP-SPH scheme to simulate the pore pressure response and flow momentum growth of debris flows on beds with varying wetness.

It is widely recognized that the mass growth and momentum feedback of debris flow from bed sediment are regulated by scale-sensitive, time-dependent pore water pressure, which exhibit pronounced anisotropy and nonlinearity. To address this issue, an efficient hydro-poro-mechanics-based pore pressure response algorithm, derived from volumetric strains and Darcy law, is extended to quasi-saturated condition and integrated into the existing SPH scheme. Especially, a Laplace model that balances accuracy and computational efficiency is adopted to solve the second derivative term in the pore pressure equation, thereby improving the accuracy of the dynamic response of pore pressure.

To mitigate the size effect, we meticulously tested the method through a comprehensive series of full-scale, well-documented entrainment experiments. The findings reveal that the model proficiently captures and replicates the intricate dynamics of flow-momentum growth, reflected in erosion-induced variations in volume and mobility. Our methodology establishes a definitive connection between volumetric water content and pore pressure response, further emphasizing its ability to characterize levee-channel and deposition morphology. This research is the first to model debris flow on beds with differing moisture levels from a particulate perspective. It addresses the enduring question of why certain erosive debris flows exhibit increased mobility and scale-up, while others show decreased mobility and volume.

(3) Construct a two-way resolved SPH-DCDEM coupling scheme for dynamic simulation of boulder-rich debris flows.

Relying solely on either individual continuum or discrete models is insufficient for accurately capturing the multi-scale, multi-phase nature of debris flows. Consequently, a two-way resolved coupling numerical method is proposed to simulate the dynamic behavior of boulder-rich debris flows. In this approach, fine-grained materials and water are collectively simplified into a viscoplastic model that follows the HBP non-Newtonian fluid constitutive behavior. The DCDEM is employed to represent irregular boulders or debris with particle sizes significantly larger than the fluid, explicitly defining the interaction forces between fluid and solid, as well as between solid particles.

To validate the proposed method, we conduct numerical tests on the collapse of multi-layered aluminum columns and an aluminum column-water dam system. The simulation results demonstrate that the model effectively captures the dynamic process of collapse and mutual collision of the aluminum cylinders, achieving high accuracy for solid-liquid systems. Additionally, the HBP-SPH-DCDEM method undergoes further validation through debris flow impact tests at different slope angles. The model accurately captures the deposition morphology and impact force on the wall of the debris flow, with boulders traveling further in a turbulent state. The simulation results effectively replicate pressure variation characteristics on the wall and align with experimental observations, verifying the model's feasibility.

(4) Apply the proposed method to full-scale events to validate its capability.

The up-scaling from laboratory to field-scale hazard prediction still encounters various conceptual and technical challenges such as scaling effect and parameter selection. To over these constraints, we selected two real cases for inversion and analysis, focusing on two typical types of debris flows: viscous debris flows and boulder-rich debris flows. For both incidents, full-scale modeling was conducted, generating millions of particles. The specific outcomes of these analyses include:

The 2010 Yohutagawa debris-flow event is selected as a case study to validate the proposed TLMP-SPH model, focusing on the complex processes of erosion, entrainment, and deposition behaviors, as well as the mass growth and feedback of viscous debris flow on wet bed sediment. The check dam in this event plays a crucial role in determining the extent of the deposition. Ultimately, the simulation results successfully capture the dynamic process of the debris flow, thoroughly depicting the deposition morphology on the alluvial fan. Notably, due to the combined response of material properties, yield criteria, and phase transition mechanisms, a certain degree of sorting is observed between the upper and lower layers of material. The sediment particles predominantly deposit in the propagation area in front of the check dam, while the overlying debris flow layer mostly overtops the dam and accumulates near the buildings on the alluvial fan. Furthermore, sensitivity analysis and calibration of the sediment water content accurately invert the entrainment volume. Additionally, the dynamic process of debris flow carrying large boulders along complex terrain is also qualitative reproduced in the 2010 Hongchun gully event.

7.2. FUTURE STUDIES

This work attempts to construct a model within the Lagrangian particle method framework that includes the interaction of multiphase materials in debris flows and depicts their dynamic processes on complex terrains. Despite efforts to incorporate various critical physical mechanisms, the current approach still simplifies or omits some key mechanisms of debris flows. These simplifications or omissions may be due to computational constraints, contentious mechanisms, or inherent limitations in the numerical framework itself. These issues will persist until the considered mechanisms are comprehensive, more refined models are integrated, and higher-precision numerical methods are employed. Specifically, future particle-based numerical simulation methods for debris flows need to focus on the following issues:

(1) Limitations of the Weakly Compressible SPH scheme in depicting the physical mechanisms of debris flows: multiphase and multiscale interactions between solid particles and interstitial fluid, particle sorting, phase transitions, dewatering, etc.

Analyzing and modeling mixed materials as weakly compressible particle-fluid mixtures is the current mainstream approach in numerical research on geophysical flows. However, it must be acknowledged that the weakly compressible scheme inherently has limitations in depicting the mechanisms involving multiscale particle interactions, which are crucial factors affecting the dynamic processes of debris flows. Additionally, the equation of state used in weakly compressible pressure calculations is often criticized for its poor stability and non-physical dependencies.

The author believes that the theoretical and computational conditions for constructing large-scale geophysical flow analyses using incompressible SPH schemes are now well-established. The problem, however, lies in the more complex modeling and parameter acquisition conditions compared to WCSPH. Addressing these issues will facilitate a better understanding and analysis of some extraordinary geophysical flow phenomena, such as long-runout landslides and the mechanisms behind reduced dissipation in large-scale avalanches.

(2) Field-scale disaster prediction considering heterogeneity

Debris flows and most geophysical flows on the Earth's surface are inherently heterogeneous. Numerical calculations often overlook these effects to simplify computations. While this may not be evident in laboratory-scale tests, field-scale disaster prediction and simulation must account for the impacts of temporal evolution and spatial distribution heterogeneity. For mountainous debris flows, these impacts include, but are not limited to, bed surface roughness, particle size distribution, changes in pore water content, sediment cohesion, and vegetation cover. Field-scale disaster predictions must fully consider the effects of heterogeneity to accurately reflect the occurrence, evolution, and impact of disasters.

(3) Multi-hazard chains induced by landslide and debris flow

The typical "earthquake-landslide-debris flow disaster chain" has garnered widespread attention because multi-hazard chains often result in more severe damage and losses compared to individual events. Debris flows and their associated hazards can occur independently, such as from a typhoon storm, or as part of a sequence triggered by earthquakes. The direct risks of such single events are evident, including high mobility with extensive run-out, erosion-induced volume increase, and substantial impact force. Although previous research has primarily focused on individual hazards, a comprehensive study of the entire chain process remains lacking. Predicting and modeling multi-hazard chains induced by debris flows is particularly challenging due to the complex nonlinear interactions between landslides, debris flows, erodible beds, dams, dammed lakes, and dam-breach floods. These secondary hazards significantly amplify the damage and involve the interaction of various physical fields.

Therefore, the numerical analysis and prediction of debris flow disaster chains require interdisciplinary knowledge. On one hand, it is necessary to overcome scale effects, address nonlinear coupling processes, and achieve multi-physical field coupling. On the other hand, attention must be paid to balancing the cost of parameter acquisition and computational efficiency. Given the massive amount of data involved in this process, it is anticipated that big data analysis and artificial intelligence technologies will be increasingly utilized. These technologies can extract patterns from extensive historical data and simulation results, optimizing model parameters and improving prediction outcomes, indicating a future trend.